Faculty of Applied Sciences
Department of Architecture, Geology, Environment and Construction
Division of Solid Mechanics, Fluids and Structures (MS^{2}F)

Study of the continuous casting of peritectic steel grades by a mesoscopic damage approach

Renée Schwartz

Jury: Jacqueline Lecomte-Beckers (ULg, President)
Anne Marie Habraken (ULg, Supervisor)
Manuel Bobadilla (ArcelorMittal, Research Center Maizière-lès-Metz)
Sylvie Castagne (Nanyang Technological University)
Dieter Senk (RWTH)
Michel Malingraux (ArcelorMittal, Industeel Belgium)

Mémoire déposé pour l'obtention du PhD en Sciences Appliquées

June, 2011

Faculty of Applied Sciences
Department of Architecture, Geology, Environment and Construction
Division of Solid Mechanics, Fluids and Structures (MS^{2}F)

Study of the continuous casting of peritectic steel grades by a mesoscopic damage approach

Renée Schwartz

Jury: Jacqueline Lecomte-Beckers (ULg, President)
Anne Marie Habraken (ULg, Supervisor)
Manuel Bobadilla (ArcelorMittal, Research Center Maizière-lès-Metz)
Sylvie Castagne (Nanyang Technological University)
Dieter Senk (RWTH)
Michel Malingraux (ArcelorMittal, Industeel Belgium)

Mémoire déposé pour l'obtention du PhD en Sciences Appliquées

June, 2011

Acknowledgments

This work has been done during the four years of my promotion at the University of Liège in the division of Solids Mechanics, Fluids and Structures.

Most especially I want to thank Anne Marie Habraken for her support, her guidance and for her patience through these years of research.

Additionally my gratitude goes to all the partners of this project coming from Charleroi, Isbergues, Metz or Aachen for their help.

My biggest gratitude goes to my colleagues and friends that I had the chance to met at the University of Liège and Aachen. Cricri, Fred, Ananas-Framboise, Cèd, Chantal, Harona, Clément, Lam, Sonia, Richard, Miry, Esra, Alex^2, Stephan and co.

Et pour finir, en français, je voudrais remercier très particulièrement ma famille qui m'a soutenue et poussée à aller au bout de ce projet.

Finalement merci à tous car j'en ai certainement oubliée et je vais m'en mordre les doigts pendant encore longtemps, en espérant qu'ils ne me le fassent pas payer.

Vielen Dank an alle.

Contents

Introduction **1**

1 Literature review **7**
1.1 Peritectic steels . . . 7
1.1.1 Peritectic transformation . . . 7
1.1.2 Peritectic steel grains microstructure . . . 9
1.1.3 Precipitation state in peritectic steels . . . 9
1.1.4 Steel microstructure observed in laboratory: challenges of sensitization . . . 10
1.2 Defects in CC products . . . 12
1.2.1 Regions of low ductility . . . 12
1.2.2 Transversal cracks . . . 14
1.3 Fracture analysis . . . 15
1.3.1 Fracture mechanisms map . . . 15
1.3.2 CC particular elements leading to fracture . . . 15
1.3.2.1 Oscillation marks . . . 15
1.3.2.2 Mechanical constrains . . . 17
1.3.2.3 Austenite to ferrite transformation . . . 17
1.3.2.4 Dynamic recrystallization . . . 18
1.4 Hot ductility analysis . . . 19
1.4.1 Ductility curves . . . 19
1.4.2 High ductility high temperature zone . . . 21
1.4.3 Transition HDH to embrittlement . . . 21
1.4.4 Ductility trough . . . 22
1.4.4.1 Austenitic grain boundary sliding (rupture at triple point) 22
1.4.4.2 Creep rupture (void nucleation, growth and coalescence) 24
1.4.5 Transition embrittlement to HDL . . . 25
1.4.6 High ductility low temperature zone . . . 25
1.5 Mechanical tests . . . 26
1.5.1 Hot tensile test . . . 26
1.5.2 Compression acoustic crack test . . . 28
1.5.3 Hot bending test . . . 28
1.5.4 Hot fatigue test . . . 28

1.6 Microalloying elements of peritectic steel grades . . . 29
1.6.1 Niobium . . . 30
1.6.2 Vanadium . . . 31
1.6.3 Combination of Niobium and Vanadium . . . 33
1.6.4 Titanium . . . 33
1.6.5 Other alloying elements . . . 33
1.6.6 Summary of the precipitates study . . . 34
1.6.7 Precipitation kinetic . . . 35
1.7 Conclusion of the literature review . . . 36

2 The damage model, its identification methodology and the sample treatment 39
2.1 Damage model description . . . 39
2.1.1 Modeling of the continuous casting process . . . 40
2.1.2 The grain . . . 41
2.1.3 The grain boundary . . . 41
2.1.3.1 The interface element . . . 41
2.1.3.2 The interface material law . . . 42
2.1.3.3 Law parameters . . . 47
2.1.4 Representative cell design . . . 47
2.1.5 Macro-Meso link . . . 51
2.2 Methodology to identify the damage model parameters . . . 54
2.2.1 Step A, the material rheology . . . 55
2.2.2 Step B, tensile tests on different geometries . . . 57
2.2.3 Step C, the representative cell . . . 57
2.2.4 Step D, the determination of the damage law parameters . . . 58
2.2.5 Step E, the simulation of the CC process . . . 59
2.3 Thermal treatment of the sample and test description . . . 60
2.3.1 Tensile test apparatus . . . 61
2.3.2 Thermal path . . . 62
2.3.2.1 Elevation of sample temperature . . . 62
2.3.2.2 Sensitization temperature . . . 62
2.3.2.3 Holding time . . . 63
2.3.2.4 Cooling of the sample . . . 64
2.3.2.5 Tensile test . . . 65
2.3.3 Conclusion on the damage model, its identification and the sample treatment . . . 66

3 Rheology and damage tests: description, results and analyzes toward the representative mesoscopic cell 67
3.1 Determination of the rheological parameters . . . 67
3.1.1 Study of the thermal cycle applied to the tensile samples . . . 68
3.1.1.1 Experimental process . . . 68
3.1.1.2 Sampling . . . 70
3.1.1.3 Metallographic results . . . 72
3.1.1.4 Conclusion of the thermal path study . . . 73
3.1.1.5 Further work . . . 75
3.1.2 Determination of the ductility trough . . . 75

3.1.2.1 Results of the ductility trough analysis . . . 75
3.1.2.2 Analysis of the precipitate effect on the ductility trough 78
3.1.3 Rheological parameters . . . 83
3.1.3.1 Hot compression tests . . . 84
3.1.3.2 Hot tensile tests . . . 86
3.1.3.3 Identification of the Norton-Hoff law . . . 86
3.1.3.4 Norton-Hoff law parameters . . . 87
3.1.3.5 Extrapolation of the results to all the required temperature . . . 91
3.1.3.6 Comparison of the tensile and compression tests and numerical results . . . 94
3.2 Tensile histories for mesoscopic application . . . 95
3.2.1 Determination of the studied cases . . . 95
3.2.2 Experimental and numerical correlation of the HTT . . . 97
3.2.3 Analysis of the differences between experimental and numerical simulations . . . 98
3.2.3.1 Finite element choice . . . 98
3.2.3.2 Mesh density . . . 98
3.2.3.3 Sensitivity of the rheological law . . . 100
3.2.3.4 Comparison of R2 and R4 sample shapes . . . 100
3.3 Representative cell design . . . 102
3.3.1 Macroscopic level - grain design . . . 102
3.4 Conclusion on the rheology and damage tests chapter . . . 102

4 Damage model identification, damage parameter analysis 103
4.1 Tensile test sample to representative cell . . . 103
4.1.1 General view of the representative cell position in the tensile test sample . . . 103
4.1.2 Determination of the location of the numerical stress-strain sampling . . . 106
4.1.3 Calculations performed for the representative cell loading . . . 109
4.2 Sensitivity analysis of the damage law parameters . . . 112
4.2.1 Damage path . . . 113
4.2.2 Analysis of the damage evolution . . . 114
4.2.3 Analysis of the crack event . . . 117
4.3 Damage law parameters fitting for peritectic steel grades . . . 119
4.3.1 Parameters taken from the literature . . . 119
4.3.2 Damage law parameters determined on the basis of rheological parameters determination . . . 119
4.3.3 Parameters determined through micrographic analysis . . . 120
4.3.3.1 SEM study on **A** steel grade . . . 121
4.3.3.2 TEM study on the peritectic steel grades studied . . . 122
4.3.3.3 STEM study on **B** and **C** steel grades . . . 127
4.3.4 Parameters adjustment . . . 128
4.3.4.1 Fitting of the damage parameters . . . 129
4.3.4.2 N_I variability as a function of temperature . . . 131
4.3.4.3 Damage law parameters fitting on grade **A** . . . 132
4.3.4.4 Damage law parameters fitting on grade **B** . . . 134

4.3.4.5 Damage law parameters fitting on grade **C** 135
4.3.5 Comparison of the damage law parameters 136
4.3.5.1 Effect of N_I and the beginning of the nucleation 138
4.3.5.2 Effect of F_n 139
4.3.5.3 Effect of N_{max}/N_I and the end of the nucleation 140
4.4 Validation of the Macro-Meso transfer 141
4.4.1 Macro-Meso transfer for steel grade **A** 141
4.4.2 Macro-Meso transfer for steel grade **B** 145
4.4.3 Macro-Meso transfer for steel grade **C** 145
4.4.4 Conclusions about the Macro-Meso transfer 148
4.5 Conclusion of the mesoscopic study of the crack appearance in CC . . . 149

5 Industrial application 151
5.1 Thercast program 152
5.2 Continuous caster results on grade **C** application 152
5.2.1 Defects detected on the continuous caster of **C** 153
5.2.2 Thercast calculations performed on **C** caster 153
5.2.3 Thercast results on **C** caster 156
5.2.3.1 Study of the thermal behavior 156
5.2.3.2 Study of the mechanical behavior 158
5.3 Continuous caster to representative cell 162
5.3.1 Data transfer from the macroscopic simulation to the mesoscopic representative cell 162
5.3.2 Calculation of the strain field 164
5.4 Data transfer validation 167
5.4.1 Classical transfer to the representative cell 167
5.4.2 Transfer tests done on one element 169
5.5 Damage results for the CC application on **C** grade 172
5.6 Conclusions on the practical case 175

Conclusion and perspectives 177

Bibliography 183

A Micrographs from B grade used for Thermal path determination A.1

B Sensitivity analysis figures B.1

C SEM-EDS study C.1

D ISO643 D.1

E Rheological law correlation with experimental HTT E.1

F Damage moments comparison of HTT flow curves F.1

List of Figures

0.1 Illustration of the different stress states experimented by the slab during CC [Pas03] . . . 2

1.1 Possible reactions between three phases in the case of a binary system . 8
1.2 Fe-C diagram . . . 8
1.3 Compilation of γ grain size at high temperature gathered from literature 11
1.4 Position and defect type in the CC slab [Bri77] . . . 13
1.5 Schematic evolution of the knowledge about the low ductility regions of peritectic steels in the hot tensile test of in-situ solidified specimens [Wol97] . . . 13
1.6 Macroscopic (a) and microscopic (b) view of a longitudinal crack on a peritectic steel grade after the CC process (data provided by Arcelor Research) . . . 14
1.7 Types of segregated cracks during CC [Pap03] . . . 15
1.8 Fracture mechanism map for pure iron for various grain size [NIST] . . 16
1.9 Classification of oscillation marks into three types; (a)hook, (b)depression and (c)folded depression type in CC [Pap03] . . . 16
1.10 Enlargement of the critical area where ductility can be decreased by the thermal path of the slab shell . . . 17
1.11 Effect of alloying elements on the steel microstructure . . . 18
1.12 Example of a ductility curve obtained by hot tensile tests [Moh02] . . . 19
1.13 Calculation of the necking for the determination of the ductility of the material . . . 20
1.14 General shape of a ductility curve in the case of peritectic steel in conditions similar to thos of CC . . . 20
1.15 Ferrite film induced cracking during $\gamma \rightarrow \alpha$ transformation for peritectic steels [Min91] . . . 22
1.16 Illustration of fracture surfaces of a Nb containing steel [Min93] . . . 23
1.17 Illustration of the damage initiation at triple grain boundaries [Yue95, Min91] . . . 23
1.18 Illustration of the grain boundary sliding (a) and fracture appearance (b) in peritectic steel pulled at 750°C and $\dot{\varepsilon}=5 \cdot 10^{-3}\mathrm{s}^{-1}$ [Suz84] . . . 23
1.19 Illustration of the mechanism of microvoid coalescence induced cracking for peritectic steels [Min91] . . . 25

1.20 Illustration of the damage at the ferrite film for the peritectic steel family in the case of transversal fracture [Suz84] 26
1.21 Presence of precipitates at the formed austenitic grain boundary in peritectic steels 31
1.22 Distribution of the V precipitates in the peritectic steel [Cro87] 32
1.23 Hardness of the Nb containing peritectic steel grade following quenching and tempering after holding for various times at 950°C [Cro87] 35
1.24 Illustration of the ductility loss and kinetic effect of V containing steels [Cro87] 36

2.1 Simulation of the CC process and transposition in the local approach [Cas07a] 40
2.2 Elements composing the grain in the mesoscopic model where circles are associated to the neighboring black dots that represents the mesh nodes 42
2.3 Discrete and continuous representations of the grain boundary: (a) Real geometry, (b) Virtual description at one integration point, (c) Void shape [Onc99] 44
2.4 Representative cell 49
2.5 (a) Metallographic inspection of the subsurface of a peritectic steel (b) with the austenite grains and ferrite grain-boundary (data provided by Arcelor Research) 49
2.6 Different ways of automatic meshing with the Delaunay-Voronoï diagrams [MATH] 50
2.7 Illustration of the meshing process for the grain boundaries [Cas07a] . . 51
2.8 Longitudinal elongation rate of the CC of Marcinelle, defining the risk of transversal cracking [Pas03] 52
2.9 Example of a slice extracted from the CC slab that has to be modeled in generalized plane strain state for the crack prediction [Pas03] 53
2.10 Thickness of the slice in generalized plane strain state [Pas03] 53
2.11 Application of the forces and degrees of freedom on the representative cell where the plane xy is associated to plane 3 in Figure 2.1 54
2.12 Diagram of the different steps which define the global strategy of modeling the crack prediction for peritectic steels during the continuous casting 56
2.13 Various sample shapes used in the hot tensile test machine, (a) without notch, (b) with 2 and 4mm notches [mm] 57
2.14 Scheme of the CC case modeling by extraction of the data recorded through macroscopic numerical simulation of the CC and application to the edges of the transition area of the representative cell 59
2.15 Schematic description of the thermal path applied for the tensile test to match the real CC conditions 60
2.16 Hot tensile test apparatus at the RWTH of Aachen 61
2.17 Precipitates formation at the equilibrium calculated for steel **B** (data provided by Arcelor Research) with the CEQCSI model 63
2.18 Shrink hole of a tensile test sample (data provided by IEHK, 2006) . . 64
2.19 Numericaly determined cooling curve of the large face of **A** slab (2.6m large) at 20cm from the corner during the CC process (data provided by Arcelor Research) 65

2.20 Stages of the ductility curve observed in function of the steel morphology and the forces recorded during hot tensile test [Pan05b] 66

3.1 Time-Temperature curves for the samples 1 to 8 69
3.2 Time-Temperature curves for the samples 9 to 10 with a provisional cycle 70
3.3 Areas of the slab that are used for sampling 71
3.4 Electron discharge machining of the cylinders in the slab slice (with Figure 3.3 orientation) 71
3.5 Grain size evolution for both tested thermal path comparisons: (a) constant holding temperature (1250 and 1350°C), (b) thermal cycles at 1350°C during 5min 74
3.6 Ductility trough results for the three steel grades studied at $10^{-3}s^{-1}$ strain rate on unnotched samples ($\circ$ **A**, Δ **B**, + **C**) 76
3.7 Ductility curves of grade **A** for various sample shapes and strain rates . 77
3.8 Ductility curves of grade **B** for various sample shapes and strain rates . 77
3.9 Ductility curves of grade **C** for various sample shapes and strain rates . 77
3.10 Evolution at the equilibrium of the Ti, Nb, Al and V precipitate quantity as a function of temperature for steel grade **A** (data provided by Arcelor Research) 79
3.11 Evolution at the equilibrium of the Ti, Nb, Al and V precipitate quantity as a function of temperature for steel grade **B** (data provided by Arcelor Research) 79
3.12 Evolution at the equilibrium of the Ti, Nb, Al and V precipitate quantity as a function of temperature for steel grade **C** (data provided by Arcelor Research) 79
3.13 Phase transformations for the three steel grades studied at equilibrium (Black **A**, Red **B**, Blue **C**) 80
3.14 Ductility trough against phase transformation and precipitation state at the equilibrium for steel grade **A** 82
3.15 Ductility trough against phase transformation and precipitation state at the equilibrium for steel grade **B** 82
3.16 Ductility trough against phase transformation and precipitation state at the equilibrium for steel grade **C** 82
3.17 Kinetic of precipitation of Nb, Ti and V for a steel composition close to **B** (data provided by Arcelor Research) 83
3.18 Numerical flow curves provided by a Norton-Hoff law fitted on compression tests for **A** (dark gray), **B** (black) and **C** (light gray) at 700°C . . 84
3.19 Thermal cycle comparison between compression and tensile tests 85
3.20 Analysis of the grain size of the compression test sample used at the ULg 86
3.21 Fitting of the flow curve of **B** grade at 1000°C 87
3.22 Comparison of the Norton-Hoff model predictions with the experimental flow curves of **A** grade tested at 900°C at several strain rates 88
3.23 Comparison of the Norton-Hoff model predictions with the experimental flow curves of **A** grade tested at 1000°C at several strain rates 88
3.24 Comparison of the Norton-Hoff model predictions with the experimental flow curves of **A** grade tested at 1100°C at several strain rates 88
3.25 Comparison of the Norton-Hoff model predictions with the experimental flow curves of **B** grade tested at 900°C at several strain rates 90

3.26 Comparison of the Norton-Hoff model predictions with the experimental flow curves of **B** grade tested at 1000°C at several strain rates 90
3.27 Comparison of the Norton-Hoff model predictions with the experimental flow curves of **B** grade tested at 1100°C at several strain rates 90
3.28 Norton-Hoff p_2 parameter extrapolation to lower and higher temperatures 91
3.29 Norton-Hoff p_3 parameter extrapolation to lower and higher temperatures 92
3.30 Norton-Hoff p_4 parameter extrapolation to lower and higher temperatures 93
3.31 Curves of the Norton-Hoff law determined at various temperatures with the parameters determined through HTT for a strain rate of $10^{-2}s^{-1}$. 93
3.32 Comparisons of the hot tensile and compression tests and the numerical results of the simulation for cases at $1 \cdot 10^{-3}s^{-1}$ strain rate where black lines represents the experimental tensile tests, the gray lines the compression tests and the dashed lines the calculation of the Norton-Hoff law with the determined parameters) 95
3.33 Values of the triaxiality at the notch root for each specimen shape at the simulation start 96
3.34 Finite element used for the stress strain comparison 99
3.35 Mesh design for the mesh density impact study with number of elements per side in green 100
3.36 Flow curves for sample meshing comparison of HTT numerical simulation with black lines representing MESH1, red lines, MESH2 and blue lines, MESH3 101

4.1 Orientation of the microscopic cell with regard to the macroscopic models and view of the representative cell within the transition area as S. Castagne did [Cas07a] 105
4.2 Reference system of the macroscopic simulation and transfer to the representative cell 105
4.3 Location of the two stress-strain fields recorded in a representation of the R2 notched tensile test sample 106
4.4 R2, 850°C, $10^{-2}s^{-1}$ tensile test simulation results at the root (-) and in the core (+) of the sample 107
4.5 Stresses from the R2, 850°C, $10^{-2}s^{-1}$ tensile test simulation (Δ) at the root and in the core of the sample compared to the results obtained by loading the representative cell (-) with the tensile test simulation records 108
4.6 R2 Tensile test simulation results at the root and in the core of the sample 108
4.7 Nodes of the representative cell edges for the loading through *.loa file 110
4.8 Tendency of the damage in the representative cell 113
4.9 Influence of the variation of the parameters F_n on the damage evolution (+ Reference, ∘ Reference - 20% ,Δ Reference + 20%) 114
4.10 Influence of the variation of the parameters N_I on the damage evolution (+ Reference, ∘ Reference - 20% ,Δ Reference + 20%) 115
4.11 Three first crack appearances for the variation of different parameters . 118
4.12 Precipitates string obtained for grade **B** through TEM observation . . 124
4.13 Grain boundary observed on the TEM micrographs of **B** grade 124
4.14 Pictures obtained by TEM for grades **A**, **B** and **C** with an enlargement of 19.000x 125
4.15 STEM analysis of different **B** steel components on a precipitate 127

4.16 Detailed designation of the testing cases studied 130
4.17 Load-Displacement curves obtained for experimental and numerical case 22085B (left) and 22090B (right) 131
4.18 Damage path for a test in the same case (32085 with ∘ for **A**, Δ for **B** and + for **C**) using the several damage parameter adjusted 138
4.19 Damage curves as a function of the temperature for the different steel grade studied with ∘ for **A**, Δ for **B** and + for **C** 139
4.20 Comparison of the stresses obtained for the same case 22085B for macroscopic and mesoscopic simulations 142
4.21 Comparison of the circumferential stress obtained for case R2, **A** for 3 different strain rates at various temperatures (- Macroscopic, + Mesoscopic, · Damage) 144
4.22 Comparison of the circumferential stress obtained for case R2, **B** for 3 different strain rates at various temperatures (- Macroscopic, + Mesoscopic, · Damage) 146
4.23 Comparison of the circumferential stress obtained for case **C** for 2 different strain rates and sample shapes at various temperatures (- Macroscopic, + Mesoscopic, · Damage) 147

5.1 Slab path through the caster and reference frame for both calculation possibilities, the transient and the ingot simulation 155
5.2 Sensor positions on the slab in the THERCAST simulation for the two options, edge or center part study 155
5.3 THERCAST graphical representation of the continuous caster of **C** . . . 156
5.4 Temperature profile of the slab extrados of the **C** case with the marked temperature area of low necking as shown in Figure 5.6 157
5.5 Temperature profile of the slab intrados of the **C** case with the marked temperature area of low necking as shown in Figure 5.6 157
5.6 Ductility curves of grade **C** determined by HTT 158
5.7 Evolution of the stress components during the CC process applied to **C** the classical cooling profile 160
5.8 Evolution of the stress components during the CC process applied to **C** for the comparison between cooling profiles 161
5.9 Nodal position of the sensor 162
5.10 Reference systems in the corresponding directions 163
5.11 Strain field obtained through calculations of the tetrahedron nodes displacement 164
5.12 Equivalent strain calculation results compared to the data provided by THERCAST 165
5.13 Results of the calculated strain components of the slab center intrados with the classical cooling profile (black line) that will be used for the representative cell loading 166
5.14 LAGAMINE reference frame 167
5.15 Stress fields comparison between THERCAST and LAGAMINE of the slab center intrados with the classical cooling profile (THERCAST, black - LAGAMINE, grey) 168
5.16 Zoom on the stress field comparison 168

5.17 Z-stress configuration comparison of the slab center intrados with the classical cooling profile (THERCAST, black - LAGAMINE, grey) 170
5.18 Damage comparison between cooling strategies (Classical temperature profile, black - Modified temperature profile, grey) 173

A.1 **S1** - 1min, 1250°C - magnification: **200x** A.2
A.2 **S1** - 1min, 1250°C - magnification: **500x** A.2
A.3 **S2** - 2min, 1250°C - magnification: **200x** A.3
A.4 **S2** - 2min, 1250°C - magnification: **500x** A.3
A.5 **S3** - 5min, 1250°C - magnification: **200x** A.4
A.6 **S3** - 5min, 1250°C - magnification: **500x** A.4
A.7 **S4** - 10min, 1250°C - magnification: **200x** A.5
A.8 **S4** - 10min, 1250°C - magnification: **500x** A.5
A.9 **S5** - 1min, 1350°C - magnification: **200x** A.6
A.10 **S6** - 2min, 1350°C - magnification: **200x** A.6
A.11 **S7** - 5min, 1350°C - magnification: **200x** A.7
A.12 **S8** - 10min, 1350°C - magnification: **100x** A.7
A.13 **S9** - 1 cycle - magnification: **200x** A.8
A.14 **S10** - 2 cycles - magnification: **200x** A.8
A.15 **S11** - 3 cycles - magnification: **300x** A.9
A.16 **S12** - 4 cycles - magnification: **200x** A.9

B.1 Layout of the sensitivity analysis graphs with in the lower right corner the reference global graph and the enlargements in the other parts of the picture with in the lower left corner, the enlargement of the nucleation start, in the upper left corner, the enlargement of the nucleation end and in the upper right corner, the enlargement of the damage moment . B.1
B.2 Influence of the variation of the parameters a_0 on the damage evolution (+ Reference, ∘ Reference - 20% ,Δ Reference + 20%) B.2
B.3 Influence of the variation of the parameters b_0 on the damage evolution (+ Reference, ∘ Reference - 20% ,Δ Reference + 20%) B.2
B.4 Influence of the variation of the parameters $\dot{\varepsilon}_c^e/\dot{\varepsilon}_B$ on the damage evolution (+ Reference, ∘ Reference - 20% ,Δ Reference + 20%) B.3
B.5 Influence of the variation of the parameters N_{max}/N_I on the damage evolution (+ Reference, ∘ Reference - 20% ,Δ Reference + 20%) B.3
B.6 Influence of the variation of the parameters ψ on the damage evolution (+ Reference, ∘ Reference - 20% ,Δ Reference + 20%) B.4

C.1 Dimensions of the mounted and polished sample - Location of the scanned area of 10mm^2 (tan arrows) and silver bypass on the Bakelite C.2
C.2 Overview of zone 1 - SE image C.3
C.3 Related BSE image of zone 1 . . . . . C.3
C.4 General EDX spectrum on zone 1 . . . . . C.3
C.5 Inclusion from the right side of zone 1 . . . . . C.3
C.6 Related EDS spectrum focused on inclusion of Figure C.5 (CaS associated with a small (Al, Mg)O) C.3
C.7 Inclusion on zone 2 (SE Image) C.4
C.8 BSE image related to Figure C.7 . . . . . C.4

C.9 Related EDS spectrum focused on inclusion of Figure C.7 and C.8 (Complex (Al,Mg)O/CaS type) C.4
C.10 Inclusion on zone 3 (BSE Image) C.4
C.11 Same as Figure C.10, with higher amplification(BSE Image) C.4
C.12 Focused EDS spectrum on inclusion of zone 3 (Complex (Al,Mg)O/CaS type) C.4
C.13 Inclusions on zone 4 (BSE Image) C.5
C.14 Inclusion on the lower area of zone 4 (BSE Image) C.5
C.15 Focused EDS spectrum on inclusion of Figure C.14 (CaS type) C.5
C.16 Inclusion on the upper right area of zone 4 (BSE Image) C.5
C.17 Focused EDS spectrum on inclusion of Figure C.16 (CaS type) C.5
C.18 Inclusion on the upper left area of zone 4 (BSE Image) C.6
C.19 Focused EDS spectrum on inclusion of Figure C.18 (CaS type) C.6
C.20 Small inclusion at the left side of bigger inclusion of Figure C.18 (BSE Image) C.6
C.21 Focused EDS spectrum on inclusion of Figure C.20 (CaS type) C.6
C.22 Overview of zone 5 - BSE image C.7
C.23 Cluster of inclusions on the right side of Figure C.22 . . . . . C.7
C.24 Focused EDS spectrum on inclusion on the left side of Figure C.23 (Complex CaS/(Al,Mg)O type) C.7
C.25 Focused EDS spectrum on inclusion on the right side of Figure C.23 (Complex (Al,Mg)O/CaS type, with small and undefined amount of Ti) C.7
C.26 Complex inclusion on zone 5 (center) - BSE Image C.8
C.27 SE image related to Figure C.26 . . . . . C.8
C.28 Focused EDS spectrum on the centre of inclusion of Figure C.26-C.27 (CaS type) C.8
C.29 Focused EDS spectrum on the upper zone of the inclusion of Figure C.26-C.27 (CaS type) C.8
C.30 Overview of zone 6, matrix - BSE image C.9
C.31 General EDS spectrum in Figure C.30 . . . . . C.9
C.32 Dark area on the upper left side of Figure C.30 (BSE Image) C.9
C.33 Related SE image of Figure C.32, with corresponding EDS marks . . . C.9
C.34 Focused EDS spectrum on the left side of Figure C.33 (dark gray area in Figure C.32) C.9
C.35 Focused EDS spectrum on the left side of Figure C.33 (light gray area in Figure C.32) C.9
C.36 Light area on the right side of Figure C.30 (BSE Image) C.10
C.37 Inclusion on the right side of Figure C.36 (BSE Image) C.10
C.38 Focused EDS spectrum on the inclusion of Figure C.37 (CaS type) . . . C.10
C.39 Globular Inclusion on zone 7 (BSE Image) C.11
C.40 SE image related to Figure C.39 . . . . . C.11
C.41 Focused EDS spectrum on the matrix in the vicinity of inclusion of Figure C.39-C.40 . . . . . C.11
C.42 Globular Inclusion on zone 7 (BSE Image) C.12
C.43 SE image related to Figure C.42 . . . . . C.12
C.44 Focused EDS spectrum on the light zone of inclusion ((Al; Mg)O associated with CaS) C.12

C.45 Focused EDS spectrum on the center of inclusion of Figure C.45((Al; Mg)O associated with CaS) C.12

D.1 ISO643 table for the visual determination of the grain size by micrographic analysis D.1
D.2 ISO643 comparison micrographs for the determination of the grain size by micrographic analysis D.2

List of Tables

0.1 Composition of the studied peritectic steel grades (in ppm) 3

1.1 Summary of the precipitation state for the peritectic steel grade family 34

2.1 Summary of the different damage law parameters and their way of identification 48
2.2 Summary of the test campaign on hot tensile test samples 58

3.1 Denomination of the samples for the thermal path study 72
3.2 Grain size of the thermally treated samples analyzed by intercept method (results with * have been determined by comparison method) 73
3.3 Composition of the studied peritectic steel grades (in ppm) 81
3.4 Thermal cycle description of both, hot compression and tensile tests driven respectively at Liège and Aachen 85
3.5 Fitted **A** and **C** parameters of the Norton-Hoff constitutive law for the HTT 89
3.6 Fitted **B** parameters of the Norton-Hoff constitutive law for the HTT . 89
3.7 Test campaign planning for determination of the damage model on R2 and R4 sample shapes 97
3.8 Correlation study between experimental and numerical HTT at various strain rates and on different sample shapes with validated cases in bold style 98
3.9 Comparison of key parameters of the mesh density study 99

4.1 Values of the reference and modified parameters for the sensitivity analysis 112
4.2 Values of the parameters B, n and Σ_0 of the damage law 120
4.3 Results of ZAF quantification on matrix 122
4.4 Sample configurations for microscopic analysis 123
4.5 Results of the microscopic TEM analysis 125
4.6 Values of the damage law parameters a_0, b_0 and ψ determined by TEM analysis 127
4.7 Quantification results of STEM analysis on one **C** precipitate 128
4.8 Initial values of the adjustable parameters of the damage law used to predict fracture extracted from [Cas07a] 129

4.9 Structure of the damage parameters accuracy by numerical crack prediction and experimental observation comparison 130
4.10 Damage analysis for grade **C** with constant N_I value 132
4.11 Values of the adjustable parameters of the damage law for grade **C** with constant N_I value 132
4.12 Values of the adjustable parameters of the damage law for grade **A** . . 133
4.13 Damage analysis for grade **A** with the determined damage parameters . 133
4.14 Values of the adjustable parameters of the damage law for grade **B** . . 134
4.15 Damage analysis for grade **B** with the determined damage parameters . 135
4.16 Values of the adjustable parameters of the damage law for grade **C** . . 135
4.17 Damage analysis for grade **C** with the determined damage parameters . 136
4.18 Comparison of the fitted damage parameters for all steel grades studied 137
4.19 Comparison of particular temperature dependent N_I parameter (**adjusted**; *extrapolated*; interpolated) 137
4.20 Concise composition of the studied peritectic steel grades (in ppm) for the damage law parameters study 137

5.1 Numerical cases studied on the **C** continuous caster 153
5.2 Heat transfer for both studied classical and modified temperature profiles determined for the study of the transversal crack in CC 154
5.3 Correspondence of the reference frames for THERCAST and LAGAMINE codes and calculation of the forces to apply to the representative cell, with representative cell size Lx, Ly and Lz as defined in Section 3.3 . . 163
5.4 Initial nodes position in m of the center extrados case sensor 166
5.5 Correspondence of the reference frames for THERCAST and LAGAMINE codes and calculation of the forces to apply to the representative cell, with cell size Lx, Ly and Lz 170

E.1 Macro-Meso flow curves of **A** steel grade for R2 sample shape E.2
E.2 Macro-Meso flow curves of **A** steel grade for R4 sample shape E.2
E.3 Macro-Meso flow curves of **B** steel grade for R2 sample shape E.3
E.4 Macro-Meso flow curves of **B** steel grade for R4 sample shape E.3
E.5 Macro-Meso flow curves of **C** steel grade for R2 sample shape E.4
E.6 Macro-Meso flow curves of **C** steel grade for R4 sample shape E.4

F.1 Macro-Meso flow curves of **A** steel grade F.2
F.2 Macro-Meso flow curves of **B** steel grade F.3
F.3 Macro-Meso flow curves of **C** steel grade F.4

Introduction

Background of the thesis

The project First DEI named QUAPERIN funded by the Walloon Region has been worked out in order to deepen the research into the field of predicting crack appearance during the CC process. This project gathers several partners, scientific ones as well as industrial ones.

- **Scientific partners**
  - University of Liège (departments ArGEnCo - MS^{2}F team and A&M - MMS team);
  - Rheinisch-Westfälische Technische Hochschule Aachen (department IEHK);
- **Industrial partners**
  - Industeel: CC mill in Charleroi;
  - Ugine & ALZ Carinox SA: CC mill in Charleroi specialized in the production of stainless steels.

In this context, a fundamental scientific work is done in order to determine the most important parameters playing a role in the damage of CC steels. This study is established as a continuance of the work on damage modeling already begun at the University of Liège [Cas07a].

Goal of the study

The aim of the current study is to predict the crack appearance as a function of different parameters, such as material composition and thermomechanical path, applied to Continuous Casting (CC). The mean is to use a **damage model** that predicts the crack appearance at the grain scale (mesoscopic scale) and to validate it on **peritectic steel** grades in CC conditions.

Continuous casting

Continuous casting of steel became in recent years the first way to produce steel in large quantities. The technology and the production speed have quickly improved

and the product quality has increased. So nowadays, to control this process in the best way and to avoid quality problems, the comprehension of the whole process applied on several steel grades must be studied.

A relevant problem in the production of low carbon and stainless steels by continuous casting is the appearance of transverse cracks. Actually, the temperatures of the steel during the process decreases from the liquidus temperature ($\simeq$ 1400°C depending on the steel grade) to the ambient passing by a very sensitive temperature range extending from 1100°C to 600°C [Bri77, Suz84] where a loss of ductility generates a weakness of the material. The material reaches in general this sensitive temperature range in the unbending area [Pas06] of the continuous casting mill. As shown in Figure 0.1, the slab presents different stress states during the process. Especially in the unbending area, where the slab is straightened, it presents the low ductility temperatures.

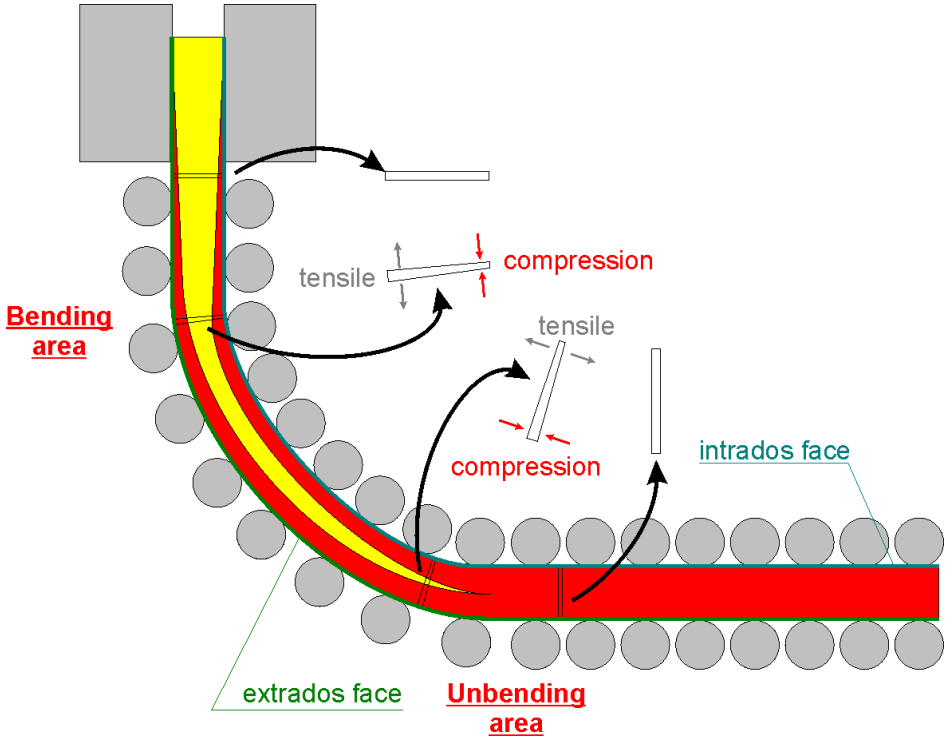

Figure 0.1: Illustration of the different stress states experimented by the slab during CC [Pas03]

The transversal cracks produced during CC process can be related to the steel grade but also to the mechanical and the thermal fields occurring during the process. Other factors such as the oscillation marks caused by the vertical oscillations of the mold can have a significant effect. The mechanical properties of steel at elevated temperatures are affected by several variables: steel chemistry, microstructure, texture, strain rate and thermal history. Thus the correlation between high temperature ductility and crack susceptibility in continuous casting has to be studied for the critical steel grades.

From an industrial point of view, the study of peritectic steels is fundamental because they are showing cracks on the surface of the slabs at the exit of the CC process. In this particular steel family it is important to choose the right steel composition in

order to study more precisely the causes suspected to be the most detrimental for crack appearance.

Peritectic steel grades

Out of the peritectic steel family, three different grades are chosen for their different Vanadium (V) and Niobium (Nb) content (Table 0.1). Steel **C** enables the study of the Nb precipitates on one hand. Then with **A** the addition of V on the crack sensitivity could be determined. Finally steel **B** shows the sensitivity of a high Nb, high V steel.

Nb and V precipitates are known to be detrimental for the material ductility. Thus, the study of these steels enables the quantification of the precipitates influence on the crack appearance. Not only the quantity, but also the distribution, the size, the shape and the position of these precipitates are taken into account through the damage model used.

Steel grade	C	Si	Mn	P	Ti	N	**V**	**Nb**	Al	S
A	1748	183	14702	117	151	54	**60**	**139**	313	66
B	576	2226	16220	119	163	45	**20**	**668**	396	24
C	1790	3253	12149	80	37	58	**1**	**161**	403	8

Table 0.1: Composition of the studied peritectic steel grades (in ppm)

Stainless steel grades

The initial project of the thesis was also to cover the stainless steel family as some grade can present transversal cracks. Discussion with the industrial partner on the material choice came to the selection of the two following steel grades.

- **AISI 304L** : After CC this steel shows almost totally austenitic structure (2-4% ferrite, 96-98% austenite)
- **AISI 410** : This steel shows a biphasic structure composed of austenite and also ferrite grains (50% ferrite, 50% austenite)

Their interest was the possibility to study the influence of the grain size and phase on the crack appearance. Indeed, the ferritic grains are smaller than the austenitic ones and thus different microstructures are chosen.

However unexpected problems in the experimental campaign as well as delays in the numerical applications explain that the thesis does not present any damage model identification and CC application on stainless steel. Nevertheless, some mechanical tests to determine the rheological parameters of these steel grades and a literature review were performed and delivered to industrial partners through internal reports.

Fracture mechanisms

In the temperature range starting at 600°C and going up to 1100°C, the crack propagation for the low carbon steel is known to be intergranular and several rupture mechanisms have been detected. They are supposed to combine to induce the fracture of the slab shell. The main damage mechanism is grain boundary sliding, which is

accompanied by creep controlled diffusion [Min91]. These fracture mechanisms have to be understood and studied in order to develop a mesoscopic model adapted to the continuous casting case. Actually the fracture model used in the current thesis is based on the opening of the cracks at the grain boundary thanks to interface elements coupled with a specific damage law. This law has been implemented by Sylvie Castagne in the finite element LAGAMINE code [Cas07a], developed and used by the department MS^{2}F at the University of Liège. This model has been developed for microalloyed steels and has already been validated on those grades.

Experimental study

In S. Castagne's work on the identification of the damage law parameters, the experimental approach was to perform compression tests on cylindrical samples [Cas07a]. These compression tests showed circumferential tensile stresses leading to fracture. The damage model developed is adapted to detect crack appearance in tension. Unfortunately the high compression stress components made difficult the identification of the damage parameters of the model, which was basically developed for tension.

The originality of the current thesis is to find other ways to identify the damage law parameters on the basis of tensile tests performed at elevated temperatures on circumferential notched samples.

Between 1100 and 600°C the ductility is strongly decreasing and the material enters a critical temperature area where the mechanical properties tends to decrease. This phenomenon can be followed thanks ductility curves that are drawn from the results of hot tensile tests. These tests are especially adapted to predict the surface cracking in the continuous casting process. Indeed, at a particular temperature a ductility loss appears that is characterized by the reduction in the necking of the tensile test sample. The different parameters affecting the depth and the width of the ductility trough are the chemical composition, the transformation austenite to ferrite, the grain size, the strain rate [Ouc82, Yue95] and the thermomechanical path [Yue95]. These material data as well as the thermomechanical history have to be defined very precisely in agreement with the values found in the process in order to get accurate results linked to the industrial observations. Thus, a good knowledge of the process is required in order to properly set the test campaign.

The methodology followed in this thesis can be divided into four main parts:

- **experimental** analyses for the adjustment of the rheology of the several studied materials,
- **microscopic** analyses for the design of the numerical mesoscopic representative cell,
- **simulation** of the tensile tests performed experimentally for the calibration of the damage model for the studied steel grades,
- **application** to the CC process and validation of the model on an industrial case.

Outline of this thesis

This report is organized as follows:

After this brief **introduction**, the practical problem we are facing is described. **Chapter 1** contains the **literature review** in the field of fracture prediction in CC. First, the description of the peritectic steel family is done, giving its properties and explaining its different characteristics in terms of micrographic morphology and mechanism of precipitates appearance. Then, this chapter presents the different defects reported in the CC process and especially those detected in peritectic steels. The mechanisms thought to induce the fracture are enumerated through a literature review. Their role is explained by analyzing the experimental tests used to characterize the ductility loss. This phenomenon is also detailed in order to understand the mechanisms of cracking in steels. Finally, the different alloying elements present in the steels are enumerated and their respective effects on fracture are presented.

Chapter 2 presents the **damage model**, its identification method and how to use it on CC case. The implementation of the **fracture model** in the LAGAMINE code is presented and explained. The different damage law parameters are listed and the experimental ways to identify their values are exposed. The specific treatment of the samples applied in order to have a representative experimental test reflecting the real process is described. Finally this chapter contains the explanation of the construction of a numerical cell representative of the steel microstructure, and the way the constraints are applied to it.

Chapter 3 describes the experimental test campaign to determine the **rheological parameters**. Their results are analyzed in regard to the ductility loss at a critical range of temperature. A macroscopic behavior rheology law is then identified. The mesoscopic cell and the experimental test campaign to determine the damage law parameters are defined according to the experimental results as well as the industrial information about the macroscopic stress, strain and temperature histories.

Chapter 4 is focused on the **damage model parameters identification** and analysis. It describes the different choices required to obtain an accurate damage parameters set. The final set is then discussed trying to link the numerically identified values to the physics underlying the parameters and the chemical composition.

Chapter 5 presents the **application on CC process**. All the steps of the determination of the damage in the **C** case are presented in details in this chapter. The macroscopic results are analyzed. The data transfer from macroscopic to mesoscopic simulations is explained and the problems which have been experienced are presented there. Finally, qualitative results of the mesoscopic study are given and conclusions are drawn from the results for the further industrial use of the model.

The **conclusion** strikes the balance of the thesis work. Its originality, lacks and successes are reported. Perspectives over development of the model toward other steel grades or numerical improvement for both, the model and its identification methodology are presented.

Chapter 1

Literature review

The following literature review tries to give an accurate overview in several fields related to this study. It is organized in six sections, each one focused on a specific topic:

Section 1.1: Specificities of the peritectic steel microstructure

Section 1.2: Defects and low ductility region in CC process

Section 1.3: Fracture mechanisms in hot process for peritectic steels, their characterization and description of the CC case

Section 1.4: Hot ductility tests and the linked damage mechanisms

Section 1.5: Review of the different ways to characterize hot ductility

Section 1.6: Effect of the microalloying elements contained in the peritectic steel grades

1.1 Peritectic steels

The continuous casting process is a very time and money saving process. Thus it has been adapted to different steel families of which the low carbon steel represents a high volume of production. This work focuses on this kind of steel. Thus, this thesis starts with a presentation of this steel family, showing its damage mechanisms and its microstructure to which the damage is strongly linked.

The peritectic grades are used for every day applications and more precisely in welded constructions and electric household appliances.

1.1.1 Peritectic transformation

Steel grades present three phase transformations during the cooling (Figure 1.1). The best known phase transformations is the eutectic reaction in which the liquid is directly transformed into a unique solid phase. The peritectic steel grades (**A**, **B** and **C**) undergo the so called peritectic reaction (Figure 1.1). In the peritectic case, a liquid (L) and a solid (α) phase in fixed proportions transform at a given temperature to form a single solid phase (β). As shown on the Fe-C phase diagram (Figure 1.2) the circle

Important three-phase reactions in binary systems

Reaction name	Phase change	System
Eutectic	$L \rightarrow \alpha + \beta$	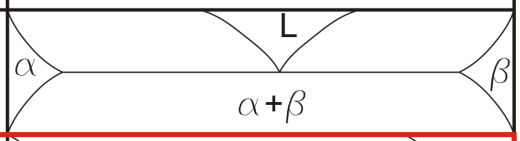
Peritectic	$\alpha + L \rightarrow \beta$	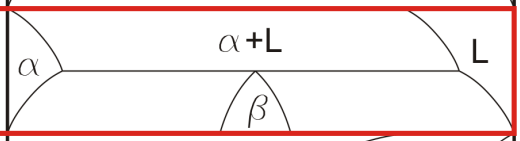
Monotectic	$L_1 \rightarrow L_2 + \alpha$	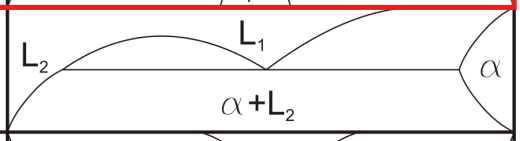
Eutectoid	$\gamma \rightarrow \alpha + \beta$	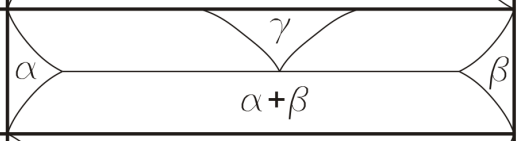
Peritectoid	$\alpha + \beta \rightarrow \gamma$	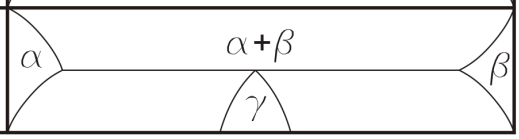

Figure 1.1: Possible reactions between three phases in the case of a binary system

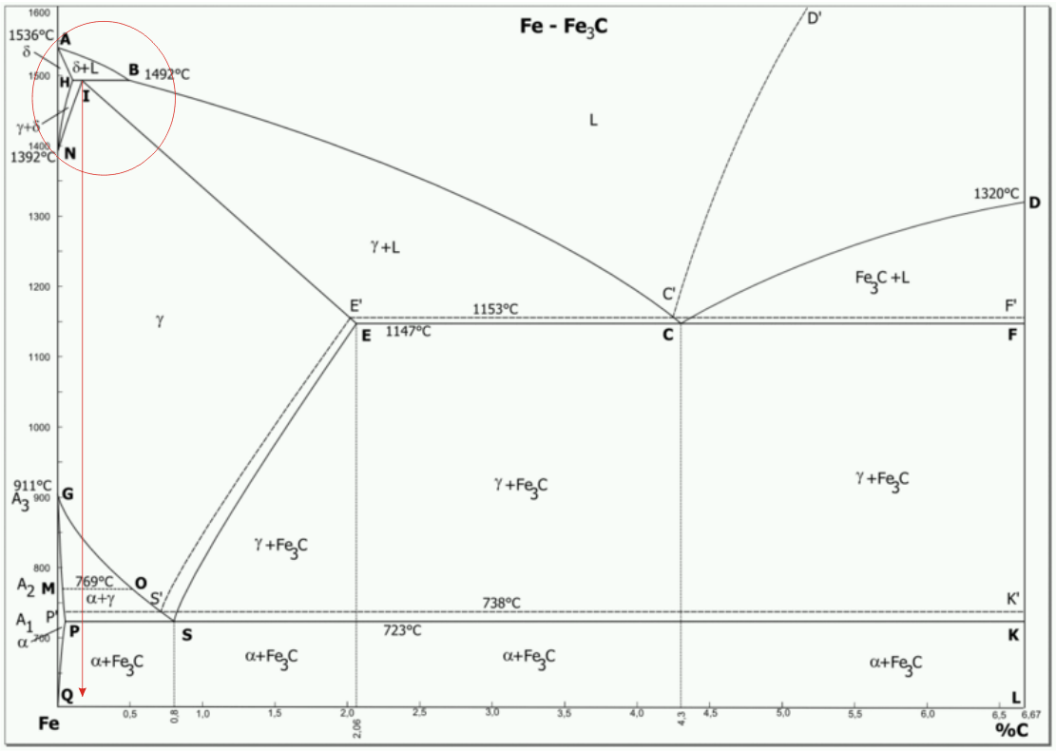

Figure 1.2: Fe-C diagram

surrounds the area where the peritectic reaction occurs. This reaction takes place near the upper-left corner between liquid steel (L), solid (ferrite δ) and gives solid (austenite γ), for low carbon contents ($\approx$0.17 mass percent of carbon) at a temperature around 1495°C.

1.1.2 Peritectic steel grains microstructure

The grain size is an important parameter and must be known because of i¨ts effect on the ductility of the material. Indeed, the ductility becomes worse with increasing grain size [Min99a]. In other words, finer grain size should lead to higher ductility [Yue95].

Even if the refining of the grain size will increase the amount of grain boundary sliding [Ash72], this phenomenon is more than compensated by:

- the resistance to crack propagation, where the grain meet a triple point. There, the smaller stress concentration are associated with shorter crack length;
- the increase in specific grain boundary area which will reduce the precipitate density on the grain boundary [Min99a].

Some empirical models for grain growth prediction exists but unfortunately it has been demonstrated that these different models are inadequate for quantitative prediction of austenite grain growth during reheating of as-cast microstructures in microalloyed steels [Man96]. It is thus important to determine the grain size with microscopic analyses of as-cast steels and to choose one mean grain size as a reference.

The values of the austenitic (γ) grain size belong to a very large range as they differ according the different studies. This observation is generally due to the different temperature paths applied to the samples before testing.

First of all, it is important to know the actual size of the austenite grains in CC conditions. Generally the studies reported hereafter are performed on steels that have almost the same composition as grade **A**. It is however important to note that all the peritectic steel grades studied present approximately identical microstructure. The differences appear in the microalloying elements contents and also in the precipitate content. So, the size of the austenite grains for conventional steels is about 200μm [Con01].

The shape of the austenite grains could also have an influence. In slabs, we do not find only equiaxial grains but also coarse columnar grains that may be part of the problem of transverse cracking [Yue95].

1.1.3 Precipitation state in peritectic steels

In a mechanical point of view, in order to have resistant low carbon steels, it is important to add some alloying elements that will be present in the steel during the whole production process. In the frame of CC, the alloying elements will appear as growing precipitates depending on the temperature reached.

The precipitates present in the samples should be like the one generated in the slab just after solidification in order to provide representative physical simulations. Even

if the goal of the wanted microstructure is known, it is quite hard to reach because of several variables in the sample treatment procedure.

It is often preferred to have no precipitate at the initial test step (goal of the sensitization/annealing procedure) and apply an adjusted history to try to recover the right precipitate size and nature to start with the best approaching material possible.

In most of the literature [Min99a, Rev94, Pan05a, Dav04, Min91, Pro00, Moh02, Suz84, Mae87] a sensitization procedure is applied but there were seldom indications about the final grain size and if the precipitates are indeed eliminated before regeneration of the microstructure.

The study of the precipitates composition, size and position in peritectic steels of the slab during the CC process is done. Such data is found in literature and some pictures of precipitates are taken. The precipitates are mostly carbonitrides (C,N) of Titanium, Niobium, Vanadium and others presented in the description of the effect of the precipitates (Section 1.6). The mean grain size of the (C,N) precipitates is about 2 to 25nm [Con01] and the detected (C,N) are randomly distributed in the matrix [Con01].

The effect of the precipitation state on the crack susceptibility of different microalloying systems has been investigated [Lud07]. They are listed hereafter:

- The precipitates that present cuboid or rod shapes, seem to induce surface cracking even at low volumes of the casted slab;
- Elliptical precipitates are worse than spherical precipitates;
- String-type precipitates appear at the prior austenitic grain boundary and so they are situated in the final grain matrix. They are expected to produce grain boundary cracks.

1.1.4 Steel microstructure observed in laboratory: challenges of sensitization

In various studies, the experimental simulation of the CC process begins with reheating the sample to a high temperature, called sensitization temperature. This temperature (approximately 1350°C according to Mintz [Min99a]) is held for a few minutes and this step is meant to dissolve all the precipitates that could be present. Thus the sample is assumed to be in the identical state as it just came from the liquid phase without presence of precipitates at all.

As seen before, the microstructure of the steel can be a worsening factor for the integrity of the material. Even small changes can influence the fracture of the steel. So the researchers have analyzed the different sample heating and cooling procedures in order to know if the structure obtained is truly the one present during the CC process.

Hereafter are listed the different measured grain sizes for different thermal treatments. Often the heating over a defined temperature involves an enlarging of the γ grains. Indeed, the γ grain size reached by reheating at 1300°C for 5 min was around 450-600μm [Moh02], except the Ti-added steel for which the grain size was around

200μm. Also steels heated to 1330°C, without holding temperature period, obtain a coarse grain size of approximatively 200μm [Min96]. Thermal treatment of 30s at 950°C involves a 10 to 20μm grain size, and a thermal treatment of 5s at 1300°C involves a grain size of about 100μm [Con01]. Samples heated to 1175°C in 20min and held at this temperature for 15min showed a coarse grain size of about 240μm [Min99b]. A sample heated in the same way to 1000°C showed a finer grain size of about 80μm [Min99a].

Figure 1.3 gives the literature results compilation of the grain size against sensitization time and temperature. It can be observed that the increasing temperature causes a grain size increase for almost the same holding time. At higher holding times, the grain size is bigger at the same temperature.

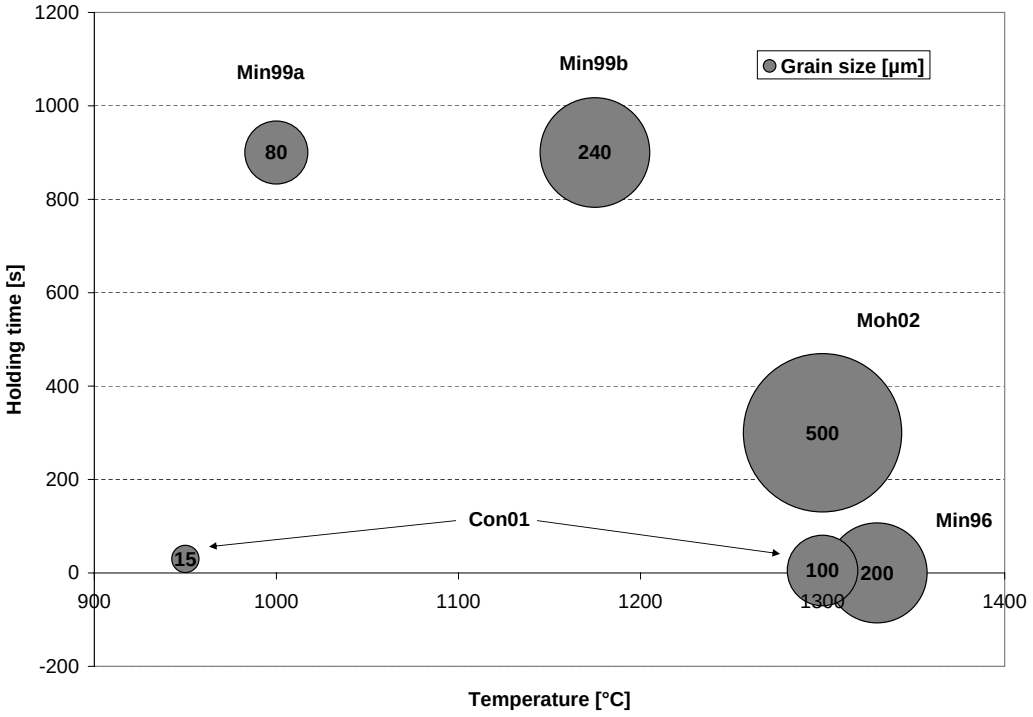

Figure 1.3: Compilation of γ grain size at high temperature gathered from literature

As mentioned before, the grain size will obviously grow with the reheating of the sample in function of temperature and holding time. Nevertheless, in a few references it was mentioned that the grain size of reheated specimens is 2 to 5 times finer than in as-cast materials [Yue95]. Unfortunately this assertion is not supported with experimental results.

Finally, it is commonly accepted that sensitization is sufficient to produce the microstructure and the hot ductilities that are representative of specimens which have been melted and then solidified [Yue95]. Thus, it is obvious that the CC grain size could be reached in the tested samples as long as an adapted thermal treatment is applied. This point was taken into account during the definition of the experimental tests and is described in Section 2.3.

1.2 Defects in CC products

Continuous casting is a very helpful process for the steel industry. Indeed, the production of steel in the form of slabs, blooms or billets is very important for productivity. CC is one of the first steps of the steel production. The melted steel produced is going through the caster in order to produce a semi-finished product that can be sold or conventionally enter the next step of the production which is generally the hot-rolling process. At this step, the continuous casting products should not show any defects and be adapted to the requirements of the next industrial steps. With time, the process had to be adapted to the modern reality. It became more and more efficient in terms of speed and of money saving, with a constant increasing of the steels quality. Anyway, the slabs still present small defects. The different defects have been registered and are shown in Figure 1.4.

1.2.1 Regions of low ductility

As seen in Figure 1.4, the defects in the CC slab have been widely studied and a huge number of different forms has been classified. The defects investigated in this study are only the near-surface cracks. Crack formation on surface is related to slab surface temperature where interdendritic or intergranular decohesion can be caused by embrittlement phenomena. Some interesting reviews are available about the wide range of surface defects of peritectic steels appearing in CC [Wol97] or more precisely about the transversal defects [Min91].

Wolf established an historical state of the art in the field of hot ductility (Figure 1.5) where the crack appearance is related to the microstructure of the steel that is evolving with temperature. In early studies, Suzuki (Figure 1.5a [Suz82]) reported about three regions of low ductility. This knowledge has been enriched by the damage mechanisms analysis as presented in Figures 1.5b and 1.5c and developed hereafter.

- The low ductility area **I** that is seen at temperatures above 1300°C is commonly connected to columnar dendritic structure. At this moment (1300°C) the liquid steel has just started its transformation into a liquid + solid state. The solid phase grows from the slab shell towards the core. Commonly this transformation happens on the slab shell just before the steel goes out of the mold and enters the first head rolls of the strand. In this temperature range the steel is very sensitive to crack appearance. This configuration is known to be responsible for the formation of internal cracks and surface longitudinal cracks [Wol97].

  An industrial case of longitudinal crack (Figure 1.6(a)) has been studied in order to know if it can be inserted in this project even if the damage model developed is intended to transversal intergranular crack appearance. After analyzing the crack appearance in the microscopic level it was established that the longitudinal cracks in this steel grade (almost the same composition as **C**) is intragranular (Figure 1.6(b)). The damage model is unfortunately not able to detect the intragranular crack appearance, thus this steel grade was dismissed of the study and replaced by **C** that presents intergranular transversal cracks.

- The low ductility regions **II** and **III** are commonly studied together as showed in further studies of ductility curves (Figure 1.5c [Tho86]) where only a differentia-

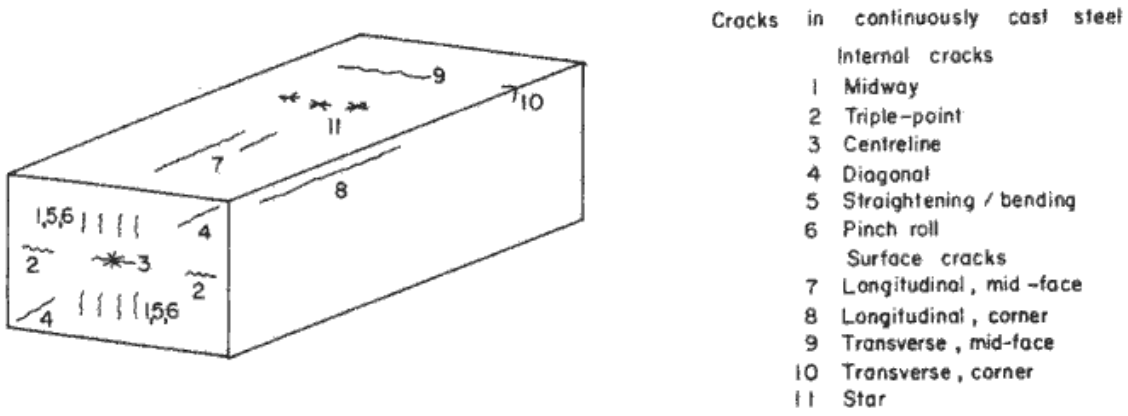

Figure 1.4: Position and defect type in the CC slab [Bri77]

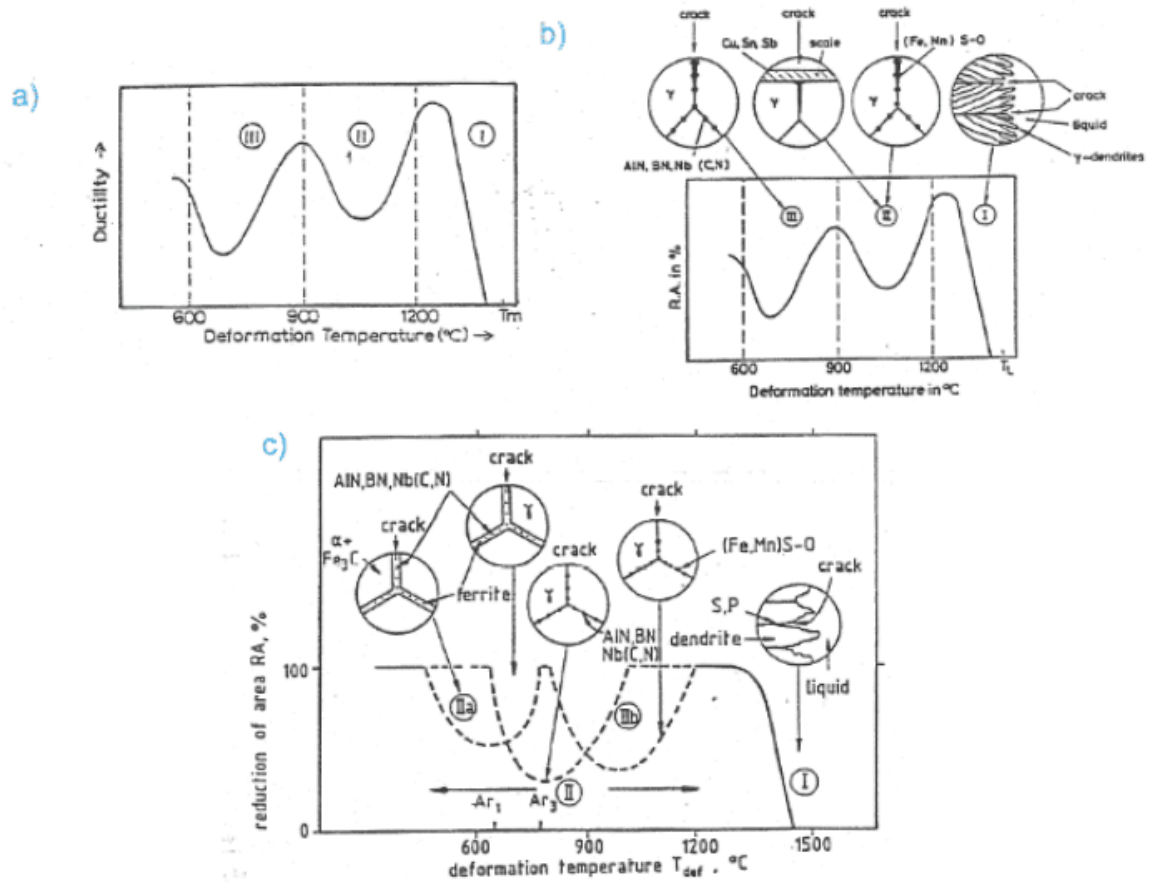

Figure 1.5: Schematic evolution of the knowledge about the low ductility regions of peritectic steels in the hot tensile test of in-situ solidified specimens [Wol97]

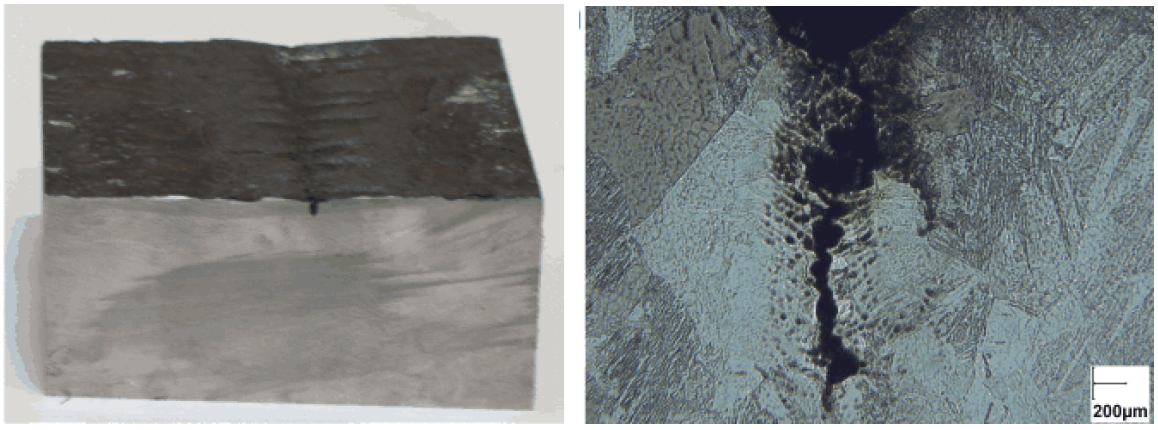

(a) (b)

Figure 1.6: Macroscopic (a) and microscopic (b) view of a longitudinal crack on a peritectic steel grade after the CC process (data provided by Arcelor Research)

tion is made between low ductility region **IIa** and **IIb**. In this temperature range going from 1100°C to 600°C the cracks are mostly intergranular and transversal due to coarse austenite grain size or to deep oscillation marks [Wol97]. Moreover, the microstructure of the steel is an important factor for crack appearance as investigated by Schwerdtfeger [Sch92]. Indeed, transversal cracks are generally related to the presence of soluble alloying elements as Aluminum (Al), Niobium (Nb) and Vanadium (V). This study [Sch92] is of prime interest since it has been practically focused on low carbon steel grades. This type of damage has also been practically detected (CC mills of the industrial partners) on stainless steels and is assumed to be due to the ferrite films formed during cooling.

1.2.2 Transversal cracks

The cracks are, most of the time, situated on the wide faces, near the corners, even if they could affect the whole width of the slab in case of defect crisis [Con01]. It is also obvious that the transversal cracks are often associated to oscillation marks (Paragraph 1.3.2) that are caused by the oscillation of the mold at the beginning of the CC process. Contrary to the longitudinal cracks that are huge, the transversal cracks are small [Con01] and can penetrate to a depth of 5-8mm below the surface of the slab [Min91].

Two different depths have been found for the cracks (Figure 1.7). Some are penetrating the surface (surface cracks) and others are located some micro- or millimeters below the surface (subsurface cracks) [Col85].

Surface cracks are extremely deleterious as they are easily oxidized and, consequently, cannot be welded together during hot deformation [Yue95]. The most critical case is reached because the transversal cracks often are not visible on the slab at the end of the continuous casting process and thus they are detected only during the following rolling process. Therefore the peritectic steel slabs are systematically milled before exiting the continuous casting production area. This step means a loss of time,

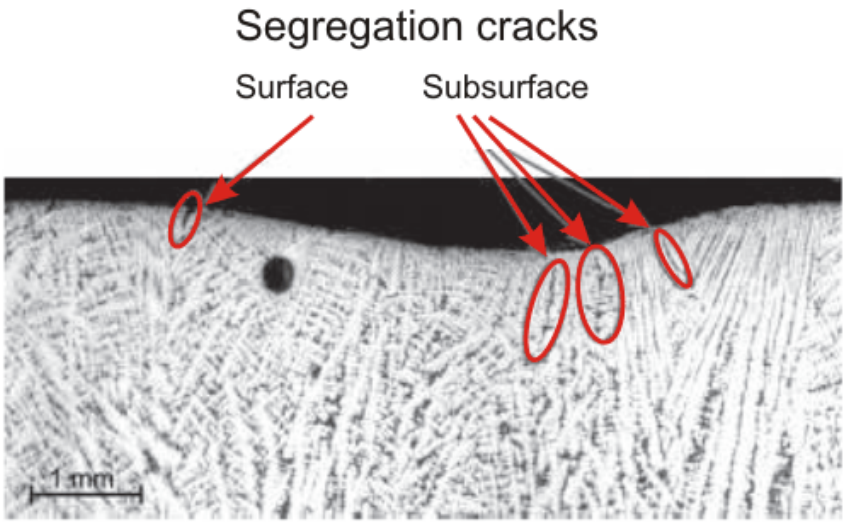

Figure 1.7: Types of segregated cracks during CC [Pap03]

of material and consequently of money.

1.3 Fracture analysis

Steels present different fracture mechanisms depending on the thermal and mechanical histories. Thus, at first, it is important to analyze the fracture mechanisms of the peritectic steel family by studying the specific fracture map and the other particularities, related to the CC case, that lead to fracture.

1.3.1 Fracture mechanisms map

The fracture mechanisms map of pure iron gives us indications about the mechanisms involved in the fracture of the steels studied. Indeed, looking at the pure iron map (Figure 1.8) it is obvious that for the particular CC conditions, i.e. high temperature and low stress (lower right corner on the picture) the mechanism of fracture is the **intergranular creep damage**.

1.3.2 CC particular elements leading to fracture

1.3.2.1 Oscillation marks

Microalloyed precipitates associated with "hook" or "fold" oscillation marks (Figure 1.9), especially those with microsegregation, will increase the probability of transverse cracking [Lud07, Mae87]. Oscillation marks are regions with high interdendritic segregation of elements as phosphor.

The gap between the strand and the water cooled mold is larger at the place of the oscillation mark, so that the rate of heat extraction is reduced in these regions, favoring both a coarse grain structure and a thinner shell [Min91]. Moreover, the oscillation marks can behave as notches, introducing high localized stress concentrations making the material more brittle [Min91].

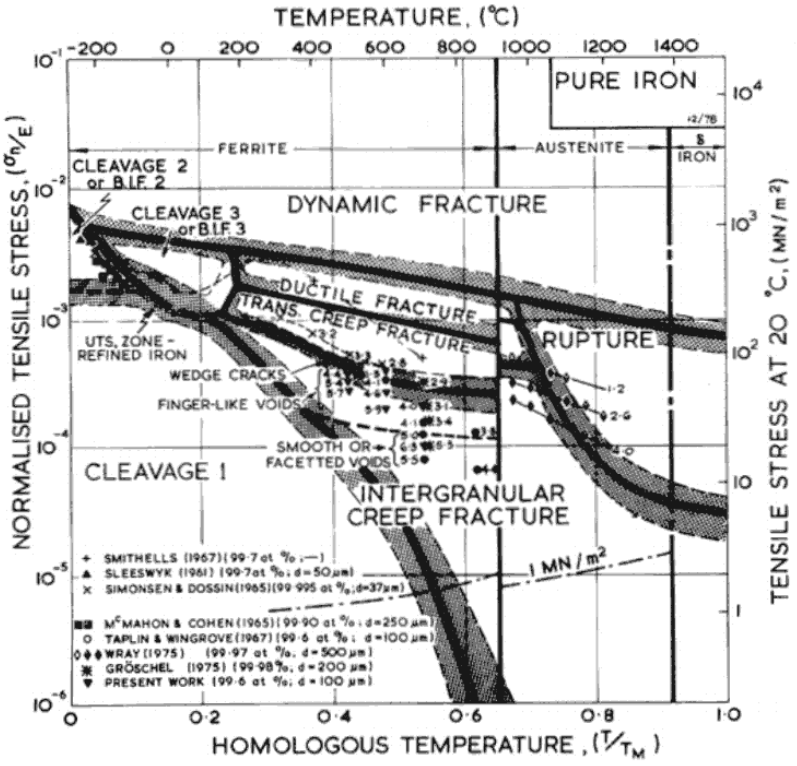

Figure 1.8: Fracture mechanism map for pure iron for various grain size [NIST]

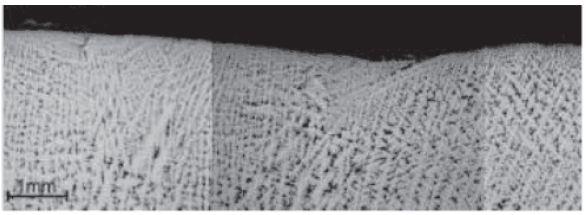

(a)

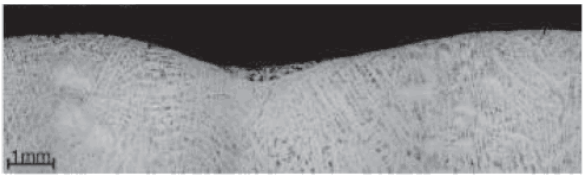

(b)

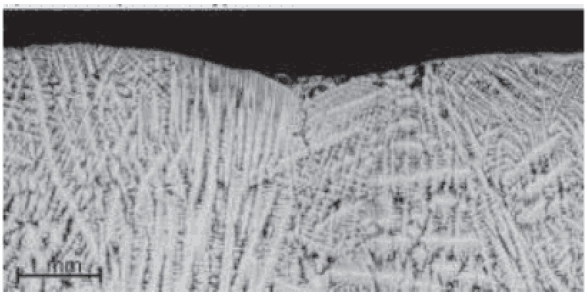

(c)

Figure 1.9: Classification of oscillation marks into three types; (a)hook, (b)depression and (c)folded depression type in CC [Pap03]

1.3.2.2 Mechanical constrains

The stresses and strains imposed to the slab during CC play an important role in the material damage. It is supposed that mechanical strains and stresses, caused by inter-roll bulging and thermal gradients induced by secondary cooling, even if very low, can lead to surface cracking before bending or straightening of the strand [Mor01].

1.3.2.3 Austenite to ferrite transformation

At the thermodynamical equilibrium, the austenite (γ) $\rightarrow$ ferrite (α) transformation begins around 850°C and ends beyond 750°C. But in CC conditions there is no thermodynamic equilibrium because of the high cooling rate and the beginning of the phase transformation is shifted to lower temperatures (≈100°C lower), depending strongly on the cooling rate [Mor01, Man96].

It is important to note this variation: the temperature in the CC process decreases at the beginning from the liquid to ≈800°C and then increases again to ≈1000°C because of the liquid core that heats up the solid shell at the outgoing of the mold. This means that the steel can undergo this situation more than once or during longer lap of time.

This phenomenon can induce a decrease of the ductility if the temperature has been low enough to transform $\gamma \rightarrow \alpha$ (Ar_3 temperature around 850°C at the equilibrium in Figure 1.10). Indeed, the precipitation of deleterious carbonitrides will be accelerated since the solubility of C in α is much lower than in γ [Yue95].

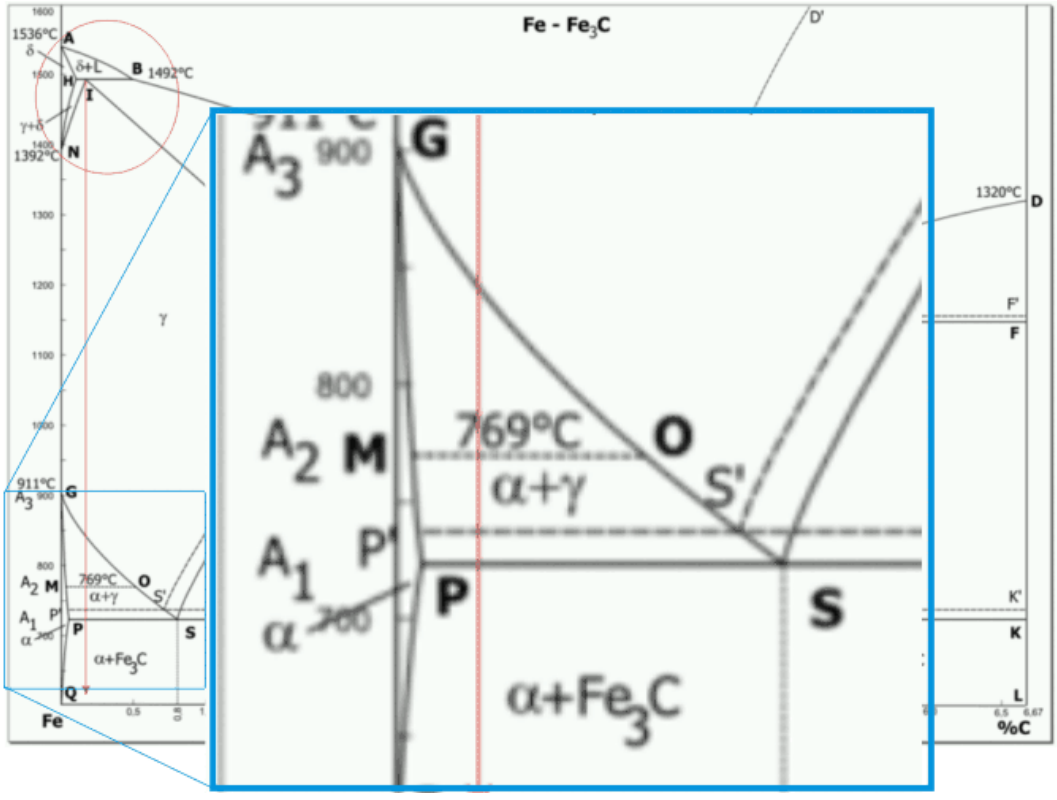

Figure 1.10: Enlargement of the critical area where ductility can be decreased by the thermal path of the slab shell

Not only the cooling rate but also the present precipitates can induce a change in the transformation temperature. As one can see in Figure 1.11(a) precipitates of Nb and V increases the strength of the material (C-Mn steel) but shifts also the transition temperature to lower ones. The decrease of the Ar_3 temperature is of about 10 to 40°C.

Figure 1.11(b) shows the relative energy of different alloying elements to act as austenite former or as ferrite former. It can be observed that, Nb and V are ferrite former. This means that the γ area is reduced if the elements are added to the steel. V has apparently a huger effect on the shift of the transition temperature.

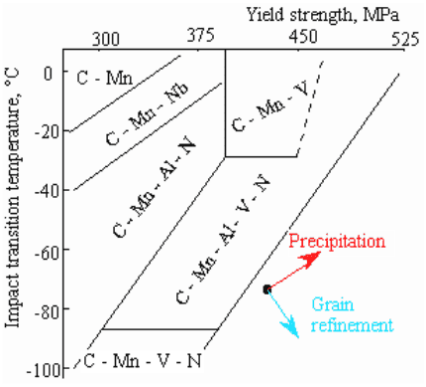

(a) Effect of alloying elements for a C-Mn steel on strength and transformation temperature [MATTER]

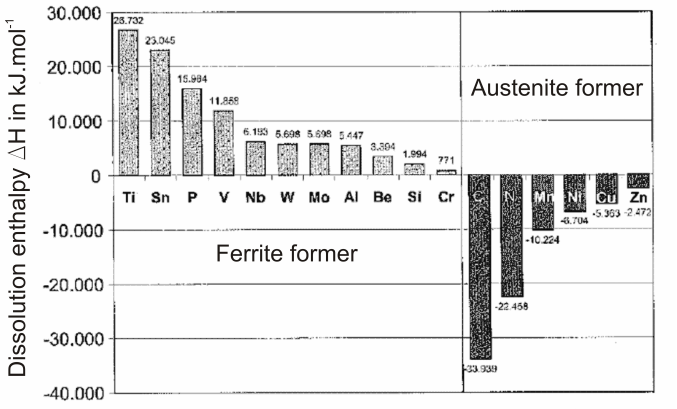

(b) Relative energy of different alloying element acting as ferrite- or austenite former [Ble04]

Figure 1.11: Effect of alloying elements on the steel microstructure

The deformation of the sample induces also a shift in the transformation temperature. When the deformation is important, the transition temperature increases [Mor01].

However, a dilatometric study [Mor01] shows that the thermal cycling in the CC process does not affect the Ar_3 temperature and no cyclic $\gamma \rightarrow \alpha \rightarrow \gamma$ transformation is occurring. That implies that consequences of cyclic phase transformation (mechanical cycling, increase in precipitation quantity) are not expected in CC process.

1.3.2.4 Dynamic recrystallization

Some authors reported for Nb-bearing steels, the fact that dynamic recrystallization takes place in the CC process during the bending and unbending operation and that the loss of ductility in the $\alpha + \gamma$ region is due to the reduction of dynamic recrystallization [Ouc82]. Indeed, the Nb precipitates form as Nb(C,N) at the austenite grain boundaries preventing the occurrence of dynamic recrystallization, encouraging the grain boundary sliding and giving rise to low ductility intergranular failure [Moh02].

However, it has also been observed that the dynamic recrystallization is not very probable because of the low values of deformation in the continuous casting process [Con01].

1.4 Hot ductility analysis

1.4.1 Ductility curves

The ductility curves are helpful for the determination of the damage conditions. They are obtained by tensile tests on cylindrical samples performed at different temperatures beginning at liquidus temperature and ending at room temperature. An example from the literature of the obtained curves is shown in Figure 1.12 where the grade containing 0.029% of Nb is similar to the grade **A** in this study [Moh02]. As short remark, one can see that the addition of V in the steel deepens and widens the trough. This study demonstrates also that Nb presents the same effect even for low addition of this component.

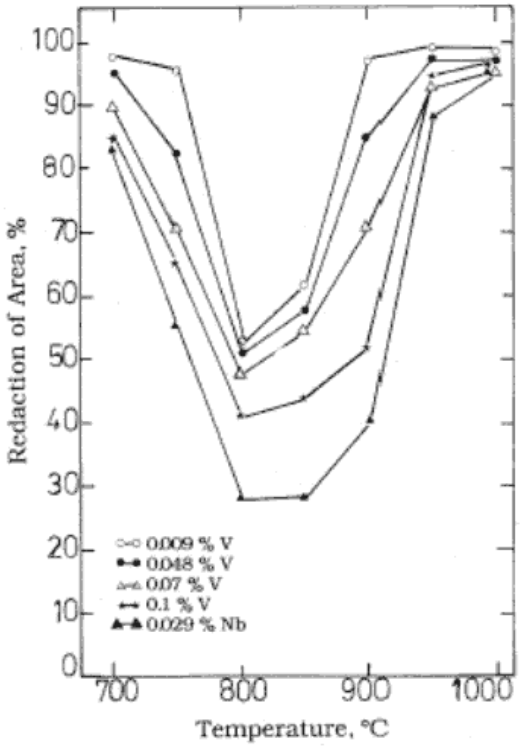

Figure 1.12: Example of a ductility curve obtained by hot tensile tests [Moh02]

As the strain rate influences the ductility of the material, it is kept constant during the different tests. The curves represent the reduction of area, called necking, on the temperature. The necking is expressed in percent and symbolize the reduction of area of the sample (Figure 1.13 and Equation 1.1). A schematic ductility curve is shown in Figure 1.14. In the temperature area which is of special interest in the current thesis (600 to 1100°C) the curve is made of three distinct regions where different mechanisms of fracture are acting on the material.

The curve can be divided, as written before, into three zones. Two areas present high ductility and the other one is the so-called ductility trough where the necking of the steel is very low (commonly lower than 50%) and thus, the ductility is bad. The zones from the highest to the lowest temperature can be respectively called High Ductility

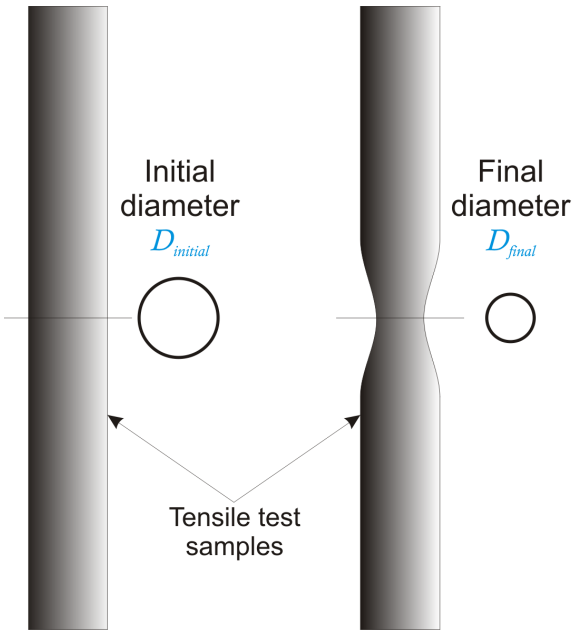

$$\text{Necking} = \frac{\text{D}_{\text{initial}} - \text{D}_{\text{final}}}{\text{D}_{\text{initial}}} \times 100 \quad (1.1)$$

Figure 1.13: Calculation of the necking for the determination of the ductility of the material

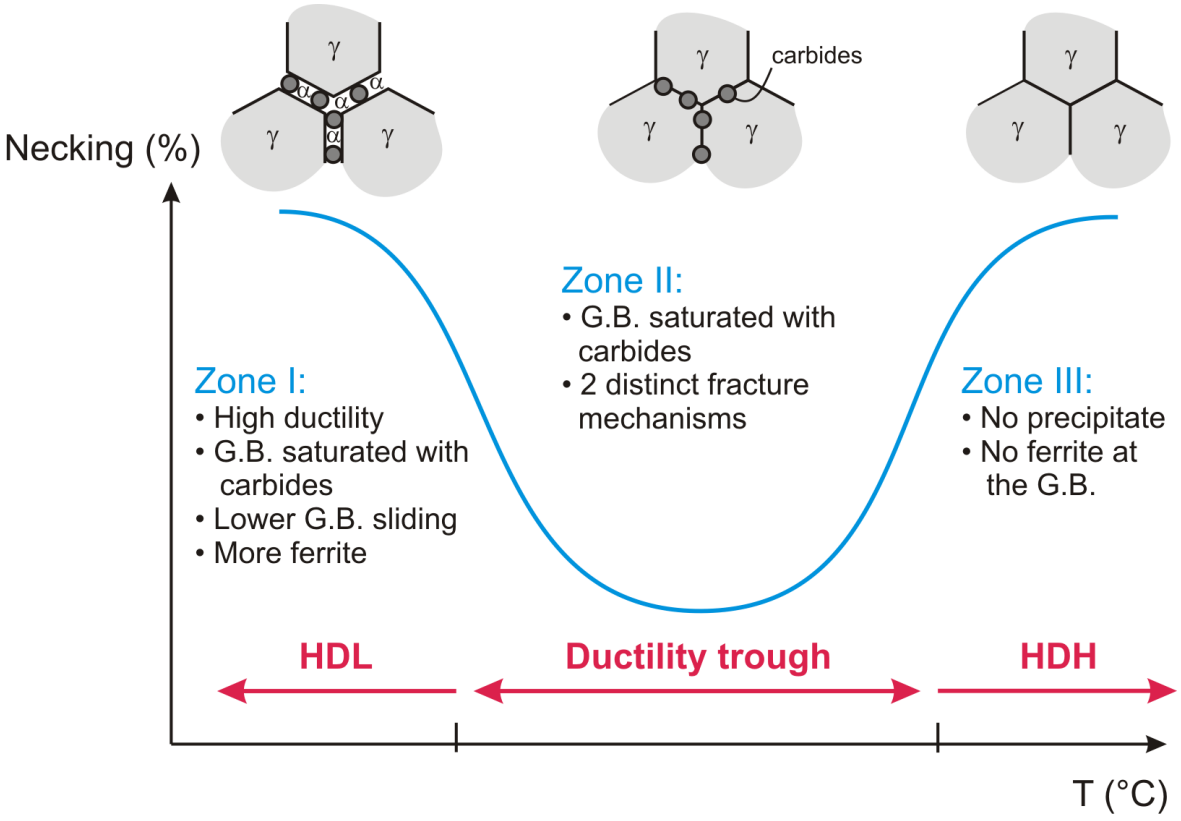

Figure 1.14: General shape of a ductility curve in the case of peritectic steel in conditions similar to thos of CC

High temperature area (HDH), ductility trough and High Ductility Low temperature area (HDL). These different areas are presented in the following paragraphs.

Practically, a hot ductility (or necking value) of more than 30% reduction on area is desirable if transverse cracking problems are to be avoided [Yue95]. The ductility trough represents then the temperature area where the failure will occur. The following paragraphs are dealing with the ductility trough and the way cracks are appearing in or around this area. Failure is encouraged by the presence of grain boundary precipitates and inclusions (the finer, the more detrimental), coarser grain size, and lower strain rates [Min91]. The propagation of the crack will be facilitated by a coarse microstructure [Con01]. The way all these material specificities are acting is detailed hereafter.

1.4.2 High ductility high temperature zone

The HDH zone is the high ductility area present at high temperatures. As shown in Figure 1.10, the peritectic steel is in the γ state at elevated temperatures. In this region, there is no intergranular precipitation of any carbide or nitride as the temperature is too high for the different components. At these temperatures the grain boundaries are still able to move and thus to migrate and dynamic recovery can occur so that the matrix remains safe of any defect.

1.4.3 Transition HDH to embrittlement

As the temperature goes down, a ferrite film appears at the austenitic grain boundaries. This ferrite film induces stress concentrations [Min91] and is favorable to crack events. The ductility begins therefore to decrease.

Intergranular crack can occur at a particular stage in $\gamma \rightarrow \alpha$ transformation when a thin film (5-20μm) of ferrite has formed around the austenite grains (Figure 1.15). The ferrite film is much softer than the austenite grain so the strain concentrates in this film, consequently leading to ductile voiding [Min91]. The ferrite film could be deformation induced and thus form before the Ar_3 transformation temperature that is observed at the equilibrium [Min91].

Wedge shaped cracks are often present at the interface between the prior austenite grain boundaries and the thin ferrite films. They are presumably formed by shear displacement of austenite grains along the softer ferrite bands, rather than by conventional grain boundary sliding [Min91]. The microcracks appear along the ferrite grain boundary [Mor01] and their formation occurred by the presence of grain boundary cavities [Con01].

An additional factor in this temperature range (generally 900°C) is that a certain quantity of precipitates begins to appear and to cause a drop in ductility. Finally, decreasing temperatures lead to higher flow stresses while dynamic recovery decreases, which increases the stress concentrations at the crack nucleation sites [Min91].

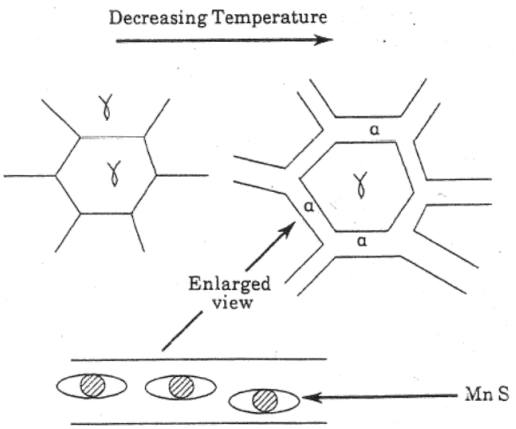

Figure 1.15: Ferrite film induced cracking during $\gamma \rightarrow \alpha$ transformation for peritectic steels [Min91]

1.4.4 Ductility trough

The second region of the curve is the ductility trough that is generally situated between 700 and 900°C. At these temperatures the grain boundaries are saturated with carbides or carbonitrides.

The ductility trough is invariably associated with intergranular fracture [Min91, Yue95]. The fracture facets present different breaking pattern (Figure 1.16). Two different types of facets can be seen, the facets covered with fine dimples or microvoids that are rough and also very smooth facets. This observation suggests two distinct fracture mechanisms. These mechanisms are the microvoid coalescence for the first facet type and the grain boundary sliding for the second type [Min91, Min99a]. Both mechanisms are presented hereafter.

1.4.4.1 Austenitic grain boundary sliding (rupture at triple point)

In the lower temperature of the austenite phase, restoration processes such as dynamic recovery or dynamic recrystallization become difficult. Thus, plastic deformation progresses via grain boundary sliding, which causes wedge type cracks at the grain boundary triple point (Figure 1.17). If there are precipitates at the grain boundary, they act as nuclei for void formation [Suz84]. So, the higher temperature side of the ductility trough corresponds to the limiting temperature of the restoration process while the lower side is determined by the grain boundary sliding or by the $\gamma \rightarrow \alpha$ transformation [Suz84].

Austenitic grain boundary sliding may be a necessary condition for initiation of a grain boundary crack, but it is not the controlling factor of hot ductility [Ouc82, Fra01]. The grain boundary sliding preferentially occurs in austenite because in ferrite, recovery is favored [Yue95]. For some authors [Suz84] the grain boundary sliding is a major embrittlement factor for plain C steels (Figure 1.18).

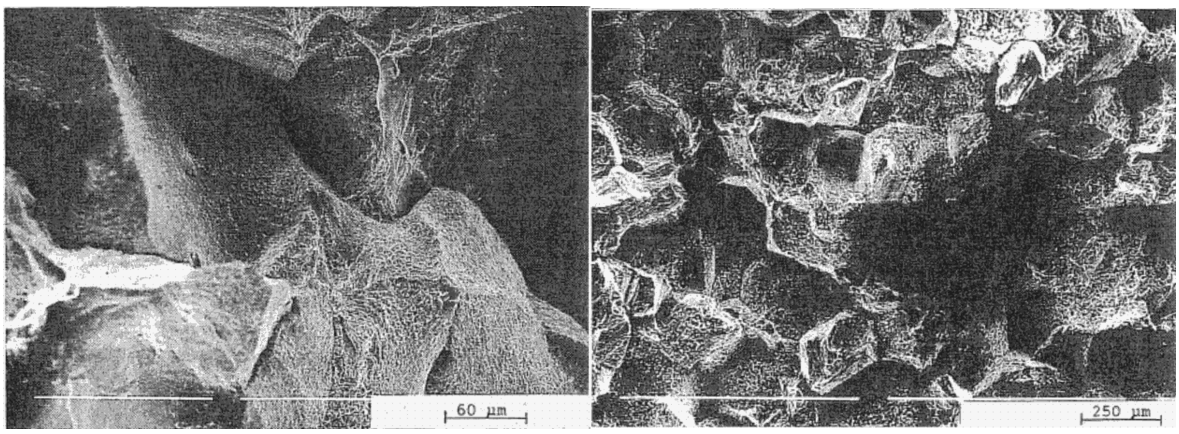

Figure 1.16: Illustration of fracture surfaces of a Nb containing steel [Min93]

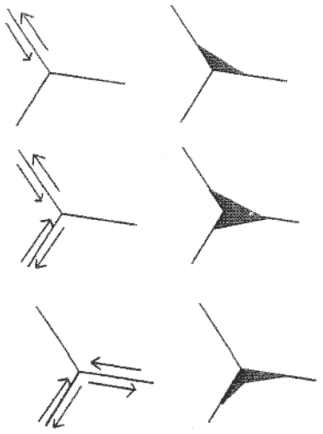

Figure 1.17: Illustration of the damage initiation at triple grain boundaries [Yue95, Min91]

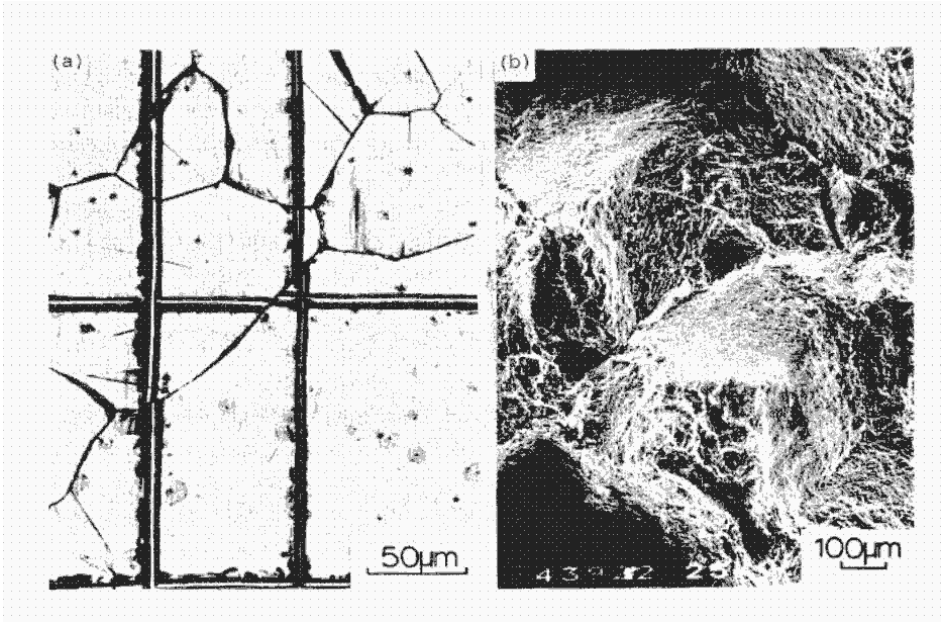

Figure 1.18: Illustration of the grain boundary sliding (a) and fracture appearance (b) in peritectic steel pulled at 750°C and $\dot{\varepsilon}$=5 · 10^{-3}s^{-1} [Suz84]

Indeed, the austenite shows only a limited dynamic recovery that prevents the accommodation of the lattice [Min91]. The stresses built up at triple points or grain boundary particles lead to intergranular failure by nucleation of grain boundary cracks (Figure 1.17). This rupture mechanism is usually associated with creep, the latter occurring at strain rates typically below $10^{-4}s^{-1}$ [Min91].

The sliding leads to the formation of cavities at the grain boundaries that are the first nucleation points of the voids [Min91]. Thus, it must be noted that the failure at grain boundaries can occur without presence of any particles or precipitates at the grain boundary [Min91]. However, the cracks formation by sliding is favored by the presence of intergranular particles [Min91].

1.4.4.2 Creep rupture (void nucleation, growth and coalescence)

The rupture mechanism by creep is divided in three stages; the nucleation of micro-cavities at the austenitic grain boundaries, then the cavities grow and finally they join together [Con01, Fra01]. The preferential sites for void initiation and fracture progress by void coalescence and crack propagation along the grain boundary are precipitates [Yue95].

The nucleation is a continuous process, the growth is proportional to the increment of the equivalent plastic deformation and is an exponential function of the stress triaxiality [Fra01]. The stress triaxiality should be taken into account for the growth stage [Fra01]. For triaxialities higher than 3, the growth of the cavity does not depend on the inclusion form [Fra01].

The final failure occurs by necking between the created voids. The fracture is localized at the austenite grain boundary with intergranular failure. It was observed as mixture of two modes, intergranular decohesion and intergranular microvoid coalescence, the second being more important [Cro87, Moh02]. Indeed, the plastic deformation can be localized at the grain boundaries and induce stress concentrations which will increase intergranular decohesions [Con01]. For example, precipitate-free zones are areas where the plastic deformation is concentrated [Yue95].

In Nb-containing steels that have been sensitized before cooling to the test temperature, precipitation takes place during deformation in the austenite. The precipitates are localized at the grain boundaries and are accompanied with a precipitates-free zone on both sides of the boundary [Min91]. A weak zone is thus forming and the rupture takes place similarly to the ferrite film induced fracture (Figure 1.19). Generally, voids appear first at larger inclusions and then progressively at smaller particles [Min91].

Precipitation of nitrides and/or carbides plays an important role in the fracture behavior [Cro87]. Indeed, the precipitation of the alloying elements generates the strength and properties in the final rolled product but the precipitates on the CC are a drawback because they reduce the ductility at high temperature and enables surface cracking on the as-cast semi products [Lud07].

In ductile fracture, inclusions plays an important role. The fracture path is then controlled by the high inclusion zone and directs its path through the inclusions [Cru59] for the case of the peritectic steel grades.

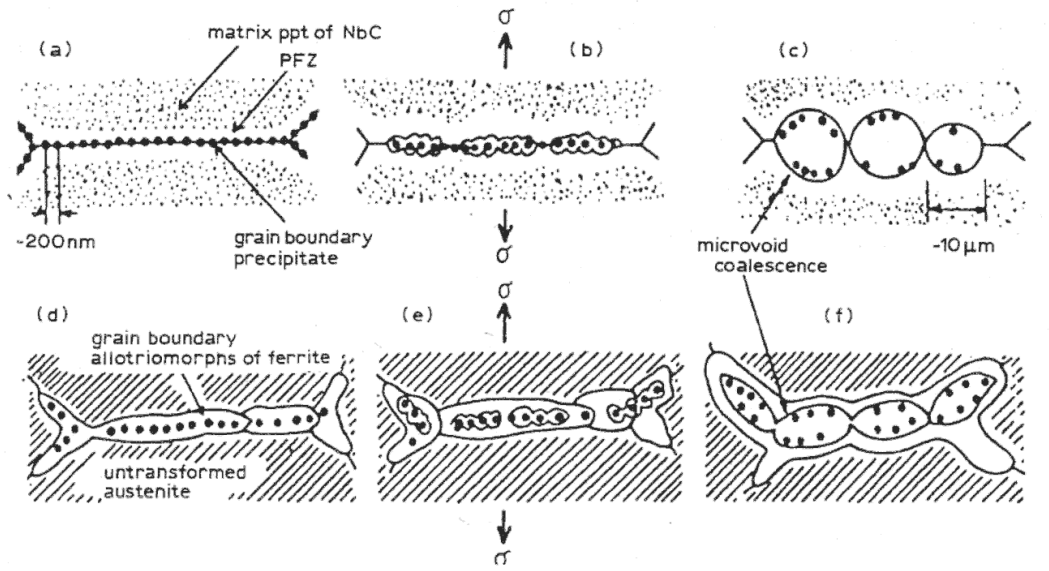

Figure 1.19: Illustration of the mechanism of microvoid coalescence induced cracking for peritectic steels [Min91]

1.4.5 Transition embrittlement to HDL

During the test, when the temperature decreased under the Ar_3 temperature (see Figure 1.2 the line between the letters GO and S), a thicker ferrite film forms around the grain boundaries and leads to a recovery of the ductility [Min91].

In this region a high volume fraction of ferrite is present. Thus, the strain concentration is more diffuse than it was in the thin ferrite film formed during cooling [Min91]. Moreover, with decreasing temperature the strength differential between austenite and ferrite decreases [Min91] and thus the ductility improves.

Ferrite has a good dynamic recovery and so the ductility is high with an important percentage of ferrite. Thus, the ferrite quickly flows at triple points to relieve stress concentrations and discouraging the initiation of sliding cracks [Min91].

1.4.6 High ductility low temperature zone

In the area situated in the high ductility region at lower temperatures, the grain boundaries are saturated with carbides. The ductility recovers because there is a grain boundary sliding at lower temperatures, due to the increased ferrite quantity so, less stress concentrations and the dynamic recovery can occur.

Higher ferrite film thickness increases hot ductility when it becomes more important [Ouc82, Con01, Mor01, Cum05]. In the $\alpha + \gamma$ region (750°C) the fracture is controlled by the thickness of the ferrite film [Ouc82, Yue95] (Figure 1.20). The ductility increases when the proportion of ferrite reaches values of 10% [Con01, Mor01].

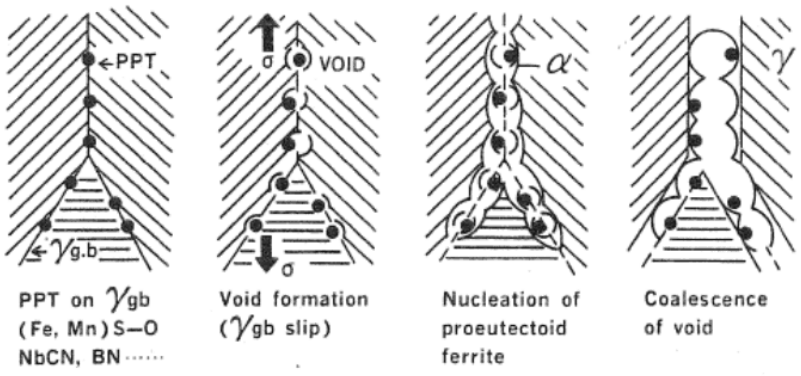

Figure 1.20: Illustration of the damage at the ferrite film for the peritectic steel family in the case of transversal fracture [Suz84]

1.5 Mechanical tests

In order to be representative of the CC process reality, the mechanical tests should be adapted and accurately simulate the stress-strain field found in the real case. Different tests have been imagined in order to simulate the CC process as accurately as possible. The tests that are usually used are the hot tensile test, the compression acoustic crack test, the hot bending test, the fatigue test or the torsion test presented in the following sections.

At high temperature, the strength, ductility, deformation and fracture characteristics are strongly affected by strain rate, grain size, prior history. Even the atmosphere in which the tests are performed is of high importance [Gra59]. Thus, it is essential to define the test conditions quite precisely in order to obtain significant data that could be applied in a CC study. It is also important to have a test adapted to the real conditions. We have hence to understand the different tests available and previously used by other authors in order to choose the more suitable for our study. In this perspective, some of the different available tests are exposed hereafter with their advantages and drawbacks.

Information from hot tensile testing has been found to be very useful in predicting the likelihood of transverse cracking under casting conditions [Min91]. This is due to the variables which influence the depth of the ductility trough, i.e. which cause intergranular failure under tensile testing conditions, which are responsible for transverse cracking.

1.5.1 Hot tensile test

The hot tensile test is the most common mechanical test for the mechanical simulation of the CC process. The principle of the test is to rise the temperature to a very high value and then to cool the specimen to the test temperature, with a CC representative thermal path, where it will be subjected to extremely low strain rate uniaxial tensile deformation to fracture. Generally a ductility curve is built with the results of the necking obtained before crack with the help of this test. As the strain rate and the temperature play an important role in the fracture behavior they have to be chosen

very carefully in order to be representative of the CC process. Generally the values of these parameters are taken to fit the mechanical loading in bending and unbending areas, these later being the areas where transversal crack initiates the most likely.

Hot tensile tests are adapted for the microcracking physical simulation in the CC process, as similarities have been observed between fractographies coming from the tensile tests and those coming from the CC slab [Con01].

As told before, the test parameters have to be chosen very carefully in order to fit the real case of study. In CC, the strain rate, the grain morphology and the temperature are parameters that influence the crack appearance and also act on ductility.

The deformation rate is one of the most influencing parameters. Indeed, these rates are very low in CC. At these low rates (10^{-5} to $10^{-2}s^{-1}$), the ductility rises when the deformation rate increases [Con01]. This is commonly dur to the creep effect that is reinforced by the process or the experimental test duration.

The weight of the thermal cycle applied to the sample has also to be taken into account. The crack sensitivity decreases when the heating temperature is low and when the cooling rate to the test temperature slows down. It can be explained because the precipitates become coarser or there are less precipitates [Con01].

Generally the hot tensile tests are realized with a constant temperature but different attempts have been made with continuous cooling and continuous heating of the specimen. The results of these tests show that the continuous cooling test are not adapted and give bad results in terms of crack prediction. On the other hand, the continuous heating test gives good information about the first area of the ductility trough [Yue95] but this way of proceeding is not especially in concordance with the real cases thermal path.

In order to understand the results given by the ductility curve, it is necessary to know the drawbacks and the inconsistencies of the tensile test.

- One drawback of the tensile test is that the deformations applied to the test sample are of about 10% while the strains in the CC case reach only a few percent. This difference enables mechanisms which are not present in the real case as dynamic recrystallisation. Also the precipitates and the ferrite formation induced by deformation will have a higher kinetics [Con01, Min91].

- After a tensile test with in-situ solidification, the microstructure of the test is not the same as in the CC process from the point of view of the grain morphology, the segregation and the precipitates size and morphology [Con01, Min91].

- The structure tested at high temperature is not always stable. Attention should be paid to oxidation, grain growth and recrystallization [Gra59].

- An important difference between test and real CC conditions is that the tensile test samples are normally very well protected from oxidation often being tested in argon atmosphere. The strand is exposed to the atmosphere and the water sprays will enhance oxidation, which may cause deterioration in ductility [Min99a].

- Finally, the physical simulation of the CC process would ideally involve applying the strain while the temperature fluctuates rather than isothermally [Yue95].

In conclusion, tensile test stays the most interesting one for this study and special attention will be paid in order to avoid most of the cited drawbacks.

1.5.2 Compression acoustic crack test

The acoustic crack tests are the tests used by S. Castagne to determine the damage law parameters [Cas07a]. This compression test was developed for the analysis and prediction of material failure based on the detection of acoustic emissions occurring during cracking. This test provides information about the stress and strain fields but also about the crack appearance thanks to the acoustic recording of the cracks sound emission [Cas07a]. It is important to underline that circumferential tensile stress happens in the middle plane.

The main drawback is that the test equipment is expensive and quite seldom used. The tests are difficult to drive at high temperature and the environment should be very quiet in order to record the crack appearance. Thus it was decided to eliminate this way of experimental testing.

1.5.3 Hot bending test

The hot bending test seems to be more representative of the mechanical loading tests in the CC process [Con01, Min91]. Indeed, the weak areas of the CC are the bending and unbending areas where the slab undergoes almost the same constraints as in the bending test.

However, because of the problem of quantifying the severity of surface cracking from such tests, it has only been used scarcely [Min91].

The results obtained for the bending test are almost the same as those obtained from the tensile test [Con01]. As performing such tests is more complex than performing tensile tests, there is no special interest in using this test in this study.

1.5.4 Hot fatigue test

Fatigue tests have been made in order to simulate the cyclic thermo-mechanical loading undergone in CC.

This thermo-mechanical cycling comes on the thermal side from the thermal cycling due to the spray cooling and from the reheating when the slab arrives between two rolls. On the mechanical side, the cycling comes from the bulging between each pair of rolls [Con01].

However it is difficult to find the good cycling conditions. Indeed, when a cycling of $\pm 75°C$ around $650°C$ is done, 50% ferrite is forming against 15% around $725°C$ and no ferrite around $800°C$ [Mor01]. The difficulty is that during the test the amount of ferrite against austenite is changing and this variable can not be taken into account in the damage law we use.

1.6 Microalloying elements of peritectic steel grades

Microalloying elements are added to steels in order to improve the mechanical behavior. The typical alloying elements that are used to generate precipitate strengthening are Ti, V, Nb and Al. These additions can be made individually but more commonly are made in combination depending on the customers requirements of material properties as strength or toughness. These alloying elements are not only used to obtain better mechanical properties but also to refine the grains during the process. Indeed, a fine precipitate distribution in a steel will restrict the growth of austenite grains at high temperature and will delay recrystallization of deformed austenite grains [MATTER].

Moreover hard inclusions can be obstacles for dislocations [Fra01] and delay or hinder the propagation of cracks. As precipitates in steels are relatively large, dislocation tend to bow between then with Orowan mechanism.

Unfortunately, it has been demonstrated that the alloying elements added in steels in order to give better properties can lead to serious defects during the continuous casting process. Especially Nb and V are very detrimental for the microalloyed steels because they increase the risk of transversal crack appearance during the CC process [Lud07, Ouc82, Ber04, Lee05, Pan05a, Yua06, Yue95, Min99a, Cum05, Rev94, Mae87].

At first sight, we can see the general effect of the precipitates on steel. The principal elements that have been shown to be deleterious are: Al, N, Nb, and S [Con01]. Ti is generally considered as beneficial during tensile tests but its influence is dependent on the thermal history of the steel [Con01].

The precipitates show different roles in promoting embrittlement. In the case of grain boundary sliding in the austenite, fine precipitation pins the boundaries, allowing the cracks to join up [Min79]. The presence of precipitates also increases the grain coarsening temperature [Pan05a] that involves a loss in ductility as coarse grain structure does.

Another deleterious effect is obtained by thermal cycling. Indeed, in CC conditions, the temperature drops below 600°C, followed by a rapid reheating from the slab interior. This induces an increase in precipitation rate and a decrease in precipitate size [Yue95] that means a decrease in ductility.

Some authors reported that the proportion of static and dynamic precipitates present is dependent on the cooling rate and more particularly on the deformation rate [Cro87]. Indeed, these precipitates do not show the same morphology and so they have a different effect on the steel behavior. But we must note that the required conditions to obtain precipitates coming from dynamic precipitation are difficult to reach as the strain rates should be of $10^{-1}s^{-1}$.

The ductility also decreases when a higher volume fraction and finer precipitates are present. Thus, particles that form during cooling to the test temperature, or during deformation, are more detrimental than particles that were not dissolved by reheating, because the latter are coarser [Yue95].

So it is important to know the position, distribution, size and shape of the precipitates formed in order to identify them and to analyze their influence.

1.6.1 Niobium

More particularly, Nb precipitates are meant to be the most detrimental ones. Microscopic analyzes have been performed on **peritectic steels containing only Nb** (almost the same composition as grade **C**) by some authors and the conclusion of their work is compiled in the following paragraph.

Nb(C,N) precipitates are present in two different forms in the as-cast material. They can be distributed randomly or in strings (strings are 10 times more present than those of the normal distributed type) and those are found at the grain boundaries [Lud07].

According to Ludlow [Lud07], the precipitates are mostly globular in form with some platelet and cuboid types, these being mainly of a larger diameter. In the core of the slab the precipitates are coarser and less numerous than at the surface (region beginning from the surface and 5mm in depth). An analysis of the surface precipitates size suggested that those in the intrados surface were larger than the others even if their number is not different between intra- and extrados surfaces.

In Nb + Ti steels, two bands of precipitates were found in the as-cast material studied by Ludlow [Lud07]. The first band is coarse (100-300nm) and the other one is finer (<20-50nm). The subsurface precipitates were (Ti,Nb)(C,N) in strings or at the grain boundaries with a typical size around 70nm. Under 100μm from the surface Ti(C,S) became significant. In addition to the coarse TiN precipitates, many fine (Ti,Nb)(C,N) particles were observed at the slab corner. Throughout the slab the precipitates were (Ti,Nb)(C,N) of three distinct types; small cuboid and globular (2.2-28.8nm), dendritic form (26-30nm) and large irregular form (40-600nm).

Strain induced precipitation of small (2-5nm) niobium carbides were identified in high strength low alloyed steels that were thermomechanically processed as given in the study of Béres [Ber04].

Through a transmission electronic microscopic (TEM) study, Béres [Ber04] showed also a distribution of the precipitates size going from 10 to 100nm with a maximum number of precipitates showing a diameter of 40nm.

It is also interesting to investigate the precipitates size after a thermal treatment of a steel containing only Nb that is comparable to grade **C**. The steel studied by Crowther [Cro87] was taken from a 50kg laboratory vacuum melt. The size of the Nb(C,N) precipitates that are appearing at the grain boundaries is about 15nm after 1s holding time. After 2h holding time the size is 25nm and after 6h, 55nm. Nb(C,N) precipitates were fine and mostly localized on the former austenite grain boundary (Figure 1.21(a) and Figure 1.21(b)) [Yue95] and nucleates preferentially on small defects [Ber04].

Different cooling rates can also induce different precipitate sizes. Indeed, with a cooling rate of 1°C.s^{-1}, coarse Nb precipitates are forming. With a cooling rate of 10°C.s^{-1}, fine Nb precipitates are formed which are believed to hinder austenite to ferrite transformation [Yua06].

The Nb precipitates are randomly distributed in the matrix and partly located at the grain boundary in ferrite [Ber04]. Row formation was also observed due to

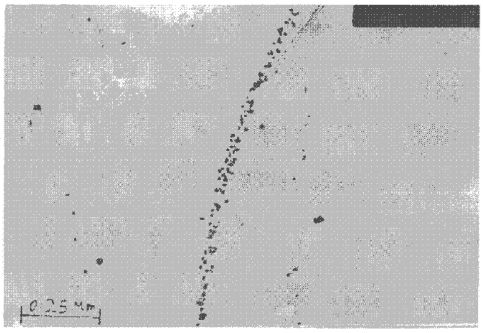

(a) String of the NbC precipitates on the austenite grain boundary [Moh02]

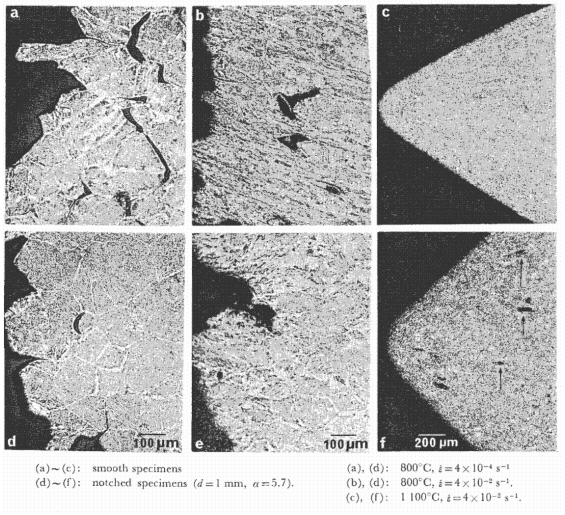

(b) Section of a tensile test specimen with rupture at the grain boundary [Mae87]

Figure 1.21: Presence of precipitates at the formed austenitic grain boundary in peritectic steels

nucleation at the interphase boundary during austenite to ferrite transition [Ber04].

The presence of Nb is responsible for several deleterious effects in the steel leading to damage. Nb content decreases the size of the polygonal ferrite grain size [Lee05]. The precipitates localized at the grain boundaries can lead to soft precipitation-free zones where the plastic deformation concentrates [Yue95].

Nb content induces solute drag effect that could delay the austenite to ferrite transformation [Yua06, Cum05, Lee05]. When the content in Nb is increased, the austenite grain becomes finer [Yua06].

Nb is one of the alloying elements that promote hot cracking susceptibility [Ouc82, Cum05]. Indeed, hot ductility decreases with increasing Nb content particularly in the lower temperature region of austenite γ, because of the formation of Nb(C,N) in the γ grain boundaries. The size of the Nb(C,N) precipitates is about 20 to 50nm [Ouc82].

The presence of Nb(C,N) decreases the possibility of dynamic recrystallization [Ouc82]. The Nb(C,N) particles formed by dynamic recrystallization are more detrimental than those formed statically, because the particle density is usually higher, both at the grain boundary and inside the grain [Yue95].

In the specific case of Nb steels, Nb(C,N) precipitates appearance before or during plastic deformation delays the recrystallization and results in significant embrittlement [Suz84].

1.6.2 Vanadium

The V precipitates have also an effect on the ductility of steel and thus on the fracture appearance. Nevertheless, VN particles seems to be less detrimental than the Nb(C,N) particles [Moh02]. The distribution, morphology and position of these precipitates

have also been discussed by some authors and their work on **V containing steels** is summarized hereafter.

In V containing steels the predominant precipitates were V(C,N). The size of these precipitates is lower than 40nm and uniformly distributed throughout the metallurgical structure (Figure 1.22) [Lud07].

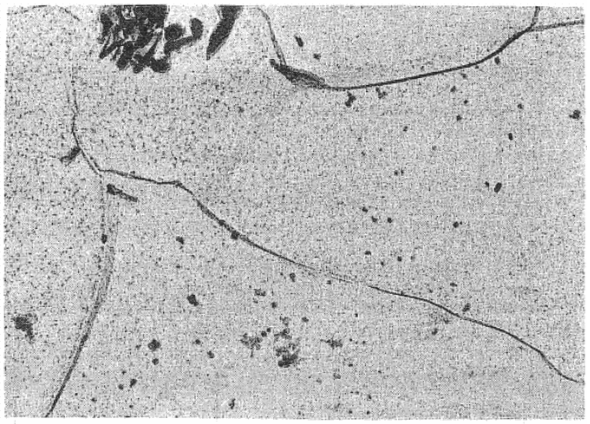

Figure 1.22: Distribution of the V precipitates in the peritectic steel [Cro87]

Compared to the Nb(C,N) precipitates, the V(C,N) ones are coarser. They are randomly precipitated for high values of V and less intense and mostly isolated for low content of V [Moh02].

When Ti is added to the grade, the encountered precipitates are the following ones: TiN, MnS and (Ti,V)N. The last one is observed at depth lower than 10mm under the surface in form of rosettes or small dendrites. (Ti,V)N appear to have formed as a co-precipitation of V on the primary TiN particles in Ludlow's study of as-cast materials [Lud07].

At 1200°C, V is completely soluble in austenite, but at lower temperatures (below 1000°C) the solubility of V decreases and it diffuses into the existing precipitate to give rise to a complex precipitate of (Nb,V)(C,N) [Pan05a].

The size of the V precipitates can also be studied as a function of the thermal treatment and especially as a function of the holding time. V(C,N) particles were randomly precipitated, having a mean size of 15nm. After a 6h holding time the precipitates coarsen (50nm) and are predominantly situated at the austenite grain boundaries on Crowther's 50kg laboratory melt [Cro87] that probably means that V precipitation is also subjected to a precipitation kinetic.

In V steels, the addition of Al appears to reduce the amount of VN precipitation within the grain [Col85]. And in V or Al bearing steels, dynamic precipitates are finer and more numerous than statically precipitated particles but do not form at the grain boundaries and are, hence, less deleterious [Yue95].

1.6.3 Combination of Niobium and Vanadium

Only few work were devoted to the effect of both Nb and V in the alloyed steels. In general the effect of each alloying element is separately known as steels are prepared with only V or only Nb for a research aim.

However, some tests have been done by Ludlow [Lud07] on Nb and V containing steels. He found out that the predominant precipitate was (Nb,Ti,V)(C,N) in globular or cuboid form but at 30mm from the surface, while angular forms were observed in Nb+V+Ti grades. The particle size increases with the depth in the slab. This is supposed to come from the kinetic because the slab core stays longer at high temperature and thus the precipitates have more time to grow

The average composition of the particles was the following: intrados, 60% Nb, 37% Ti and 3% V whereas in the extrados, 76% Nb, 21% Ti and 3% V.

1.6.4 Titanium

In Ti containing steels, the predominant precipitates are Ti(C,S), Ti(C,N), oxides and sulphides of Ti, Mn, Al, Fe, Cr and Si according to Ludlow [Lud07]. TiN precipitates at the reheating around 1300°C.

There are three different size distributions; fine (lower than 20nm diameter), medium (20-50nm) and coarse (50-350nm). Precipitates increase in size as the distance from the surface increases [Lud07].

The distribution of the precipitates is in general irregular, but cubic Ti(C,N) and coarse $Ti_4C_2S_2$ tend to be in bands parallel to the direction of solidification [Lud07].

It was found that the addition of Titanium is interesting as it increases the capacity of the steel to be safe [Lud07]. Indeed, it reduces the amount of N which can be combined with Nb [Ouc82] because its affinity to N is higher.

With an increasing level of Ti, the carbonitrides precipitate in the liquid phase. Thus they will be intragranular and will enrich in Nb and C while avoiding the precipitation at the grain boundary [Con01].

The addition of Ti decreases the final grain size of the product. This can be reached with a stoichiometric ratio Ti/N of 3.4 [Con01]. TiN are not detrimental because they are formed during solidification, and are therefore coarse, and not present at grain boundaries [Yue95].

1.6.5 Other alloying elements

Aluminum containing steels

Al is used in order to improve the quality of the steel. These steels are called Al-killed steels. The ductility troughs associated with V and Al precipitates are not as severe as those attributable to Nb(C,N), because V precipitates are more randomly distributed, and Al precipitates are coarser [Yue95].

However, the AlN precipitates have a deleterious effect on the crack appearance in comparison with a steel that does not contains any precipitates. It increases the

size of the ductility trough [Con01]. The precipitation of the particles is very slow in austenite, it is induced by deformation [Con01].

Al is an element that precipitates easier in ferrite than in austenite [Con01]. Thus, thermal cycling, particularly if ferrite is formed, can lead to deleterious AlN precipitates at the grain boundary [Yue95].

For the precipitation of AlN, cooling rates of less than $1°C.min^{-1}$ are required during continuous cooling [Cro87]. This low cooling rate is not reached in CC and thus it has been noticed that AlN precipitates are not likely to form under normal CC conditions all the more, they precipitate very sluggishly [Yue95]. Moreover, it is extremely hard to precipitate AlN after sensitization [Cro87].

Sulphur containing steels

S is a very deleterious element for the steel [Con01]. But it has been demonstrated that S has no effect on transverse cracking when the test samples are not brought to the liquid phase before testing [Min99a]. Thus the chosen thermal cycle for the mechanical tests is of an extreme importance (see Paragraph 2.3).

Calcium containing steels

Ca has been identified as very beneficial on the transverse cracking since it has a great affinity for S [Con01]. The addition of Ca is thus preferable and the recommended Ca/S ratio is of about 2 or 3 [Con01].

1.6.6 Summary of the precipitates study

Table 1.1 compiles all the knowledge gathered in the literature review over the precipitation state in peritectic steels at high temperature. This table helps to have an easy overview of the precipitation state that could be found in peritectic steels. This work is the basis of the microscopic study that is performed in the current thesis.

It should be mentioned that the values given are mean values of the different researches for a mean test configuration. As it has been showed before, the test configuration and especially the temperature path before experimental mechanical test is the key parameter to obtain the wanted precipitation state. Thus, these values are only references and the real precipitation state have to be determined on CC steel samples coming from each grade studied.

Precipitates	Size [nm]	Shape	Distribution	Position	Precipitation form
Nb	10-70	Globular	Strings	γ grain boundary	(Ti,Nb)(C,N)
V	<40	Rosettes Small dendrites	Random	γ grain boundary	V(C,N) (Ti,V)N
Ti	fine <20 medium 20-50 coarse 50-350	/	Random Strings	Intragranular	Ti(C,S) Ti(C,N)
Nb + V	/	Globular Cuboid	Random	/	(Nb,Ti,V)(C,N)

Table 1.1: Summary of the precipitation state for the peritectic steel grade family

1.6.7 Precipitation kinetic

The phenomenon of precipitation kinetic should be taken into account in our study. Even if no concrete numerical results are available to predict the precipitates appearance and thus, the precipitates size, this phenomenon is present, especially in the CC process where the slab cools down very fast.

On the curves showing the loss of secondary hardness (Figure 1.23) where the time is in logarithmic representation, the Nb(C,N) precipitates start to form slowly and an important decrease in hardening is seen after 1000s until 10000s before reaching a more slow decrease again. The end of the strong hardness loss could be related to the size of the precipitates that reaches the equilibrium, that is to say, the maximal diameter.

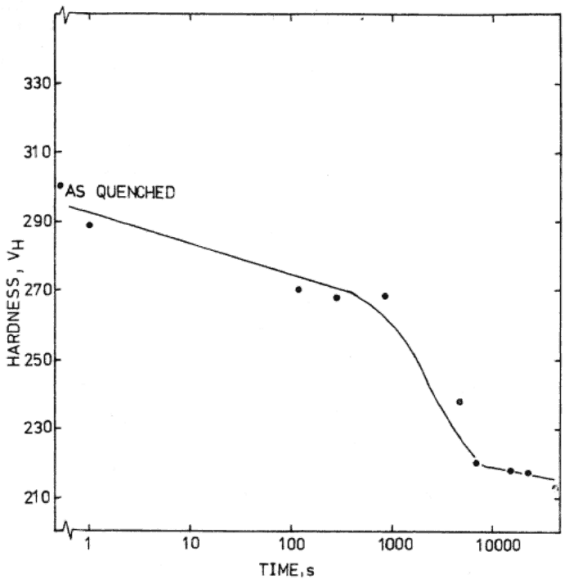

Figure 1.23: Hardness of the Nb containing peritectic steel grade following quenching and tempering after holding for various times at 950°C [Cro87]

The kinetic of precipitation in the Ti-V containing steel is slower than in the Nb-V steels. The precipitates have low solubility in austenite, Nb(C,N) may form at high temperatures of about 1200°C [Pan05a].

In Lee's study [Lee05], the samples taken from a 25kg melt showed no trace of NbC precipitates when cooled with nitrogen at $50°C.s^{-1}$. Thus, when quenched, the NbC precipitates do not have time enough to form.

The static precipitation of V(C,N) was also followed using the method of loss of secondary hardening. As shown for the Nb containing steels, the V containing steels present the same hardening curve in function of time (Figure 1.24(a)). The hardness decreases strongly between 100 and 1000s. This observation means that the kinetic of precipitation of V particles is faster than the one of the Nb particles. This fact can also be seen on the ductility curves of a V containing steel with two different holding times at high temperature. The curve of the longer exposed sample is deeper around 800°C (Figure 1.24(b)). The precipitates have more time to form and thus to increase

their detrimental effect.

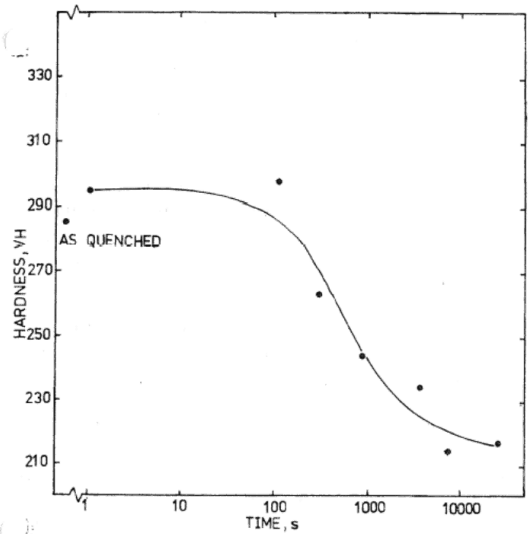

(a) Hardness of the V containing peritectic steel grade following quenching and tempering after holding for various times at 850°C

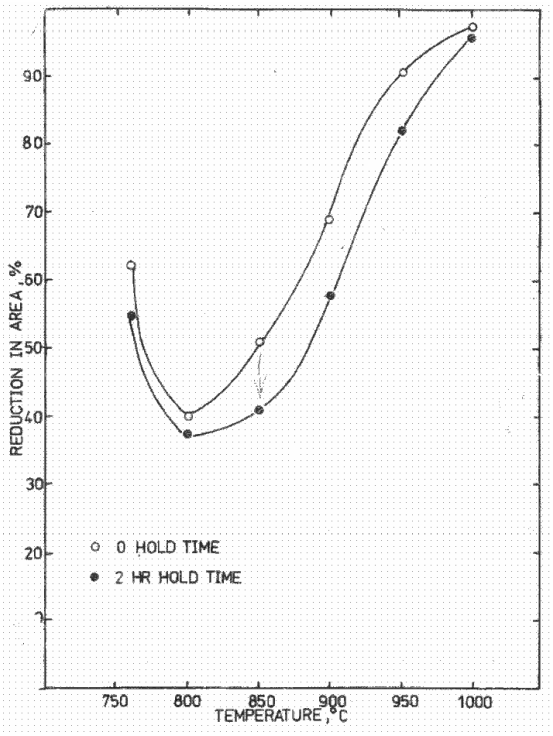

(b) Ductility curves of a V containing peritectic steel for different holding times

Figure 1.24: Illustration of the ductility loss and kinetic effect of V containing steels [Cro87]

1.7 Conclusion of the literature review

The literature research performed covers a large range of topics (microstructure of the studied steels, defects in CC slabs, fracture mechanisms, microalloying of steels). All these are related to the crack appearance in continuous casting and have been investigated as precisely as possible. Hereafter, a brief summary of the state-of-the-art in the explored domains is provided.

The damage of steels in CC is strongly linked with the **microstructure of the steels**. Thus it is important to know the microstructure of the peritectic steel grade in the temperature range where the cracks can occur. The grain size information found about the peritectic grades shows a great distribution going from 80μm to 600μm depending on the thermal treatment imposed. In the current thesis it is important to know the size of the prior austenite grain present in CC process without thermal treatment in order to reproduce this grain size in the experimental study and thus it should be determined through microscopic analysis.

It has been recognized by the industrial partner that **intergranular transversal cracks** are very deleterious for the peritectic steels grades. Thus, it is not surprising that numerous researchers wrote on this topic. The main conclusions that could be brought out from the literature review are the following ones:

- The transversal cracks appear in a range of temperatures extending from 600°C to 1100°C and is more pronounced at approximately 900°C where a presence of a ductility loss is detected.
- The critical temperature range is reached in the CC slab in the zone where the bending and the straightening of the slab induces high stresses in the shell.

The aim of this thesis is to model the crack appearance between the grains of a CC slab. For that reason, the **fracture mechanisms** should be known and understood. The different mechanisms occurring in the different steel grades studied are the following ones:

- austenitic grain boundary sliding,
- creep rupture composed of nucleation of microcavities, growth and coalescence.

These mechanisms are mainly due to respectively:

- the ferrite film present at the austenite grain boundaries,
- the precipitates forming at the austenite grain boundaries.

Nevertheless other elements could lead to fracture as the oscillation marks or the strong mechanical constrains.

It has been reported that the main parameters affecting the cracks appearance in steels are the **precipitates size** and the **precipitation state**. Thus a literature research about the alloying elements of the peritectic steel grades have been performed in order to know their shape, distribution, size, position and the most important, their effect on the crack appearance. The conclusions that could be brought out are the following ones:

- The precipitated carbonitrides showing a deleterious effect are: Al, N, Nb, S and V.
- The most deleterious precipitates and those who are added to the steel grades studied are: Nb and V knowing that Nb has a greater effect on crack appearance.
- The precipitates are commonly found at the grain boundary, which explains the crack appearance at the weakened grain boundaries.
- Nb(C,N) begins to precipitate at ≈1200°C.
- V(C,N) begins to precipitate at ≈1000°C.

This information will be exploited in this study for the creation of the representative cell (steel microstructure), the choice of the fracture model (fracture mechanisms) and the development of a methodology for the experimentation (steel microstructure, precipitation state).

Chapter 2

The damage model, its identification methodology and the sample treatment

This chapter tries to set the theoretical methodology and the experimental approach in order to reach the thesis goals. The main objective is to determine the crack appearance in peritectic steels during continuous casting and to establish the parallel with the steel composition.

- In Section 2.1, the model used to predict the damage is presented and the key parameters entering the model are identified.
- Section 2.1.4 presents the explanation of the way the representative cell is designed for this particular study.
- The link between the macroscopic simulation of the CC and the mesoscopic point of view of this study is given in Section 2.1.5.
- Section 2.2 presents the methodology of this study, which is described following the several steps in which it has been divided.
- The last part of this chapter (Section 2.3) is devoted to the thermal treatment that will be applied to the sample before performing the mechanical tests. This step is called the sensitization and represents the way to prepare the sample microstructure in order to bring it to correspond to the real industrial case.

2.1 Damage model description

Transverse cracking is a severe problem of the CC process. A damage model able to predict this sort of defect has been developed at the University of Liège in a previous thesis [Cas07b]. This damage model uses the finite element method (FEM) and more particularly, the non-linear code Lagamine developed at the MS^2F department of the University of Liège.

This model has already been validated on microalloyed steels and should be adapted on other steel grades presenting transversal cracks. In the current thesis, the particular

steel grades studied belong to the peritectic steel family. The fracture model takes into account the fracture mechanisms occurring at high temperatures in microalloyed steels. These mechanisms of decohesion and of grain boundary sliding were explained in Chapter 1.

The aim of this study is to model the CC process and the evolution of the damage at the grain scale. The results of a macroscopic scale CC simulation feed the microscopic scale damage model. The reason why a model of the whole structure at the mesoscopic scale is not possible is that the amount of computational resources would be too huge. As the critical areas for crack initiation are well known (see Section 2.1.1) specific zones can be defined for the finite element meshes and calculations in order to take into account the critical area in which damage occurs.

In this Section 2.1 the objective is to explain the way the model has been implemented into the LAGAMINE code and how the different crack mechanisms have been taken into account. The finite element model is developed at the mesoscopic scale. A representative cell has been designed (Section 2.1.4) and comprises interface and solid elements used in combination with a damage constitutive law. The solid elements are presented in Section 2.1.2, the interface elements in Section 2.1.3.1 and finally the damage law is explained in Section 2.1.3.2.

2.1.1 Modeling of the continuous casting process

The CC process has already been studied at the macroscopic scale by numerous authors [Pas03, Tho02, Hei03]. The mold geometry, the casting powder composition, the secondary cooling, the roll position are some of the parameters of the process. The macroscopic study of the CC is done to improve the casting speed and the quality of the product by localizing the weakest areas and the causes of the defect appearance by modeling various CC conditions. It is then possible to concentrate the work on these special areas and observe the damage at the grain scale.

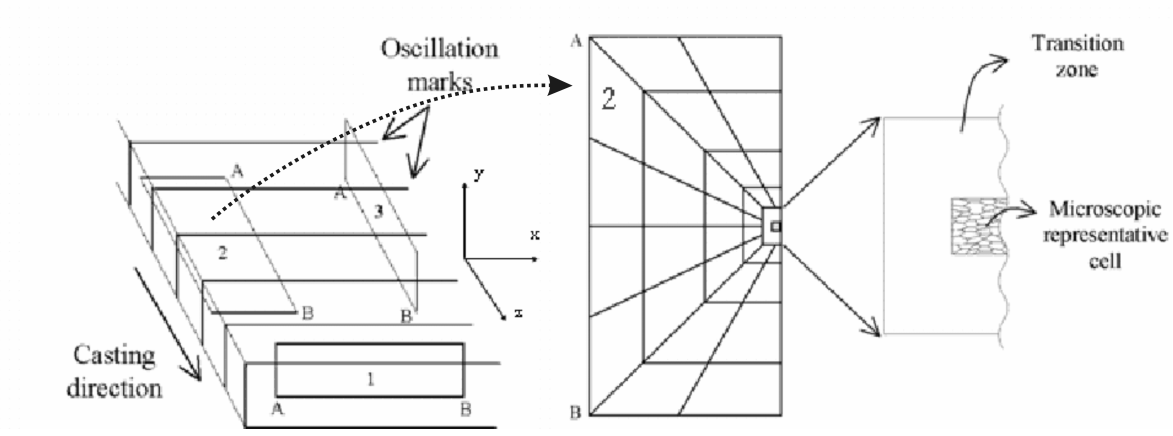

Figure 2.1: Simulation of the CC process and transposition in the local approach [Cas07a]

The aim of the current thesis, is the extension of the model developed by S. Castagne to predict crack at the grain level. The mesoscopic model requires information from the

macroscopic scale, which are available through the previous macroscopic finite element analysis of the continuous process.

2.1.2 The grain

In order to model intergranular creep fracture, the present model contains two dimensional (2D) finite elements for the grains and one dimensional (1D) interface elements for their boundaries [Onc99]. Inside the grains, a classic elastic-viscous-plastic law is used, and at its boundaries a damage law is defined.

The grains are modeled by thermo-mechanical 4-nodes quadrilateral elements of mixed type with one integration point [Zhu95]. This element contains anti-hourglass stresses that prevent zero-energy hourglass deformation modes to appear. A law of Norton-Hoff type [Pas07] is used to quantify the viscous-plastic behavior inside the grain for the studied steel. Its expression in terms of equivalent stress σ_e, strain ε_e and strain rate $\dot{\varepsilon}_e$ is given by equation 2.1:

$$\sigma_e = \varepsilon_e^{p_4} \cdot \mathrm{e}^{(-p_1 \varepsilon_e)} \cdot p_2 \cdot \sqrt{3} \cdot \left(\sqrt{3} \cdot \dot{\varepsilon}_e\right)^{p_3} \tag{2.1}$$

where the parameters p_1 to p_4 are temperature dependent. p_1 defines the effect of softening, p_2 is linked to the maximum value of the curve, p_3 models the viscosity and p_4 the hardening.

2.1.3 The grain boundary

2.1.3.1 The interface element

The 2D elements modeling the grains are connected by interface elements to account for cavitation and sliding at the grain boundary. As the thickness of the grain boundary is small in comparison with the grain size for conventional ones, the grain boundary can be modeled by 1D interface elements. These elements have two nodes and two integration points and are associated with a constitutive law which includes parameters linked to the precipitate and void density. The damage variable D_{dam} explicitly appears in this law and is defined in Section 2.1.3.2.2.

The interface element is defined by one contact element associated with one edge of the solid element (solid element i, j or k in Figure 2.2) and a set of foundation segments defining all grain boundaries. The contact search algorithm finds the closest foundation segment defining the current neighboring element.

The triple point between grains i, j and k is defined by three nodes having exactly the same coordinates:

- E belonging to grain i,
- B belonging to grain k,
- H belonging to grain j.

The contact element $\overline{DE}$ is linked to the nearest foundation segment of the neighboring elements i and j. In this case, it is associated with $\overline{AB}$. With the evolution of the mesh during deformation it could change its neighbor to take always the nearest.

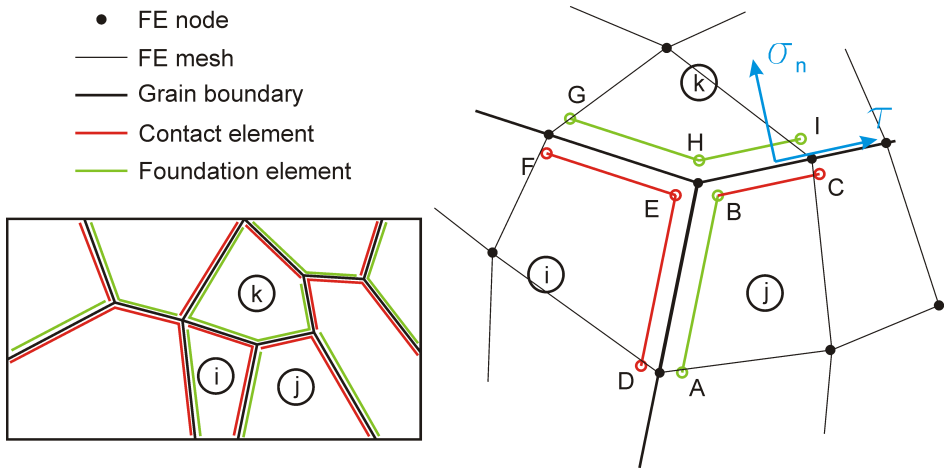

Figure 2.2: Elements composing the grain in the mesoscopic model where circles are associated to the neighboring black dots that represents the mesh nodes

The state variables for the interface element are computed using information from the two solids elements in contact. The state variables as stress and strain in the interface element are the corresponding mean values of the integration points value of both considered elements.

The original contact element was described by Habraken et al. [Hab98] and is usually combined with a Coulomb's friction law. This element has been modified in order to introduce the damage interface law and a cohesion criterion. The stress components, σ_n and τ, of the contact element are represented in Figure 2.2, their evolution is described by the following incremental relationships:

$$\dot{\tau} = k_s \left(\dot{u} - \dot{u}_s\right) \quad and \quad \dot{\sigma}_n = k_n \left(\dot{\delta} - \dot{\delta}_c\right) \tag{2.2}$$

In this penalty method the penalty coefficients k_s and k_n are large enough to keep the deviations $\dot{u} - \dot{u}_s$ and, $\dot{\delta} - \dot{\delta}_c$ small. $\dot{u}$ and $\dot{\delta}$ are respectively the relative sliding velocity of adjacent grains due to shear stress τ and the average separation rate between two adjacent grains. This latter rate direction is normal to the contact element, and the normal stress σ_n is responsible of the damage growth. These variables are directly computed from nodal displacements. $\dot{u}_s$ and $\dot{\delta}_c$ are the similar variables to $\dot{u}$ and $\dot{\delta}$ but related to the damage law. Their evolutions are described in the Section 2.1.3.2 (Equations 2.3 and 2.19). Equation 2.2 enforces $\dot{u}$ and $\dot{\delta}$ to be equal to $\dot{u}_s$ and $\dot{\delta}_c$, respectively.

2.1.3.2 The interface material law

As discussed in Section 1.3, the major damage mechanisms at the grain scale are viscous grain boundary sliding, nucleation, growth and coalescence of cavities leading to intergranular microcracks, which subsequently leads to the formation of a macroscopic crack.

The model was developed by [Onc99] and implemented by Sylvie Castagne [Cas07b] in LAGAMINE FE (finite element) code.

2.1.3.2.1 Grain boundary sliding

Grain boundary sliding is governed by a relation linking the applied stress τ to the sliding rate $\dot{u}_s$:

$$\dot{u}_s = w\frac{\tau}{\eta_B} \tag{2.3}$$

where $\dot{u}_s$ is the relative velocity between two adjacent grains, w is the thickness of the grain boundary and η_B is the grain boundary viscosity. However w/η_B can be expressed in terms of the strain-rate parameter $\dot{\varepsilon}_B$ defined as follows:

$$\dot{\varepsilon}_B = \dot{\varepsilon}_0 \left(\frac{w\sigma_0}{\eta_B d\dot{\varepsilon}_0} \right)^{\frac{n}{n-1}} \tag{2.4}$$

where d is the grain size and n is the creep exponent [Onc99]. σ_0, $\dot{\varepsilon}_0$ are reference stress and strain rate that depend on the steel grade. The intergranular sliding can be characterized by the ratio $\dot{\varepsilon}_e/\dot{\varepsilon}_B$ between inside grain equivalent deformation rate $\dot{\varepsilon}_e$ and boundary strain rate $\dot{\varepsilon}_B$. This ratio measures the relative deformation resistance between the grain and the grain boundary. In case of free sliding $\eta_B = 0$ and $\dot{\varepsilon}_e/\dot{\varepsilon}_B = 0$. When there is no sliding $\eta_B \to \infty$ and $\dot{\varepsilon}_e/\dot{\varepsilon}_B \to \infty$.

The classic creep law is defined as:

$$\dot{\varepsilon}_e = \dot{\varepsilon}_0 \left(\frac{\sigma_e}{\sigma_0} \right)^n = B\left(\sigma_e\right)^n \tag{2.5}$$

where σ_e is the equivalent von Mises stress inside the grain and B a material creep constant.

Using equations 2.4 and 2.5 the ratio w/η_B becomes:

$$w/\eta_B = d\left(\dot{\varepsilon}_B\right)^{\frac{n-1}{n}} \left(B\right)^{\frac{1}{n}} \tag{2.6}$$

Four parameters are then necessary to define the boundary sliding: the creep exponent n, the creep parameter B, the grain size d and the parameter characterizing the viscosity ratio $\dot{\varepsilon}_e/\dot{\varepsilon}_B$. The two first parameters can be determined through macroscopic hot tensile tests, $\dot{\varepsilon}_e/\dot{\varepsilon}_B$ is chosen equal to an intermediate value of 10 [Onc99] and microscopic measurements provide the grain size.

2.1.3.2.2 Voids evolution

In the context of damage at high temperature, the mechanism of voids nucleation, growth and coalescence is established.

The model uses an idealized formulation of the grain boundary geometry where the cavities are supposed to be distributed on each grain boundary segment and defined

at each integration point with an average spacing $2b$ and a diameter $2a$. Figure 2.3 illustrates this idealized representation; in Figure 2.3(a) each individual void is represented and in Figure 2.3(b) the voids are replaced by a continuous variable δ_c. Its evolution rate $\dot{\delta}_c$ is computed at the integration points of the interface contact elements to account for the evolution of the interface thickness due to the presence of voids at the grain boundaries (Equation 2.2). Detailed equations for the variables used for the computation of δ_c are presented in the next sections. A fracture criterion is also proposed.

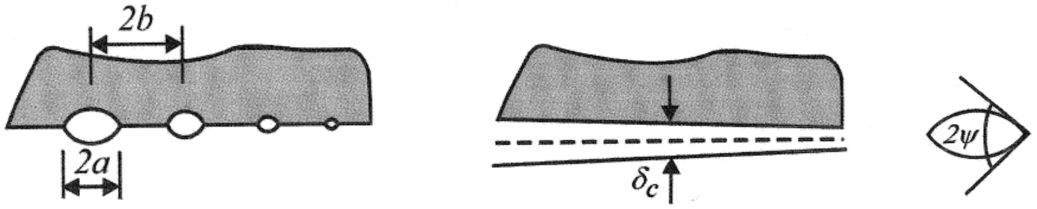

(a) (b) (c)

Figure 2.3: Discrete and continuous representations of the grain boundary: (a) Real geometry, (b) Virtual description at one integration point, (c) Void shape [Onc99]

Void nucleation, computation of the cavity spacing growth rate $\dot{b}$

In most engineering alloys, cavities have been observed to continuously nucleate. The following experimental relation has been suggested by [Gie94]:

$$\dot{N} = \beta \sigma_n^2 \dot{\varepsilon_e} = F_n \left(\frac{\sigma_n}{\Sigma_0} \right)^2 \dot{\varepsilon_e} \quad with \quad \sigma_n \geq 0 \tag{2.7}$$

N is the average number of cavities per unit length of grain boundary. $\dot{\varepsilon_e}$ is the total equivalent creep strain rate from Equation 2.1. The Norton law assumes that elastic strain rate is negligible and uses the total strain rate as creep strain rate. It is computed as the average value of the neighboring solid elements associated with contact element and foundation segment. σ_n is the normal stress (computed as the projection in direction perpendicular to the contact element of the average stress tensor), introduced to allow a faster nucleation on those grain boundaries that are perpendicular to the loading direction. β is a material constant [Gie94] which is related to Σ_0 and to F_n. Σ_0 is a normalization constant representative of the average stress level in the material surrounding the crack. F_n is the microstructural parameter which influences the nucleation rate at the grain boundary. Zones where nucleation is more important can be introduced through this parameter. F_n can model, among others, the precipitation state or the influence of the thin ferrite film generated at the grain boundary leading to strain concentration [Min91]. According to Equation 2.7, the nucleation will begin with the plastification. However, experience shows that nucleation appears later, so a threshold is used to define the beginning of the nucleation. For this purpose, the parameter S which combines the stress and the cumulated equivalent strain is defined:

$$S = \left(\sigma_n / \Sigma_0 \right)^2 \varepsilon_e \tag{2.8}$$

The parameter S characterizes the state of the material before nucleation. It will grow with the strain until the threshold value S_{thr} is reached. S_{thr} is assumed to be related to the minimum cavity density N_I from which nucleation can be observed and to the factor F_n telling the importance of the nucleation activity of the material:

$$S_{thr} = N_I / F_n \tag{2.9}$$

Once nucleation begins the parameter S is not used anymore in the model.

Finally, experience shows that the cavity density tends to saturate for large creep strains, then the nucleation of new cavities stops when N reaches the value N_{max}. If $2b$ is the cavity spacing (Figure 2.3(a)), N is computed by:

$$N = \frac{1}{\pi b^2} \tag{2.10}$$

The evolution of the cavity spacing is found by derivation of Equation 2.10:

$$\dot{b} = -\frac{1}{2}\frac{\dot{N}}{N} b \tag{2.11}$$

By substituting Equations 2.7 and 2.10 in Equation 2.11, we have:

$$\dot{b} = -\frac{\pi}{2} b^3 \beta \sigma_n^2 \dot{\varepsilon_e} \tag{2.12}$$

The nucleation rate $\dot{N}$ (Equations 2.7 and 2.11) is related to the internal state of the material N as well as to the stress σ_n and strain rate ε_e states on the grain boundary. With a one-dimensional element, this nucleation rate $\dot{N}$ can be interpreted as a measure of the evolution rate of the cavity spacing $\dot{b}$. In practice, the finite element model uses as leading equations, Equations 2.7 and 2.11, to compute the decrease rate of b due to continuous nucleation of cavities.

Void growth, computation of the cavity size growth rate $\dot{a}$

A detailed formulation of the cavity growth under diffusion and creep deformations was proposed by Tvergaard [Tve84].

For a cavity tip angle ψ (Figure 2.3(c)), the cavity growth rate is:

$$\dot{a} = \dot{V} / \left[4\pi a^2 h(\psi)\right] = \left(\dot{V_1} + \dot{V_2}\right) / \left[4\pi a^2 h(\psi)\right] \tag{2.13}$$

where $h(\psi) = \frac{(1+cos\psi)^{-1} - 0.5cos\psi}{sin\psi}$ is a shape function of the cavity and $\dot{V}$ is the total cavity volume growth rate, which is divided into diffusion growth rate $\dot{V_1}$ (Equation 2.14) and creep deformation rate $\dot{V_2}$ (Equation 2.15):

$$\dot{V_1} = 4\pi D \frac{\sigma_n}{ln(1/f) - (3-f)(1-f)/2} \tag{2.14}$$

$$\dot{V}_2 = \begin{cases} -A\left(\frac{3}{2n}\left|\frac{\sigma_m}{\sigma_e}\right| + C\right)^n & \text{for} \quad \frac{\sigma_m}{\sigma_e} < -1 \\ A\left(\frac{3}{2n} + C\right)^n & \text{for} \quad \left|\frac{\sigma_m}{\sigma_e}\right| \leq 1 \\ A\left(\frac{3}{2n}\frac{\sigma_m}{\sigma_e} + C\right)^n & \text{for} \quad \frac{\sigma_m}{\sigma_e} > 1 \end{cases} \tag{2.15}$$

where $C = \left[(n-1)\left(n+0.4319\right)\right]/n^2$ and $A = 2\pi\dot{\varepsilon}_e a^3 h\left(\psi\right)$. D is the diffusion parameter (Equation 2.17), n the creep exponent, σ_n, σ_e and σ_m are respectively the normal, equivalent, and mean stresses applied to the grain boundary (average value of the two solid elements linked to the contact element and the foundation segment defining the grain boundary). The variable f, used in Equation 2.14 is defined as follows:

$$f = max\left\{\left(a/b\right)^2, \left[a/\left(a+1.5L\right)\right]^2\right\} \tag{2.16}$$

where $L = \left(D\sigma_e/\dot{\varepsilon}_e\right)^{1/3}$.

The coupling between diffusive and creep contribution to void growth is introduced through the length scale L. For small values of a/L, cavity growth is dominated by diffusion while for larger values, creep growth becomes more and more important.

The diffusion parameter can be expressed as a function of the temperature by:

$$D = \frac{D_{b0}\delta_b\Omega}{kT} \cdot exp\left(-\frac{Q_b}{RT}\right) \tag{2.17}$$

with $D_{b0}\delta_b$ the grain boundary diffusion coefficient, Ω the atomic volume, Q_b the activation energy, T the temperature in Kelvin, $k = 1.3807 \cdot 10^{-23}\text{J}\cdot\text{K}^{-1}$, the Boltzmann's constant and $R = 8.3145\text{J}\cdot\text{mol}^{-1}\text{K}^{-1}$, the universal gas constant. The particular values for austenitic steel are the following ones: $D_{b0}\delta_b = 7.510^{-14}\text{m}^5\text{s}^{-1}$, $\Omega = 1.21 \cdot 10^{-29}\text{m}^3$ and $Q_b = 159\text{kJ}\cdot\text{mol}^{-1}$ [Nee80].

Finally the discrete cavity distribution is replaced by a continuous distribution on the contact element of the grain boundary so that the average separation between two grains δ_c, which is equivalent to a grain boundary thickness, evolves in a continuous way on the contact element (Figure 2.3(b)). δ_c is determined using the volume of grain boundary cavities V and their average spacing b:

$$\delta_c = \frac{V}{\pi b^2} \tag{2.18}$$

Then, the separation rate $\dot{\delta}_c$ used in Equation 2.2 is given by:

$$\dot{\delta}_c = \frac{\dot{V}}{\pi b^2} - \frac{2V}{\pi b^2}\frac{\dot{b}}{b} \tag{2.19}$$

To solve the equations of this section, the following additional independent parameters have to be defined: the initial void size a_0 and the voids spacing b_0, the nucleation parameter F_n, the normalization constant Σ_0, the cavity tip angle ψ, the cavity density for nucleation start N_I and the maximum cavity density N_{max}. So, seven input parameters are needed in order to model the progression of the crack. One additional D_{dam} parameter is implemented. This one defines the rupture and is described hereafter.

Voids coalescence and fracture criterion

Coalescence takes place when cavities are sufficiently close to each other to collapse. The parameter used to define the coalescence activation is the ratio a/b.

$\dot{a}$ and $\dot{b}$ are the leading variables that are first computed. Their values allow to update the other parameters like N and δ_c allowing the evolution of the crack in the material and finally the damage is quantified trough a and b ratio.

The ratio a/b, the damage variable, in the current model. When this ratio reaches a critical threshold D_{dam}, coalescence is triggered and a crack appears. At this moment the contact is lost between the foundation and the contact element of the interface element where the criterion has been reached and a crack physically appears in the finite element model.

2.1.3.3 Law parameters

The different parameters that have a particular role to play in the physical understanding of the rupture phenomena are used in the damage law to determine the evolution of the failure during the several stages of microscopic changes in the steel when going through the continuous caster. The parameters that needs to be determined in this study are listed in Table 2.1.

2.1.4 Representative cell design

The creation of the representative mesoscopic cell is based on the method proposed by S. Castagne [Cas07b]. It is composed of a central part (Figure 2.4(b)) that is the mesoscopic cell containing the grains with their grain boundaries and a surrounding part called the transition zone (Figure 2.4(a)).

The transition zone serves to get homogeneous stress and strain fields around the cell. So it is possible to know quite precisely the average of the stress and strain fields in the cell and to compare them to the actual values occurring in the tensile test or the CC process. The grains and the transition zone are modeled with elements following a Norton-Hoff creep law given by Equation 2.1. It represents the Von Mises equivalent stress σ_e as a function of the equivalent strain ε_e and the equivalent strain rate $\dot{\varepsilon_e}$.

The grain boundaries are modeled thanks to 1D elements taking into account the cavitation and the sliding at the grain boundary as described in Section 2.1.3. These elements are associated with the damage law which includes parameters linked to the presence of precipitates, voids, etc. In this law, a damage parameter explicitly defines the crack phenomenon. This law follows the cracking of the cell and determines the

Parameters	Description	Determination of the value
d [mm]	Mean grain size	**Microscopic analysis**
$D_{b0}\delta_0$ [$mm^5 \cdot s^{-1}$]	Boundary diffusivity	**Literature** [Nee80] data for austenite
Ω [mm^3]	Atomic volume	
Q_b [$N \cdot mm \cdot mol^{-1}$]	Activation energy	
$\dot{\varepsilon}_e/\dot{\varepsilon}_B$	Grain viscosity parameter	
a_0 [mm]	Initial cavity size	**Micrographic analysis** of the precipitation state
b_0 [mm]	Initial distance between cavities	
ψ [°]	Cavities angle	
F_n [mm^{-2}]	Nucleation parameter	**Hot tensile tests** with different sample shapes (cylindrical, notched) $700°C < T < 900°C$ $\dot{\varepsilon} = 1 \cdot 10^{-2}s^{-1}$ to $1 \cdot 10^{-3}s^{-1}$
N_I [mm^{-2}]	Initial density of cavities	
N_{max}	Nucleation threshold	
a/b	Rupture criterion	
n (T)	Creep exponent	**Compression and tensile tests** for T = 700, 800, 900, 1000, 1100 °C and $\dot{\varepsilon}$= 0.01, 0.001, 0.0001s^{-1} Adjustment of the Norton-Hoff law parameters (Equation 2.1)
B (T) [$MPa^{-n} \cdot s^{-1}$]	Creep parameter	
Σ_0 (T) [MPa]	Normalization stress	
k_n [$MPa \cdot mm^{-1}$]	Penalty coefficient on the contact pressure	**Literature** [Cas07b]
k_s [$MPa \cdot mm^{-1}$]	Penalty coefficient on the shear frictional stress	

Table 2.1: Summary of the different damage law parameters and their way of identification

first crack appearance occurring through the mechanism of grain boundary sliding or voids nucleation, growth and coalescence at high temperature.

The way to proceed in order to create the representative cell is the following one:

Step A: First, a random set of n points is defined in a chosen area in function of the grain size and the number of grains wanted. Two different approaches are studied: The micrographic and the Voronoï approaches.

Micrographic approach for the design of the representative cell

At the study beginning, the representative cell is designed on the basis of the micrography Figure 2.5 representing the primary austenitic grains. Each node of a triple point between grains is determined and introduced manually. The segments joining them and representing the grains contour and the segments for the damage computation (contact elements and foundations) have been introduced also manually.

Voronoï approach for the design of the representative cell

As the meshing of the mesoscopic cell represents a huge work and a lot of time, it could be possible in the future to take advantage of the Voronoï triangulation in order to automatically create the representative cell (Figure 2.6). Such representative cells have already been designed by Liu [Liu98] using the Voronoï triangulation as well as the same damage law used in this study.

Step B: The second step is to mesh the cell grains.

Micrographic approach for the design of the representative cell

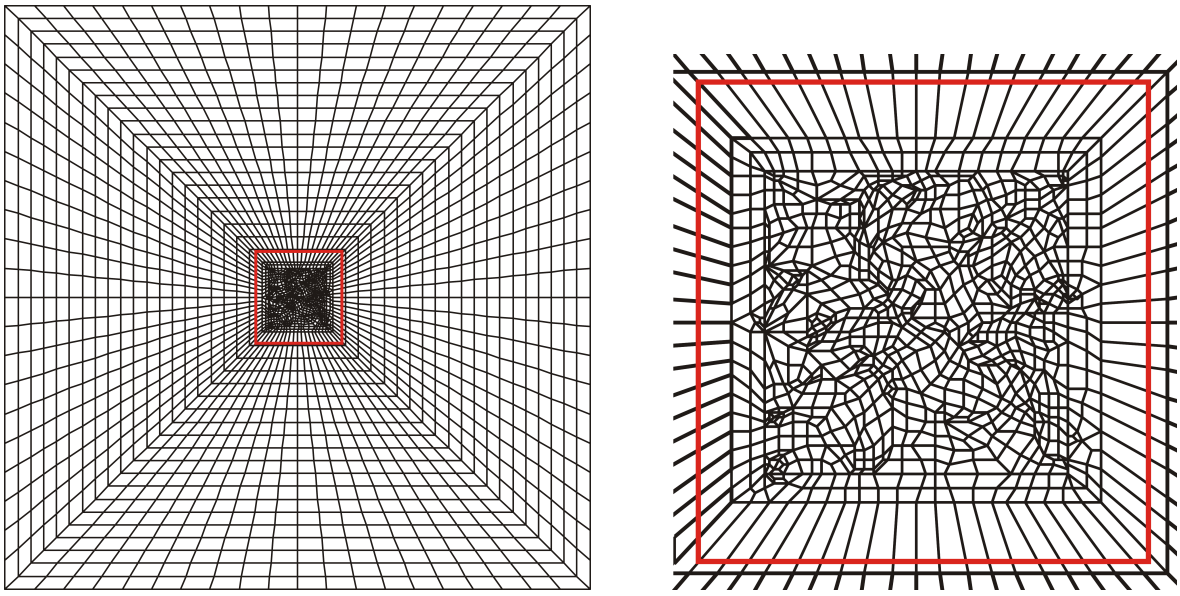

(a) Transition zone and mesoscopic cell (b) Mesoscopic cell

Figure 2.4: Representative cell

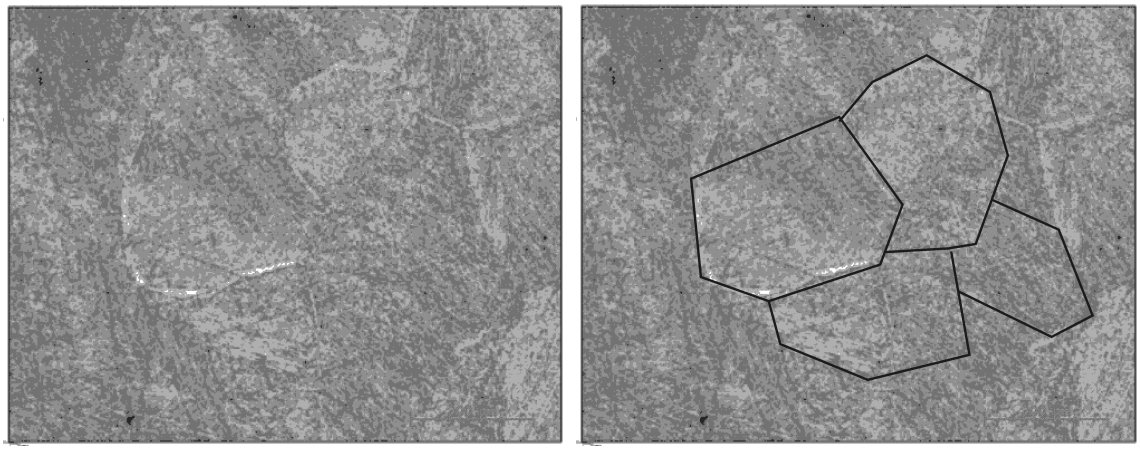

(a) (b)

Figure 2.5: (a) Metallographic inspection of the subsurface of a peritectic steel (b) with the austenite grains and ferrite grain-boundary (data provided by Arcelor Research)

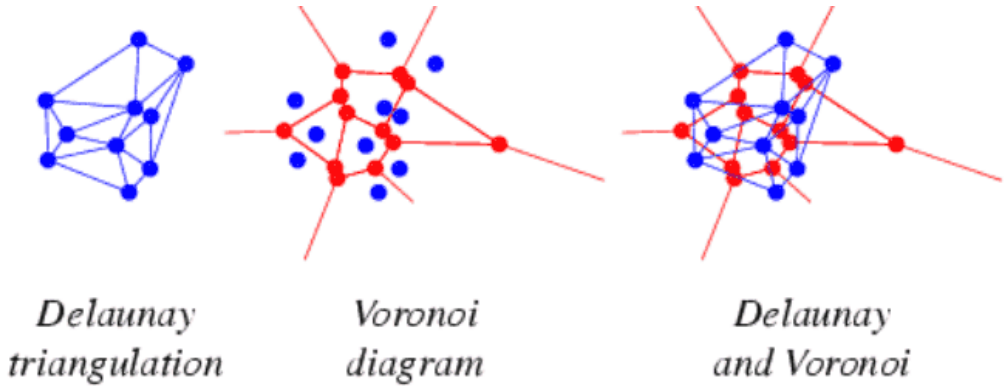

Figure 2.6: Different ways of automatic meshing with the Delaunay-Voronoï diagrams [MATH]

In the micrographic approach, the nodes are manually linked to each other in order to create the microstructure representative grains. Then the software GMAILL is used in order to built the mesh of the representative cell.

VORONOÏ APPROACH FOR THE DESIGN OF THE REPRESENTATIVE CELL

In the Voronoï approach, this is done with the help of the Voronoï tessellation. The Voronoï tessellation consists in partitioning the plane with n points into convex polygons such as each polygon contains exactly one generating point and every point in a given polygon is closer to its generating point than to any other. The cells produced are called Voronoï polygons. After this step, the software GMAILL could be used in order to create the FE mesh.

STEP C: The third step is to create the contact elements and their associated foundation segment list in the same way S. Castagne implemented for her thesis.

As explained before, the grains are able to split off from their neighbors. This is possible because each grain is considered as a separated entity that is fixed to its neighbor thanks to interface elements. The contact element attached at one side of a grain checks and detects the nearest foundation segments linked to the boundary of another grain (the neighbor).

In order to be able to detect the foundation, the orientations of each contact and foundations elements are important as it determines the orientation of the external normal vectors which are used to check if the contact is possible.

The idea for the cell design is, in a first step, to place the contact elements counter-clockwise by following each grain contour and defining the nodes of an element when no one has already been detected, as shown in Figure 2.7. The part of the grain where there is no contact element receives a foundation element that is defined clockwise.

By this way, the contact element mesh is correctly oriented.

STEP D: The last step is to produce the transition zone around the representative cell in order to obtain an homogeneous zone of stresses applied to the mesoscopic representative cell described before (Figure 2.4). Around this mesh (mesoscopic cell and transition zone), forces and displacements are applied and the stresses

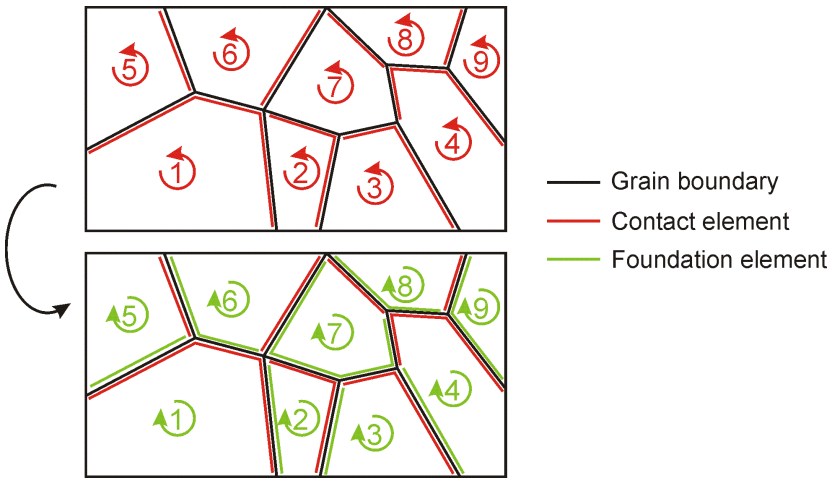

Figure 2.7: Illustration of the meshing process for the grain boundaries [Cas07a]

and strains generated inside the cell are then homogeneously distributed on the representative cell.

The Voronoï approach can be helpful, knowing that the representative cells for the different steel grades studied have to be designed. However, in a first approach the microstructure is assumed to be the same for the three peritectic steel grades so the representative cell does not change with the grade. To be more efficient in the cell creation, the development of the Voronoï method should be investigated.

2.1.5 Macro-Meso link

The macroscopic mechanical data have to be transferred to the representative cell as forces and/or displacements along the cell mesh boundaries. Thus it is necessary to precisely define the way of transfering the data.

As explained in Section 2.1.1 the damage evolution is analyzed at the grain scale. Thus, specific areas of the slab should be defined for the finite element calculations. Some models, as the one available at the University of Liège [Pas03] and the FEM model Thercast used by ArcelorMittal, provide results on the possible macroscopic location of the crack (Figure 2.8). The stress and strains in the steel slab at the integration point are computed and stored by ULg program. The temperature, stress and displacement fields are provided at each node by Thercast. The risk areas are identified and the values of temperature, stress and strain fields and of their histories are extracted from the macroscopic simulation. A representative microscopic cell is then meshed in this zone and the history of the thermo-mechanical loading is applied on the edges of the microscopic cell.

From a mechanical point of view, the mesoscopic cell is a slice in **generalized plane strain state**. This formulation allows applying forces and/or displacement histories in the out-of-plane direction. In Figure 2.9 a thin slice, perpendicular to the casting axis is modeled. The middle plane of this slice is meshed (Figure 2.10) and its thickness e at any point of coordinate (x,y) in the domain is governed by three degrees of freedom

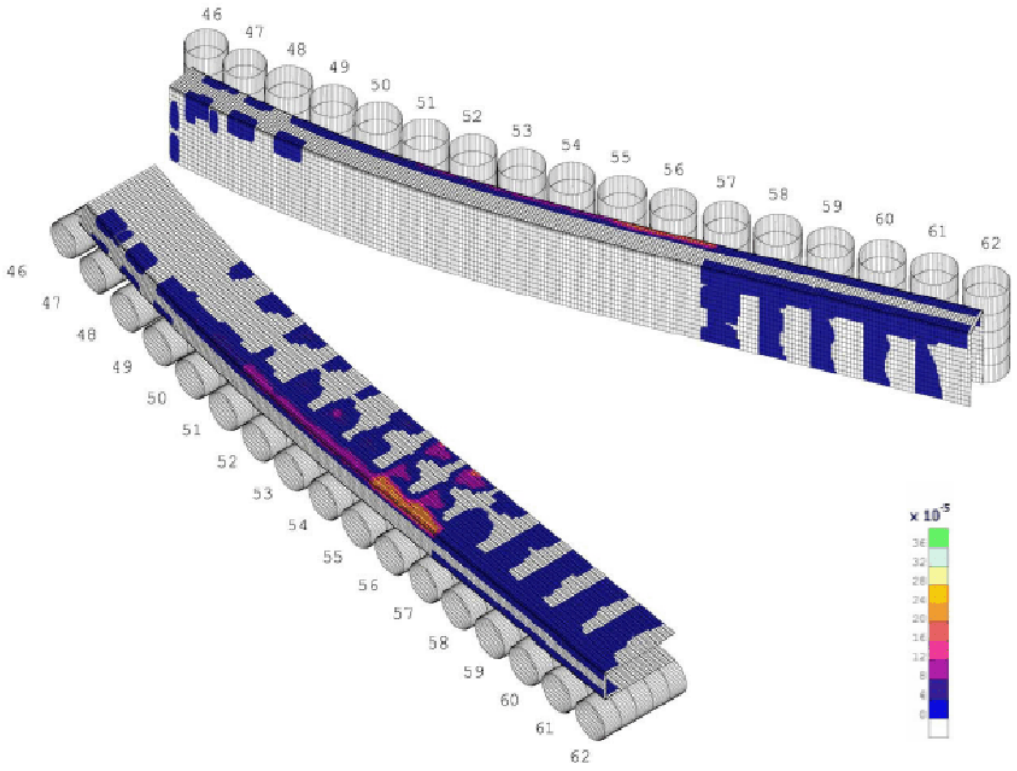

Figure 2.8: Longitudinal elongation rate of the CC of Marcinelle, defining the risk of transversal cracking [Pas03]

α_0, α_1 and α_2 according to the following equation [Pas03]:

$$e(x, y) = \alpha_0 + \alpha_1 x + \alpha_2 y \tag{2.20}$$

where α_0 corresponds to the thickness of the slice at the origin of the axes x and y. α_1 and α_2 are representative of the gradient of thickness respectively along x and y axes.

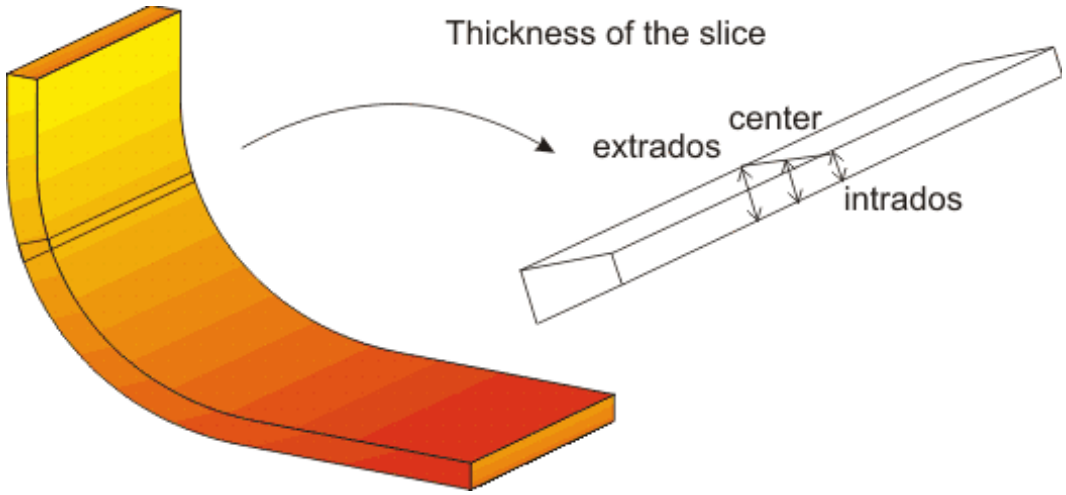

Figure 2.9: Example of a slice extracted from the CC slab that has to be modeled in generalized plane strain state for the crack prediction [Pas03]

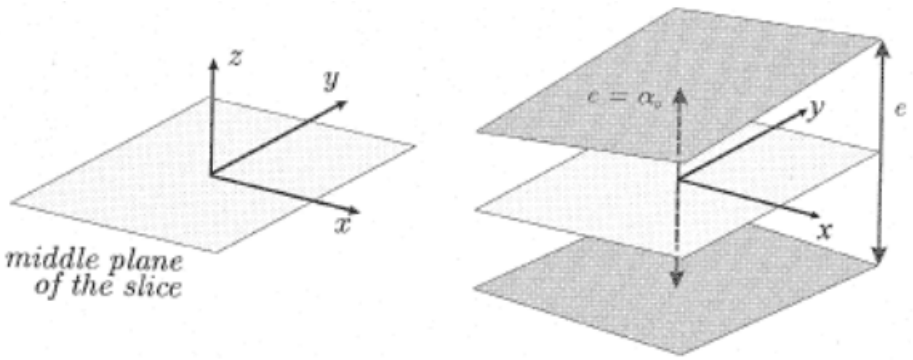

Figure 2.10: Thickness of the slice in generalized plane strain state [Pas03]

The results provided by the macroscopic numerical simulation of the CC process are the thermal, the stress and the strain fields [Pas07, Pas03, Pas06]. The results from the macroscopic simulations have to be transformed and adapted to the representative cell. Several dispositions have been tested as the following ones knowing that imposed forces are better for the calculations accuracy.

- The application of forces in the three direction lead to convergence difficulty.
- The application of two forces and one displacement in z direction (lowest strain direction in the tensile test sample) is conclusive.

The last tested configuration has been taken into account in the current thesis (Figure 2.11).

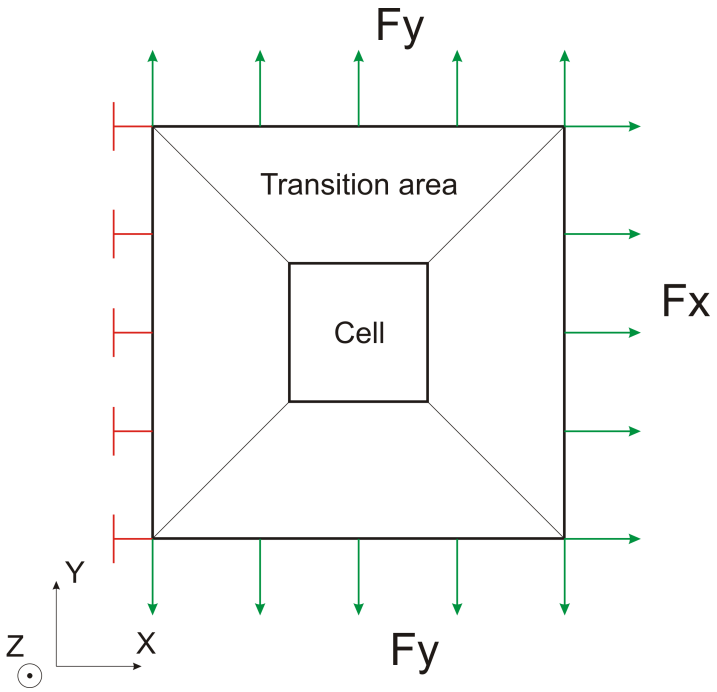

Figure 2.11: Application of the forces and degrees of freedom on the representative cell where the plane xy is associated to plane 3 in Figure 2.1

To allow the transfer of data from the macroscopic model to the mesoscopic one, the mesoscopic cell has to be surrounded by a transition zone as shown in the previous section. The mechanical field is imposed on each node of the boundary of the transition zone through above edge loading. The stress and strain components found in this transition zone should correspond to the one taken from the macroscopic simulation. The thermal field is imposed on each node in both transition zone and mesoscopic cell.

2.2 Methodology to identify the damage model parameters

The goal of the experimental campaign is to determine rheological and damage parameters for each material. The material parameters should be measured in identical loading conditions than CC process. They will describe the mechanical and damage behavior of the different steels studied. It is important to find a single set of parameters to predict cracks at the grain interface in CC. In order to reach this final goal, different steps summarized in Figure 2.12 are necessary:

Step A: The grain model (Norton-Hoff type) is identified by hot tensile or compression tests on classical tensile or compression samples (not notched).

Step B: Hot tensile tests applied on samples with different notches are performed in order to get different macroscopic stress-strain histories. They allow to validate the parameters identified in the Step A and to collect data about rupture.

Step C: A representative mesoscopic cell is designed with the same microscopic features as the material in the specific CC conditions.

Step D: The representative cell is loaded by the macroscopic stress, strain and temperature histories recovered from Step B. Both curves, the one coming from the experimental tensile test (Step B) and the one coming from the mesoscopic simulation are compared. The damage simulation of the notched samples should predict the crack appearance.

Step E: The final data set is used in the simulations dedicated to crack predictions in the CC process.

All these different steps are described hereafter and the results of each part are given in the following chapters:

- Step A ⇒ Paragraph 3.1.3.4
- Step B ⇒ Section 3.2
- Step C ⇒ Section 3.3
- Step D ⇒ Section 4.3
- Step E ⇒ Chapter 5

Hereafter, more details are given on each step.

2.2.1 Step A, the material rheology

The first step of this work is to determine the mechanical behavior of the studied material for different strain rates and temperatures. The temperature, the displacement and the strain rate are chosen to cover the loading history applied on the sample in CC process. The rheological model used is an elasto-visco-plastic law type where the parameter are temperature dependent. The law used here is the Norton-Hoff law given in the Section 2.1.2 (Equation 2.1). It contains four parameters, p_1 to p_4.

In practice, the rheological parameters are determined by hot tensile tests. The chosen strain rates are close to the one in CC; $1 \cdot 10^{-3}$, $5 \cdot 10^{-3}$ and $1 \cdot 10^{-2}s^{-1}$ (a summary of hot tensile test campaign is presented in Table 2.2). The sample geometry is described in Figure 2.13. The temperature is also varied between the tests in order to determine the dependence of the parameters to this variable. The temperature range in CC where the damage might occur is between 700 and 1100°C as seen in literature [Moh02]. Thus the temperatures chosen are 900, 1000 and 1100°C.

Another important data for each steel grade is the ductility curve. This curve, as explained in Section 1.4.4, helps to identify the temperature range where the ductility is weaker. This experimental result is used in the Step B to choose the test temperatures around the weak area.

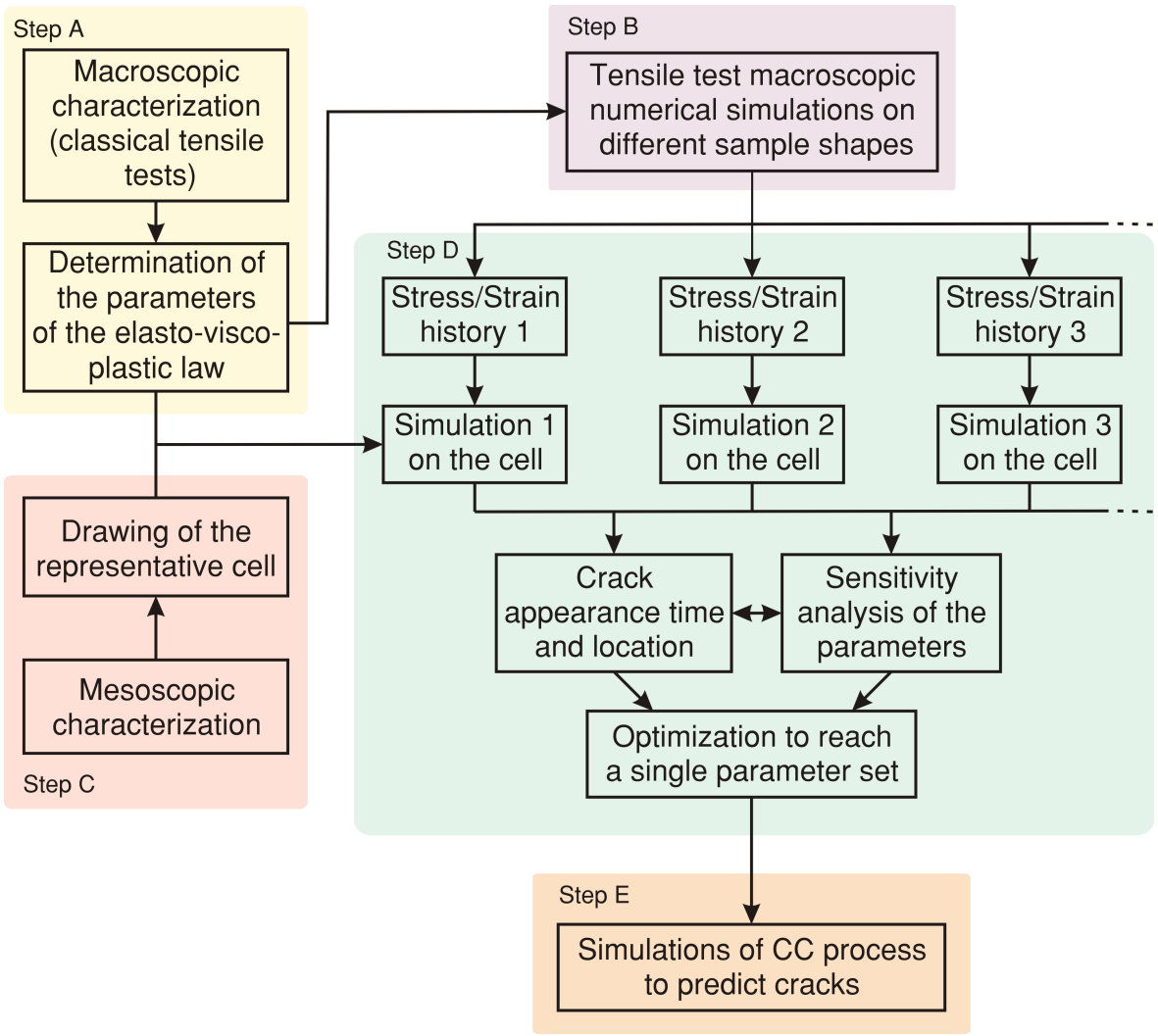

Figure 2.12: Diagram of the different steps which define the global strategy of modeling the crack prediction for peritectic steels during the continuous casting

2.2.2 Step B, tensile tests on different geometries

In order to determine a single set of damage parameters, different mechanical tests are performed to generate various stress and strain histories at different temperatures. The way to obtain different types of flow curves is to modify the sample shape.

The sample shape is defined in Figure 2.13. The shape is similar to the one used in the Step A but with the addition of a small round notch machined in the center part of the sample. The presence of the notch modifies the distribution of the stresses and thus the triaxiality value in the cross-section of the sample, especially at the notch root.

The different cases are compiled in Table 2.2.

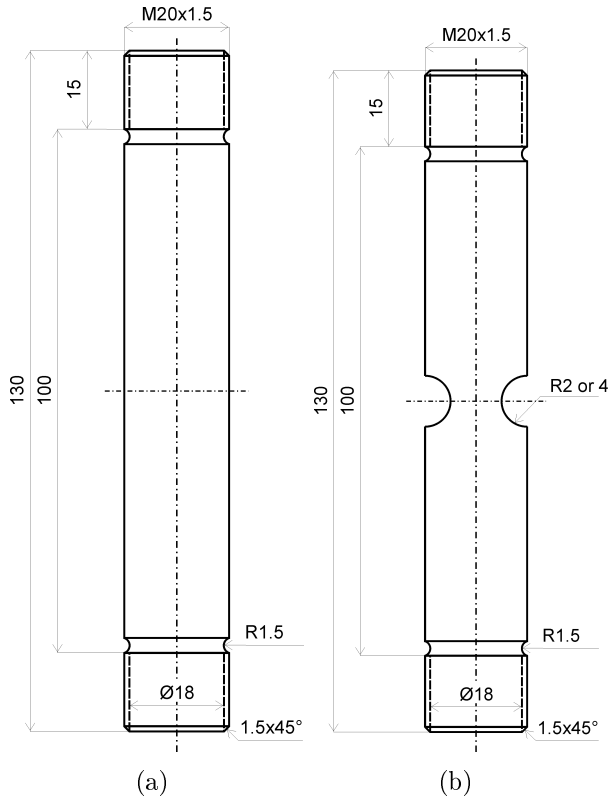

Figure 2.13: Various sample shapes used in the hot tensile test machine, (a) without notch, (b) with 2 and 4mm notches [mm]

2.2.3 Step C, the representative cell

An important step of the experimental approach is the identification of the representative cell. It contains the microstructural information of the steel: the shape and size of the grains. This cell will be used in Step D to apply the mechanical stresses coming from Step B in order to determine one single set of damage parameters.

The observation of the steel microstructure gives the primary austenitic grain size and the precipitation state at a determined temperature. The grain size found is exploited in order to compute the required size of the representative cell.

Shape	Strain rate [s^{-1}]	B A C [°C]
R0	$1 \cdot 10^{-3}$	700 → 1350°C (50°C steps)
	$1 \cdot 10^{-2}$ $5 \cdot 10^{-2}$	900, 1000, 1100
R2	$1 \cdot 10^{-3}$ $5 \cdot 10^{-3}$ $1 \cdot 10^{-2}$	3 temperatures around the ductility trough
R4	$1 \cdot 10^{-3}$ $5 \cdot 10^{-3}$ $1 \cdot 10^{-2}$	3 temperatures around the ductility trough

Table 2.2: Summary of the test campaign on hot tensile test samples

The observation of the precipitates present in the steel matrix enables to identify a certain number of parameters in the damage law as the initial cavity size, shape and their interdistance for each steel grade studied. The voids are assumed to form by decohesion between the matrix and the precipitates.

In order to proceed to observations, two different apparatus are used. The first analysis is done thanks a scanning electron microscope (SEM) and the second analysis with a transmission electron microscope (TEM) for a closer look. Indeed, the austenite grain size is in the micrometer range. The precipitates are in the nanometer range. This difference requires the use of the two different types of apparatus with their specificities in terms of analysis range.

The SEM enables the accurate view of elements in the micrometer range. After a sample preparation (Bechet-Beaujard etching), the primary austenitic grain is revealed and could be analyzed. The electron beam hits the surface of the sample and the electrons re emitted by the surface are analyzed in order to characterize the surface of the sample and to detect the grain boundaries.

The precipitates that are smaller than the micrometer are not observable with the SEM. Thus an apparatus that permits the analysis of smaller elements is used. This apparatus, the TEM, permits the analysis of nanometric elements because of its higher magnification capabilities. One of the drawbacks of this apparatus is that it is more difficult to use. One reason is that the samples preparation is complex. One has to cut a very thin slice of material so that the electron beam is able to cross the sample in order to be captured by the the sensor and analyzed.

2.2.4 Step D, the determination of the damage law parameters

The fourth step of the study is to load the representative cell to determine by inverse analysis the parameters of the damage law used in the grain boundary at the interface between two grains (Section 2.1.5).

The forces and displacements applied on the microscopic cell are determined via FEM simulation of hot tensile tests on different specimen shapes, temperatures and strain rates. The tensile test simulation provides stress, strain and temperature fields. These are taken in the area where the stresses are the highest as explained in Section

4.1.2. Finally they are applied on the edges of the representative cell. The simulation of the damage in the mesoscopic cell is then performed and the parameters of the law are adapted using an inverse method so that the fracture moment identified when the damage parameter a/b reaches the critical threshold corresponds to the experimental hot tensile test results on different specimen shapes and with different thermal constraints.

2.2.5 Step E, the simulation of the CC process

The final stage is to use the damage law in a CC case. The damage law parameters were determined in the previous step for a particular steel grade. This law is applied on the contact elements of a mesoscopic cell adapted to the CC case (Figure 2.14). This cell is surrounded by a transition zone that serves to homogenize the stress and strain fields around the cell. The stresses applied on the edges of the transition zone are coming from the CC process. The stress, strain and temperature fields are taken from a slice of a numerical simulation of the whole CC slab. This approach enables to apply the whole force, displacement and temperature histories of the steel during the CC process. Thus, we are able to detect the damage appearance in the slab at various positions in the slab or in the continuous caster.

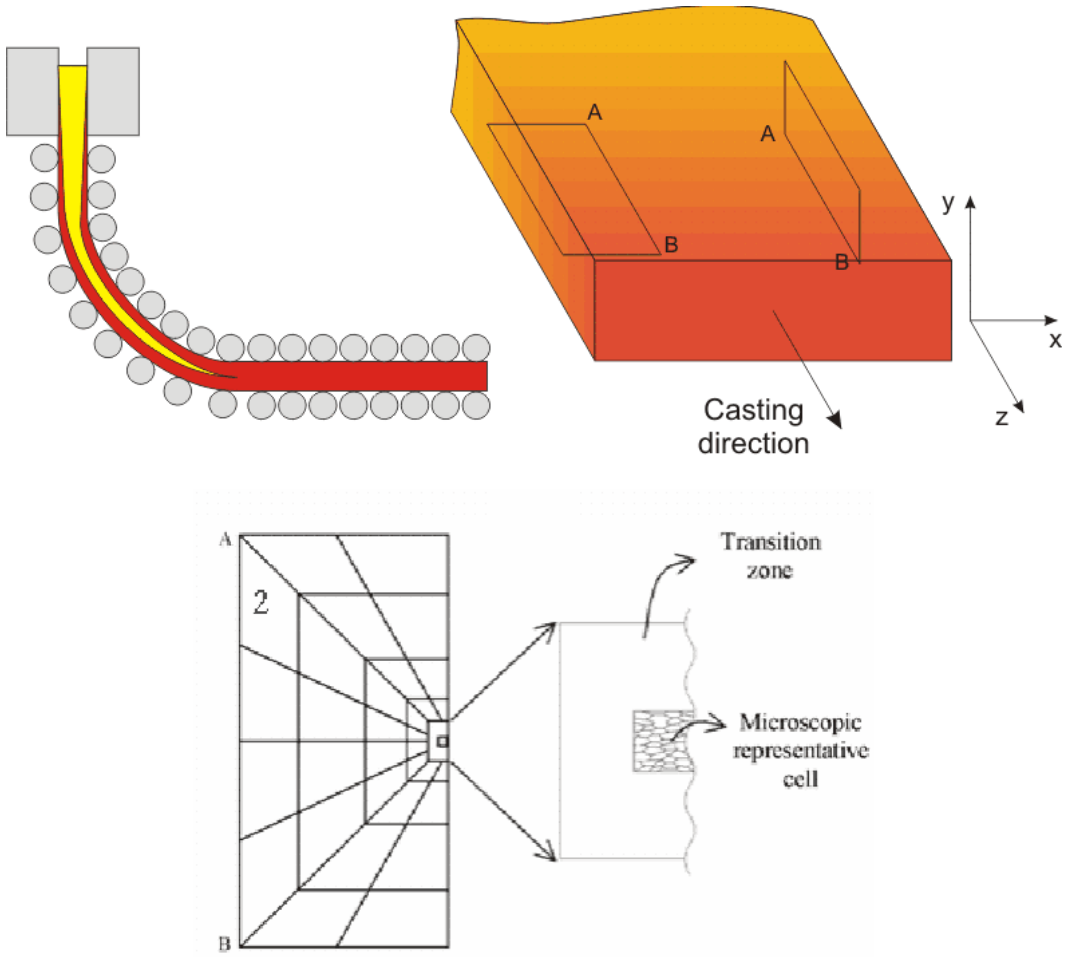

Figure 2.14: Scheme of the CC case modeling by extraction of the data recorded through macroscopic numerical simulation of the CC and application to the edges of the transition area of the representative cell

2.3 Thermal treatment of the sample and test description

In literature, different ways to perform hot tensile tests are used in order to impose boundary conditions close to the one encountered in CC. Indeed, each author using tensile tests, applies a different thermal path to the sample before and during testing. Each solution is more or less adapted to generate the real mechanical stress and temperature fields supported by the slab during CC and the identical initial microstructure within the sample. More especially, the different phases of the thermal path before and during testing have to be considered and seriously taken into account as it strongly modifies the microstructure which influences the damage behavior. Several thermal paths are applied in literature (see Chapter 1) and the one applied here is described hereafter (Figure 2.15).

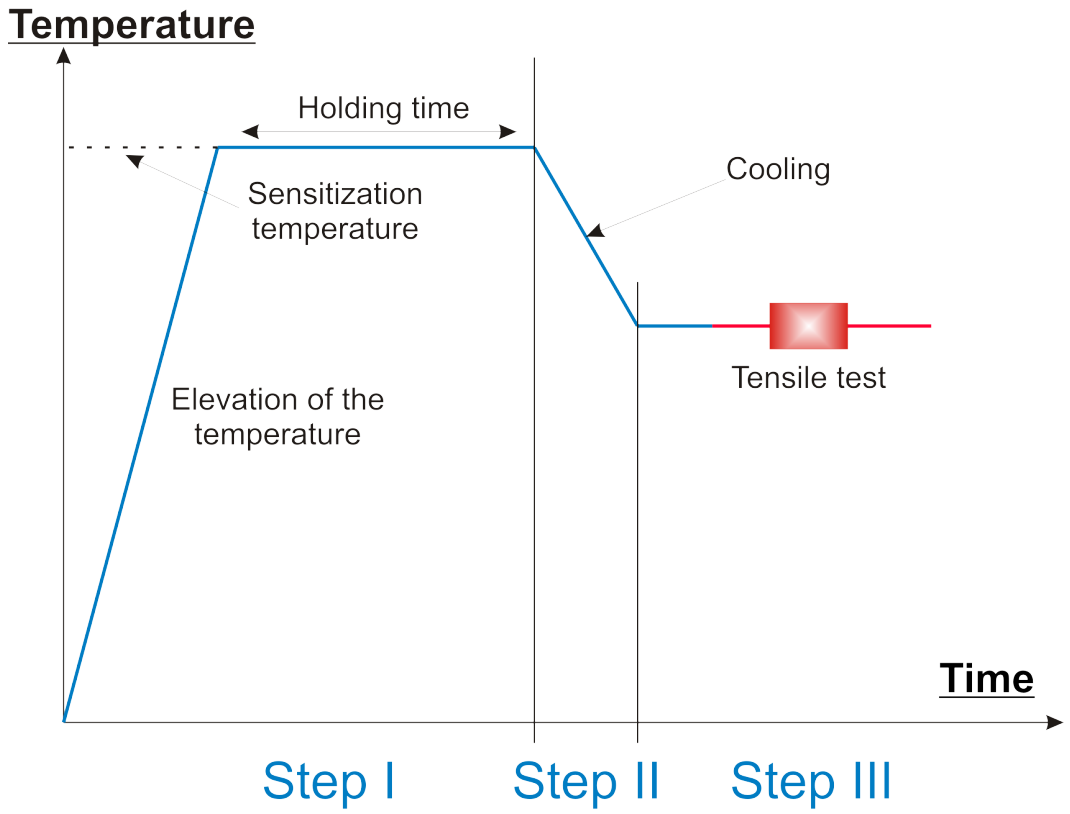

Figure 2.15: Schematic description of the thermal path applied for the tensile test to match the real CC conditions

- The first step is the elevation of the sample temperature until sensitization temperature and then the application of a constant temperature field during a determined holding time. This part is very important because the goal is to start from a material that has the same properties as in the solidified shell of the CC process, that is to say without precipitates and with the adequate grain size.
- The second phase is the decrease in temperature to the test temperature. The best way to perform this decrease in temperature is to take the cooling condition of the CC and to apply it to the sample. Unfortunately, this is usually not possible

as the temperature history of the shell is quite complex and the temperature is usually constantly decreased at variable speeds that must be determined. Thus, a mean temperature slope should be determined (see Section 2.3.2.4).

- The last important step is the temperature chosen to perform the tensile test at a constant temperature. However in some articles [Yue95], the temperature is constantly increased or constantly decreased during the test. Indeed, in the CC process the slab temperature is continuously changing.

These three stages are separately discussed in the following sections. But at first the testing material should be presented in order to know the capacity of the tensile testing apparatus used.

2.3.1 Tensile test apparatus

The apparatus used for this study is the usual hydraulic tensile test machine, with a fixed and a mobile grip. The sample is screwed between these grips in order to impose a tensile strength on it. The particularity of the TREBEL apparatus used at the RWTH of Aachen is that the sample is placed in a controlled atmosphere (inert gas or vacuum) chamber as shown in Figure 2.16. The sample is held in a glass tube in order to be able to elevate the temperature over the melting point with the help of an induction coil surrounding the sample.

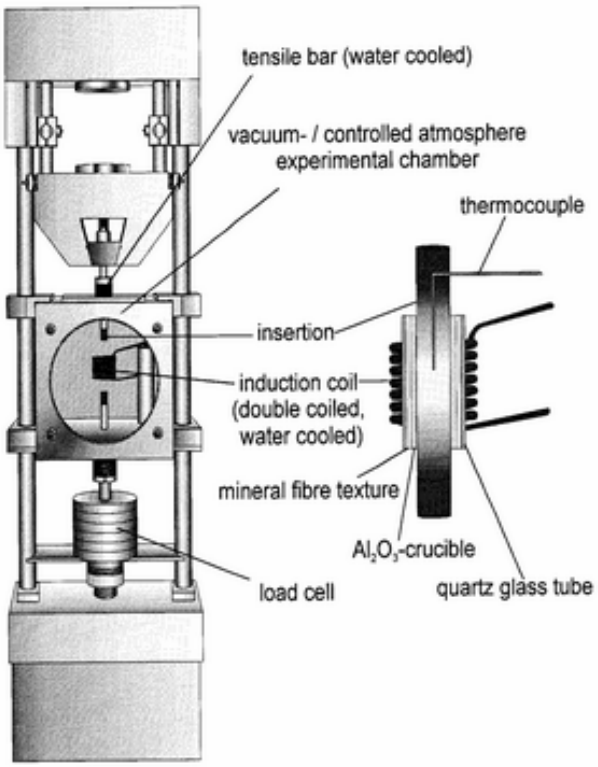

Figure 2.16: Hot tensile test apparatus at the RWTH of Aachen

The mobile grip can be driven by displacements with speeds going from $0.001\text{mm}\cdot\text{s}^{-1}$ to $10\text{mm}\cdot\text{s}^{-1}$ or by forces. But the most interesting possibility is to apply a constant

strain rate as it easily allows to identify the viscosity term through tests at different strain rates. Keeping $\dot{\varepsilon}$ constant during the whole test is possible by imposing a non linear displacement on the mobile transverse beam.

Also interesting is the capacity of the machine to record with accuracy a wide range of forces. Indeed, the measured forces can go from 2kN to 100kN by placing the adapted load cell in the apparatus. When performing the tests on heated samples, the forces recorded are very low.

The cooling of the sample is also an key point because the decrease of temperature has to be mastered during the test in order to remain close to the one observed in CC. Unsuited cooling implies, with our steels, missing the desired microstructure. Indeed, a too fast cooling an impact on the precipitation state whereas, a too slow cooling extends the testing time and change the grain size of the studied steel. The maximum cooling rate on the TREBEL apparatus is $6\text{K}\cdot\text{s}^{-1}$.

2.3.2 Thermal path

2.3.2.1 Elevation of sample temperature

The first increase in temperature can generally be done in two different types of furnace.

The first one is a common **radiation furnace**. In this type of furnace the temperature of the sample is increasing very slowly and the austenitic grain growth has the time to begin and to continue over a long period of time. This grain growth induces coarse austenitic grains not representative of the real microstructure generated in the CC case.

Thus, we choose to use a second type of furnace; the **induction furnace**. This technology permits to increase the sample temperature very quickly. The temperature increasing rate can go up to $100°\text{C}\cdot\text{min}^{-1}$. Thus the temperature can be brought to 1000°C in a few minutes. This rate limits the austenitic grain growth since the temperature threshold for quick austenitic grain growth is reached but held for short time. Further, with a well chosen holding time and sensitization temperature, the grains have the adequate size and the precipitates are dissolved as demonstrated by Mintz [Min99a].

2.3.2.2 Sensitization temperature

The holding temperature has to be carefully chosen: not too high, in order to avoid to have a too strong increase of the size of the austenitic grains, and not too low, in order to dissolve all the precipitates in the sample. The sensitization temperature depends on the different precipitates found in the sample. Indeed, the precipitation and dissolution temperatures are different for each component. It is assumed that for Nb and V steel grades a sensitization at a temperature higher than 1300°C is enough to completely dissolve the precipitates [Min99a]. Looking at Figure 2.17 this is valid for the peritectic steel grades studied. At the equilibrium state, the observed Nb component precipitates around 1100°C and V at approximately 600°C. These temperatures of precipitation are slightly dependent on the global steel composition but they give a good approximation

of the beginning of the phenomena. Remember however that the precipitation is time dependent.

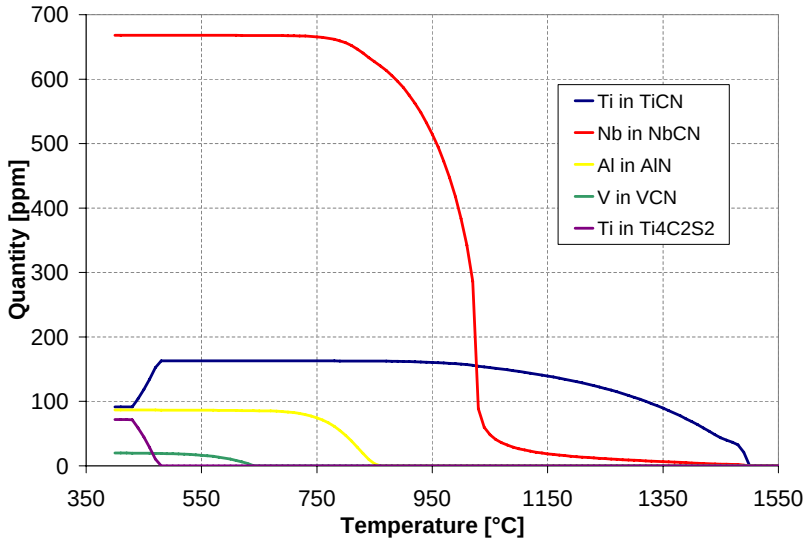

Figure 2.17: Precipitates formation at the equilibrium calculated for steel **B** (data provided by Arcelor Research) with the CEQCSI model

Another way to eliminate all the precipitates by staying close to the CC conditions is to melt the sample. Some authors prefer this thermal path because it is much closer to the one supported by the sample during CC. Indeed, the sample life starts in the liquid phase, then it is cooled down as in the CC process. The precipitates that were initially dissolved are growing and the microstructure of the sample is the same as the one of the steel during CC.

Unfortunately this test procedure has some drawbacks. The most important one is the fact that after cooling the sample presents a hole in its core (Figure 2.18)observed during experimental tests at the RWTH. The test is then not performed on a simple cylindrical sample but on a defective sample containing a shrink hole. It appears because the cooling of the sample starts from the surface layer to the core and an empty volume is thus generated in the center of the sample. This hole is supposed to strongly influence the forces and displacements. Its exact shape, size and location is random and unknown. Finally, the numerical simulation of this test is difficult to perform as the hole size and place are unknown variables.

In conclusion it is more convenient to chose a thermal path not going through the liquid phase to avoid a difficult analysis. Without hole, the stress and strain histories are easily extracted from the hot tensile tests and they are finally closer to the one of the CC process without melting.

A general sensitization temperature range found in literature is 1100 to 1300°C [Lud07, Pan05a, Moh02, Min99a].

2.3.2.3 Holding time

The holding time at the sensitization temperature has its importance. Indeed, at this elevated temperature the grain growth continues. However, the temperature of the

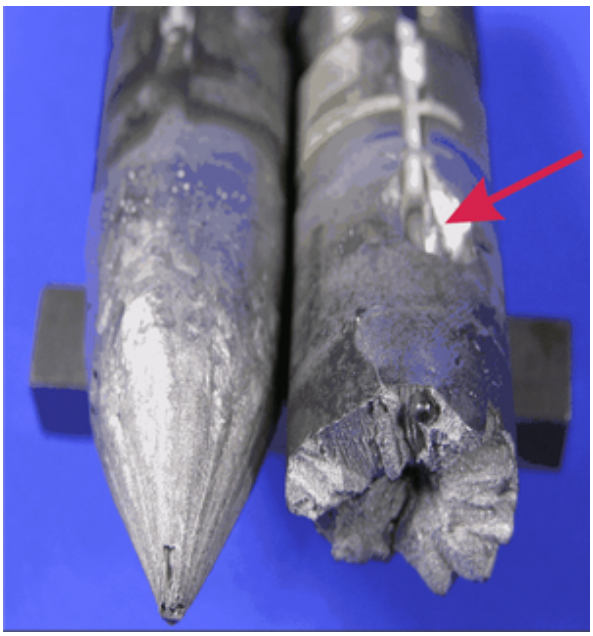

Figure 2.18: Shrink hole of a tensile test sample (data provided by IEHK, 2006)

sample has to be homogenized and all the precipitates must disappear. Thus it is important to find a balance in order to obtain the right grain size and an homogeneous sample without precipitate. The trend is to proceed as fast as possible. So most of the authors choose to heat the sample up as fast as possible in a induction furnace and to hold the temperature during 1 minute [Min91, Suz84]. It is important to keep in mind that this holding time has to be adapted to the temperature level chosen before and to the material studied. This temperature path should therefore be studied by testing different cases and studying the microstructure of the sample as done in Section 3.1.1.

2.3.2.4 Cooling of the sample

The cooling of the sample after sensitization is as important as the sensitization itself. Generally the temperature is decreased constantly down to the test temperature. The cooling rate has to be the same or should approach the one of the real case. In the real case the temperature is actually fluctuating because of the transition between water sprays, surplus of water on rolls, blind areas that are not sprayed and rolls (Figure 2.19). The cooling curve shows different cooling speeds during the process (0 to 1 meter, 1 to 4m and 4 to 23m). Usually this complex thermal path is simplified and a constant cooling rate is chosen. In general the cooling rate used is a mean value of the one obtained in CC and is $60°C \cdot min^{-1}$ [Moh02, Min91].

Few experiments have been done with a bilinear constant cooling. This way of cooling is closer to the CC case. Indeed, the temperature decreases very quickly from the melt to approximately 1100°C with a rate of about $300°C \cdot min^{-1}$ while the steel is cooled down in the mold. This stage requires a strong cooling in order to obtain a solid shell at the exit of the mold. After the mold, the mean temperature decrease is the same as the one chosen if only one rate is adapted, i.e. $60°C \cdot min^{-1}$. Of course these two cooling rates depend on the cooling strategies used in the industry but these above rates are commonly seen. Unfortunately, the material used to perform the tests do

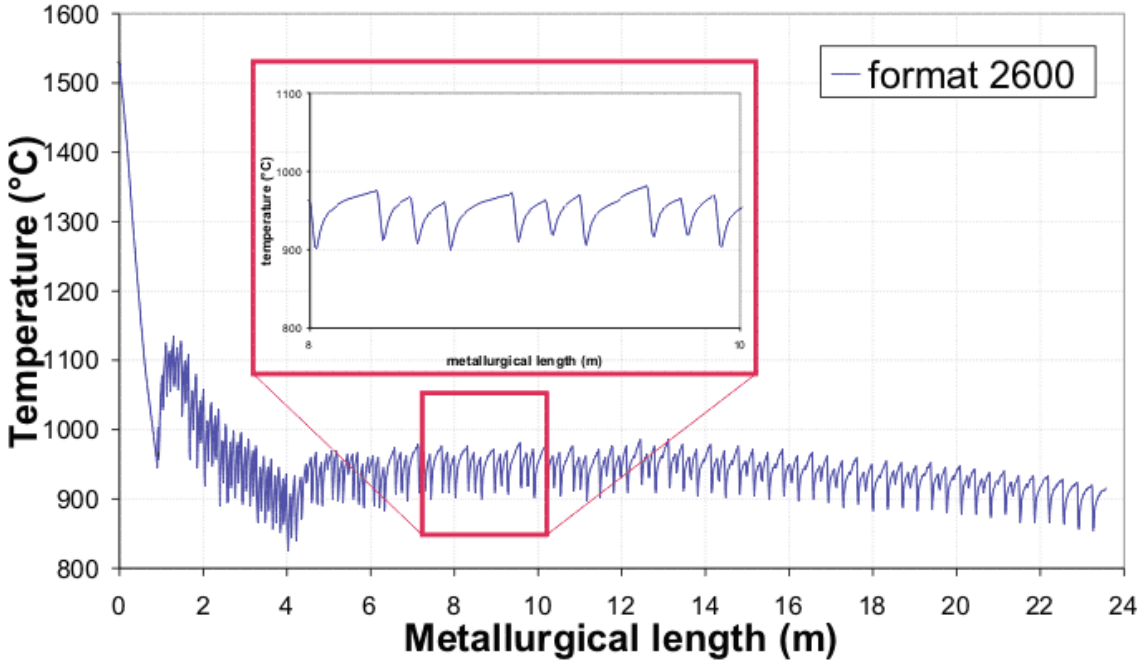

Figure 2.19: Numericaly determined cooling curve of the large face of **A** slab (2.6m large) at 20cm from the corner during the CC process (data provided by Arcelor Research)

not allow to decrease the temperature at a rate of $300°C \cdot min^{-1}$. Thus, the monolinear case, to give a mean cooling to the sample has been chosen.

2.3.2.5 Tensile test

Finally the third part of the test is actually the tensile test of the sample. In most of the cases, once the prescribed temperature is reached, it is held for a few minutes in order to homogenize the sample temperature before pulling on the sample. The testing temperatures go generally from 500°C to the sensitization temperature or just below the melting temperature. These tests, at different temperatures, enable us to draw a representative ductility curve on which we can see the different stages of zero ductility (T_{ZD}), zero strength (T_{ZF}) [Str07] and microstructural changing happening as described in Figure 2.20.

Now the tensile test in itself is a delicate procedure. Indeed, the strain rate has to be determined to fit also the real case. Thus the strain rate used lays between $10^{-3}s^{-1}$ and $10^{-4}s^{-1}$ as they are measured in the CC process during cooling and straightening respectively [Min93] and as predicted by CC FE simulations [Pas06].

Generally the tensile tests are performed with a constant temperature in order to draw the ductility curve but in some cases, on-heating and on-cooling tests are performed but as said before, according to [Yue95] the on-cooling tests give wrong results and the on-heating tests are not suited to the CC case. These tests are more adapted to welding simulations [Dav04] and therefore not used in this study.

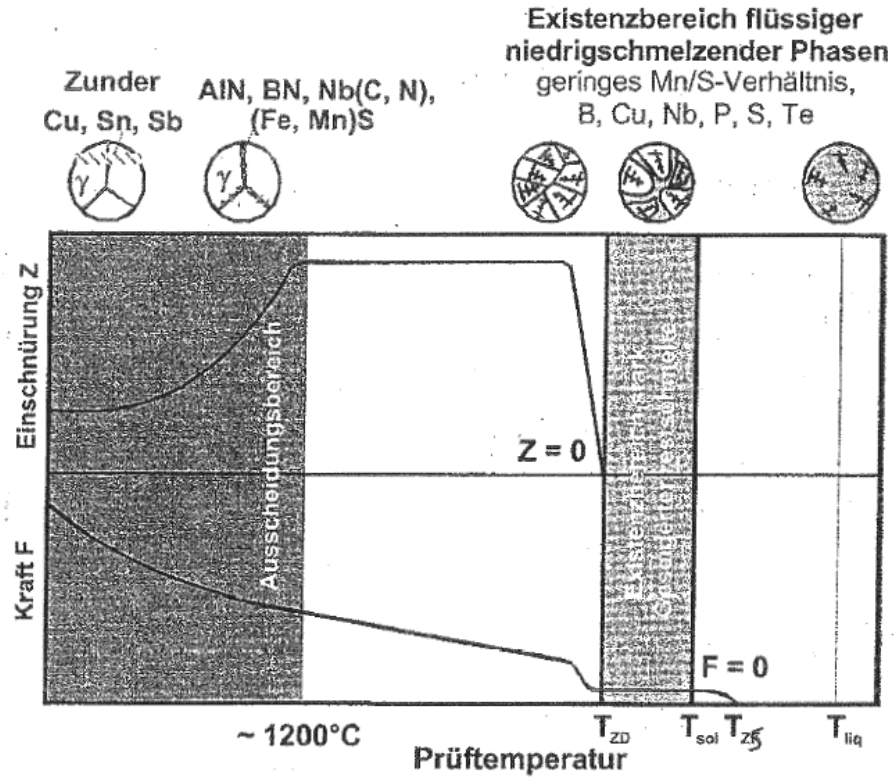

Figure 2.20: Stages of the ductility curve observed in function of the steel morphology and the forces recorded during hot tensile test [Pan05b]

2.3.3 Conclusion on the damage model, its identification and the sample treatment

The following topics have been treated and explained.

- The damage FE model and the way it is implemented in the LAGAMINE code have been presented. The material parameters are compiled in one table in order to have a good overview of the parameters playing a role in the damage and the way they can be determined.
- The construction of the mesoscopic representative cell has been detailed.
- The scale transition between macroscopic and mesoscopic numerical simulations has been described.
- The procedure of the model identification through experimental and numerical test comparisons has been set.
- The thermal treatment methodology of the test samples has been explained in order to obtain samples representative of the CC case.

Chapter 3

Rheology and damage tests: description, results and analyzes toward the representative mesoscopic cell

The experimental part of the research is structured and divided into two major parts.

- The first one is the macroscopic part that helps to build the foundations of this study by characterizing the material in a mechanical and microscopical way.
- The second part is a mesoscopic numerical study that enables to determine the damage behavior of the material.

In order to explain the study, the first part, that is more technical is discussed in the current chapter when the second part is described in Chapter 4. As presented in Section 2.2, the macroscopic part consists in three different sections:

Section 3.1. Hot Tensile Tests (HTT) on cylindrical samples are done in order to determine the rheological parameters of the material studied.

Section 3.2. Macroscopic numerical simulations without damage elements of the experimental tensile tests on cylindrical samples and on notched samples are done in order to generate the various stress-strain histories. Such data are applied on the representative cell at the mesoscopic level to identify the damage model parameters.

Section 3.3. Microscopic analyses are done in order to be able to design a representative cell able to react like the material at the grain level.

3.1 Determination of the rheological parameters

As detailed in Section 2.3, it is important to study the thermal cycle that has to be applied to the samples before HTT. Indeed, the damage behavior is related to the precipitation state (i.e. size, number, shape of the precipitates) of the material. As this

influence is studied here, the material should present the same properties as the steel in CC conditions. This subject has been often discussed in literature and some particular values are taken into account as the sensitization temperature. Unfortunately, the thermal cycle changes for each volume of material and alloying elements concentration. Thus, a microsctructural study has been performed on the HTT as shown hereafter in order to precisely determine the thermal cycles needed in correlation with the materials chosen for this study.

3.1.1 Study of the thermal cycle applied to the tensile samples

The way the tensile tests are performed is of highest relevance as explained in the Chapter 2. The goal of the thermal cycle study is to reach in the HTT samples an austenitic grain size of 200μm as determined on micrography Figure 2.5 of Section 2.1.4. So, first of all, the way to impose the thermal path on the tensile samples before performing the experimental tests is studied.

As the steel grades studied belong to the same family, a similar behavior is assumed. Therefore, the research of the thermal cycle is performed on only one grade (**B**) but applied to the three different materials.

3.1.1.1 Experimental process

The tensile tests are performed in an induction furnace and the sample is placed in an inert chamber as explained in Section 2.3.1. Two different thermal path strategies, have been applied to the samples in order to modify their microstructure.

- The first strategy is to increase the temperature constantly until the temperature and to maintain it during a certain time. The sensitization temperature will influence the precipitation dissolution whereas the holding time mainly influences the grain size.
- The second strategy consists in applying one or more thermal cycles on the sample. The temperature is first increased just enough (900°C) to form austenite grains (first size), then decreased to obtain ferrite and increased again to form smaller austenite grains. This cycle can be repeated and the last time the sensitization temperature is maintained in order to dissolve the precipitates that are caught in the microstructure. This strategy should enable a reduction in the austenitic grain size.

These different strategies are described in details hereafter.

Strategy 1: Classical thermal cycle

The classical thermal cycle consists in elevating the sample temperature and to hold it for a determined time as we can see in Figure 3.1, with the following test characteristics:

- ***Warming:*** 6°C·s^1 (general value used for warming at the IEHK in Aachen to obtain an homogeneous temperature);
- ***Sensitization temperature:*** 1250 and 1350°C (two temperature levels are tested in order to know if precipitates are dissolved);

- ***Holding time:*** 1, 2, 5 and 10 minutes (four holding times to quantify the grain growth);
- ***Cooling:*** quenching in argon (quenching to freeze the microstructure at the end of the test).

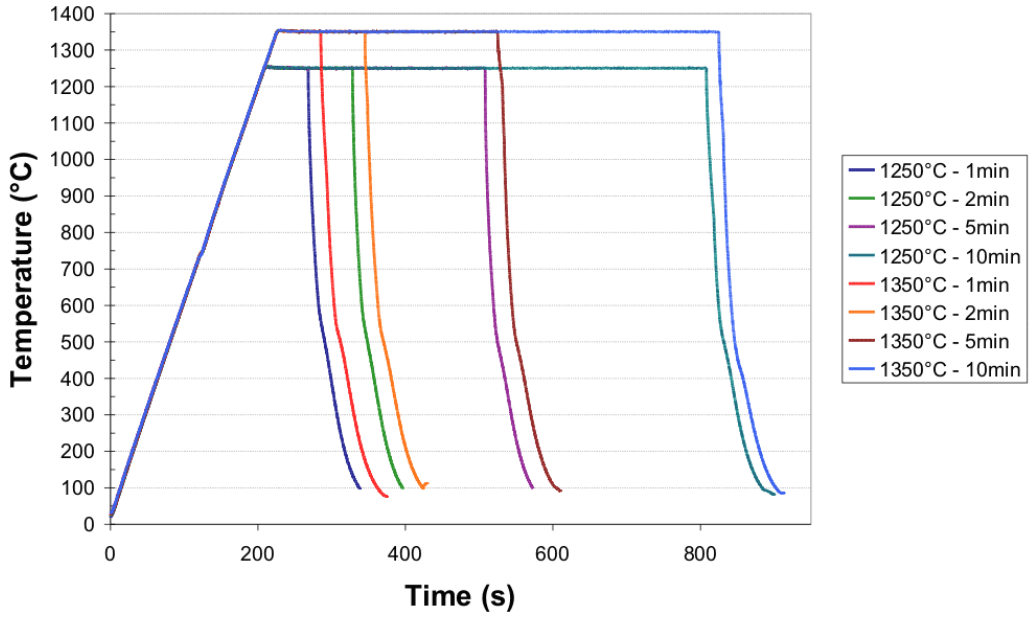

Figure 3.1: Time-Temperature curves for the samples 1 to 8

Strategy 2: Phase transformation thermal cycle

The second approach presents different cycles before the maintaining step that has been chosen equal to 5 minutes at the temperature of 1350°C as shown in Figure 3.2. The cycles are supposed to reduce the austenite grain size of the steel by successive phase transformations. This approach balances the final austenitic grain growth happening at the sensitization temperature. The holding time is not reduced in order to dissolve the precipitates.

The cycling effect could be explained this way: when the steel structure transforms into austenitic phase, the grains have a certain size. With the back transformation to ferrite, the grains split in several little grains since ferrite nucleates at different places in the austenite grain. If the temperature is increased and the transformation from little ferrite grains to austenite happens, the grain size of the austenite is smaller than the first one, as the original grain size is now the one of the former ferrite grains. Thus a special cycling scheme should be applied to the sample. This cycling scheme could be reproduced a few times in order to reduce more and more the austenitic grain size.

The applied cycle consists in elevating the temperature of the sample to 900°C (the microstructure is austenitic) then cooling down to 600°C with natural cooling (the microstructure is ferritic). This cycle is done one to four times (Figure 3.2) in order to know if the grain size of the sample is reduced by this cycling. The test characteristics are the following ones:

- ***Warming:*** 6°C·s^{1} (idem);
- ***Sensitization temperature:*** 1350°C (temperature at which all precipitates are supposed to be dissolved);
- ***Holding time:*** 5min (medium holding time supposed to be enough to dissolve the precipitates);
- ***Cooling:*** quenching in argon (idem);
- ***Number of cycles:*** 1 to 4 (four cycles to quantify the reduction of the austenite grain size).

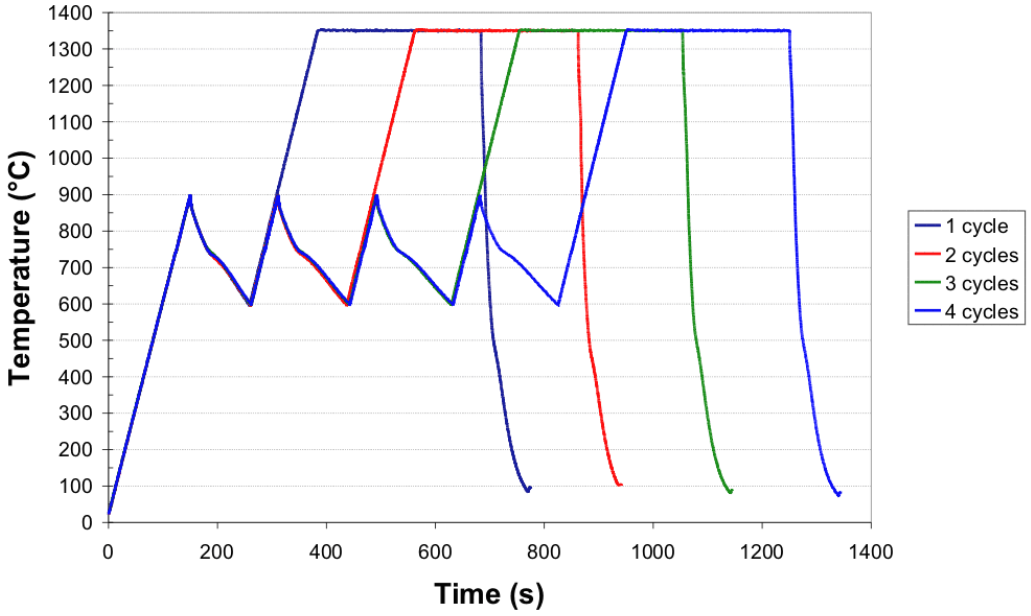

Figure 3.2: Time-Temperature curves for the samples 9 to 10 with a provisional cycle

3.1.1.2 Sampling

Size and quantity of samples

The samples used for the experimental study and particularly for the ductility curve drawing and the determination of the damage law parameters are tensile test samples. The machined cylinders are 130mm long with a diameter of 20mm (Figure 2.13 left sample without the notch).

Looking at the twelve different thermal paths, ***twelve samples*** are needed, as tests are not repeated because of restricted budget.

Extraction of samples in the slab

The zones subjected to the highest constraints and where transversal cracks happen are the intrados and the extrados shells of the slab. Thus, in order to perform representative tests, the samples are taken in these areas, so their grain sizes and precipitation contents are representative of the studied material state.

As shown in Figure 3.3 slices of 60mm are taken from the slab on the intrados and the extrados surfaces. The samples are taken in any directions, the axial length of the sample parallel to the surface plane of the slab.

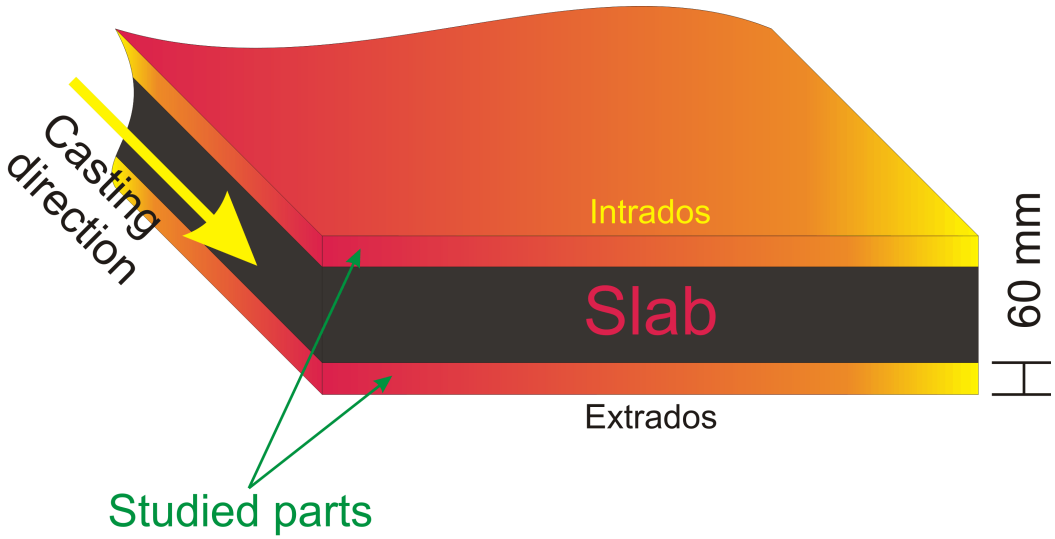

Figure 3.3: Areas of the slab that are used for sampling

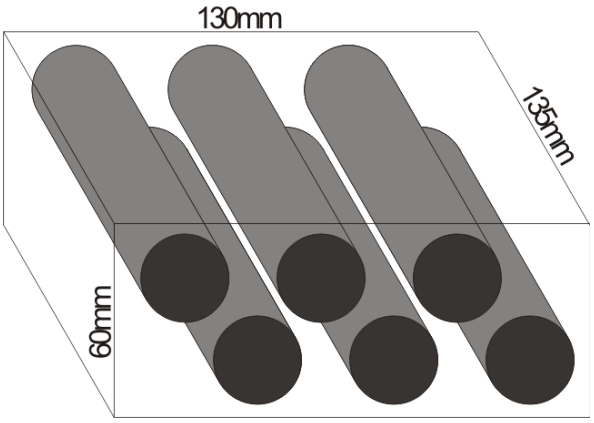

Figure 3.4: Electron discharge machining of the cylinders in the slab slice (with Figure 3.3 orientation)

Sample mechanical preparation

The parts extracted from the slab are parallelepipeds. The future samples have to be turned in order to obtain the cylindrical shape. Unfortunately, to turn the samples into the final cylindrical shape, they have to be cylindrical from the start on. Indeed, the turning of parallelepipedic samples is detrimental for the tools and finally for the metal working lathe. Thus the samples are extracted from the slab slices into cylindrical shape thanks to the electron discharge machining.

The slab slices are cut into different parts of dimensions 130x135x60mm in order to be convenient to enter the electron discharge apparatus. Each part of this size can provide 6 tensile test samples as they are taken with the height in the 135mm direction (Figure 3.4). For the needs of this study, 2 parts have been cut down.

3.1.1.3 Metallographic results

In order to recognize the samples, they were renamed as shown in Table 3.1.

Description		Sample Name
Classical thermal cycle Holding temperature: **1250°C**	**1**min	**S1**
	2min	**S2**
	5min	**S3**
	10min	**S4**
Classical thermal cycle Holding temperature: **1350°C**	**1**min	**S5**
	2min	**S6**
	5min	**S7**
	10min	**S8**
Phase transformation thermal cycle Holding temperature and time: **1350°C, 5min**	**1**cycle	**S9**
	2cycles	**S10**
	3cycles	**S11**
	4cycles	**S12**

Table 3.1: Denomination of the samples for the thermal path study

Their grain size has been measured (Table 3.2) using two different methods.

The first method is the mean line intercept method as described in ASTM Standard E 112-88. According to this method, the test line should cut 50 grain boundaries. Unfortunately the magnification did not allow the presence of 50 grain boundaries but mostly 10 to 20. The intercept method is however used. It exists two different ways to measure the grain size:

- The first one is to count the intercepts. An intercept is the segment of the test line which overlays one grain. **1** is counted for each intercept and **1/2** each time an end of the test line falls in a grain.
- The second one is to count the intersections. An intersection is the point where the test line cuts a grain boundary. For each intersection **1** is counted, for each tangential intersection **1** is also counted, **1/2** is counted when an end of the test line exactly ends on a grain boundary and **1.5** when the intersection occurs at a triple point.

The strategy chosen is to count the intersections on 3 blindly selected lines that are oriented differently in order to avoid any influence of orientated structure of the steel grains on the micrographs shown in Appendix A.

As explained before, the intercept method requires a huge number of grains in the picture, so a second grain size determination method is used in complement. This method is less accurate for the grain size quantification but will help us to know the range of the grain size. This method is based on ISO643 and it is called the comparison

method. The micrographs obtained through optical analysis are compared to standard micrographs (Appendix D) obtained for the same magnification. They are classified into different categories so that the grain size could be estimated.

Hereafter are the results of the micrographic study of the thermal path influence on the microstructure of **B** grade. The grain sizes not determined by the intercept method have been estimated thanks to the ISO643. They are marked with an asterisk in the results table, Table 3.2.

Samples	ISO 643	Grain size (μm)	holding conditions
S1	9	**15***	1min, 1250°C
S2	8	**19**	2min, 1250°C
S3	6	**27**	5min, 1250°C
S4	5	**42**	10min, 1250°C
S5	4	**80**	1min, 1350°C
S6	4	**81**	2min, 1350°C
S7	3	**87**	5min, 1350°C
S8	1	**250***	10min, 1350°C
S9	3	**84**	1 cycle
S10	3	**81**	2 cycles
S11	3	**73**	3 cycles
S12	1	**250***	4 cycles

Table 3.2: Grain size of the thermally treated samples analyzed by intercept method (results with * have been determined by comparison method)

The results show that two different thermal paths could be adapted to obtain the target grain size (200μm. These two solutions are **S8** and **S12**.

S12 thermal path shows a strange behavior since the grain size is growing while it should decrease with increasing the number of grain refining cycles. Thus it was decided to drop this solution.

The remaining thermal path is the **S8** one consisting in a holding time of 10 minutes at a sensitization temperature of 1350°C. However, some complementary micrographic analysis should be performed in order to confirm the grain size as it has been determined by the comparison method that is less accurate than the intercept one.

3.1.1.4 Conclusion of the thermal path study

These results are plotted in order to check the evolution of the grain size as a function of time for the different holding temperatures (Figure 3.5(a)) and the effect of the number of thermal cycles on the grain size (Figure 3.5(b)).

Evolution of the grain size with time and temperature

We can see in Figure 3.5 left that the grain size grows with longer holding time but also with higher sensitization temperature.

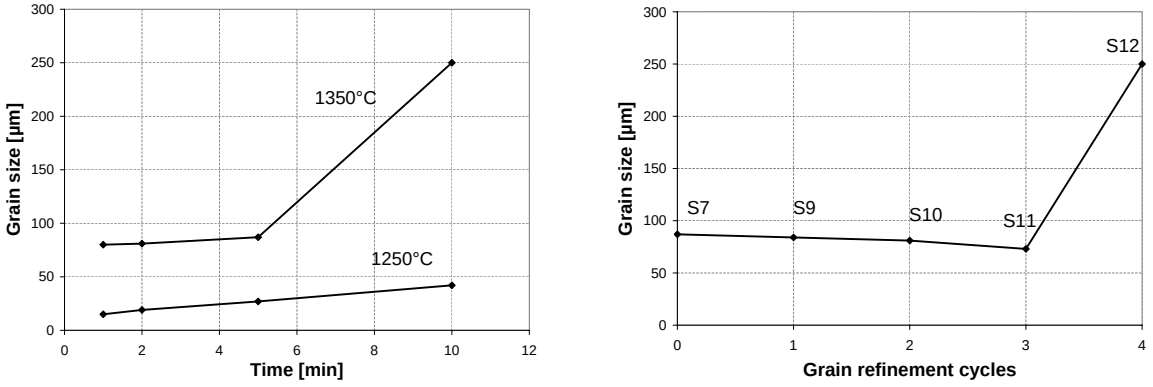

(a) (b)

Figure 3.5: Grain size evolution for both tested thermal path comparisons: (a) constant holding temperature (1250 and 1350°C), (b) thermal cycles at 1350°C during 5min

Indeed, the grain size evolves with **time**. For each maintained temperature the size of the grain grows from 19μm (**S2**) to 42μm (**S4**) and from 80μm (**S5**) to 87μm (**S7**).

We can remark that the grain size is evolving faster when the grain size is smaller and for lower temperatures. This observation is certainly due to the fact that the grain growth reaches a saturation state after which it evolves more slowly. This assumption could be verified by testing longer holding times at 1250°C to reach the predicted saturation.

We also remark that the grain size grows with the **temperature**. As we can observe in Figure 3.1, both temperatures (1250°C and 1350°C) are reached at almost the same time but we observe that the grain sizes are much larger at 1350°C (87μm for 5min) than at 1250°C (27μm for 5min). This can be due to the fact that over a certain temperature the grain growth is accelerated before reaching the saturation.

Another explanation is that the grain growth occurs just around 1250°C but with an extremely fast kinetics and the extra time spent to increase the temperature from 1250°C to 1350°C is enough to show these differences in the grain sizes.

Evolution of the grain size with the number of cycling

In the case of the samples that have been subjected to thermal cycles before maintaining the temperature at 1350°C for 5min, we observe a decrease in the grain growth when the number of cycles is increasing. This observation is in reality the expected effect.

Indeed, by elevating the temperature to 900°C, austenitic grains are formed and grow. As the temperature is decreased, the austenitic grains split apart in little ferritic ones. As the temperature increases again, the austenitic grains forms themselves starting from the little ferritic grains and so are evolving to smaller grains at the end. For two cycles the grain size is reduced once again before elevating the temperature to the holding temperature.

It has also been observed that the grain sizes of **S9**, **S10** and **S11** thermal paths are almost equal to those found for the first test with no cycling and the same holding temperature and time conditions **S7** ($\approx$80μm). This results confirms that the results

between the different thermal paths are consistent and could be kept. However, the result for **S12** has to be taken with care because the grain size is extremely higher than the previous ones.

3.1.1.5 Further work

In conclusion, it has been observed that the required grain size (200μm) is achieved thanks to the test **S8** without cycling. As explained in Chapter 1, the precipitates should have been dissolved since Nb precipitates are dissolved under 1200°C and V precipitates under 850°C. However it is important to be aware that these values of precipitation temperatures are calculated for static conditions and not for dynamic ones as observed in our tests. Thus, it is important to know if all the precipitates have been dissolved during this sensitization at 1250°C. This analysis could be performed thanks ICP (Induction Coupled Plasma) analyses but has not been performed within the thesis.

3.1.2 Determination of the ductility trough

To know in which temperature ranges the ductility troughs are localized for each steel grade, a bench of tests at different temperatures over the temperature range going from 1350 to 700°C every 50°C at a strain rate of $10^{-3}s^{-1}$ on unnotched samples have been performed. The interval built around this minimum will be used to decrease the number of experimental tests performed on notched samples to determine the damage parameters. Additional tests on notched samples allow to investigate the strain rate effect on the ductility troughs.

3.1.2.1 Results of the ductility trough analysis

For **A** grade, the ductility trough is situated between 700 and 950°C as presented in Figure 3.6. The interval studied for damage identification was chosen from 850 to 950°C before the results for the temperature range from 700 to 800°C were determined. Unluckily these results show a second ductility trough even deeper at 750°C than the first one. Thus it could have been interesting to investigate lower temperatures for the damage determination. However, the research schedule prevents any new investigation.

The ductility trough was analyzed in Section 1.2.1. The first dip is representative of precipitates formation and the second one represents the building of a thin ferrite film at the austenite grain boundaries.

For grade **B**, the ductility trough has been chosen over a wide range of temperatures going from 750 to 950°C even if the test result at 700°C shows a second decrease of the ductility as it is observable in Figure 3.6. This decrease could be representative of the second part of the ductility trough that is meant to be due to ferrite formation even if at these low temperatures it can also be due to the usual decrease of ductility with temperature. Lower temperatures should be tested in order to determine the reason of the ductility decrease for grade **B** under 750°C.

In the case of **C** grade the ductility loss is high and perfectly marked and the interval chosen goes from 700 to 900°C where the value of the necking is always lower than 55%.

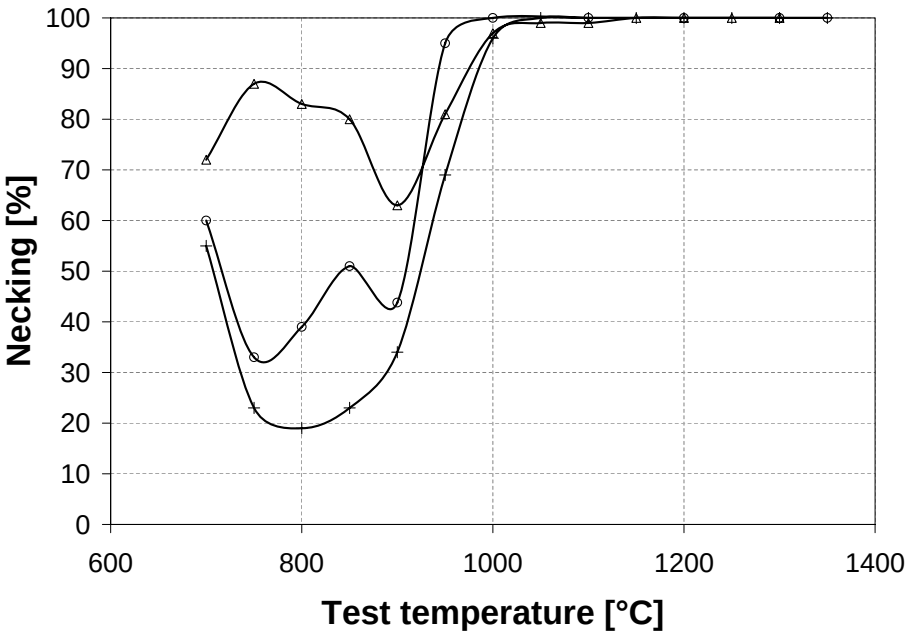

Figure 3.6: Ductility trough results for the three steel grades studied at $10^{-3}s^{-1}$ strain rate on unnotched samples ($\circ$ **A**, Δ **B**, $+$ **C**)

This ductility trough analysis will be used later (Section 3.2.1) in order to determine the hot tensile tests performed on notched samples for the damage law parameters identification.

The ductility study done permits also to discuss about the strain rate effect on ductility and differences have been shown between the three studied steel grades as explained hereafter.

Effect of the strain rate

As seen in Figures 3.7 to 3.9, an increasing strain rate induces a less deep ductility trough. This effect is checked for **B** and **C** grades but not for **A** grade even if the lowest strain rate induces always the deepest trough, the fastest produces not necessarily the smallest trough. Even though, it seems logic that the trough becomes deeper for lower strain rates. When the strain rate decreases, the material has time to adapt to the deformation and produce thus a more important necking in the center part of the sample.

Differences between steel grades

As shown in Figure 3.6, the three grades studied have a very different behavior. Indeed, the **B** ductility trough is not really marked and it seems to be less deleterious than **A** and **C** which have more or less the same level of necking. Between these two last steel grades, the differences are the double ductility trough and the start temperature of the loss of ductility. These differences could be explained through an analysis of the precipitation state and the particular effect of each precipitate present in the steel matrix. The ductility trough shift between steel grade could also be explained by the phase transformation from austenite to ferrite as presented in next section.

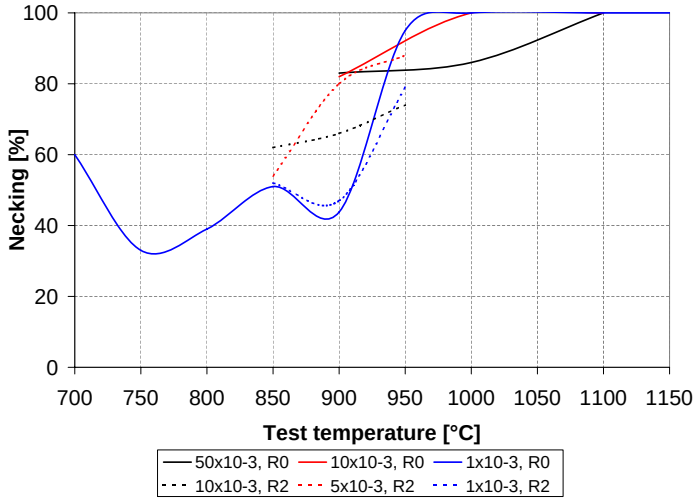

Figure 3.7: Ductility curves of grade **A** for various sample shapes and strain rates

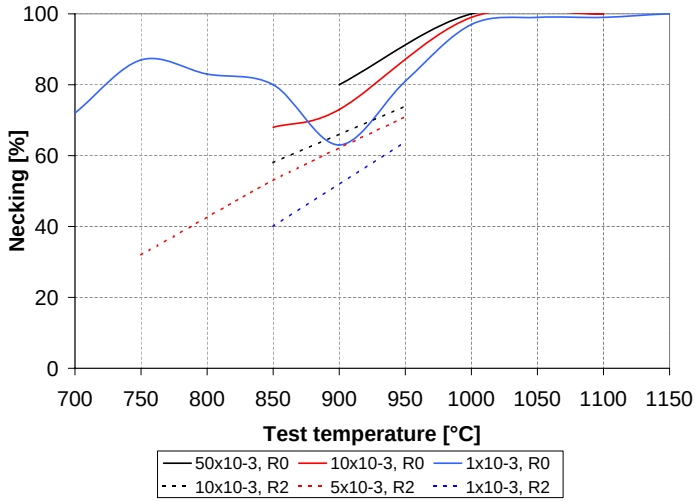

Figure 3.8: Ductility curves of grade **B** for various sample shapes and strain rates

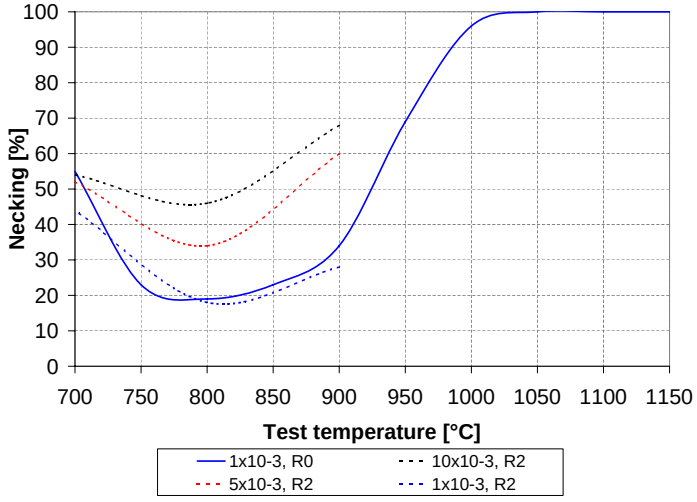

Figure 3.9: Ductility curves of grade **C** for various sample shapes and strain rates

3.1.2.2 Analysis of the precipitate effect on the ductility trough

Precipitation calculations at the equilibrium (CEQCSI)

The precipitation kinetic calculations have been performed with the software CEQCSI developed by ArcelorMittal. These results compute the temperature where the different components of the steel precipitate into the solid phase. This precipitation phenomenon is one of the explanation for the presence of a ductility loss of the material in a given temperature range as explained in Section 1.3. The second reason of the ductility loss is the formation of thin ferrite films at the grain boundary during the phase transformation from austenite to ferrite.

The results give the appearance of all the components in the steel under various forms and combinations during cooling and thus their precipitation behavior (Figures 3.10 to 3.12). Also the phase transformation has been plotted into a graph for each steel grade studied (Figure 3.13). These results are exploited in the following analysis of the precipitates effect.

At high temperatures, Ti will react very fast with N. As soon as there is no free N anymore, it will react with carbon. After Ti, Nb will precipitate followed by Al.

Ti is the first component to precipitate. As said before, it will react fast and take N and C out of the matrix. In each case, Nb starts to precipitate very early. At first slowly and around 1000°C the precipitates become more frequent.

For Al, the precipitation start depends on the quantity of Al present at the beginning in the melted steel. The more Al is in the matrix, the earlier it will precipitate.

The content in V precipitates is always very low and this component precipitates later than the others. Its precipitation moment depends also of its quantity at the beginning. As for Al, the higher is the V content, the earlier is the precipitation during cooling.

Looking at the graph of phase transformations (Figure 3.13), it is obvious that grade **B** has a different behavior from **A** and **C**. **B** samples should break earlier as the ferrite film that is formed earlier than for the other two steel grades.

The combination of the effects of precipitation and ferrite formation has to be studied in order to have a clear view about these two detrimental passages of the steel during cooling in the continuous caster.

Precipitates effect on the ductility trough shape

To have a general point of view on the effect of alloying elements added within different steel grades studied, it is interesting to summarize the knowledge about those and their beneficial or detrimental effect on ductility. Some precipitates are well known and their effects have been studied.

For instance, Al nitrides form small precipitates that are detrimental for ductility in CC steels.

In contrary, Ti has a favorable effect because it forms TiN at the beginning of the precipitation. These nitrides are big in size and spread out randomly through the whole matrix and so, they help to avoid a too important creation of other detrimental nitrides as NbN, AlN or VN. These nitrides are mostly situated at the grain boundary

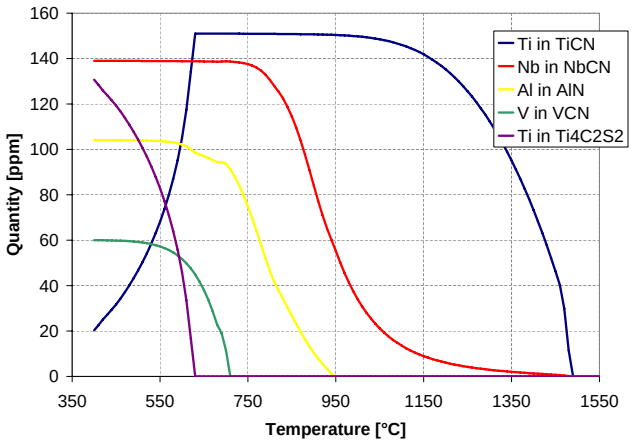

Figure 3.10: Evolution at the equilibrium of the Ti, Nb, Al and V precipitate quantity as a function of temperature for steel grade **A** (data provided by Arcelor Research)

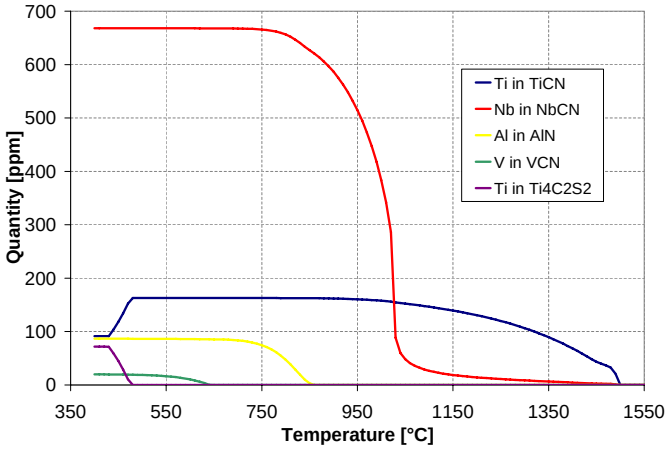

Figure 3.11: Evolution at the equilibrium of the Ti, Nb, Al and V precipitate quantity as a function of temperature for steel grade **B** (data provided by Arcelor Research)

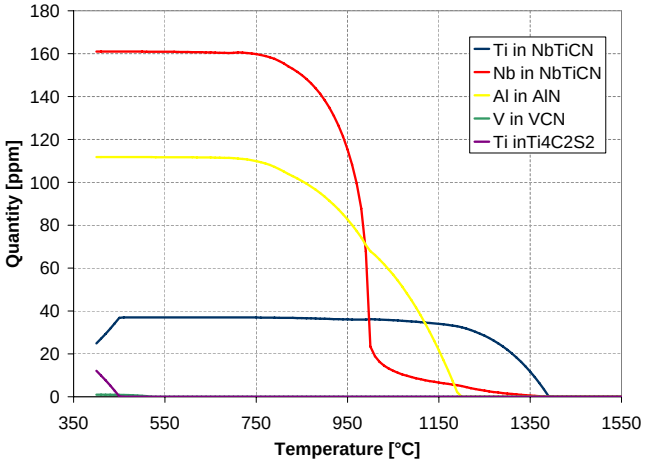

Figure 3.12: Evolution at the equilibrium of the Ti, Nb, Al and V precipitate quantity as a function of temperature for steel grade **C** (data provided by Arcelor Research)

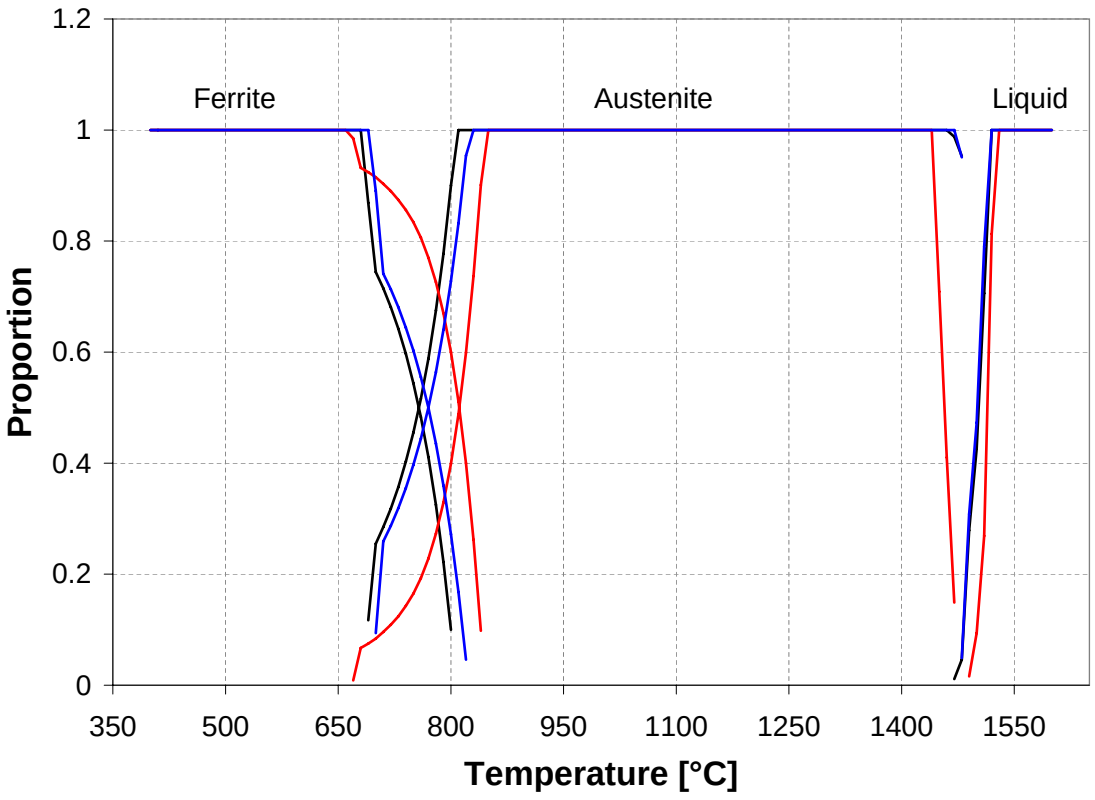

Figure 3.13: Phase transformations for the three steel grades studied at equilibrium (Black **A**, Red **B**, Blue **C**)

and they present small diameters.

S precipitates with Mn. They do not have special effect but if S stays alone it could build cavities around the other precipitates. Thus, a sufficient Mn content should be present to prevent a low amount of sulfur to remain in the steel and to avoid its deleterious effect.

At this stage of the study, the studied peritectic steel grade compositions should be reminded (Table 3.3).

Steel grade	C	Si	Mn	P	Ti	N	**V**	**Nb**	Al	S
Grade **A**	1748	183	14702	117	151	54	**60**	**139**	313	66
Grade **B**	576	2226	16220	119	163	45	**20**	**668**	396	24
Grade **C**	1790	3253	12149	80	37	58	**1**	**161**	403	8

Table 3.3: Composition of the studied peritectic steel grades (in ppm)

The ductility trough for **B** grade (Figure 3.6) is not very deep. This could be explained by the small amount of C that induces a small grain size. The grain size obtained will shift the solidification temperature to a lower value and delay the austenite grain growth. Within this grade, Nb is also the only element that increases the precipitation at the grain boundary. Even if the content in V is high, it does not form precipitates until approximatively 650°C. The formation of AlN begins also very late and in a limited way as the available amount of N is lowered by the high amount of Ti and Nb.

The second decrease in necking could be due to the formation of ferrite that starts early, at 800°C for **B** grade. With a slight kinetic effect due to continuous cooling, the decrease could be shifted to lower temperatures than here, 700°C. This assumption should be analyzed by micrographic analyses in order to characterize the microstructure at this temperature. Note that, kinetic effects could be avoided by a very low decrease of temperature. Nevertheless, the study performed here has been designed to be representative of the real behavior of thermal and mechanical variables of the CC process. Thus, only assumptions could be made about this last decrease of necking. As explained earlier, tests at lower temperatures should be performed in order to ensure that the last decrease in ductility does not correspond to precipitations or transformation within of the matrix.

The trough for **C** grade is very pronounced because of the high N and the low Ti and Nb content. The remaining N after Ti combination precipitates very early with Al, and is detrimental for ductility, AlN compounds could be at the origin of the strong ductility loss. The increase of Nb(C,N) at approximately 1000°C joins the AlN detrimental effect and produces a pronounced trough as it is observable in Figure 3.16.

A grade lays between the two others in the view of microalloying components and thus presents an intermediate trough size. The trough is composed of two dips. As presented in Section 1.2.1, the first one, less deep, is related to precipitation (Figure 3.14). Especially Nb seems to be the ductility loss cause. The second one is related to ferrite formation at approximately 850°C. This second reason of ductility loss deepens the first trough.

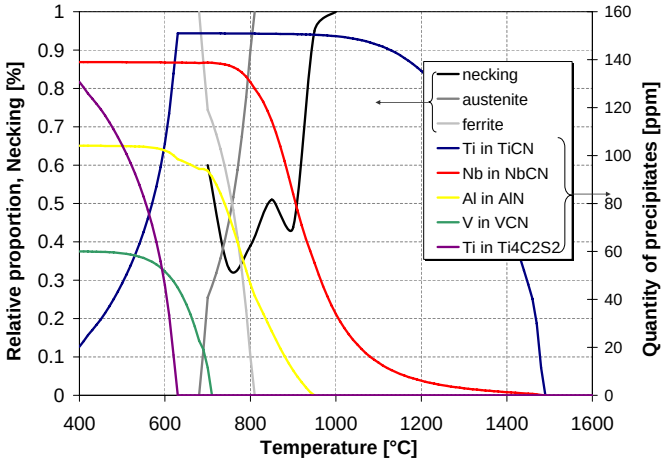

Figure 3.14: Ductility trough against phase transformation and precipitation state at the equilibrium for steel grade **A**

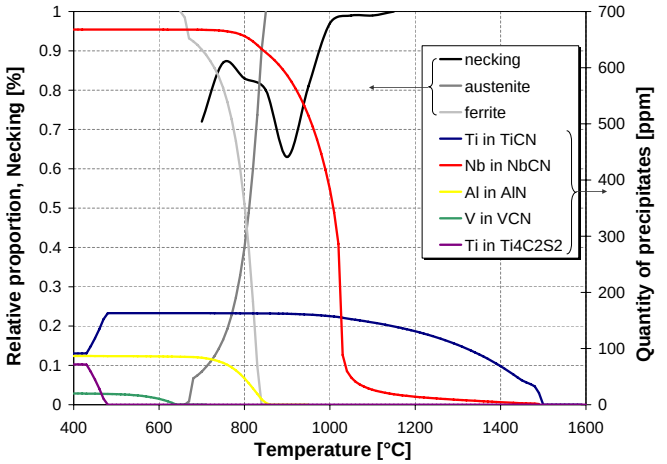

Figure 3.15: Ductility trough against phase transformation and precipitation state at the equilibrium for steel grade **B**

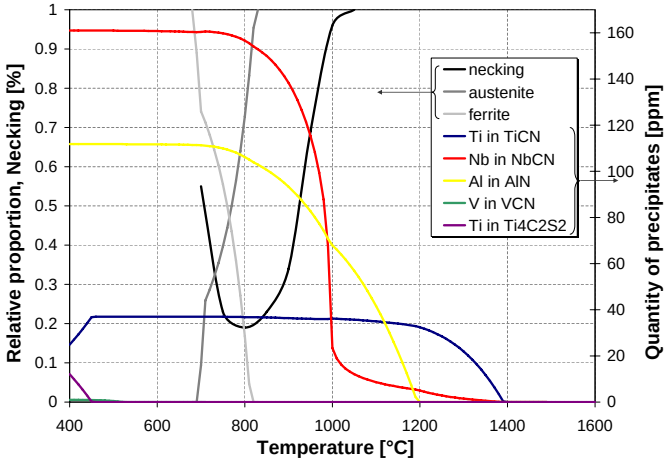

Figure 3.16: Ductility trough against phase transformation and precipitation state at the equilibrium for steel grade **C**

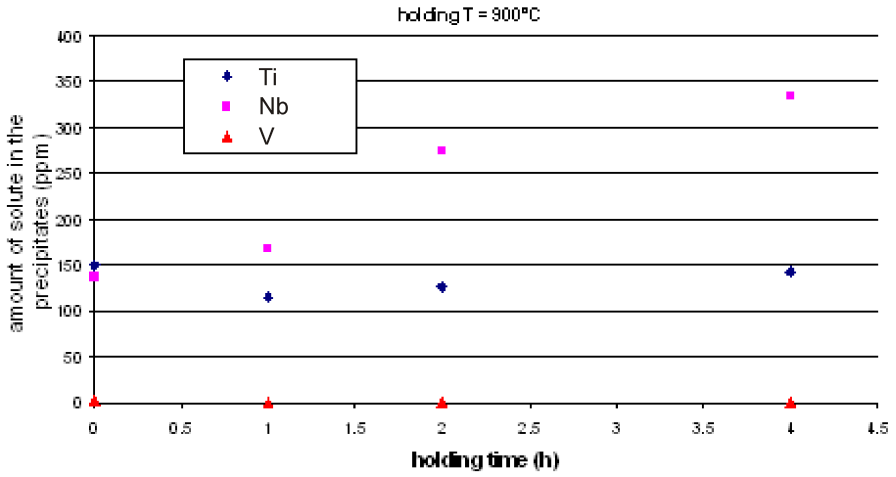

Figure 3.17: Kinetic of precipitation of Nb, Ti and V for a steel composition close to **B** (data provided by Arcelor Research)

Analysis of the ductility trough start

The ductility decrease can be associated with the beginning of the forming of precipitates in the steel matrix. In particular, the Nb(C,N) formation moment corresponds to the beginning of the ductility gap.

The Nb(C,N) contents is the highest for **B**, and higher for **C** than **A** grade. Its formation rates present strong gradients for **B** and **C** when **A** presents a lower one over a large temperature range. Both, the content and kinetic of Nb(C,N) can explain the delayed start of the ductility trough for **A** grade.

Knowing about precipitation kinetics

It is interesting to take a closer look at the precipitation kinetic as the continuous casting never allows equilibrium, except if the precipitation starts very fast depending on the component. This has to be taken seriously into account because it has an important impact on the calculations as shown in the example hereafter.

As it is possible to observe in Figure 3.17 for **B** grade at 900°C, the CEQSCI calculations predicts a concentration of 586ppm of Nb. On the contrary, the kinetic measurements after 4 hours of maintenance at temperature gives a concentration of 338ppm.

It has been demonstrated that Nb has a low precipitation kinetics. It is also accepted that Ti has a high kinetics because of its early appearance at high temperatures. V in contrary has an extremely low kinetics and thus, probably a very low amount of V(C,N) will precipitate at the austenite grain boundary.

3.1.3 Rheological parameters

The Norton-Hoff rheological law used in this study contains four parameters that are determined by HTT. They are temperature dependent. As the stress curve is strain rate dependent, the parameters should be determined by tests at different temperatures and strain rates.

Before the HTT campaign, a previous compression test campaign at high temperature had been performed in order to determine specific tendencies of the steel grades studied. It should be noticed that the reason why the whole campaign has not been made with compression tests is that this test is not representative of the stresses found in the material during CC while HTT is.

3.1.3.1 Hot compression tests

The three steel grades studied were tested at the University of Liège in compression at three different temperatures (700, 900 and 1100°C) and three different strain rates ($1 \cdot 10^{-2}$, $1 \cdot 10^{-3}$ and $1 \cdot 10^{-4}\text{s}^{-1}$).

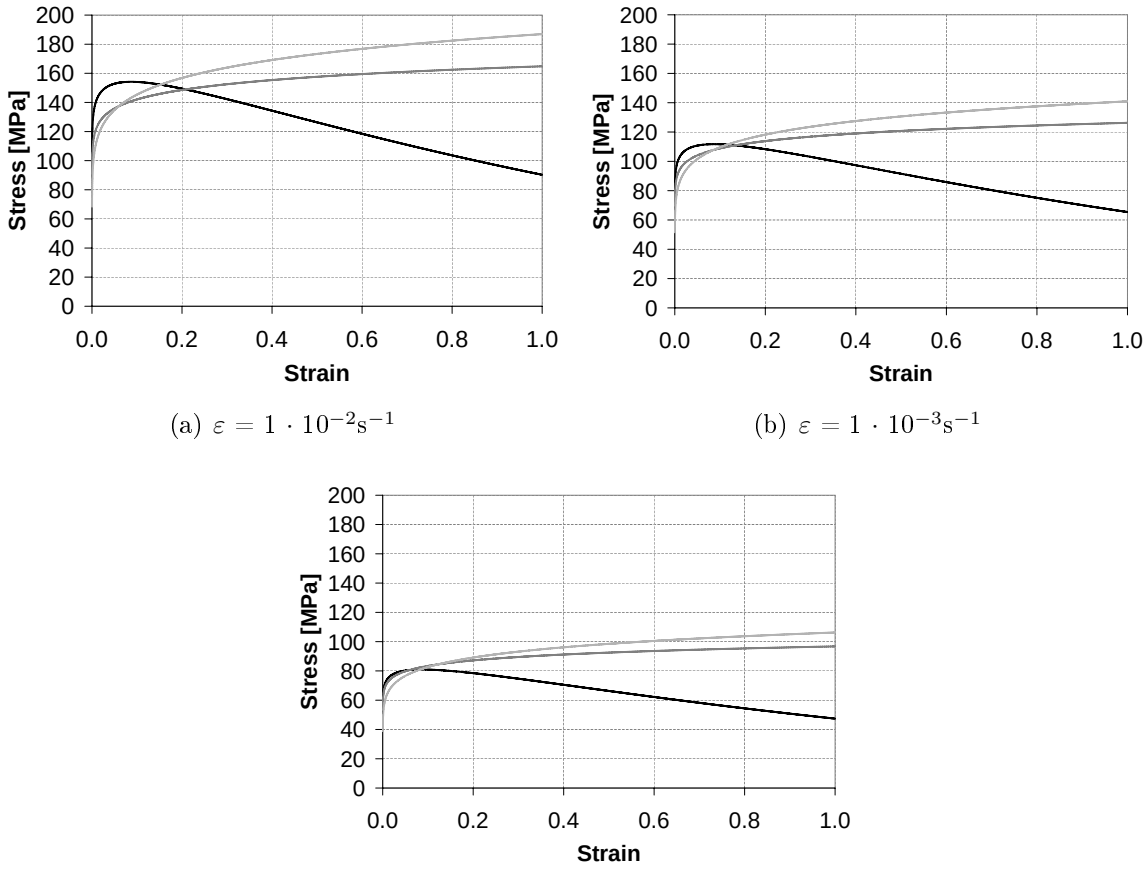

(a) $\varepsilon = 1 \cdot 10^{-2}\text{s}^{-1}$

(b) $\varepsilon = 1 \cdot 10^{-3}\text{s}^{-1}$

(c) $\varepsilon = 1 \cdot 10^{-4}\text{s}^{-1}$

Figure 3.18: Numerical flow curves provided by a Norton-Hoff law fitted on compression tests for **A** (dark gray), **B** (black) and **C** (light gray) at 700°C

In general we can see that the curves obtained thanks to the fitted Norton-Hoff law parameters at different temperatures and various strain rates are close for the three grades studied (Figure 3.18). Nevertheless it could be noticed that in some specific cases the curves are not exactly identical.

It is possible to conclude from this curve analysis that the **B** grade has a different behavior from the others and that **A** and **C** are close at each temperature and each strain rate.

The consistency of the experimental results from compression and tension was difficult. The reason for this discrepancy was partially analyzed. The tensile tests were performed in Aachen (RWTH) where the thermal cycle determined in Section 3.1.1.1 could be applied on the samples. The compression tests were performed in Liège (ULg) where another thermal cycle was applied due to the limitation of the furnace capacity (see Figure 3.19).

The microstructure generated by each treatment was different. Indeed, according to Section 3.1.1.1, the tensile test samples have a grain size of 200μm when the one measured on ULg samples is 1000μm (Figure 3.20).

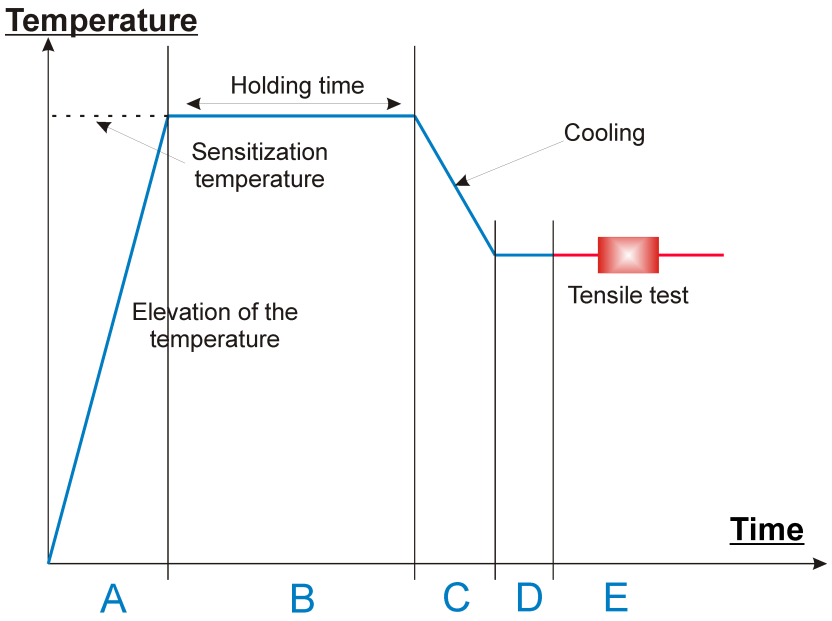

Figure 3.19: Thermal cycle comparison between compression and tensile tests

	Furnace	Temperature measurement	A	B	C	D	E
Liège	Halogen lamps	Sample core	2°C·s^{-1}	5min 1100°C	2min	2s Test temp.	Test time Test temp.
Aachen	Induction	Sample surface	6°C·s^{-1}	5min 1350°C	60°C·min^{-1}	20s Test temp.	Test time Test temp.

Table 3.4: Thermal cycle description of both, hot compression and tensile tests driven respectively at Liège and Aachen

The differences could be explained by a too low sensitization temperature in Liège. As the precipitates are not dissolved, they could affect the plastic stress in a different way. The holding time has been lengthened in order to compensate the lower temperature.

Another possibility is a test problem. For instance, specific strain rates tests were dropped from RWTH results because of non reliable behavior.

From an historical point of view, all this information did not arrive simultaneously. As it was necessary to go on with the test campaign, it has been chosen to perform a

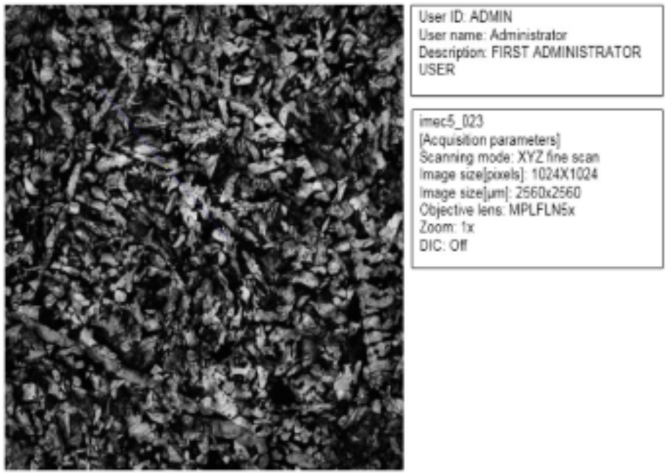

Figure 3.20: Analysis of the grain size of the compression test sample used at the ULg

whole set of tensile tests because their thermal treatment produced samples closer to the material state in CC. Another argument to justify this choice is that tensile state in closer to the loading producing cracks in CC.

Section 3.1.3.6 demonstrates the final agreement that could be found between experimental tension, compression and numerical Norton-Hoff predicted curves.

In conclusion this compression study gave us arguments to decide that the hot tensile tests to determine the rheology will only be performed on **B** and **A** steel grades. The parameters obtained from the **B** experimental hot tensile tests will be used only for this steel grade. Contrary, the **A** parameters determined through fitting of the experimental hot tensile test curves will be used to model the behavior of both, **A** and **C** grades. This choice enables the reduction of the number of expensive HTT.

3.1.3.2 Hot tensile tests

The rheology of the two steel grades (**B** and **A**) is tested at three different temperatures (900, 1000 ans 1100°C) and with three different strain rates ($5 \cdot 10^{-2}$, $1 \cdot 10^{-2}$ and $1 \cdot 10^{-3}s^{-1}$) on the TREBEL hot tensile testing apparatus described in Section 2.3.1.

The temperature range chosen for the tensile tests is less broad than for the compression tests. At this step of the study, tests at temperatures lower than 800°C could not have been performed because of the limitations of the force recording cell.

3.1.3.3 Identification of the Norton-Hoff law

The first attempts made to fit the rheological parameters to obtain a similar curve in simulation as in experience have been performed taking the whole experimental curve into account. As shown in Figure 3.21(a), the fitting follows almost the experimental curve. It is especially acceptable at the end of the deformation. But at the beginning, where the variations of slope are important, the fitting is not satisfying. Thus it has been decided to proceed to a second type of fitting that focuses on the first 20% of strain. This choice is justified by the fact that low strains happen in CC. The necking event after the curve maximum decrease also the reliability of the curve.

This fitting enables a better prediction of the behavior of the material for strains under 20% as shown in Figure 3.21(b).

What is also important is that the flow curve presents a necking at approximately 20% strain (Figure 3.21(b)). The accurate moment of the necking event can be difficult to model with rheological models. During the HTT in Aachen, there is no optical or mechanical measurements of the section history. So, the experimental stress is computed as the force measured by the load cell divided by the section computed from an hypothesis of volume conservation and homogeneous stress state. Once necking has started, this experimental stress is far from being accurate. With the Norton-Hoff law and the softening parameter p_1, one can predict the necking. However, as the experimental target is not reliable, it was chosen to keep a non softening law ($p_1 = 0$) identified only on the first 20% of strain, as the curve maxima happen around 22% strain.

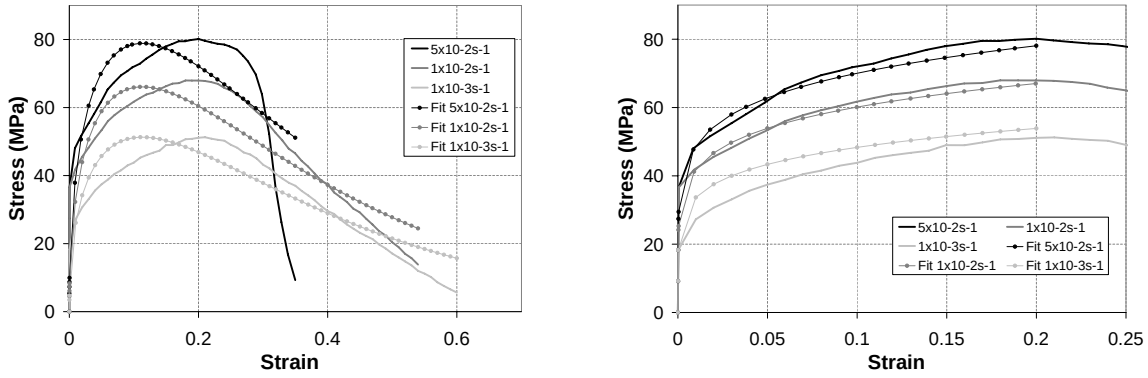

(a) Whole experimental curve

(b) Focus on 20% strain

Figure 3.21: Fitting of the flow curve of **B** grade at 1000°C

Looking at these figures, it is possible to observe that the numerical curves are closer to the experiments when limited to 20% of strain. This last model is accurate when the material undergoes only small strains. In the macroscopic simulations of the CC process the maximum expected strains are 1 to 2%. In the mesoscopic model, higher strain can happen due to local grain deformation but it remains under 20%.

The results obtained for each studied steel grade are presented in the following part.

3.1.3.4 Norton-Hoff law parameters

The fitting of hot tensile tests with the least square method has been used to identify the parameters of the Norton-Hoff law. The fitting gives the results for parameters p_1 to p_4 for **A** and **C** in Table 3.5 and **B** in Table 3.6.

Parameters for A and C grades

Figures 3.22 to 3.24 present the fitting of **A** steel grade at 900, 1000 and 1100°C.

At 900°C the correlation between experimental and fitted curves is good until 20% of strain. At 1000°C the mean values found for the parameters correctly fit the stress

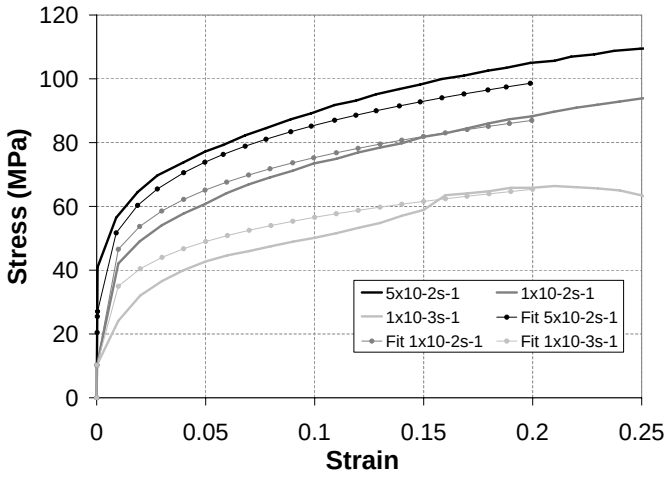

Figure 3.22: Comparison of the Norton-Hoff model predictions with the experimental flow curves of **A** grade tested at 900°C at several strain rates

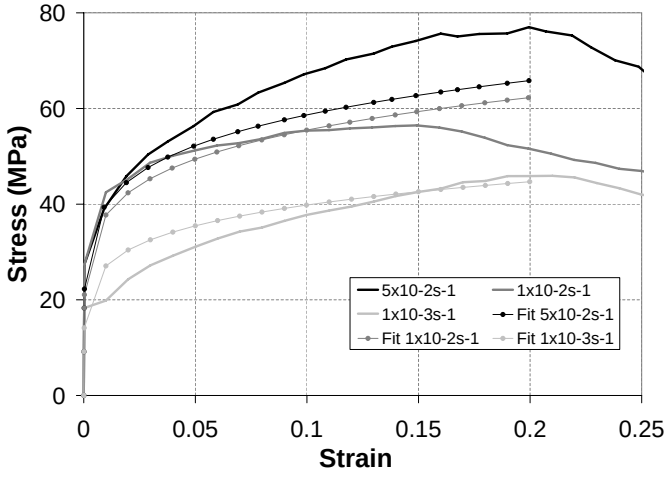

Figure 3.23: Comparison of the Norton-Hoff model predictions with the experimental flow curves of **A** grade tested at 1000°C at several strain rates

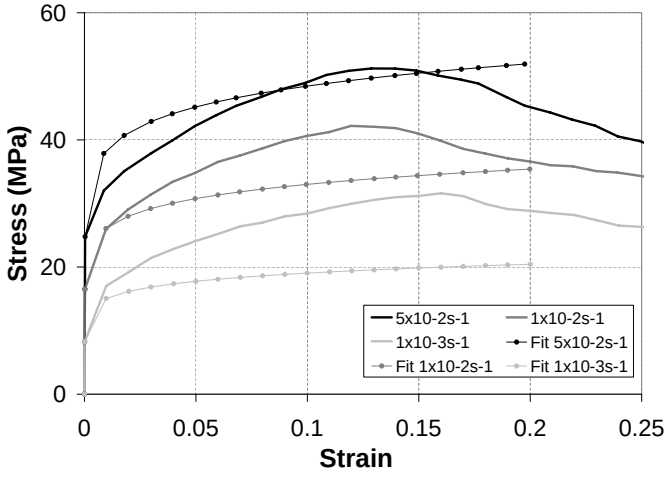

Figure 3.24: Comparison of the Norton-Hoff model predictions with the experimental flow curves of **A** grade tested at 1100°C at several strain rates

strain curves at strain rates 10^{-2} and $10^{-3}s^{-1}$ but the highest strain rate gives slight differences between experimental and numerical curves.

Figure 3.24, at 1100°C, shows a more difficult correlation between curves. The slowest strain rate is clearly not well fitted. Nevertheless, the two other curves for strain rates 10^{-2} and $5 \cdot 10^{-2}s^{-1}$ are approximatively fitted.

The rheological law parameters are given hereunder.

A- C	p_1	p_2 [MPa]	p_3	p_4
900°C	0	108.72	0.11	0.21
1000°C	0	79.32	0.14	0.17
1100°C	0	63.34	0.24	0.10

Table 3.5: Fitted **A** and **C** parameters of the Norton-Hoff constitutive law for the HTT

The parameter p_2 decreases with increasing temperature. As explained in Section 2.1.2 this parameter influences the level of the curve. Indeed, with higher temperatures, the stress reached will be lower for the same strain. The material is more deformable.

p_3, which is linked to the viscosity, is increasing with increasing temperature. This means that the strain rate effect becomes more marked at higher temperatures.

The last parameter p_4 models the hardening effect. It decreases with temperature so that the stress for high temperatures increases slower.

Parameters for B grade

Figures 3.25 to 3.27 present the fitting of **B** steel grade at 900, 1000 and 1100°C.

Looking at the curves at 900, 1000 or 1100°C, the Norton-Hoff law perfectly fits the experience. The only curve where the adjustment is reliable only until 15% of strain is the one at the highest temperature (1100°C) and the lowest strain rate ($10^{-3}s^{-1}$). At this temperature the stress obtained is very low. This is reinforced by the slow strain rate effect that lowers a little bit more the stress. Thus, in these conditions, the forces and the displacements are difficult to record with the TREBEL machine. The flow curves should be carefully taken into account. So **B** fitting results are totaly acceptable and the parameters used and implemented in the rheological law are the following ones (Table 3.6).

B	p_1	p_2 [MPa]	p_3	p_4
900°C	0	117.42	0.09494	0.23
1000°C	0	73.17	0.09482	0.16
1100°C	0	50.13	0.09470	0.17

Table 3.6: Fitted **B** parameters of the Norton-Hoff constitutive law for the HTT

As for **A**, the parameter p_2 of the law fitted for **B** decreases with increasing temperature. Contrary, p_3 has an other behavior. The value of this parameter decreases with increasing temperature. Thus, for **B**, the strain rate effect influences less the flow curve at higher temperatures.

p_4 presents the same behavior as for **A**. It decreases with temperature.

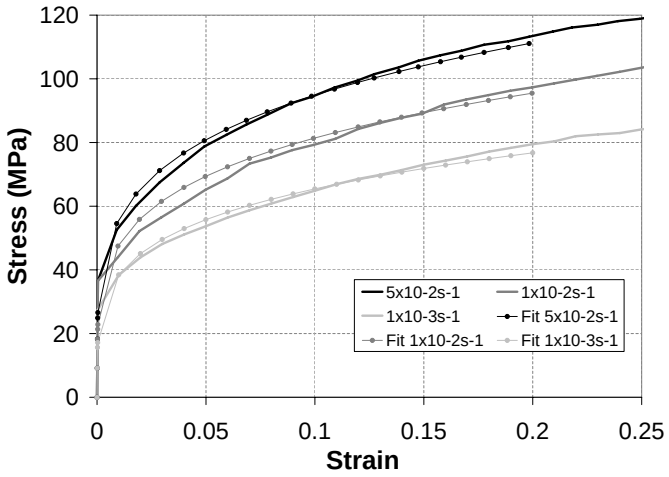

Figure 3.25: Comparison of the Norton-Hoff model predictions with the experimental flow curves of **B** grade tested at 900°C at several strain rates

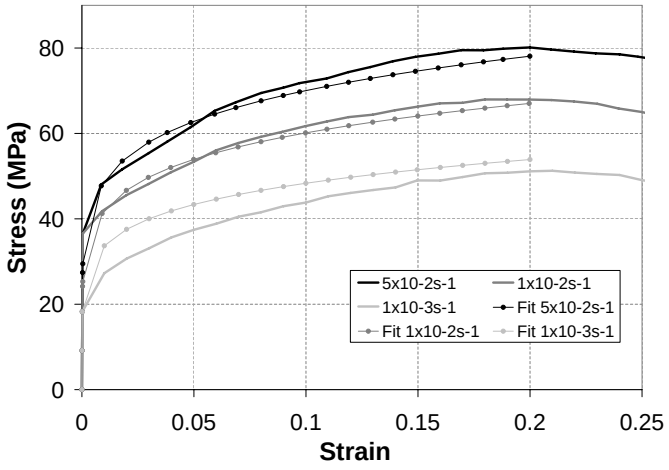

Figure 3.26: Comparison of the Norton-Hoff model predictions with the experimental flow curves of **B** grade tested at 1000°C at several strain rates

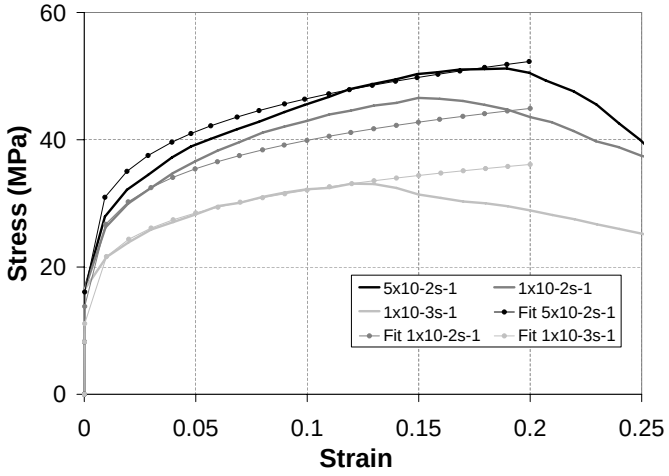

Figure 3.27: Comparison of the Norton-Hoff model predictions with the experimental flow curves of **B** grade tested at 1100°C at several strain rates

3.1.3.5 Extrapolation of the results to all the required temperature

In order to feed the CC simulation the rheological parameters have to be extrapolated to extend the rheological parameter values to lower and higher temperatures. Indeed, the steel running through the continuous caster cools down from the liquid phase to the solid state. This covers more or less a temperature range from 1550°C at the exit of the mold to 700°C at the end of the process.

The Norton-Hoff law is implemented in the LAGAMINE FE code with no extrapolation when the temperature is out of the given temperature rage. However, the nearest given value is taken into account. This procedure is implemented in order to avoid false extrapolations but is suitable only for small temperature range exceeding. In our case, the temperature range is exceeded at the upper bound by 450°C (1550-1100°C) and at the lower bound by 200°C (900-700°C).

The extrapolation is thus done for each parameter separately and the consistency is checked after.

PARAMETERS p_2

For the parameter p_2 the extrapolation has been performed in two steps. At first, the low temperatures have been extrapolated (700 and 800°C) and then, another extrapolation has been made for the higher temperatures. This procedure is necessary because, when extrapolated to low temperatures, the curve is the one given in Figure 3.28. When using this curve for higher temperatures values, p_2 becomes negative which is inconsistent. So, a change of slope has been imposed for this parameter for both steel grades (Figures 3.28(a) for **A** and 3.28(b) for **B**). In fact, the high temperature extrapolation is made between the value at 1100°C and a given value at 1550°C that is close to zero.

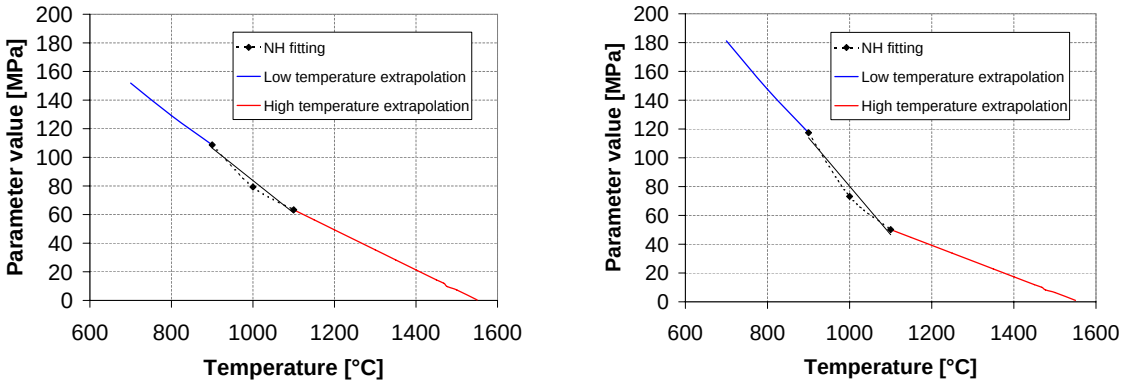

(a) **A** (b) **B**

Figure 3.28: Norton-Hoff p_2 parameter extrapolation to lower and higher temperatures

At high temperatures p_2 have the same behavior for both steel grades. When at low temperatures the parameter presents higher values for **B** grade. **B** grade presents higher strength at low temperatures. As already discovered, the grain size of the steel and the precipitates of Nb gives to grade **B** a stronger structure with more grain

boundaries and precipitates that are able to stop crack when trying to go through the steel matrix. This characteristic yields also to a higher strength.

Parameters p_3

Neither for **A**, nor for **B** grade, the curve equation had to be adapted at high temperature in order to keep the parameter values consistent. Indeed, the p_3 parameter stays between 0 and 1 after extrapolation.

As introduced earlier, the slopes of p_3 parameters are different for **A** and **B** grades (Figure 3.29). For **B**, the strain rate dependency of the Norton-Hoff law is more or less constant in function of temperature. It varies from 0.095 to 0.094 that is almost the same at this level. In contrary, the **A** grade presents an other behavior for p_3. It starts at the level obtained for **B** grade and increases exponentially with temperature. So for **A** grade, the strain rate influences more the rheology, particularly at high temperatures.

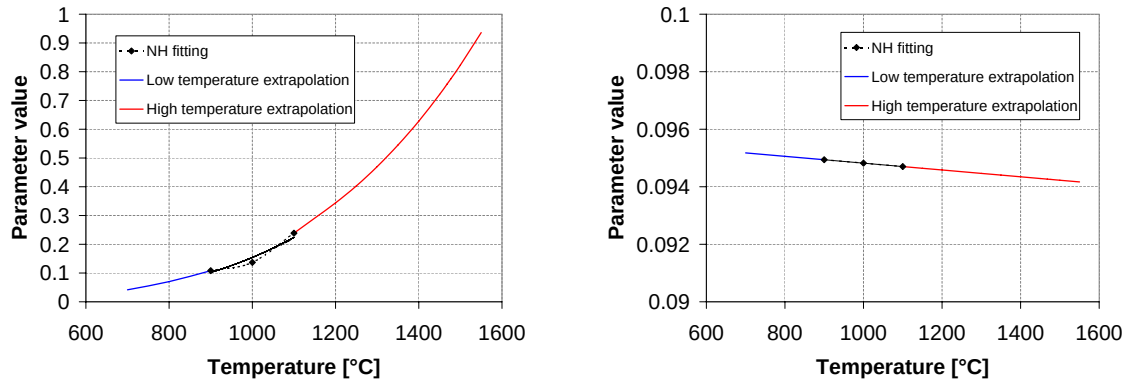

(a) **A** (b) **B**

Figure 3.29: Norton-Hoff p_3 parameter extrapolation to lower and higher temperatures

Parameters p_4

Tendencies of parameter p_4 are equal for **A** and **B**. The values decrease with temperature from approximately the same level (0.3) and end both at 0.025.

The immediate response of the material to a loading is equal for both steel grade at each temperature even if the fitting had to be adjusted for **A** because of a too fast decrease at high temperatures. In the range of HTT **A** is more sensitive to temperature changes for p_4.

For **B**, the it has been chosen to keep a constant decrease of p_4 parameter even if the results show an increase of this value after 1000°C.

Validation of numerical flow curves generated by Norton-Hoff model

The last step of the rheological parameters fitting is to check the consistency of all the parameters together in the Norton-Hoff law by drawing the numerical curves at the same strain rate ($10^{-2}s^{-1}$) and for various temperatures for **A** and **B** steel grades.

In Figure 3.31 it is possible to observe the continuity of the evolution of the Norton-Hoff flow curves as a function of temperature. The stress level reached for both grades

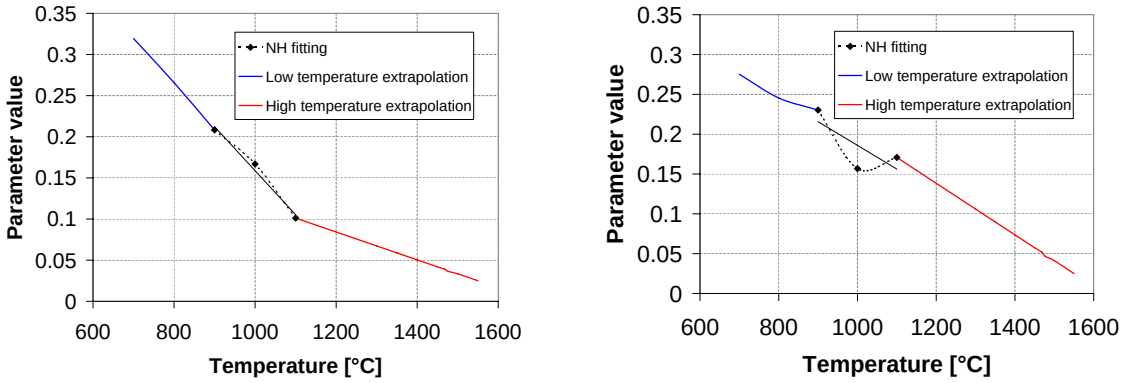

(a) **A** (b) **B**

Figure 3.30: Norton-Hoff p_4 parameter extrapolation to lower and higher temperatures

is almost the same. This result is consistent with the fact that both steel grades belong to the same family and thus should have close mechanical properties.

Observing the stress level, it is obvious that at low temperatures (700°C) **A** and **B** presents the same stress level. Nevertheless, from 800°C to very high temperatures this tendency is inverted and **B** presents the highest stress level as expected by p_2 parameter. Numerically, this could be explained by the counterbalancing **A** p_3 parameter that is lower than the one for **B** at 700°C. From this point of view, it is important to compare all the parameters working together in order to identify potential errors in parameter adjustments.

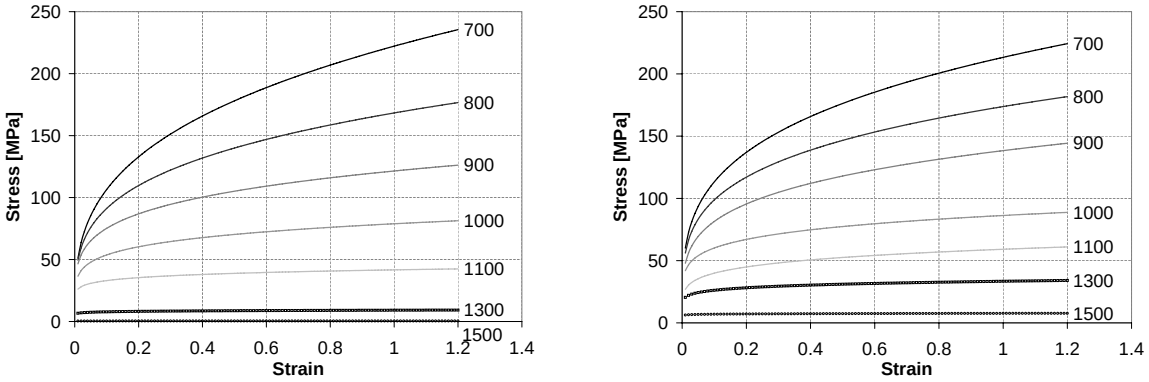

(a) **A** and **C** (b) **B**

Figure 3.31: Curves of the Norton-Hoff law determined at various temperatures with the parameters determined through HTT for a strain rate of $10^{-2}s^{-1}$

In conclusion, despites some discrepancy between the model predictions and experiments, especially for **A**, the identified parameters generate an expected behavior and the different steel grades could be modeled with them. The parameters obtained for **A** are applied on **C** in the rheological point of view (Norton-Hoff model) but not for the damage model. These parameters will be used to model the material behavior during HTT.

3.1.3.6 Comparison of the tensile and compression tests and numerical results

In order to finish up the whole experimental study, the results of the HTT performed at Aachen, the hot compression tests done at Liège and the rheological Norton-Hoff law flow curves with the identified parameters have been collected.

The three studied steel grades flow curves results have been compared for the strain rate of $1 \cdot 10^{-3}\text{s}^{-1}$ on R0 samples for the available temperatures, 700, 900 and 1100°C (see Table 3.32).

The stress and the strain (Equations 3.1 and 3.2) are calculated without necking in tension. The reactions recorded on the hot tensile testing machine are taken supposing an homogeneous elongation and volume conservation. As the necking appears at an undefined moment no correction can be used.

$$\sigma = \frac{\text{Force}}{\text{Section}} \qquad (3.1) \qquad \varepsilon = Ln(1 + \frac{\Delta L}{L}) \qquad (3.2)$$

In compression, the stress is calculated using a barreling correction (Equations 3.3) described in an ULg internal report based on Orowan theory.

$$\sigma_{compression} = \frac{F}{\pi \cdot R^2_{real}(d)} \qquad (3.3)$$

where the stress is calculated on the basis of the real sample radius with barrel shape R_{real} at a given transverse beam displacement d. The real radius is calculated the following this equation:

$$R_{real}(d) = R_H(d) + \frac{d}{d_{final}}(R_{real,final} - R_{H,final}) \qquad (3.4)$$

with R_H the homogeneous radius calculated through volume conservation.

The barreling appears as soon as the test sample is loaded and thus the correction can be applied along the compression test. This can explain some differences in the experimental results at the moment where the necking appears in tension.

The experimental compression and tensile tests are in good correlation, for a strain rate of $1 \cdot 10^{-3}\text{s}^{-1}$, in almost all the cases even if the thermal cycle and therefore the microstructure is different.

The divergence are more elevated at 1100°C as the compression tests at the University of Liège were difficult to realize at such elevated temperatures, knowing that 1100°C is the limit of capacity of the furnace and that the recording noise was more or less of the same level as the forces recorded. That is why the compression curve for **C** at 1100°C has not been exploited.

The Norton-Hoff law parameters values are in concordance up to the threshold strain value equal to 0.2.

Hence, the extrapolated values of the rheological law are assumed pertinent in order to simulate the steel behavior at these temperatures.

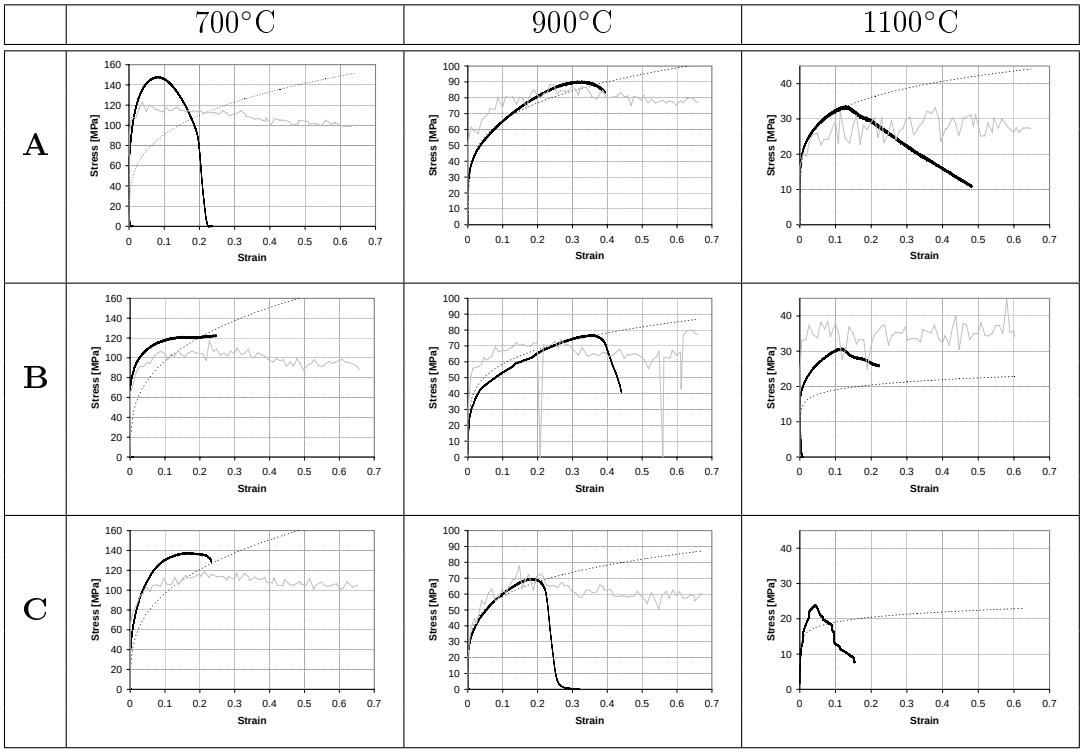

Figure 3.32: Comparisons of the hot tensile and compression tests and the numerical results of the simulation for cases at $1 \cdot 10^{-3}\text{s}^{-1}$ strain rate where black lines represents the experimental tensile tests, the gray lines the compression tests and the dashed lines the calculation of the Norton-Hoff law with the determined parameters)

3.2 Tensile histories for mesoscopic application

In order to determine the damage parameters of the law presented Section 2.1, it is necessary to perform a bench of tensile tests. To reduce the number of tests, it is important to focus on temperatures within the ductility trough. The test temperatures were determined in Section 3.1.2. Different strain rates tests also help us to properly fit the damage parameters.

3.2.1 Determination of the studied cases

The hot tensile tests performed for the damage law parameters adjustment are determined through the variation of three variables:

- The sample geometry;
- The strain rate;
- The temperature.

Determination of sample geometry

In order to have different stress and strain histories, various sample shapes have been chosen. The one selected, R2 and R4, present different triaxialities (χ) at the notch root (justification of the location in Section 4.1.2).

The first point is to determine the different triaxialities (Equation 3.5) given by various notch radii (2 and 4mm) in order to be sure that the strain stress histories will be different. Hence, the tensile tests have been simulated with the different notch radii. The triaxialities have been recorded as a function of time within the middle cross section. The value at the notch root at the beginning of the test is given (Figure 3.33).

$$\chi = \frac{\sigma_m}{\sigma_{eq}} = \frac{(\sigma_{xx} + \sigma_{yy} + \sigma_{zz})/3}{\sigma_{eq}} \tag{3.5}$$

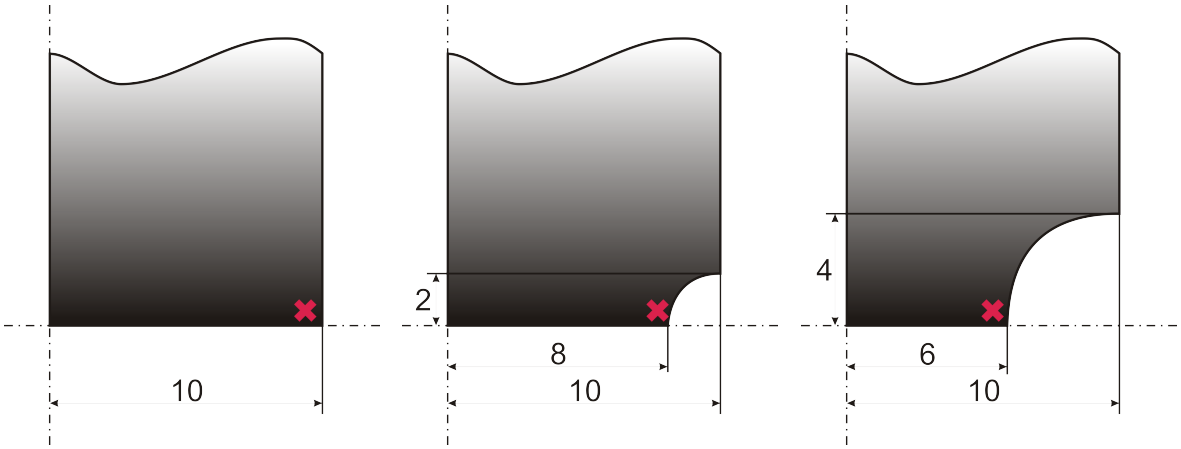

(a) R0 - $\chi = 0.33$ (b) Notch R2 - $\chi = 0.48$ (c) Notch R4 - $\chi = 0.55$

Figure 3.33: Values of the triaxiality at the notch root for each specimen shape at the simulation start

The triaxiality is growing with increasing notch radius. Indeed, the smooth sample gives a low triaxiality (0.33). Whereas, the 2mm radius, that is the intermediate one, gives higher triaxiality (0.48) and thus a different stress and strain history compared to a 4mm radius (0.55).

R0 shape also could have been used but the numerical application of this case is more difficult. Indeed, the necking does not appear easily within the simulations as a hardening viscoplastic law has been chosen. One should add an artificial defect in the sample center part. As the stress strain history of the middle section shape was not recorded during the test, this artificial defect should be determined arbitrarily. Hence, R0 shape samples is only used for the hot ductility trough location and not for the damage parameters determination.

In conclusion the sample shapes R2 and R4 are adequate to model different histories and provides various cases exploited later in the mesoscopic study (Chapter 4).

Determination of strain rate

As the rheological law depends on the strain rate, three different strain rates have been chosen in order to be able to fit parameters as close as possible to the real industrial cases studied. The strain rate in CC is near to 10^{-5} to $10^{-4}s^{-1}$. Thus, the strain rates have been chosen to be very low, knowing that the lower bound of the tensile test apparatus is $10^{-3}s^{-1}$. The values 10^{-2}, $5 \cdot 10^{-3}$ and $10^{-3}s^{-1}$ have been chosen.

Determination of temperature

Three temperatures have been chosen depending on the ductility troughs detected for each steel grade as presented in Section 3.1.2.

For **A** grade, the ductility trough was assumed to be centered between 850 and 950°C from the partial results available at the moment of decision. The three chosen temperatures to study are 850, 900 and 950°C.

For **B** grade, the ductility trough is situated between 750 and 950°C which is a larger range. Even though, three temperatures have been chosen: 750, 850 and 950°C.

The studied temperatures for **C** which has a deep ductility situated between 700 and 900°C, are 700, 800 and 900°C.

Overview of the studied HTT cases

In conclusion, nine different cases are available for each steel grade as summarized in Table 3.7 where all the performed tests on notched samples are compiled.

Shape	$\dot{\varepsilon}$ [s^{-1}]	A [°C]	B [°C]	C [°C]
R2 R4	$1 \cdot 10^{-3}$	850	750	700
	$5 \cdot 10^{-3}$	900	850	800
	$10 \cdot 10^{-3}$	950	950	900

Table 3.7: Test campaign planning for determination of the damage model on R2 and R4 sample shapes

For each steel grade the tested cases are different due to the determination made on the basis of the ductility troughs observation. Not all the cases are available. Some tests have not been performed because of material lack or the results are not exploitable as presented in the following chapter.

3.2.2 Experimental and numerical correlation of the HTT

The numerical simulations of the tensile tests have been performed. In order to validate those, the results of force against displacement have been confronted to the experimental data.

The displacement values applied on each test have been extracted from the experimental data and applied on the numerical sample in order to be the nearest possible to the test case. The displacement has been recorded in function of the loading at the notch root of the numerical simulation in order to compare both results.

The measured and predicted forces are compiled in Appendix E. Depending on the test, some results are in very good correlation and others not.

The validated cases and the dropped results are shown in Table 3.8 for the three steel grades studied. For **A**, 8 cases are available whereas 7 are for **B** and 9 for **C**.

In a general point of view, the results for R4 sample shape are not in good correlation with the numerical results. This could be due to the lower stress level reached and

thus, small force values. However, the HTT tests for **C** present good correlations with rheological law on R4 samples.

A clear correlation between sample shape and the accuracy of the measured and experimental curves comparison has not been established. For the following study, the bold cases in Table 3.8 will be used for the damage parameter study in order to stay as accurate as possible.

	A		**B**		**C**	
	R2	R4	R2	R4	R2	R4
$1 \cdot 10^{-3}$ s^{-1}	**850**	850	**750**	750	**700**	**700**
	900	900	**850**	850	**800**	800
	950	950	950	950	**900**	**900**
$5 \cdot 10^{-3}$ s^{-1}	**850**	850	**750**	750	**700**	700
	900	900	**850**	850	**800**	800
	950	950	**950**	950	**900**	**900**
$10 \cdot 10^{-3}$ s^{-1}	**850**	850	**850**	750	700	700
	900	900	**950**	850	800	800
	950	950			900	900

Table 3.8: Correlation study between experimental and numerical HTT at various strain rates and on different sample shapes with validated cases in bold style

3.2.3 Analysis of the differences between experimental and numerical simulations

The discrepancy between the experimental and the numerical results even in the non softening part was a big concern. Investigations have been led in several directions.

3.2.3.1 Finite element choice

The element used initially is the element BLZ2T as the damage element in the representative cell is associated to this type of element.

In order to be sure that the BLZ2T element gives right results for the loading performed it has been compared with PLXLS (Figure 3.34).

PLXLS is a classical isoparametric element, while BLZ2T is a mixed type, Hu-Washizu variational element with hourglass stress and one integration point.

Their results are identical for similar meshes as long as the following criteria on the element shape of BLZ2T are respects:

- good ratio between the element length $\rightarrow L_1/L_2 < 3$ (implemented in the code);
- no sharp or too large angles (visual check).

3.2.3.2 Mesh density

A rapid study of the mesh density impact on the accuracy of the results showed us that, when changing the mesh density, the values resulting from the calculations are presenting differences.

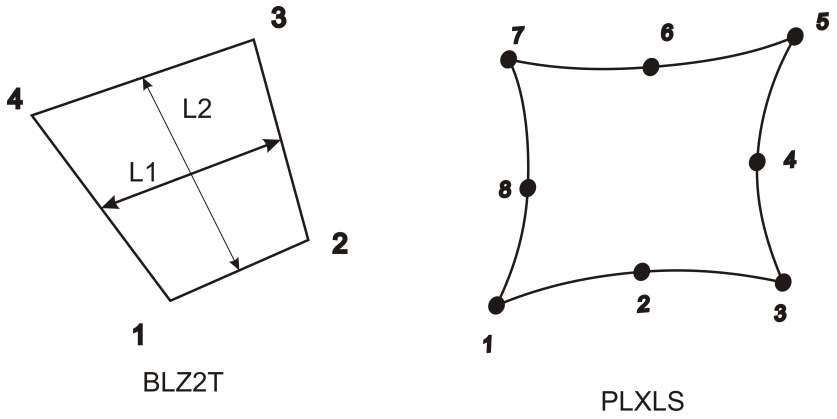

Figure 3.34: Finite element used for the stress strain comparison

Some tests have been performed in order to determine the best strategy to mesh the sample during the numerical simulations. The calculations haven been performed on a sample shape R2. The test temperature was 700°C and the strain rate, $1 \cdot 10^{-2} s^{-1}$. Three different mesh densities have been tested in this study (Figure 3.35). The root element size for each case is compiled in Table 3.9.

Mesh denomination	Number of elements	Size of the root element that will be studied [mm]
MESH1	1050	$1.9415 \cdot 10^{-2}$ (0.26650 x 0.07285)
MESH2	8000	$9.2524 \cdot 10^{-4}$ (0.02905 x 0.03185)
MESH3	13500	$4.5748 \cdot 10^{-4}$ (0.01450 x 0.03155)

Table 3.9: Comparison of key parameters of the mesh density study

In order to compare the consistency of the different meshes studied, the forces against the displacement in the section of the sample (Figure 3.36(a)) have been plotted.

At the beginning, the reactions are equal and thus the meshes are equivalent. However, the curve of the MESH1 mesh diverges from the others after around 3mm of displacement which approximately corresponds to a strain of 6%.

Looking at the flow curves in Figure 3.36(b) it is possible to analyze the local behavior of the different meshes. Indeed, locally the stress distribution will be affected by the mesh density. However drawing the flow curve of the equivalent stress at the root of the notch, the global loading is identical for each case, the same curves are recovered as expected.

But even so, the stress components entering the composition of the equivalent stress can follow different slopes. Looking at the stress components (Figure 3.36(c)), the radial, axial and circumferential stresses are put together in order to be able to compare them.

It is possible to observe that the mesh MESH1 has different slopes for each stress while meshes MESH2 and MESH3 that are equivalent. Thus, mesh MESH1 is not fine enough for these numerical simulations. The results for meshes MESH2 and MESH3

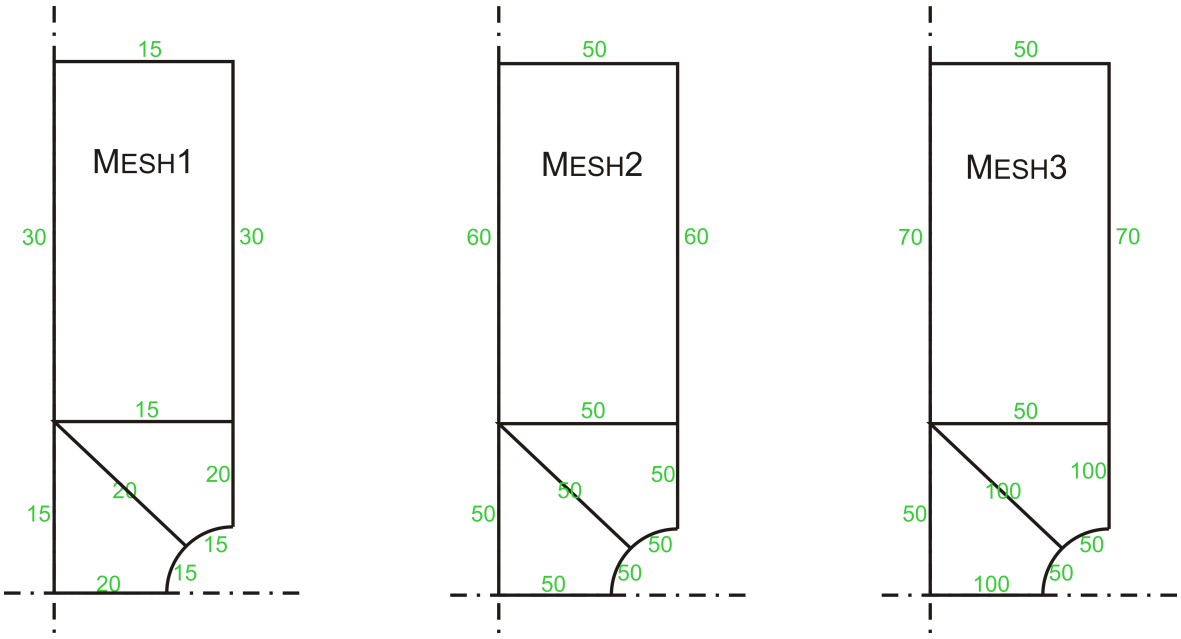

Figure 3.35: Mesh design for the mesh density impact study with number of elements per side in green

are equivalent. So, these results could be taken as the reference. Thus mesh MESH2 is used for further calculations in order to optimize the calculation speed.

3.2.3.3 Sensitivity of the rheological law

The sensitivity of slight modifications of the p_1, p_2, p_3 and p_4 of the Norton-Hoff law has been checked. The effect on the global Force-Displacement curves has been plotted.

As strain rate in the simulation of the notch test ($\dot{\varepsilon}_{max} = 7.5 \cdot 10^{-2}\text{s}^{-1}$ at the root of the R2 notch at 950°C and a strain rate imposed to the sample of $2 \cdot 10^{-2}\text{s}^{-1}$) can locally be larger than the one in the tests used to adjust Norton-Hoff parameters (maximum strain rate 10^{-2}s^{-1}), it was decided to focus on parameter p_3. However, only a large modification of p_3 allowed to become closer from experimental notched tests. In this case the reasonable agreement found on the HTT was lost.

3.2.3.4 Comparison of R2 and R4 sample shapes

Analysis of R2 and R4 simulation results for **B** grade, demonstrates that triaxiality and plastic gradient are higher in R4 and less homogeneous than in R2 simulation. But this variation seems still too low to induce any numerical problem requiring non local law and explaining the huge incoherency between experimental and numerical results.

All these investigations helped to identify a simulation giving reliable stable results for a reasonable computation time but did not solve the discrepancy between simulation and experiments.

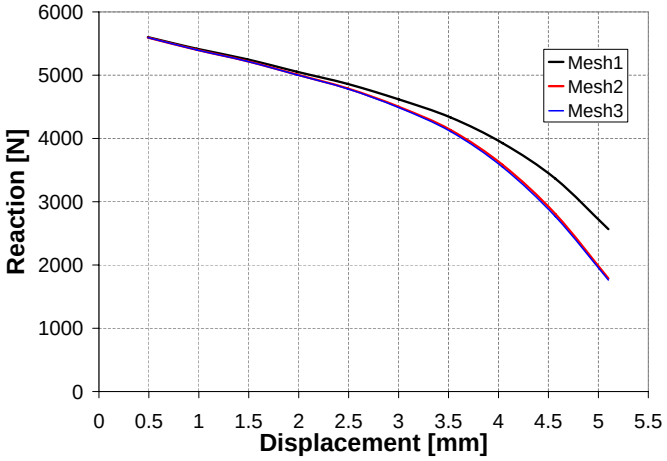

(a) Reactions in the cross section

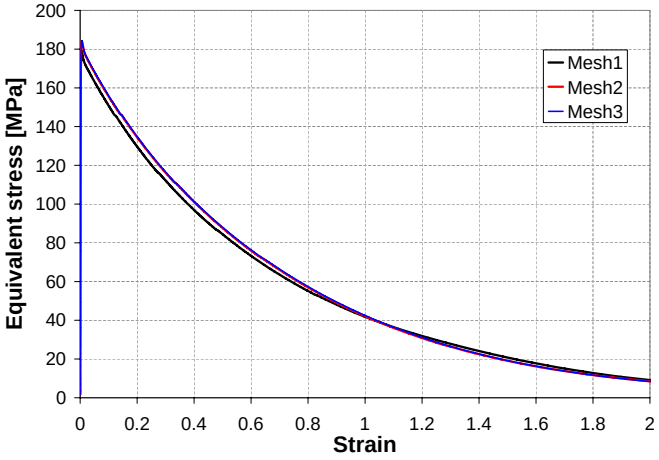

(b) Equivalent stress

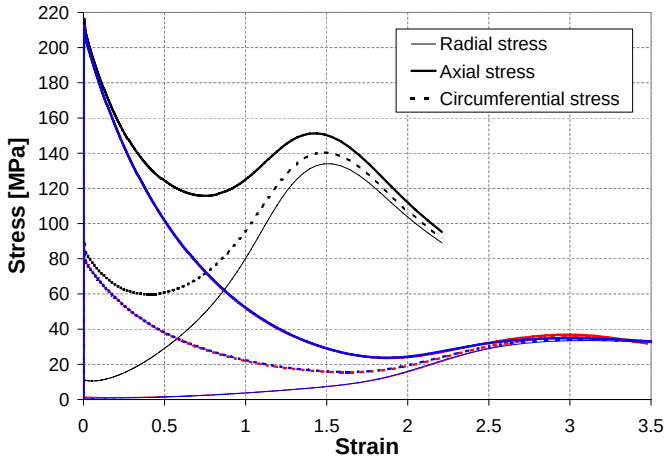

(c) Stress-Strain curves

Figure 3.36: Flow curves for sample meshing comparison of HTT numerical simulation with black lines representing MESH1, red lines, MESH2 and blue lines, MESH3

3.3 Representative cell design

3.3.1 Macroscopic level - grain design

The design of the cell is based on a micrography of an austenitic steel grade which was provided by the industrial partners (Figure 2.5). It is representative of the peritectic grade studied here. On this micrography the grain size has been approximated to 200μm.

The size of the cell (Figure 2.4(a)) is calculated in order to have more or less 100 grains in the center cell (Figure 2.4(b)). So, with an approximative calculation the dimensions are the following ones:

$$\begin{aligned} \text{Cell} &= \text{2x2mm} \\ \text{Cell + transition zone} &= \text{20x20mm} \end{aligned}$$

In order to draw the inner cell with representative grain shape, the grains from the micrography Figure 2.5 have been drawn on a sheet of paper and extended to the wanted size of the 2x2mm cell. The method used to draw the cell was a manual one. Indeed, the grain size is almost the same for each steel grade studied and so, the same cell is used for each grade. Hence, each point has been localized with its coordinates and the grains and grain boundaries have been designed one by one as explained in Section 2.1.4.

3.4 Conclusion on the rheology and damage tests chapter

The determination of the rheological parameters had to be started with the study of the right thermal path to apply to the sample in order to reproduce the best way the industrial problematic and to obtain a comparable steel microstructure. Having the thermal path, the low ductility area of each steel grade is determined by HTT at various temperatures. This study permitted to know in which temperature range the cracks are expected and to focus on it. The locations of the ductility troughs is explained with the precipitation formation at the equilibrium and the phase transformation curves.

After the study of the temperature range in which the damage occurs, the rheology is determined by making HTT on three different temperatures and three different strain rates. The Norton-Hoff elasto-visco-plastic law parameters where set for each steel grade studied.

The test campaign for the determination of the damage law parameters is determined by choosing the studied sample geometries, the test strain rates and temperatures in order to obtain different stress-strain histories for the mesoscopic application. The experimental tests have been driven at the IEHK in Aachen and have been compared to the numerical simulation results of the same HTT modeled with Lagamine and the previously determined rheological law parameters.

Finally, the basic representative cell design is explained.

Chapter 4

Damage model identification, damage parameter analysis

In Chapter 3 the macroscopic point of view has been exposed. The rheology of the peritectic steel has been determined and the representative cell designed. The present chapter describes the damage parameter identification that constitutes the mesoscopic part of this study.

The first part of this chapter is dedicated to the analysis of the crack initiation location in tensile test samples. The stress-strain history at this particular location yields to rupture and is required to identify the damage law parameters.

In the second step, the parameters of the damage law are analyzed to determine their sensitivity: what is the effect of a relative variation of each parameter?

The third part explains the determination of the damage parameters and presents the results obtained for each grade studied.

4.1 Tensile test sample to representative cell

4.1.1 General view of the representative cell position in the tensile test sample

In the first trials of S. Castagne, displacements were imposed in the three directions as the simulations usually have a better convergence when the loadings are imposed through displacements only. Although the correct equivalent stress was applied to the mesoscopic cell, it appeared that the stress components distribution was not correct. This is due to the formulation of the elastic-viscous-plastic law, which is given in terms of equivalent stress and strain. Indeed, different stress components distributions can correspond to the same equivalent stress. The cell loading should thus be studied and the data transfer from the macroscopic tensile test to the mesoscopic representative cell has to be mastered.

During the data transfer, the objective is to reproduce in the mesoscopic cell the stress-strain field recorded at the critical point of the parent macroscopic simulation.

The representative cell will then be subjected to forces and/or displacements. In her previous work, Sylvie Castagne demonstrated that the best way to load the representative cell is to apply forces in y and z directions and a displacement in x direction corresponding to those extracted from a compression simulation of the macroscopic sample as showed in Figure 4.1. This loading pattern has been especially chosen in order to be as accurate as possible by imposing the forces in the two directions where the stresses are the largest. The experimental tests Sylvie used to adjust the damage parameters were compression tests. The axial and circumferential stresses are applied in form of forces in y and z directions respectively. The displacement in x direction is deduced from the radial displacement. In this case, the loading pattern rules are respected. Indeed, the crack initiates along the grain boundaries perpendicularly to the maximum principal stress. During the compression tests, this stress corresponds to the circumferential stress σ_θ. At the critical point where the crack is initiated in compression, the radial stress σ_r is equal to zero as well as the shear stress $\tau_{r\theta}$. They were not taken into account during the data transfer.

In the case of this study, the tests performed to adjust the parameters are tensile tests. This first loading pattern has been tested on the representative cell with results coming from the notch root of the simulation of a hot tensile test. In conclusion, applying the loading history in tension is not the best strategy to get the correct results, as the stress field in the transition zone of the representative cell was not in agreement with the one in the macroscopic tensile test.

In tension tests, as observed in different test simulations, the highest values of stress component is found in the axial direction σ_{zz} (Figure 4.2). The crack is supposed to appear in the notch root perpendicularly to the axial macroscopic direction as observed by during experimental tests. The cell should then be placed in the following way (Figure 4.2):

- x_{micro} → radial direction of the tensile specimen (σ_{rr})
- y_{micro} → axial direction of the tensile specimen (σ_{zz})
- z_{micro} → circumferential direction of the tensile specimen ($\sigma_{\theta\theta}$)

The loadings should apply to the cell the forces coming from the highest stress component of the tensile test. Thus, in the y_{micro} direction the highest stress σ_{zz} is applied. Both other stresses are equivalent at the beginning of the simulation so it has been chosen that a force is applied in the x_{micro} direction (σ_{rr}) and a displacement in the z_{micro} direction ($\sigma_{\theta\theta}$).

This rule has been chosen independently on the fact that after a little deformation, the circumferential stress increases and becomes larger than the radial stress. Knowing this fact, the second force should have been placed in the z_{micro} direction and the displacement in the y_{micro} direction. Historically, the first tests have been performed on sample without notches, so that $\sigma_{rr} = \sigma_{\theta\theta} \approx 0$. However, the results (stress-strain field in the transition zone = stress-strain history of the chosen material point in macro tensile sample) provided by this loading pattern are satisfying and exploited in the rest of this study in order to determine the damage law parameters.

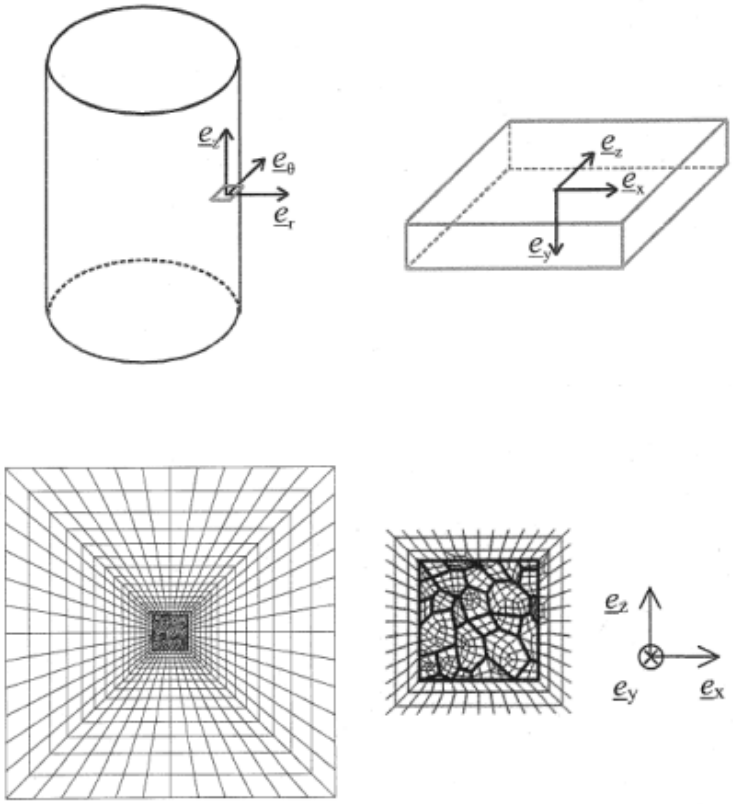

Figure 4.1: Orientation of the microscopic cell with regard to the macroscopic models and view of the representative cell within the transition area as S. Castagne did [Cas07a]

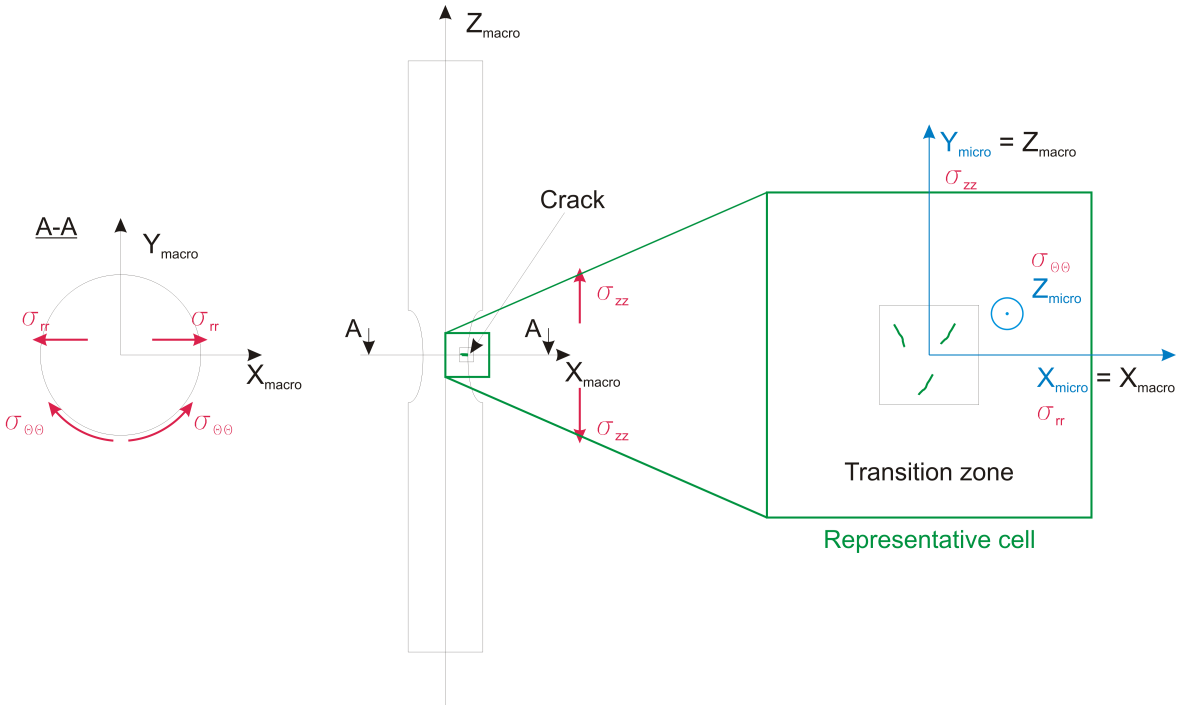

Figure 4.2: Reference system of the macroscopic simulation and transfer to the representative cell

4.1.2 Determination of the location of the numerical stress-strain sampling

At the beginning of this study the location where the numerical stress-strain values had to be considered was not clear. Indeed, the stress triaxiality field shows that in the central part of the sample, the triaxialities are more elevated than at the circumference of the sample. With this result one could chose the material point within the center part as it could be assumed that the maximum of triaxiality induces the maximum damage. Nevertheless, this section presents the results obtained comparing root and core records of the hot tensile test simulation. It has been found that this assumption had to be verified because the maximum principal stress is situated at the notch root and could also generate high damage as seen hereafter.

The stress-strain field has been observed in the core and at the notch root of the same simulation (sample shape R2, strain rate $10^{-2}s^{-1}$, temperature 850°C, law parameters **A** divided into core and root results, Figure 4.3). The rheological law parameters used at this moment were not the last ones fitted but the results of the performed simulations gives a good view of the stresses present in the sample during hot tensile test.

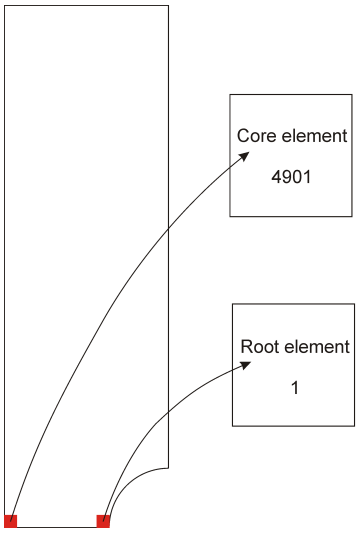

Figure 4.3: Location of the two stress-strain fields recorded in a representation of the R2 notched tensile test sample

Tensile test simulation results

The results of the tensile test simulation on a R2 notched sample show that in general all the stresses components are larger at the notch root than in the sample core as one can observe in Figure 4.4(a). In both cases (core and root), the shear stress is negligible. In the center of the samples, the radial and circumferential stresses are equal (circumference = 0mm on the symmetry axis of the sample).

Looking at the triaxialities (Figure 4.4(b)) in the tensile test sample, the root element presents a short-time more elevated triaxiality than in the core. However, this tendency is quickly reversed and the triaxiality in the core becomes much higher than

at the root, as deformation is going on.

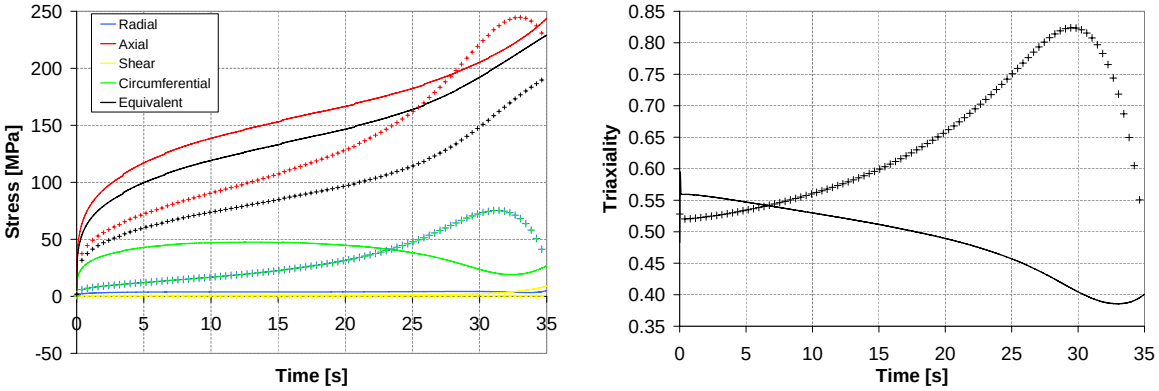

(a) Flow curves

(b) Triaxiality values

Figure 4.4: R2, 850°C, $10^{-2}s^{-1}$ tensile test simulation results at the root (-) and in the core (+) of the sample

In this observation lays the ambiguity of the location selection of the reference material point history providing highest damage. Its macroscopic stress-strain history will feed the mesoscopic representative cell. To avoid making a bad choice, both root and core stress-strain fields are applied on the representative cell through forces and displacements and the mesoscopic and macroscopic stress fields are compared as well as the damage field generated by those.

Representative cell results

Applying the two different loading (the first one in the tensile sample's center and the second on the notch root), the flow curves are analyzed. The figures representing the different stresses as a function of equivalent strain (Figures 4.5) clearly show that the stresses in the inner par of the sample are much larger than those in the root for a same strain. This has to be connected to the fact that the sample is less deformed in the center part of the sample.

In Figure 4.6(a) it can be observed that the equivalent strain at the notch root is larger than in the sample's core at a same moment of the simulation. This induces that a higher stress level will be reached at the notch root of the sample at a given displacement even if for the same strain the stress is higher in the core as seen in Figures 4.5. Indeed, the leading parameter for the tensile test simulation in this study is the time. Looking at Figure 4.6(b), it is possible to observe that the damage grows faster at the notch root than in the center part of the tensile test sample for the same set of parameters.

Thus, the damage, in the case of this study, has to be related to the high stress and strain levels and so, the data that have to be recorded from the hot tensile test have to be situated at the notch root in order to be able to observe the very first crack appearing in the structure of the test sample.

It has also been demonstrated (Section 3.2.1) that the histories obtained with both sample shapes (R2 and R4) are different and will be helpful for the identification of

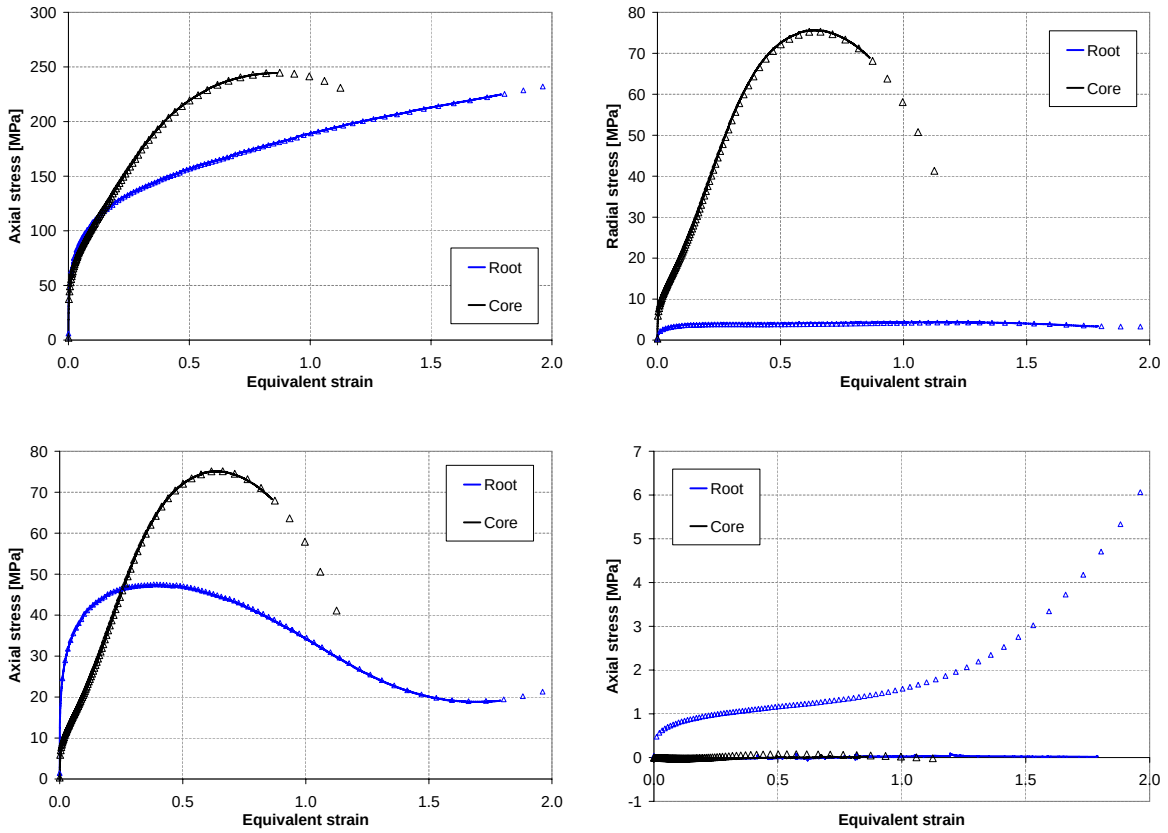

Figure 4.5: Stresses from the R2, 850°C, $10^{-2}s^{-1}$ tensile test simulation (Δ) at the root and in the core of the sample compared to the results obtained by loading the representative cell (-) with the tensile test simulation records

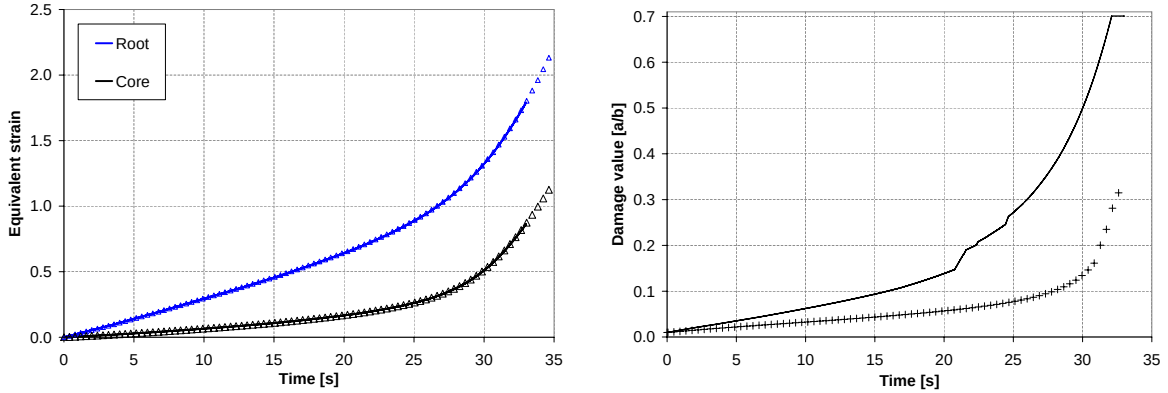

(a) Equivalent strain with Δ for the tensile test simulation and - for the representative cell results

(b) Damage value with - for the root and + for the core results

Figure 4.6: R2 Tensile test simulation results at the root and in the core of the sample

the damage parameters.

4.1.3 Calculations performed for the representative cell loading

In order to prepare the Macro-Meso data transfer from the macroscopic numerical simulation to the particular 20x20mm mesoscopic cell (Figure 4.7), some parameters are recorded during the numerical calculation and compiled in a test file used to load the representative cell.

The several steps of this work are the following:

- The initial position in x and y directions of the 4 nodes of the studied element (element 1 as written at **line 14**) are recorded for a further use (**line 17 to 26**).
- Every 5 time steps, the current x and y positions of the 4 nodes are recorded (**line 28 to 36**).
- The strain field is the element is calculated following Equation 4.1 (**line 38 and 39**) for the calculation of the radial strain, Equation 4.2 (**line 40 and 41**) for the circumferential strain and Equation 4.3 (**line 42**) for the axial strain.

$$\varepsilon_{radial} = \frac{1}{2}\left[log\left(\frac{X_{t,3} - X_{t,4}}{X_{i,3} - X_{i,4}}\right) + log\left(\frac{X_{t,2} - X_{t,1}}{X_{i,2} - X_{i,1}}\right)\right] \tag{4.1}$$

$$\varepsilon_{axial} = \frac{1}{2}\left[log\left(\frac{Y_{t,3} - Y_{t,4}}{Y_{i,3} - Y_{i,4}}\right) + log\left(\frac{Y_{t,2} - Y_{t,1}}{Y_{i,2} - Y_{i,1}}\right)\right] \tag{4.2}$$

$$\varepsilon_{circumferential} = log\left(\frac{X_{t,1} + X_{t,2} + X_{t,3} + X_{t,4}}{X_{i,1} + X_{i,2} + X_{i,3} + X_{i,4}}\right) \tag{4.3}$$

  where $X_{t,1}$ represents the position in x direction at time t of the calculation for node 1 (XT1 in the following code), $X_{i,1}$ represents the initial x position (X01 in the following code) and the values beginning by Y represents the positions in y direction for each node of the studied element.

- The corresponding displacement in the representative cell is calculated in function of the cell size (**line 44 to 46**). The representative cell is the same for all the calculations done at the mesoscopic scale. The size of the cell has been discussed in Section 3.3 where it has been set that in x and y directions, the transition zone surrounding the cell is a 20x20mm square and the thickness of it, that enables the plane generalized plane strain measures 1mm (z direction).
- *.dep file that represents the imposed displacements during the calculation is prepared. The time where the displacement is imposed is written in an *.F77 output file and the displacement in the z direction (DTZ) of the generalized plane strain previously calculated is added for each time step calculated (**line 48 and 49**).

- *.loa file where the forces to impose to the calculation is prepared in an *.F74 output file (**line 51 to 69**). This part can be separated into 6 parts depending on the nodes driven by force (4.4). Difference is made between directions and node position (edge or corner).

$$\mathrm{F}_{\mathrm{direction}} = \frac{\mathrm{Surface}}{\mathrm{Number\ of\ edge\ divisions}} \cdot \sigma_{\mathrm{direction}} \tag{4.4}$$

line 52 to 54: Calculation of the F_y forces (Equation 4.5) to impose on the upper corner nodes of the cell in y direction (nodes 506 and 507).

line 55 to 57: Calculation of the F_y forces (Equation 4.6) to impose on the upper edge nodes of the cell in y direction (nodes 1098 to 1116).

$$F_{y,corner} = \frac{\mathrm{DTX} \cdot \mathrm{DTZ}}{40} \cdot \sigma_{yy} \quad (4.5) \qquad F_{y,edge} = \frac{\mathrm{DTX} \cdot \mathrm{DTZ}}{20} \cdot \sigma_{yy} \quad (4.6)$$

line 58 to 60: Calculation of the F_y forces ($-F_{y,corner}$ of Equation 4.5) to impose on the lower corner nodes of the cell in y direction (nodes 504 and 505).

line 61 to 63: Calculation of the F_y forces ($-F_{y,edge}$ of Equation 4.6) to impose on the lower edge nodes of the cell in y direction (nodes 1060 to 1078).

line 64 to 66: Calculation of the F_x forces (Equation 4.7) to impose on the right corner nodes of the cell in x direction (nodes 505 and 506).

line 67 to 69: Calculation of the F_x forces (Equation 4.8) to impose on the upper edge nodes of the cell in x direction (nodes 1079 to 1097).

$$F_{x,corner} = \frac{\mathrm{DTY} \cdot \mathrm{DTZ}}{40} \cdot \sigma_{xx} \quad (4.7) \qquad F_{x,edge} = \frac{\mathrm{DTY} \cdot \mathrm{DTZ}}{20} \cdot \sigma_{xx} \quad (4.8)$$

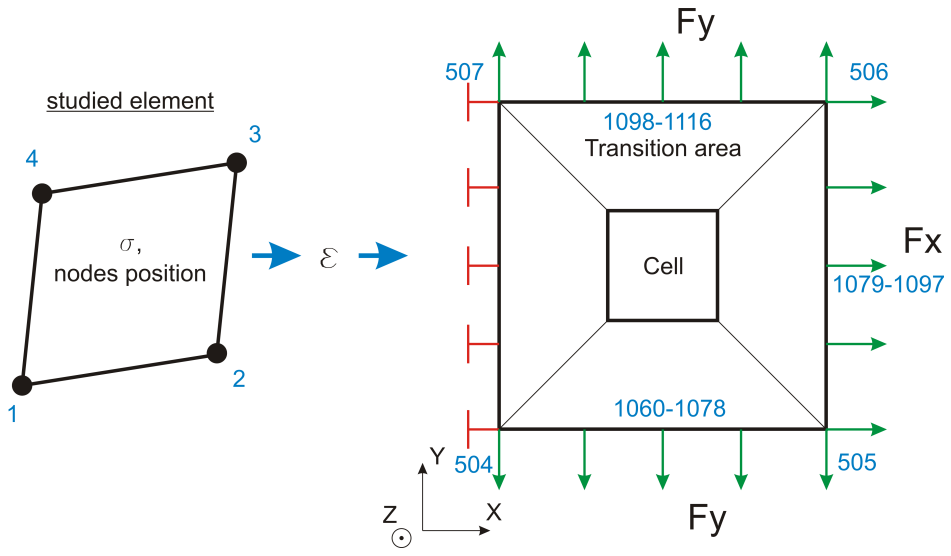

Figure 4.7: Nodes of the representative cell edges for the loading through *.loa file

```
C=====================================================================
C
C      SCHWARTZ IDENT 67xx (TREBELVERSUCH _ TRACTION IEHK)
C                            AUG 06 - JAN 10
C
C             Modeling of the hot tensile test performed at
C                      the University of Aachen - RWTH
C
C        Calculations in order to prepare the *.loa (*.F74)
C        and *.dep (*.F77) files used for the mesoscopic simulation
C
C=====================================================================

       if (IELEM==1 .AND. IDENT==6714) then
C        Remember the values of the initial coordinates of the first element's node
C        used for the further calculations of the deformation of the element
         if (ISTEP==1) then
           XI(1) = CONEC(NODES(4),1,1)
           XI(2) = CONEC(NODES(1),1,1)
           XI(3) = CONEC(NODES(2),1,1)
           XI(4) = CONEC(NODES(3),1,1)
           YI(1) = CONEC(NODES(4),2,1)
           YI(2) = CONEC(NODES(1),2,1)
           YI(3) = CONEC(NODES(2),2,1)
           YI(4) = CONEC(NODES(3),2,1)
         endif

         if (MOD(ISTEP,5)==0) then
           XT1 = CONEC(NODES(4),1,1)
           XT2 = CONEC(NODES(1),1,1)
           XT3 = CONEC(NODES(2),1,1)
           XT4 = CONEC(NODES(3),1,1)
           YT1 = CONEC(NODES(4),2,1)
           YT2 = CONEC(NODES(1),2,1)
           YT3 = CONEC(NODES(2),2,1)
           YT4 = CONEC(NODES(3),2,1)

           EPSR = 0.5D0*(DLOG((XT3-XT4)/(XI(3)-XI(4)))
     .            +DLOG((XT2-XT1)/(XI(2)-XI(1))))
           EPSV = 0.5D0*(DLOG((YT3-YT2)/(YI(3)-YI(2)))
     .            +DLOG((YT4-YT1)/(YI(4)-YI(1))))
           EPSC = DLOG((XT1+XT2+XT3+XT4)/(XI(1)+XI(2)+XI(3)+XI(4)))

           DTX = DEXP(EPSR)*20.D0
           DTY = DEXP(EPSV)*20.D0
           DTZ = DEXP(EPSC)*1.D0

           write(74,6705) TIME              ! *.F74 -> *.dep
           write(74,6703) 3141, 1, DTZ

           write(77,6705) TIME              ! *.F77 -> *.loa
           do IncDepCoinY=506,507
             write(77,6704)  IncDepCoinY, 2, DTX*DTZ/40.D0*SIGVA(2)
           enddo
           do IncDepY=1098,1116
             write(77,6704) IncDepY, 2, DTX*DTZ/20.D0*SIGVA(2)
           enddo
           do IncDepCoinYNeg=504,505
             write(77,6704) IncDepCoinYNeg, 2, -DTX*DTZ/40.D0*SIGVA(2)
           enddo
           do IncDepYNeg=1060,1078
             write(77,6704) IncDepYNeg, 2, -DTX*DTZ/20.D0*SIGVA(2)
           enddo
           do IncDepCoinX=505,506
             write(77,6704)  IncDepCoinX, 1, DTY*DTZ/40.D0*SIGVA(1)
           enddo
           do IncDepX=1079,1097
             write(77,6704) IncDepX, 1, DTY*DTZ/20.D0*SIGVA(1)
           enddo
         endif
       endif

```

```
73  6703 format (2(I5),1F20.18)                    ! Format for *.F74 -> *.dep
74  6704 format (2(I5),1F20.15)                    ! Format for *.F77 -> *.loa
75  6705 format (1F9.4)                            ! Format for *.F77 and *.F74 time line
```

4.2 Sensitivity analysis of the damage law parameters

The "sensitivity analysis" consists in determining the sensitivity of the crack appearance to the different parameters of the damage model. This study is done by running numerical simulations on the representative cell always with the same macroscopic history, representative of the same shaped samples and modifying the value of only one damage parameter.

Among the input parameters of the damage law, seven have been studied. The impact of a slight change in these values on the calculations have been studied. One value has been held constant during the whole study: the rupture criterion a/b that is imposed at 0.5. This study has been led first on the parameters determined by Sylvie Castagne in order to understand their effect on the damage. After the parameters have been correctly fitted on each steel grade (Section 4.3), the set of parameters obtained for **C** has been exploited in order to have a current view of the leading parameters of the damage law and their influence on the damage behavior. Only these last results are shown in this chapter.

All the sensitivity analysis is based on the comparison of the effect of several changes of damage law parameters on the damage behavior as a function of a reference set of parameters. The reference values of the damage law parameters are presented in the Table 4.1 in the particular column "Reference values". As announced in the same table, the reference values are modified by increasing or decreasing the reference by 20%. Each case will be tested separately, that produces 15 cases to study. The reference case and the positive and negative variations of the reference values, one by one.

The seven parameters which have been modified are the initial cavity size a_0, the initial distance between cavities b_0, the nucleation parameter F_n, the initial cavity density for appearance of nucleation N_I, the viscosity parameter $\dot{\varepsilon}_e/\dot{\varepsilon}_B$, the multiplication factor N_{max}/N_I of the threshold of the end of the nucleation N_{max} and the cavity tip angle ψ.

The effect of each parameter is studied through the analysis of their effect on the different steps of the damage curve and especially the instant of the three first crack events has been checked.

	-20%	**Reference values**	**+20%**
a_0 $(\cdot 10^{-5})$	2.4	3	3.6
b_0 $(\cdot 10^{-2})$	4	5	6
F_n $(\cdot 10^{5})$	1.2	1.5	1.8
N_I $(\cdot 10^{2})$	4.8	6	7.2
$\dot{\varepsilon}_e/\dot{\varepsilon}_B$	8	10	12
N_{max}/N_I	32	40	48
ψ	72	90	108

Table 4.1: Values of the reference and modified parameters for the sensitivity analysis

4.2.1 Damage path

In order to understand the acting of the parameters, the different stages of the damage should be understood. The Figure 4.8 describes the common damage path. The curve is divided into different steps that are representative of grain nucleation, growth and coalescence.

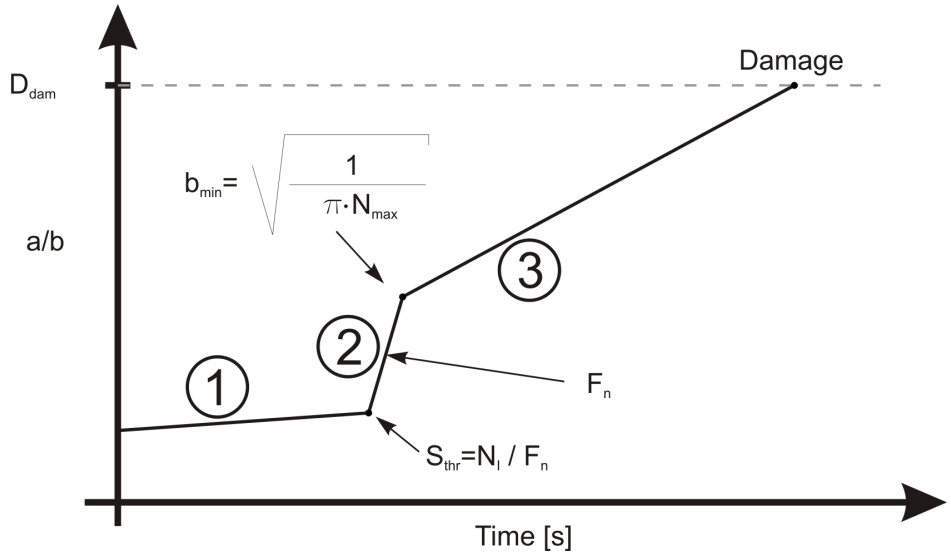

Figure 4.8: Tendency of the damage in the representative cell

Step ①, where the slope of the curve is low, extends to the threshold S_{thr} that is the beginning of the nucleation of cavities. This first step is led by the growth of the cavities, related to the precipitates already present in the studied matrix. Here, the parameters F_n and N_I have a major meaning and lead the junction to the second step, particularly N_I, that is the initial density of cavities needed to nucleate.

Step ② starting from S_{thr} and ending at the following slope change is characterized by a really fast growth of the damage. Indeed, this step describes not only the continuing growth of the cavities but also the germination of new cavities in the matrix that implies the fast decrease of the cavity interdistance b and thus, the increase of a/b.

The speed of the growth only depends on F_n. When F_n is large, the nucleation is easy and the slope becomes steep. In contrary, when F_n is smaller, the slope decreases in intensity.

As soon as the threshold interdistance between cavities b_{min} is reached, the nucleation of new cavities stops and only the growth of the actual ones occurs as characterized by the change of slope from ② to ③ .

The crack event occurs as soon as the ratio a/b, representative of the ratio of damaged material over healthy material reaches the damage threshold called D_{dam}.

As introduced before, the sensitivity analysis is performed in order to identify the critical parameters of the law. Those who have an important part on the damage evolution but also on the crack event. These both phenomenons are studied hereafter.

4.2.2 Analysis of the damage evolution

In order to analyze the various effects of the parameters on damage, figures have been constructed for each parameter variation so that the differences could be well seen on the whole damage curve. A representation of the whole curve is given in the lower right corner. This figure is accompanied by zooms made on the main parts of the initial curve. The main parts are the two slope changes of the damage evolution. The first one around the beginning of the nucleation in the lower left corner, the second around the end of the nucleation in the upper left corner and a last zoom includes the damage moment in the upper right corner. A detailed description is given in Appendix B.

Each parameter influences the damage evolution as observed in Figures 4.9 and 4.10 for F_n and N_I and in Appendix B for the other damage law parameters. The first figure represents the effect of a change by + and - 20% of the nucleation parameter value. It is obvious that the whole nucleation part changes dramatically between the reference value and the two variations. The second figure represents the effect of the variation of the parameter N_I on the damage evolution. Here, from the nucleation start until the damage moment, the curve is impacted by the parameter variation.

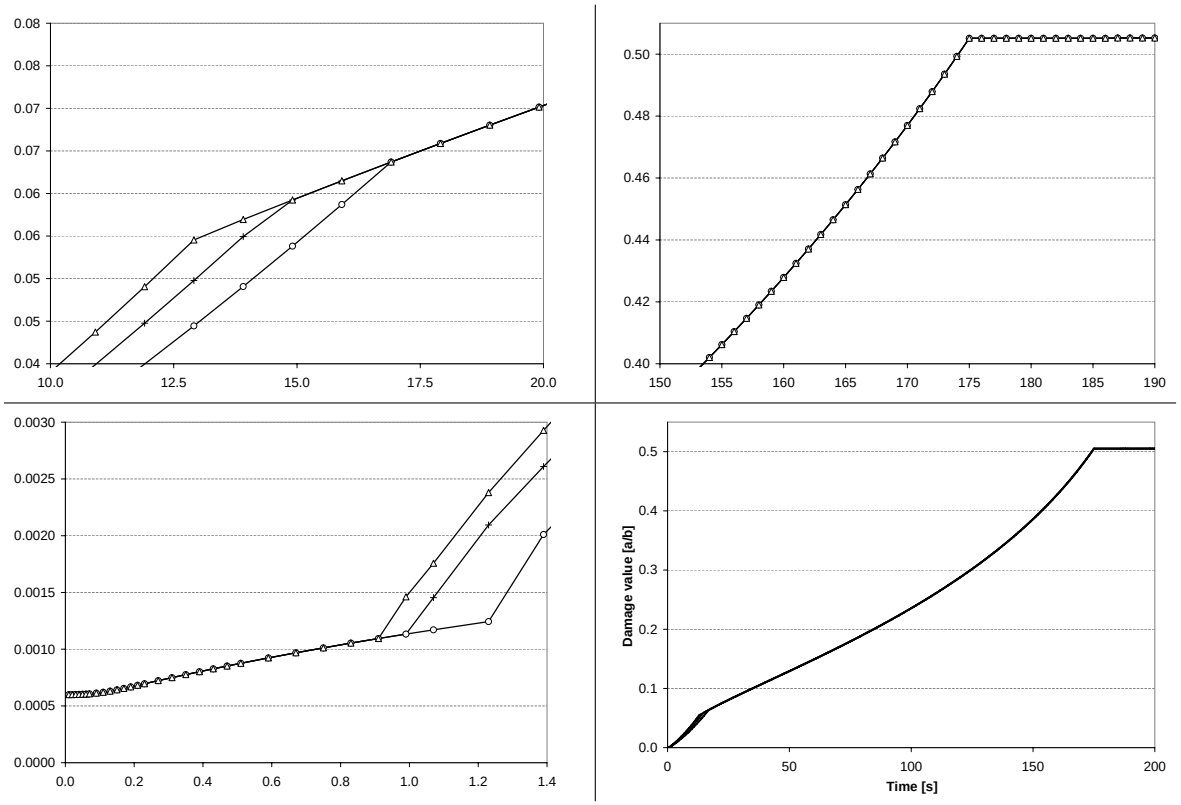

Figure 4.9: Influence of the variation of the parameters F_n on the damage evolution (+ Reference, ∘ Reference - 20% ,Δ Reference + 20%)

In the current study, hot tensile tests provides the stress and strain history until the crack appears. Only this information could be used to identify the damage parameters. On the damage curve, the only indicator will be the damage occurrence. Thus, the

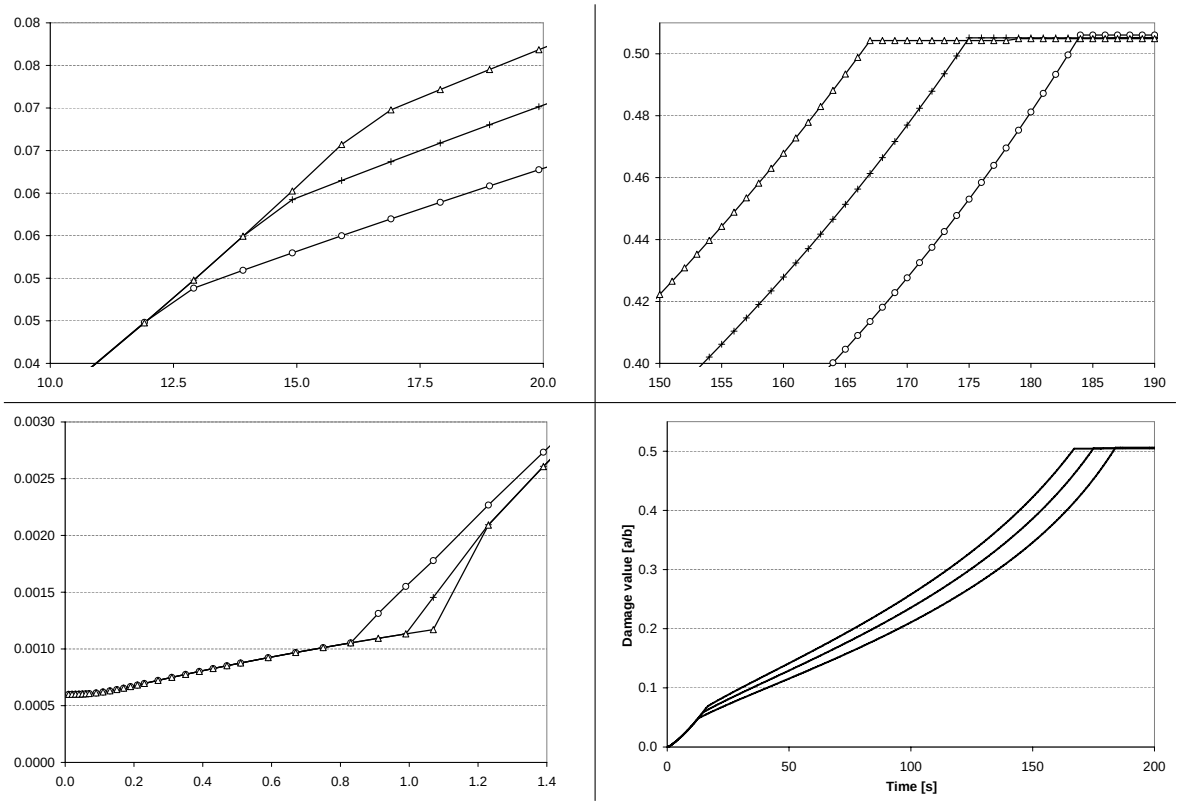

Figure 4.10: Influence of the variation of the parameters N_I on the damage evolution (+ Reference, ∘ Reference - 20% ,Δ Reference + 20%)

identification of the parameters which play a role on the damage moment will be easier to identify and their values will be more accurate. It is hence important to know and to understand the contribution of each parameter to the damage behavior, by analyzing precisely the damage curves obtained by the variation of each damage law parameter. Their respective effect on the damage evolution is explained hereafter.

Effect of a_0

The figure of the effect of a_0 is in Appendix B, Figure B.2. A change in the value of a_0 can be used to define an initial damage that could be different in the several parts of the matrix, between two grains of different structure or simply to insert some weakened zones in the material. It shifts the whole curve whether to higher damages with an augmented value or a lower when decreasing the value of the cavity size. This appears to be logical because when the damage starts on cavities with bigger diameters, the damage will grow from a more elevated value at the start. This small difference between modified values and the reference is kept during the whole evolution. The variation around the reference value do not become greater so the change in this parameter could modify slightly the crack event.

Effect of b_0

b_0 has an effect on the first part of the damage evolution (Figure B.3 in Appendix Appendix B). When the cavities interdistance is smaller it means that there are more precipitates in the matrix. Thus, the initial damage is at a higher level when b_0 is

decreased of 20%. The nucleation start is affected by the variation of this parameter but is fastly covered by the nucleation effect that provides much more cavities. This way, the value of b_0 has not a remarkable effect on the damage moment. It could be interesting to analyze the case where, from the start on, a huge amount of precipitates are present and the nucleation is very low. In this case, the variation of b_0 might have an effect on the end of the damage evolution.

Effect of F_n

F_n, as mentioned before, has a great influence on the nucleation phase of the damage evolution (Figure 4.9). When F_n is increased by 20%, the nucleation is faster and begins earlier. However, when the nucleation is faster, it reaches earlier the threshold of the maximum cavities that could be built in the matrix. So, as it is observable in Figure 4.9 in the zoom on the nucleation end, the damage after this point evolves on exactly the same slope until damage. Thus, the effect on the crack appearance moment is null, except if the damage occurs during nucleation. In this last case, the nucleation variation will have a huge effect on the damage of the material. The parameter F_n could be used in order to specify different nucleation behaviors due to several microstructure changes like gradients of grain size depending on the distance from the surface. In this study, it is tried to produce the damage after the nucleation completly occured. So, this parameter will be very hard to determine and other experimental tests should be designed in order to caracterize this part of the damage evolution.

Effect of N_I

In the damage calculation, N_I stands for the minimum cavity density from which the nucleation can be observed. It is a sort of incubator. If N_I is increased, the nucleation is delayed, then the nucleation takes place, and the end of the nucleation will end later also (Figure 4.10). For a decrease of the value, the damage evolves otherwise. The nucleation start happens earlier and thus, the end of the nucleation occurs before the one of the reference value. This difference at the end of the nucleation step is kept until the damage appears. It means that it is less detrimental for the material to start the nucleation earlier and it could be interesting to think about provoking this nucleation at the wanted moment in order to obtain the desired microstructure according to the duties of the end material. So, the crack appearance is very sensitive to any modification of this parameter and thus, it will be easy to identify it precisely.

Effect of $\dot{\varepsilon}_e/\dot{\varepsilon}_B$

The viscosity, $\dot{\varepsilon}_e/\dot{\varepsilon}_B$, has an influence on the last part of the curve (Appendix B, Figure B.4). Indeed, the viscosity has an important effect only when the stresses are huge enough to generate sliding between two grains. At the beginning of the damage, when the forces are low, the viscosity has no effect on the damage. In this particular case, the effect begins to appear during nucleation. The increase of the viscosity handicaps the grains sliding and thus diminishes the damage caused by this phenomenon. When $\dot{\varepsilon}_e/\dot{\varepsilon}_B$ value is decreased by 20%, the sliding between two grains becomes easier and the damage evolves faster to the threshold. The variation of this parameter induces then different damage moments. In this study, it has been chose to keep this parameter constant, at 10 because the tests performed could not give indications on this phenomenon that is meant to be more related to the steel family

or temperature than to the nucleation of cavities. Different tests should be used to characterize this parameter independently from the others.

Effect of N_{max}/N_I

The variation of the factor N_{max}/N_I in the calculation of N_{max} has exactly the same effect as the modification of the parameter N_I (Appendix B, Figure B.5). N_{max}/N_I has an effect on the end of the nucleation. This means that, with an increase of this value, the nucleation lasts longer. Thus, more cavities are formed, that is more detrimental for the material. The difference with the modification of N_I only lays in the damage evolution part that is affected first. A change in N_I provokes a difference already at the nucleation start where the modification of N_{max}/N_I only appears at the end. Nevertheless, the results obtained are the same because the calculation of the threshold b_{min} that characterizes the end of the nucleation provides the same result. So, the change in both values N_I and N_{max}/N_I could have a huge impact on the damage evolution and these parameters have to be determined precisely.

Effect of ψ

The parameter ψ is used in the calculation of the evolution of the cavity size a. Thus, is has an effect on the whole damage evolution (Appendix B, Figure B.6). For a value 20% over the reference, a evolves slower and thus, the damage value is also lowered and the crack appears significantly after the reference crack. The effect of this last analyzed parameter is present during the whole damage process and thus, the difference between reference and variations becomes always bigger and bigger until the crack appears. In this particular case, the effect of ψ is more important than the one of N_I. That means that the microstructure and especially the precipitates shape is of highest importance for the damage evolution. When the precipitates present a platelet shape with sharp angles, the damage will grow faster than with cuboid or big round precipitates. The damage could then be lowered according to the needed material, with controlled precipitates appearance and shape.

4.2.3 Analysis of the crack event

The moments of the appearance of the three first cracks were also recorded and the diagram of the first cracking grain boundaries has been drawn on one figure (Figure 4.11) in order to compare the effect of the damage law parameters on the moment of the damage. As explained before, this moment of damage will be the reference for the damage law parameters fitting of this study by comparing the numerically to the experimentally obtained ones.

On Figure 4.11, it is possible to see clearly which parameter variation has an effect on the damage moment.

Parameters a_0, b_0 and F_n have no effect on the moment where the damage reaches the threshold D_{dam}. This is not really relevant for the two first parameters because they will be determined through micrographic study of the precipitates and set to these values. For F_n, this means that the precise determination of this parameter will be more difficult than the following ones. Indeed, the only criterion that could be imposed to F_n is that the damage happens after the nucleation has finished.

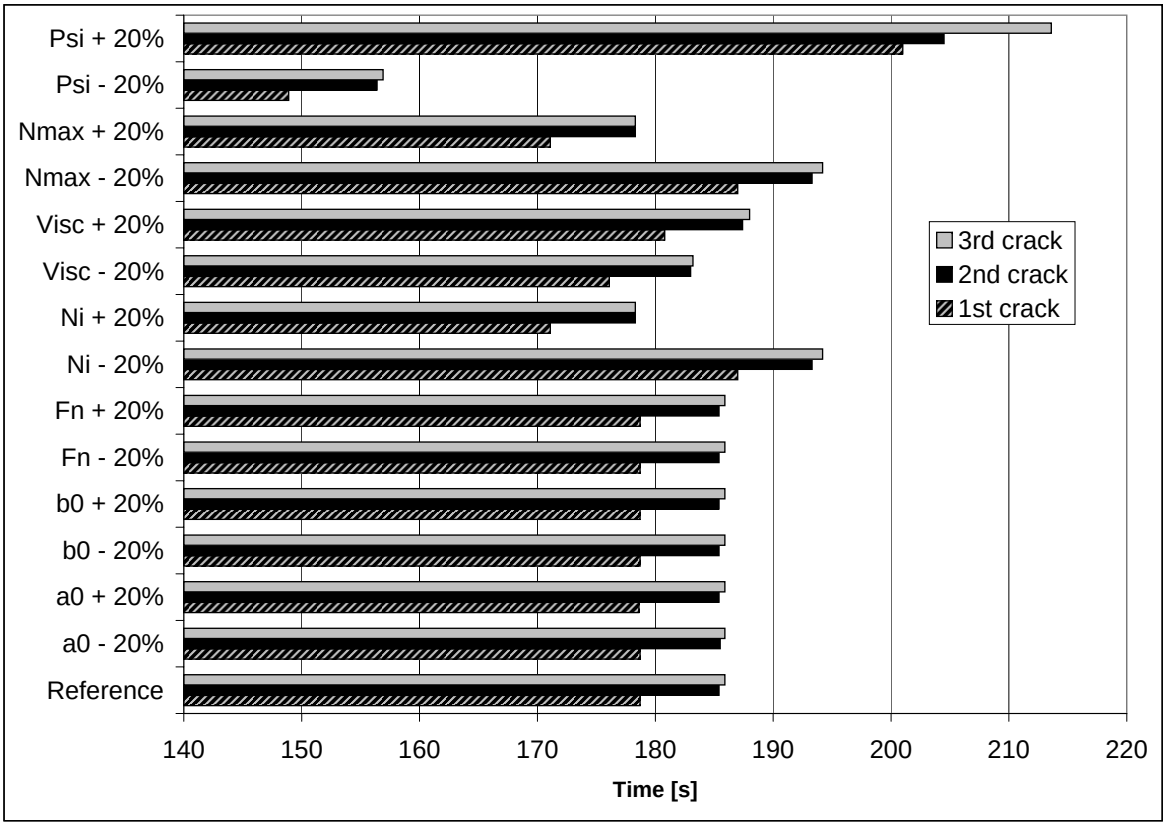

Figure 4.11: Three first crack appearances for the variation of different parameters

As already observed, N_I and N_{max}/N_I produces the same modification on the damage evolution and thus on the three first cracks recorded. Their effects are clearly marked and their determinations will thus be easier than the one of F_n.

The change of the viscosity parameter has also a slight effect on the damage moment but as mentioned before, this value will be set as a constant during the whole study. Nevertheless, the influence of this parameter should not be neglected and further studies should be performed in order to determine this parameter for the studied steel grades.

The parameter, which variation shows the hugest effect in this case is ψ. This parameter will be determined as a_0 and b_0 through micrographic analyzes. Thus, the angle of the cavities in the law will be directly related to the observation of the precipitates shape. This parameter could be used as an indicator of the presence of several types of precipitates with different shapes and thus, different severity on the damage of the matrix.

Some fundamental parameters of the used damage model were analyzed with other reference parameters published in [Sch07] and the analysis gives the same kind of answers. How the model reacts to each parameter was studied. It has been seen in Section 2.1 that a_0 and b_0 are the guiding parameters and also thresholds for the damage. As soon as the ratio a/b reaches the value of 0.5, a crack can appear in the structure and the grains are separating from each other. In fact all the parameters described in the Table 2.1 are relevant for the calculation of the damage. It is hence important to notice that the determination of all these parameters has to be done in the best way in order to get the most accurate values for these parameters. Some parameters are easier to

determine than others but all the parameters have their own role to play in the damage evolution. Of course, not only the damage law parameters presented before have an impact on the damage but the variation of the damage moment can also be shifted to other values according to the needs and the experimental appropriateness of the numerical simulations.

4.3 Damage law parameters fitting for peritectic steel grades

The Table 2.1 of Section 2.1.3.3 gives the list of all the parameters required within the damage law of the LAGAMINE code. Some of them are taken from the literature, others determined through microscopic analyses or calculated as a function of the rheological law determined before, and a few are left and have to be fitted using hot tensile tests in various conditions. The goal of this study is to find one sole set of parameters for each steel grade, describing the material behavior during damage.

4.3.1 Parameters taken from the literature

In the damage law, one parameter is a material constant: Ω, the atomic volume of the compound studied has been taken from literature. The general atomic volume of steel is chosen, $\Omega = 1.21 \cdot 10^{-20}\text{mm}^3$, even if it could be slightly different according to the alloying elements added and the primary production process used.

Other parameter values, like the grain viscosity ratio between core and grain boundary $\dot{\varepsilon_e}/\dot{\varepsilon_B} = 10$ the boundary diffusivity $D_{b0}\delta_0 = 7.5 \cdot 10^{-5}\text{mm}^3\text{s}^{-1}$ and the activation energy $Q_b = 159 \cdot 10^6$ mJ $\cdot$ mol^{-1} are all taken from Needleman and Rice study [Nee80].

The two last parameters taken from literature are k_n and k_p that are penalty coefficients within the interface element given by Equation 2.2. They impose identical displacement of the crack edges expressed by the nodal displacements and computed by the damage law. These coefficients have been determined by Sylvie Castagne on basic cells. She found k_n and k_p equal to $10^5\text{MPa}\cdot\text{mm}^{-1}$ in her study [Cas07a], so that the stresses in a cell containing damage elements correspond to the ones in a cell free of any damage element.

All these parameters taken from the literature are the same for each steel grade studied. They are relative to the peritectic steel family studied.

4.3.2 Damage law parameters determined on the basis of rheological parameters determination

The parameters determined on the basis of the experimental test used to determine the rheological law are B, n and Σ_0. B, the creep parameter, and n, the creep exponent, are used in the calculation of the grain boundary sliding as explained in Paragraph 2.1.3.2.1. Σ_0, described in Paragraph 2.1.3.2.2, is a temperature dependent constant and is representative of the average stress level in the area surrounding the crack.

Determination of B and n

In equation 2.5, the classical creep law gives B and n as a function of the equivalent stress and the equivalent strain rate. With the parameters deduced from the Norton-Hoff creep law, the parameters B and n could be determined.

The following equation (Equation 4.9) presents the relation between the classical and the Norton-Hoff creep law parameters. The creep coefficient B is determined for a chosen value of the equivalent strain ε_e.

$$B = \frac{1}{\sqrt{3}} \left(\frac{1}{p_2 \sqrt{3}} \right)^{\frac{1}{p_3}} \qquad \text{and} \qquad n = \frac{1}{p_3} \tag{4.9}$$

Determination of Σ_0

The determination of Σ_0 is made visually on the flow curves obtained through HTT. The value is deduced from the tensile test flow curves at the various wanted temperatures, a strain rate of 10^{-3}s^{-1} and a strain equal to 7%. The curves at 900, 1000 and 1100°C are used and the other values are inter- or extrapolated on the basis of the three values visually determined.

Results

As explained in the macroscopic study, the rheological parameters for **A** and **C** are the same as they are taken from the same experimental tests.

Temperature [°C]	**A**			**B**		
	B	n	Σ_0 [MPa]	B	n	Σ_0 [MPa]
900	$5.29 \cdot 10^{-22}$	9.25	53	$2.81 \cdot 10^{-25}$	10.53	59
1000	$1.38 \cdot 10^{-16}$	7.31	35	$3.84 \cdot 10^{-23}$	10.55	40
1100	$1.64 \cdot 10^{-9}$	4.19	19	$1.95 \cdot 10^{-21}$	10.56	30

Table 4.2: Values of the parameters B, n and Σ_0 of the damage law

4.3.3 Parameters determined through micrographic analysis

The first parameter that has to be fitted is the primary austenite grain size. This diameter has been determined in the macroscopic study presented in Section 3.3 in order to design the representative cell. The diameter of the grains has been determined by optical microscopy and set to 200μm.

The other parameters a_0, b_0 and ψ are related to the microscopic state. In Section 2.1, the law is said to be led by cavity growth. In the industrial case, the precipitates are meant to cause damage.

Indeed, as explained in Section 1.4.4.2, the damage is caused by the precipitates around which cavities are growing. Assuming that matrix precipitate decohesion yields to void, the initial cavity size needed will be connected to the precipitates size found in the steel matrix. In the same way, the cavity interdistance will be associated to the precipitates interdistance and the cavity angle can be found through the precipitates shape.

The following parameters are determined through microscopic study with SEM and TEM apparatus: a_0, the initial cavity size; b_0, the interdistance between cavities; ψ, the cavity angle.

The precipitation state has been observed on the slab coming from the continuous caster with the help of SEM/EDS (Energy Dispersive Spectrometry) analysis. This analysis allows knowing the size and distribution of the precipitates in the steel grades observed under the industrial CC conditions.

4.3.3.1 SEM study on A steel grade

Sampling and preparation

In order to perform the SEM/EDS analysis, one sample has been taken in the studied area of the CC slab described in Section 3.1.1.2, where the thermal and mechanical constraints lead to transversal cracking. A cube sample from grade **A**, with a very restricted size (max. 1x1x1cm) is needed. The sample is embedded in a Bakelite sample holder and it is polished mechanically as explained in Appendix C where the micrographic results of the SEM analysis are available.

Results

The micrographs of the precipitates detected in the studied sample are shown in Appendix C. Three types of results for the same scanned area are given.

- The first is the secondary electron micrography where a 3D picture is given. Indeed, the secondary electron is a low energy electron that comes from the surface of the sample. It reveals the surface composition and its topography.

- The second figure associated to the studied area is the backscattered electron which is representative of a deeper area of the sample. The high energy electrons enter the matrix and show the composition differences of the steel. Heavier atoms could be visualized thanks this method.

- The last type of electrons studied are the X photons that have a characteristic energy representing each layer of an atom.

These three pieces of information enable the determination of the steel microstructure and the composition of the steel and the precipitates.

In order to quantify more in details the results, a ZAF quantification is performed as presented in Table 4.3. The ZAF analysis enables the correct quantification of the weight concentration of an element (only the matrix for this study) in the sample.

EDS ZAF quantification is a defined algorithm which gives an estimation of the content of an element right from the area under the related peak appearing on X rays spectrum. EDS ZAF quantification leads to rough values of the chemical composition. An overestimation of carbon content is always done in those calculations. Though values obtained for other elements are then underestimated, the results can show possible segregations on the sample.

Region	Related spectrum in Appendix C	C (% - wt)	Si (% - wt)	Mn (% - wt)	Fe (% - wt)
6	Figure C.31	2.31	0.40	2.28	95.01
6 dark gray	Figure C.34	2.57	0.51	1.96	94.96
6 light gray	Figure C.35	2.55	0.47	2.34	94.64
7	Figure C.41	2.44	0.50	1.72	95.34
Average		2.47±0.12	0.47±0.05	2.08±0.29	94.99±0.29

Table 4.3: Results of ZAF quantification on matrix

In this study, the ZAF quantification has been used to compare chemical analyses from one zone to another one of the given sample and the results are compiled in the following table (Table 4.3).

Observations and conclusions

The ZAF quantification shows no difference between the different areas of the steel matrix. It is homogeneous around the precipitates.

The conclusion that could be made from the results shown in Appendix C is that most of the inclusions found are of CaS globular type (Calcium sulphur) with a maximum size around 5μm. These sulphurs are often associated with oxides (Alumina or complex Ti) found in the vicinity of a specific CaS inclusion that seems to be related to an embedded nitride.

Further work

The precipitates involved in the damage phenomenon are mostly carbonitrides types. These precipitates are very small and thus have not been observed in the current study. In-depth analyses are needed for the exact observation of the precipitates and the quantification of their size and distribution.

The carbonitrides researched are known to have a maximum diameter of approximately 50nm. Furthermore (V, Nb, Ti)(C,N) are mostly located at grain boundaries. The observation of these boundaries could not be performed during the SEM study because the specified etching was not efficient on those. Nevertheless, during the following micrographic studies, the grain boundary observation continues to be done.

The appropriate tool to study small precipitates is TEM, where higher magnifications are expected. 40 000 times on TEM could allow the identification of (V, Nb, Ti)(C,N) precipitates.

4.3.3.2 TEM study on the peritectic steel grades studied

The goal of the following microscopic work is to characterize the precipitation state and in particular to observe the precipitation behavior of the alloying elements known to be detrimental for the peritectic steel family studied in this thesis. The elements observed are Nb and V in particular. Other alloying elements are added to this study in order to observe the potential combinations with other elements and to observe their the effect on the damage. The samples for this study are taken in a same configuration

for all the steel grades studied.

Thus it has been chosen to perform the microscopic analyses on the center part of the tensile test samples that have undergone the following thermal and mechanical path described in Table 4.4.

	Shape	Temperature [°C]	Strain rate [s^{-1}]
grade **A**	R2	950	$5 \cdot 10^{-3}$
grade **B**	R0	900	$1 \cdot 10^{-3}$
grade **C**	R0	900	$1 \cdot 10^{-3}$

Table 4.4: Sample configurations for microscopic analysis

The precipitation state found during the test is supposed to be the one at equilibrium because the thermal treatment during the testing period let to the precipitates the time to develop. Moreover, the samples are not quenched after the tests.

A better view of the precipitates for this study could have been to take the sample just after the primary thermal path and just before the tensile test. The quenched specimen would have shown the precipitation state needed in order to adjust certain parameters of the damage law.

Unfortunately, this study could not have been performed because the primary thermal path tests should have been performed again and the samples quenched. The time and the money were not enough for this study and it has been tried to use tested samples in the same configuration. The other reason for this, is that the steel state reached after quenching did not permit the observation of precipitates in TEM analysis for the first attempt.

It can be noticed that grade **A** is not coming from the same test case than **B** and **C**. Indeed the test on this grade were performed before the two others and thus, because of a budget question, the TEM observation on the sample coming from the same test configuration has not been performed. Nevertheless the results seem to be consistent with the ones of the two other steel grades.

The precipitates observed were situated in the steel matrix (Figure 4.14) when they were expected at the former austenite grain boundary (Figure 4.13). Nevertheless, a few precipitates strings has been observed at a grain boundary for grade **B** (Figure 4.12). The statistically analyzed precipitates are those found in the steel matrix as their number were more representative.

For grade **B**, the precipitates are strongly present because of their heavy contrast and their frequency as shown in Figure 4.14. The precipitates seem to be bigger than those seen in the **C** picture. Nevertheless the contrast of these precipitates is also very good and thus are relatively easy to check.

On the contrary, the precipitate distribution is not clear in grade **A**. At some places darker dots are observable and were used for the calculation of the mean precipitates diameter and the surface fraction of those.

The results are shown in the following table (Table 4.5) where it can be seen that **A** and **C** present almost the same precipitates configuration at the equilibrium.

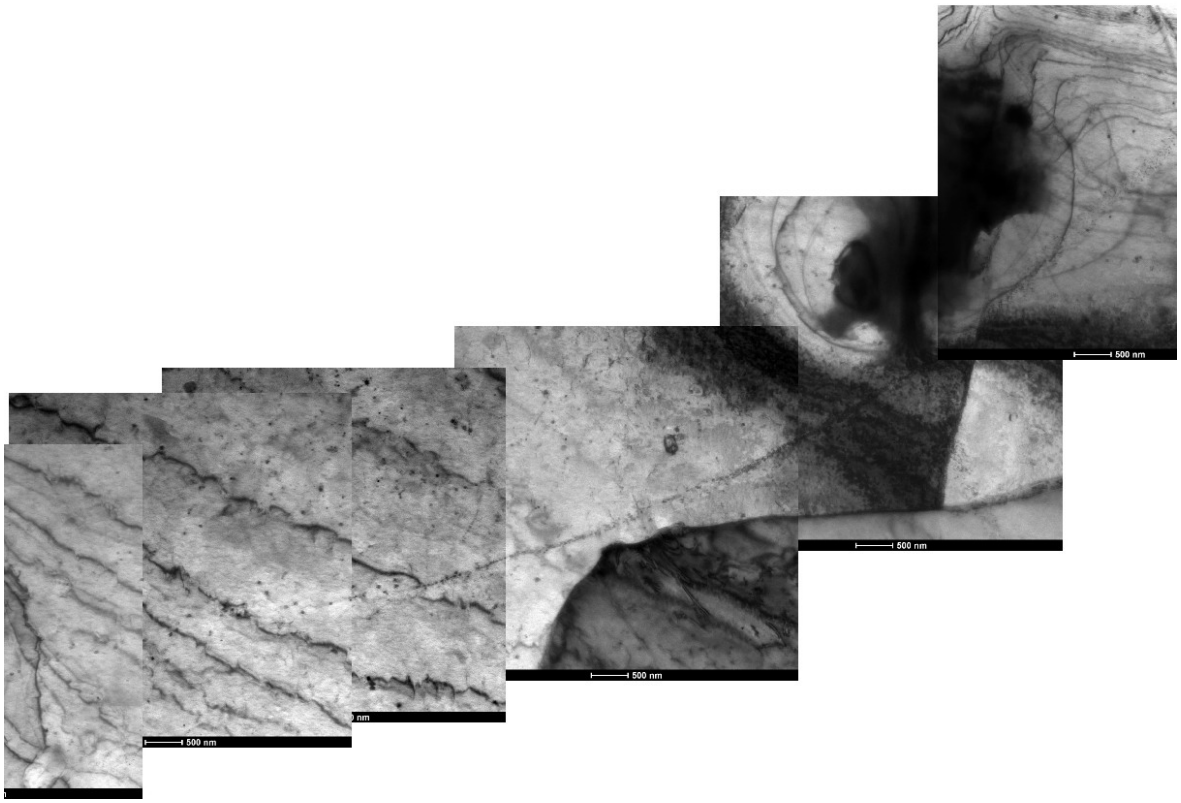

Figure 4.12: Precipitates string obtained for grade **B** through TEM observation

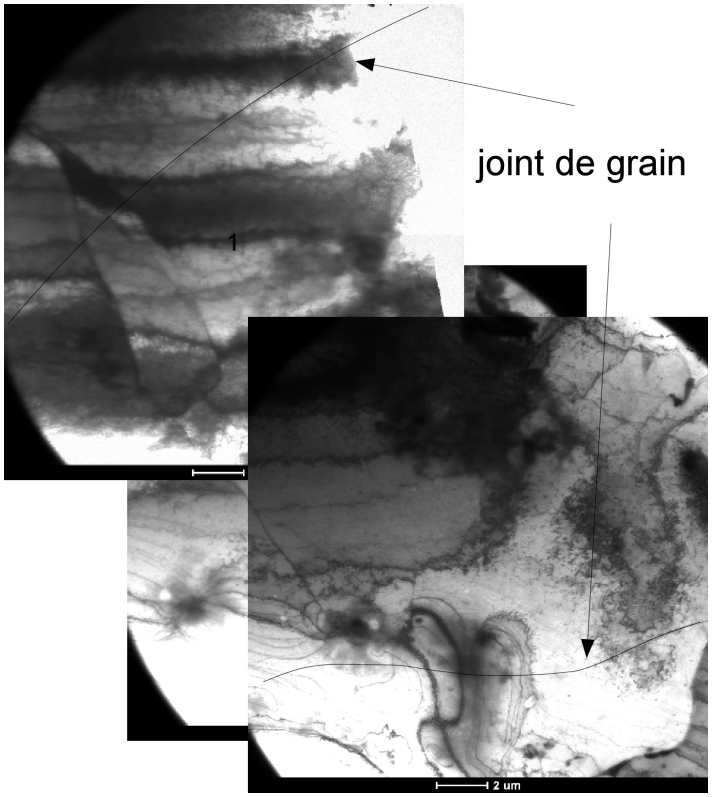

Figure 4.13: Grain boundary observed on the TEM micrographs of **B** grade

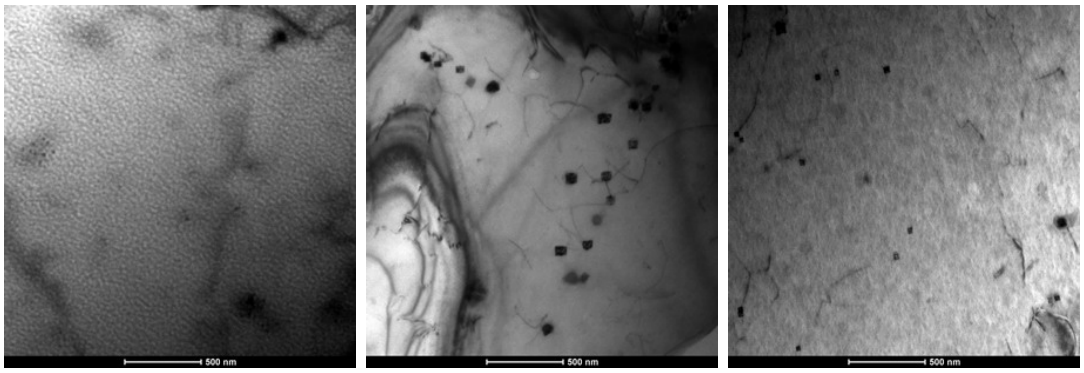

(a) **A** (b) **B** (c) **C**

Figure 4.14: Pictures obtained by TEM for grades **A**, **B** and **C** with an enlargement of 19.000x

	Precipitates mean diameter [nm]	Surface fraction of precipitates [%]
grade **A**	30	0.059
grade **B**	50	1
grade **C**	30	0.06

Table 4.5: Results of the microscopic TEM analysis

The results of Table 4.5 are an approximation of the precipitates mean diameter for each steel grade studied. The mean diameter has been determined through the analysis of more than 10 grains randomly chosen for each steel grade and more than 100 precipitates. For each graph, the TEM images have been analyzed with an image analysis software in order to obtain a mean precipitate area. Considering in first approximation that the precipitates are spherical, a mean diameter was derived from the measurement of the precipitate area and reported Table 4.5. The mean diameter could be directly related to the initial precipitates size, a_0.

Also the surface fraction of precipitates is given. The surface covered by the precipitates has been divided by the surface of matrix of each steel sample. This value permits a first approximation of the initial interdistance between various precipitates, b_0.

The last value that has been extracted from the TEM study is the precipitates tip angle ψ. As it has been observed, the precipitates present a cuboid form. Thus, for all the steel grades studied, the value of ψ has to be set to 45°.

For the steel grades **A** and **C**, both values of the precipitates diameter and the surface fraction are close. Indeed, the composition of both steels is more or less equivalent in regard to the Nb content.

B presents coarser precipitates and a huger surface fraction of precipitates. This is consistent following the Nb content. This grade presents 5 to 6 times more Nb than **A** or **C**.

These differences in surface fraction of precipitates will lead to differences in the b_0 value that is deduced from the first approximation. Some calculations and hypothesis are needed in order to determine the cavity interdistance b_0. These are explained hereafter.

Calculation of b_0

On the basis of the primary austenite grain size determined before (d=200μm), the precipitates size (50nm for **B** grade) and the proportion of precipitates in matrix estimated with TEM images (1% for **B**) the interdistance can be estimated by making an important hypothesis on the precipitates position in order to simplify the calculation. The precipitates are supposed to be randomly distributed on the grain boundary even if it is obviously not the case. Indeed, it has been shown in Section 1.6 that the precipitates on which this study is focused could be found under colony form on the grain boundaries. Nevertheless, it has not been shown in the current TEM study as the concentration of precipitates is not elevated.

By considering one grain, it is possible to calculate the grain boundary size (GB).

$$GB = \pi \cdot d = 628\mu m \tag{4.10}$$

If 1% of the grain boundary is covered with cavities, one grain is surrounded by 6.283185μm cavities and the number of cavities could be deduced from this value divided by the precipitates size: 126 cavities are present on one grain boundary.

At the end, by dividing the grain boundary size by the number of cavities present, the approximative interdistance of the precipitates is calculated. For the example of **B** grade, the value of b_0 is 5μm.

This first approximation on b_0 is sufficient for the determination because this parameter has been shown to have a low influence on the damage prediction as previously observed in Figure 4.11. Moreover, as observed on the micrographs (Figure4.12), when the precipitates are situated on the grain boundary, they are not distributed randomly but in colonies. This means that this parameter should be adjusted in function of some parameters that have to be determined by further micrographic analyzes. The variability of b_0 in function of the grain boundary observed could be taken into account by giving different values to each boundary in the Lagamine code.

The other steel grades cavity interdistance has been calculated the same way.

Values of the parameters a_0, b_0 and ψ

As explained before, the parameter a_0 and ψ[1] are directly linked to the precipitation size and shape found in the micrographic TEM analysis. Parameter b_0 has been calculated as presented before and the values of the parameters that will be used for the various steel grades studied coming from these observations and calculations are given in Table 4.6.

[1]The value of the tip angle ψ used throughout the calculations and applications of this study is 90°. This is due to the misinterpretation of Figure 2.3. ψ has been misinterpreted as the whole tip angle instead of 2ψ.

	a_0 [nm]	b_0 [μm]	ψ [°]
grade **A**	30	50	45
grade **B**	50	5	45
grade **C**	30	50	45

Table 4.6: Values of the damage law parameters a_0, b_0 and ψ determined by TEM analysis

The parameters based on this micrographic study are especially the precipitate size a_0 and their interdistance b_0. One should think about adjusting these parameters according to the kinetic of the precipitation of each component of the steel as a function of the temperature and the time for a future work.

4.3.3.3 STEM study on B and C steel grades

Further STEM (Scanning Transmission Electron Microscopy) analyzes have been performed on **B** and **C** steel grades.

This analysis consists in focusing on one precipitate in order to determine the chemical components present on this particular spot. The elements tested were the one expected to be present in the steel matrix studied. These elements are Nb, Ti, V, C and other as presented in Figure 4.15.

These analyzes on **B** grade showed that the observed precipitates in the steel matrix mainly contains Nb (Nb-K, Nb-L), C (C-K) and Ti (Ti-K, Ti-L). The spot where high contrast differences are visible on the pictures of Table 4.15 is representative of the presence of this element on the specific precipitate place. This precipitate is probably gathered as TiNb(C,N), formed at the equilibrium. No V and no Mn could have been found as presented in the table hereunder.

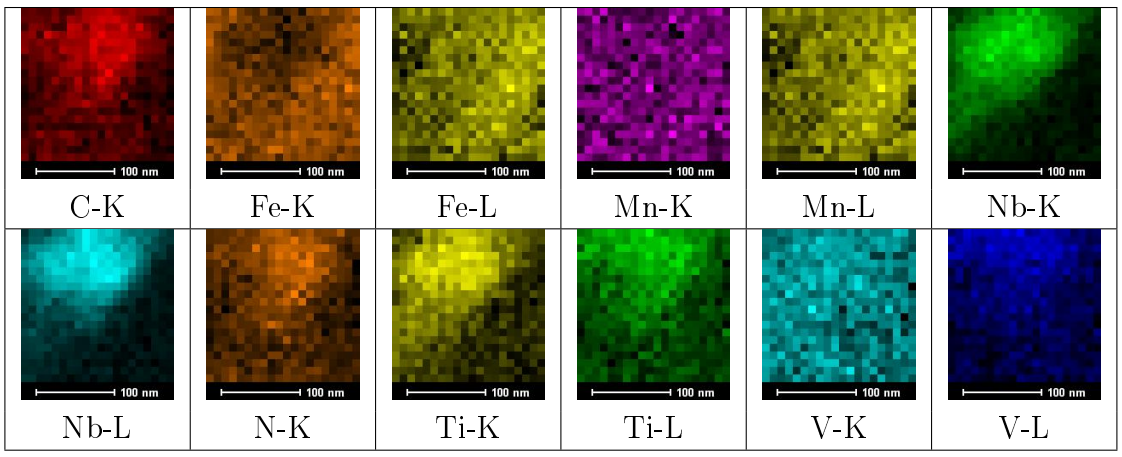

Figure 4.15: STEM analysis of different **B** steel components on a precipitate

From the analysis of one precipitate of grade **C** in Table 4.7 it is possible to observe that the Fe component is the most present. Indeed, the matrix around the precipitate is taken into account in these results. By comparing these results to the one of **B**, it is possible to observe in Table 4.15 that Fe is located in the right lower part as the precipitate is situated in the left upper corner. Thus, the last one is meant to be the precipitate, where the other part is the steel matrix containing Fe.

The other components present are Nb, C, Ti, Mn and V in a decreasing order of atomic percentage. Mn was not a component expected to be in the precipitate. By comparing with **B** results, even if the color contrast is not high and knowing this last result, it could be distinguished that Mn-L and Mn-K seems to be located in the matrix as Fe.

Element	Weight [%]	Atomic [%]	Uncert. [%]
C(K)	0.42	1.97	0.83
Ti(K)	0.57	0.66	0.35
V(K)	0.25	0.28	0.37
Mn(K)	0.58	0.59	0.41
Fe(K)	93.50	93.67	2.27
Nb(K)	4.65	2.80	1.57

Table 4.7: Quantification results of STEM analysis on one **C** precipitate

At the end, Nb, C and Ti are present in important percentage and on the micrographs clearly situated on one particular spot that is expected to be the precipitate on which the study has been performed. The atomic percentage confirms the presence of these three components when the precipitate is focused.

Concerning V, the concentration is not very high and on the micrographs it is not possible to determine the position of this component even if **B** grade has been chosen for this study because of its highest V concentration. It could be interesting to continue this study by focusing the tests on several precipitates in order to characterize a representative number of those.

Unfortunately this STEM analysis does not exclude the Al presence, as this component has not been registered. This could have been interesting to do because of the potential detrimental effect of Al.

4.3.4 Parameters adjustment

This part of the study consists in **Step D** of the methodology (Figure 2.12 in Section 2.2.4). Indeed, the goal is to load the representative cell containing damage elements with the stresses and the strains obtained through different HTT and to compare both force-displacement curves. Finally, the loading parameters of the cell should be adjusted so that the difference between both, mesoscopic and macroscopic stress-strain-time curves becomes small enough and the damage law parameters should be identified so that the rupture of the cell happens as good as possible at the same time than in the experimental condition.

The parameters of the damage law that have to be determined through correlation of numerical simulation results with experimental tests are listed hereunder and have been described in Section 2.1.

- F_n : Nucleation parameter
- N_I : Initial cavity density for nucleation

- N_{max}/N_I : Multiplication factor of N_I to determine N_{max}, the maximum cavity density

- D_{dam} (a/b ratio) : Rupture criterion

The fitting of the damage parameters has to start from a reference point. Thus, the initial parameters values were extracted from Sylvie Castagne's study on low alloyed steels (Table 4.8).

F_n [mm^{-2}]	$0.169 \cdot 10^5$
N_I [mm^{-2}]	$1.273 \cdot 10^4$
N_{max}/N_I	40
D_{dam}	0.7

Table 4.8: Initial values of the adjustable parameters of the damage law used to predict fracture extracted from [Cas07a]

4.3.4.1 Fitting of the damage parameters

The fitting of the damage parameters is based on a manual inverse method. The parameters of the law will be changed until the numerical damage fits the experimental one. By manipulating one parameter after the other, they can be set for one case and then extended to the others by a sharper adjustment of these parameters.

Thus, with the help of HTT the parameters will be adapted to the case of damage in tension under high temperature. Indeed, the transverse cracks appear almost always in the unbending area. In this area tension is present in the inner curve of the slab. The temperature of this area is situated more or less between 800 and 1000°C (Figure 2.19 for grade **C**) where the material undergoes a loss of ductility. This weakness is caused by the decohesion between the matrix and precipitates due to precipitation of some special alloying elements as Nb or V under carbo-nitrides form. These precipitates are the one expected to cause transversal cracking in peritectic steels under CC conditions.

The HTT tests have been performed and, depending on the steel grade, different set of HTT are available as shown in Section 3.2. 8 tests are available for grade **A**, 7 for **B** and 9 for grade **C**. The initial reference case is chosen arbitrarily throughout the available HTT tests. The damage parameters are first adjusted on this case and then, thanks to all the HTT cases, the parameters are adjusted a second time in order to fit to all the experimental tests available, the best way.

As explained before, the damage variable a/b should reach its threshold (crack prediction) when the experimental crack happens. This is not feasible exactly for all HTT cases chosen. Thus, the chosen parameter set should yields to predict cracks in the best way for all the cases. In order to have a global view on the results and the way they fit the experimental observation, they are compiled in Table 4.9 and the different columns are explained hereafter.

Case	Real strain rate	Experimental displacement	Numerical displacement	Difference	Relative difference

Table 4.9: Structure of the damage parameters accuracy by numerical crack prediction and experimental observation comparison

Column **Case** contains, strain rate, notch size, temperature, and steel grade. A single designation has been found for each case studied to describe all these parameters. It contains all the case information and is described in Figure 4.16.

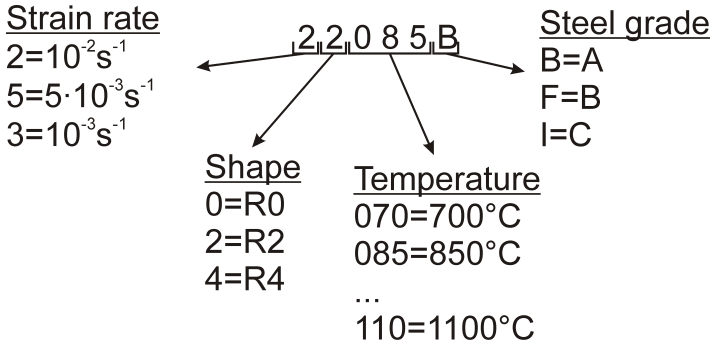

Figure 4.16: Detailed designation of the testing cases studied

The second column of the comparison table between numerical and experimental damage moments is the **Real strain rate**. This column is necessary because the HTT have not been performed with the expected strain rate. The fact that the strain rate applied is not the one asked for, is not of high relevance. Indeed, the tensile test simulation is the same as the experimental one in terms of sample displacement as the one applied to the simulation has been taken from the experiment. However, it yields to different strain rates between tests that were assumed identical. This column gives an indication of the strain rate differences in our study.

The **Experimental displacement** (in [mm]), is the displacement reached by the mobile part of the tensile test machine when crack happens. It is recorded during the experimental test. The simulated and experimental initial sample length being identical, the experimental and numerical displacement should define identical value.

The experimental damage moment has been chosen by analyzing the Load- Displacement curves obtained by HTT. For some curves the recording stopped at the damage moment as it is observable on the experimental curve 22085B of Figure 4.17. In other cases, like for case 22090B of Figure 4.17, the recording continues and a remarkable point has to be chosen. Generally the damage is characterized by a more or less visible inflexion point on the curve. In the last cited case, the damage point has been chosen at the approximately 11mm and materialized by a black dot and a change of curve style.

Numerical displacement also in [mm] represents the displacement of the upper part of the simulated sample at the moment of the appearance of the first crack. That for, the damage parameter has been set to the value of 0.5. This value has been chosen different to the one used at first by Sylvie Castagne. Two reasons for this change are

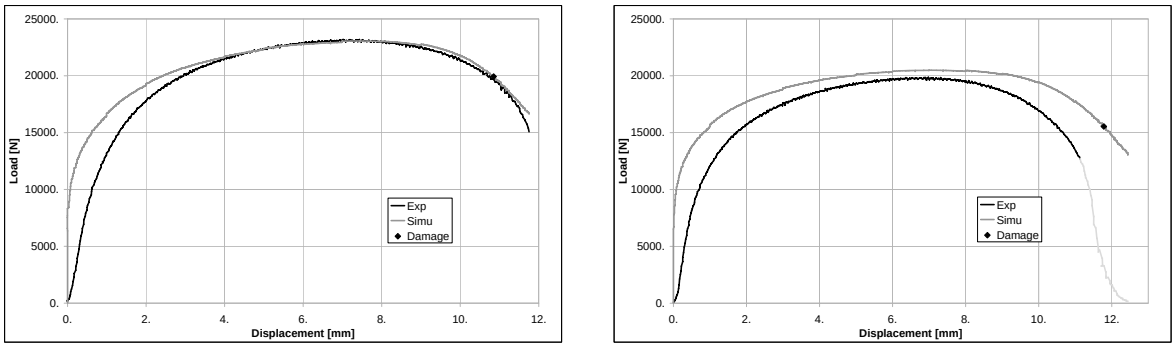

Figure 4.17: Load-Displacement curves obtained for experimental and numerical case 22085B (left) and 22090B (right)

mentioned. The first one is that, at the end of her study, Sylvie Castagne reduced her damage parameter from 0.7 to 0.5 in order to fit with the experimental tests she performed. The second reason is that the first attempts of adjustment showed better behaviors when this value has been set to 0.5. As the damage behavior is the same for each steel grade studied here, it has been chosen to keep D_{dam} constant.

The column **Difference** is a calculation of the variation between the reached experimental and numerical displacements before damage.

As the experimental displacement given in the column *Experimental displacement* is a visually approximated value, it is taken into account for the calculation with an error of $\pm 5\%$. The numerical and experimental **Difference** calculated is the smallest one by taking into account the reading error on the damage moment. It is also the absolute value of the difference so it does not tell whether the numerical or the experimental simulation breaks first.

Last column is called **Relative difference** (in [%]) and is the relative value of the previous column **Difference** in function of the mean experimental displacement recorded. In order to validate the set of parameters, the relative error difference between experimental and numerical damage moment values should be inferior to 20%.

The first criteria is that all the cases are under 20%. If this criteria could not be achieved, the average relative difference over all the cases should be under 20%. Unless, other HTT should be performed in order to validate the first one and then modify the damage law parameters or, in order to add more representative tests for the adjustment.

4.3.4.2 N_I variability as a function of temperature

Making a first attempt of adjustment on **C** steel grade, the damage parameters analysis table (Table 4.10) has been obtained. This table represents the best correlation of the numerical and experimental damage occurrence obtained with the set of parameters presented in Table 4.11.

Observing the different damage displacements, it is possible to see that, according to the temperature, the deviation is occurring the same way. When temperature is low, the numerical damage occurs after the experimental damage as indicated by plus and minus signs. On the contrary, when testing temperature increases, the numerical damage

Case	Real $\dot{\varepsilon}$ [s^{-1}]	Experimental disp. [mm]	Numerical disp. [mm]	Difference [mm]	Relative difference [%]	
32070I	0.0025	8.46	10.70	1.82	21.51	+
52070I	0.014	10.12	12.31	1.68	16.61	+
34070I	0.005	4.53	4.89	0.13	2.87	+
32080I	0.0045	4.99	9.18	3.94	78.99	+
52080I	0.015	8.00	5.58	2.02	25.29	-
32090I	0.0046	6.81	6.73	0.08	1.16	-
52090I	0.015	10.97	8.99	1.44	13.08	-
34090I	0.01	5.97	3.80	1.87	31.29	-
54090I	0.006	4.22	3.00	1.00	23.79	-

Table 4.10: Damage analysis for grade **C** with constant N_I value

F_n [mm^{-2}]	$1.5 \cdot 10^5$
N_I [mm^{-2}]	1200
N_{max}/N_I	40
D_{dam}	0.5

Table 4.11: Values of the adjustable parameters of the damage law for grade **C** with constant N_I value

happens before the experimental one. In the middle case, the numerical damage can occur after or before. This remark allows the assumption that one of the four adjustable parameters is temperature dependent.

Thanks to the sensitivity analysis developed before, it has been demonstrated that among all the adjustable parameters, N_I (initial density of cavities before nucleation start) is a major parameter of the damage law.

Moreover, the density of cavities before nucleation varies with temperature as the nucleation energy in the steel matrix at various temperatures is not the same.

Indeed, at low temperatures, the mechanical energy necessary to built new cavities is higher than at high temperatures where the thermal energy helps the nucleation of new cavities.

Thus, for low temperatures, N_I will show higher values than at high ones.

The methodology followed to determine the last four parameters of the damage law is improved. Indeed, the four parameters will be adjusted on one case as explained earlier. Then the detailed adjustment is done on all the cases available and to end, the parameter N_I is adjusted alone as a function of temperature.

In the following sections, the adjustment of the three different steel grades studied is discussed separately. The first two adjustment steps are not shown but the final parameters and displacement results are given.

4.3.4.3 Damage law parameters fitting on grade A

The final values of the damage parameters of grade **A** are shown in Table 4.12.

F_n [mm^{-2}]	3 ·10^5
N_{max}/N_I	30
D_{dam}	0.5

Temperature [°C]	N_I [mm^{-2}]
850	1100
900	600
950	200

Table 4.12: Values of the adjustable parameters of the damage law for grade **A**

As expected, N_I decreases with increasing temperature. N_{max}/N_I is more or less at the same level as expected by the initial parameters.

The values of F_n and N_I are more or less multiplied and divided respectively by a factor 10 compared to the initial values used (Table 4.8). The threshold S_{thr} is totally different. The parameters for low C steels are not suitable at all for the peritectic steel family description of the damage.

In the following adjustments, the initial guess for the values of the parameters will be the set of parameters of **A** in order to reach faster the best-fitting parameters.

The Table 4.13 shows the convergence of the numerical results compared to the experimental results for all the studied **A** HTT cases validated.

Case	Real $\dot{\varepsilon}$ [s^{-1}]	Experimental disp. [mm]	Numerical disp. [mm]	Difference [mm]	Relative difference [%]
22085B	0.03	11.75	11.00	0.17	1.42
52085B	0.015	9.06	10.49	0.98	10.78
32085B	0.003	9.97	8.79	0.68	6.87
22090B	0.03	11.13	11.34	0.21	1.88
52090B	0.015	11.24	10.87	0.37	3.31
32090B	0.003	9.10	9.26	0.16	1.80
22095B	0.03	12.02	12.64	0.62	5.15
52095B	0.015	11.96	12.01	0.045	0.38

Table 4.13: Damage analysis for grade **A** with the determined damage parameters

In this table, the strain rates achieved during the test present the same proportion as the expected ones. Indeed, the real $\dot{\varepsilon}$ is always three times higher than the one asked for. Thus, the different results could be compared according to the strain rate. Nevertheless, no real tendency of the experimental displacement values until damage could be observed. The values obtained are very close. In regard to the numerical displacement, the damage happens later for high strain rates. Indeed, in the case of peritectic steels, at high $\dot{\varepsilon}$ the material becomes stiffer as the dislocations are present and blocked in the matrix because of the velocity of the test. By low $\dot{\varepsilon}$, the dislocations formed by the deformation of the steel have time to move to critical areas where they can cause damage. No tendency in function of $\dot{\varepsilon}$ could be observed in the absolute and relative difference.

In function of temperature, no real tendency could neither be deduced from the experimental displacements. However, by taking the mean value for each temperature, it is possible that with increasing temperature, the displacement reaches higher values. This is validated by the numerical displacements. This behavior shows that with higher temperatures, the material does not contain many dislocations as the material is more

ductile and could be deformed more. From this point of view, the *Difference* and the *Relative difference* do not give any information about a temperature dependence of the damage law parameters.

In conclusion, the parameters are adjusted the best way. The results for 850°C show the largest difference. This difference can not be adjusted better because the numerical displacement at damage is whether after or before the experimental one. The results obtained are the best adjustment possible at each temperature.

It is possible to observe that the relative differences are in all cases under the 20% target, thus validated.

In order to have a better view on the damage moment difference between experimental and numerical results, the damage moments are materialized on the load-displacement graphs (Appendix F, Table F.1).

Most of the curves are in total adequacy when looking at the experimental and numerical loading curves and the numerical damage moments are close to the experimental ones.

Some curves are particular, such as case 52095B. The loading curves diverges at the end of the simulation but the displacement at damage is nevertheless the same. On this example, the numerical load level at damage is not the one expected through the experimental recording. This point is taken into account even with this difference as the reference has been chosen to be the displacement.

In a further study, such cases could be avoided by taking the two damage moments as a function of both parameters, displacement and loading.

4.3.4.4 Damage law parameters fitting on grade B

The values of the damage parameters of grade **B** are shown in Table 4.14.

F_n $[mm^{-2}]$	$1 \cdot 10^5$
N_{max}/N_I	70
D_{dam}	0.5

Temperature [°C]	N_I $[mm^{-2}]$
750	1000
850	900
950	200

Table 4.14: Values of the adjustable parameters of the damage law for grade **B**

The differences between the damage parameters of **B** and **A** do not rest on N_I parameter. Indeed, they are almost in the same range. But looking at F_n and N_{max}/N_I, it can be seen that F_n is drastically reduced and N_{max}/N_I increased. These parameters tend to lengthen the time before damage and thus, the displacement.

Table 4.15 shows the convergence of the numerical results compared to the experimental results.

In this case, the strain rate is not always equal to three times the expected one but stays though very close. Thus, in this case again, the tendencies according to this parameter could be observed. As for **A**, the experimental displacement do not show any tendency as observed in the numerical results. In the case 32075F, the displacement reached is very high with respect to the other ones obtained. This value could

Case	Real $\dot{\varepsilon}$ $[s^{-1}]$	Experimental disp. [mm]	Numerical disp. [mm]	Difference [mm]	Relative difference [%]
52075F	0.014	9.22	11.75	2.07	22.44
32075F	0.003	18.36	10.04	7.40	40.30
22085F	0.03	10.31	10.31	0.00	0.01
52085F	0.014	10.22	9.50	0.20	2.00
32085F	0.003	7.97	7.24	0.33	4.11
22095F	0.03	12.79	10.05	2.10	16.40
52095F	0.017	8.93	9.33	0.05	0.51

Table 4.15: Damage analysis for grade **B** with the determined damage parameters

be wrong. However, the experimental and numerical loading curves (Table F.2) are equivalent, so the results have been taken into account and the high *Relative difference* is representative of this exceptional value and has to be fitted like all the others. For the temperature dependence of the parameters, also no relation could be drawn.

In the cases of **B**, the rule of the 20% could not have been respected for 2 cases, both at 750°C. In this case, again, the values could not be ajusted better. Indeed, in one case the simulated damage time is after the experimental one and in another case it is the inverse. For all the other cases, the results are acceptable. Especially at 850°C where the relative difference never exceeds 5%. Thus, the average relative difference is equal to 12% that is under 20%.

Here again, the damage moments can be compared on the load displacement graphs (Appendix F, Table F.2). The curves obtained for **B** are in very good adequacy in each case. Nevertheless differences between the experimental and numerical damages are clearly visible. As said before, the loading level should also be taken into account for the adjustment of the damage parameters.

4.3.4.5 Damage law parameters fitting on grade C

The values of the damage parameters of grade **C** are shown in Table 4.16.

F_n $[mm^{-2}]$	$1.5 \cdot 10^5$
N_{max}/N_I	40
D_{dam}	0.5

Temperature [°C]	N_I $[mm^{-2}]$
700	1900
800	1700
900	600

Table 4.16: Values of the adjustable parameters of the damage law for grade **C**

Clearly, for **C**, the N_I values are higher than those of **A** or **B**. The nucleation step is therefore delayed. This could be due to the lower amount of additional compounds in this grade as explained in Section 4.3.5 where the differences of parameters are compared according to the steel grades.

F_n is more or less equivalent to the one of **B** and N_{max}/N_I to the one of **A**.

The convergence of the numerical and experimental results for the displacement until damage is shown in Table 4.17 hereafter.

Case	Real $\dot{\varepsilon}$ $[s^{-1}]$	Experimental disp. [mm]	Numerical disp. [mm]	Difference [mm]	Relative difference [%]
32070I	0.0025	8.46	11.12	1.24	14.64
52070I	0.014	10.12	11.56	0.93	9.18
34070I	0.005	4.53	4.41	0.11	2.42
32080I	0.0045	4.99	8.40	3.16	63.39
52080I	0.015	8.00	5.22	2.38	29.77
32090I	0.0046	6.81	8.49	1.34	19.63
52090I	0.015	10.97	10.40	0.02	0.16
34090I	0.01	5.97	4.35	1.32	22.14
54090I	0.006	4.22	3.57	0.44	10.34

Table 4.17: Damage analysis for grade **C** with the determined damage parameters

More comparable cases are available for **C**. Especially, tests on R4 sample shapes have been validated for the adjustment.

The real strain rate here can not be taken into account and all the same $\dot{\varepsilon}$ configurations should be observed separately. Thus, even with the same temperature configuration, the numerical results could not be compared as the strain imposed to the numerical calculation comes from the experimental recordings. The results are not coherent in function of what could be expected as explained in the study of **A** results.

No general trend could be observed but, at 800°C, the relative difference between numerical and experimental damage is very high. Though, all the results are calculated together and give a global value of 19% that is under the 20% threshold imposed.

In order to have a better view on the damage moment difference between experimental and numerical results, the damage moments are materialized on the force-displacement graphs (Appendix F, Table F.3).

Like for **B**, the comparison of the experimental and numerical curves of **C** is better. The divergence of the damage moments is clearly visible on the graphs at 800°C: one numerical crack occur before the experimental crack (52080I) and the other after (32080I). Therefore, no further adjustment could be done in order to decrease the values of the relative difference that is very high for these both damages.

4.3.5 Comparison of the damage law parameters

All the parameters of the damage law determined before have a physical meaning in regard of the microstructure of the different steel grades. The damage law is driven by parameters that represent the microstructure as a and b, respectively the cavity size and interdistance, and by parameters translating the evolution of the microstructure that are the last parameters fitted (F_n, N_I and N_{max}/N_I).

The last step of the validation of these parameters is thus to compare their value for the different steel grades and to make the correlation with the microscopic state of the steel grades studied. Table 4.18 contains all the fitted parameters for all peritectic steel grades studied.

N_I parameter that is temperature dependent is given in a separate table (Table

	A	**B**	**C**
F_n $[mm^{-2}]$	$300 \cdot 10^3$	$100 \cdot 10^3$	$150 \cdot 10^3$
N_I $[mm^{-2}]$	f(T)	f(T)	f(T)
N_{max}/N_I	30	70	40
D_{dam}	0.5	0.5	0.5

Table 4.18: Comparison of the fitted damage parameters for all steel grades studied

4.19).

Temperature [°C]	**A**	**B**	**C**
700	*1150*	*1050*	**1900**
750	*1100*	**1000**	1850
800	*1050*	950	**1700**
850	**1000**	**900**	1150
900	**600**	550	**600**
950	**200**	**200**	*575*
1000	*150*	*150*	*550*
1050	*125*	*125*	*525*
1100	*100*	*100*	*500*

Table 4.19: Comparison of particular temperature dependent N_I parameter (**adjusted**; *extrapolated*; interpolated)

Also the composition is recalled in a concise form (Table 4.20).

Steel grade	C	Ti	N	V	Nb	Al
Grade **A**	1748	151	54	60	139	313
Grade **B**	576	163	45	20	668	396
Grade **C**	1790	37	58	1	161	403

Table 4.20: Concise composition of the studied peritectic steel grades (in ppm) for the damage law parameters study

In order to understand the effect of each parameter, the damage curves are drawn for a same configuration (32085 for each steel grade) and the different slopes could be analyzed (Figure 4.18).

In Figure 4.18(a), that is the zoom on the beginning of the damage curve, the long nucleation of **B** clearly appears. Even if the slope is not as steep as for **A** or **C** due to the lower value of the F_n parameter, the nucleation lasts much longer for **B** than for the two others, due to the high value of N_{max}/N_I.

It is also possible to see that **B** begins with a higher value of damage due to the different values of a_0 and b_0 determined by TEM microscopy. Indeed, **B** contains larger precipitates and a much greater amount of those in its matrix, so the damage is more elevated at the beginning of the simulation.

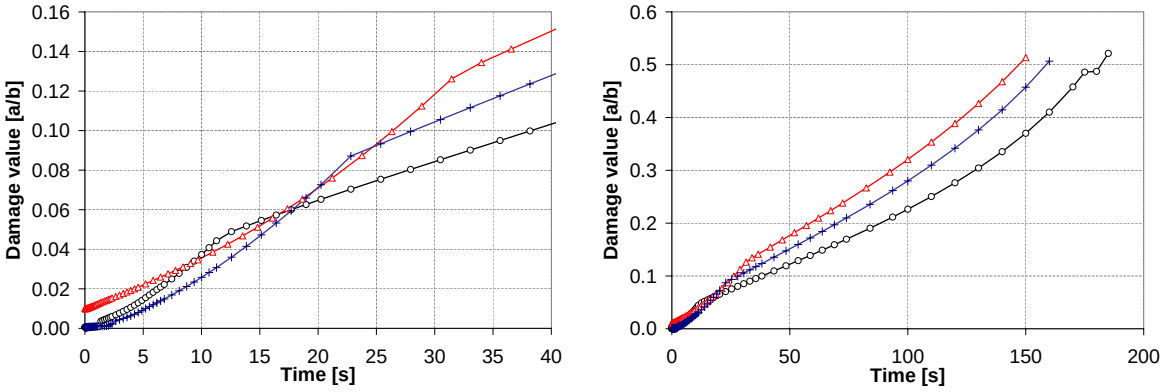

(a) Enlargement of the beginning of the damage

(b) Whole damage path

Figure 4.18: Damage path for a test in the same case (32085 with ∘ for **A**, Δ for **B** and + for **C**) using the several damage parameter adjusted

Comparing the beginning of the **C** and **A** curves, **A** damage grows faster but the end of the nucleation appears earlier. Indeed, **C** has a lower value of F_n that slows down the nucleation and a higher N_{max}/N_I that lengthen it, as for **B**. Thus, in a less pronounced way, it behaves like this one. The nucleation of **C** is a little bit slower but it lasts longer than **A**.

For all the steel grades, step ① of the damage curve could not be seen. This is due to the low value of S_{thr}, the ratio of N_I over F_n. This seems to be totally normal because at such temperatures, enough energy is available in the matrix to build new precipitates, in other words to nucleate early.

Looking at the Figure 4.18(b), the end of the curve is showed. The evolution of the damage is more or less the same for each steel grade. The growth of the cavities is not the dominating damage driving force as the nucleation. Indeed, the level of damage reached after nucleation is representative of the damage moment. When the precipitates have nucleated long, the damage is more elevated at the end of the nucleation and the damage appearance will be early. On the contrary, when the nucleation was short, the damage level reached after this step is low and the material takes more time to reach the failure.

So, **B** is the first one to present failure. It is followed by **C**. And the last one to reach damage is steel grade **A**.

In order to understand this damage evolution comparison, the following paragraphs expose the effect of the three last fitted parameters on the damage curve of the various steel grades studied according to the composition.

4.3.5.1 Effect of N_I and the beginning of the nucleation

Looking at the Figure 4.19(a) that represents the evolution of N_I against temperature for each steel grade, it is obvious that **C** presents significantly higher values in comparison with **B** and **A** on the whole temperature range studied.

N_I strongly influences the beginning of the nucleation through the parameter S_{thr} (Figure 4.19(b)). Whenever N_I presents high values, S_{thr} also does and the nucleation

starts later. However the effect of N_I is counterbalanced by F_n for the beginning of the nucleation as it is possible to see comparing the curves **A** and **B** that have almost the same N_I values but with very different S_{thr} values.

N_I has more an effect on the whole precipitation as it enters also in the calculation of b_{min} at the end of the nucleation contrary to F_n that has a dedicated effect. Thus, N_I should be related to a precipitation state or shape that will be present during the whole CC process and not only to the precipitation moment of a compound.

The evolution of this parameter with temperature has to be related to the huge differences in Ti additional element. Indeed, **C** contains less Ti than the other two steel grades. Small Ti(C,N) appear thus at the end of the solidification. The formation of small precipitates is positive for the distribution and the homogeneity of those in the steel matrix. At contrary, **A** and **B** contains a big amount of Ti. This Ti level initiates the early formation of then growing big precipitates around which the other precipitates will appear and concentrate.

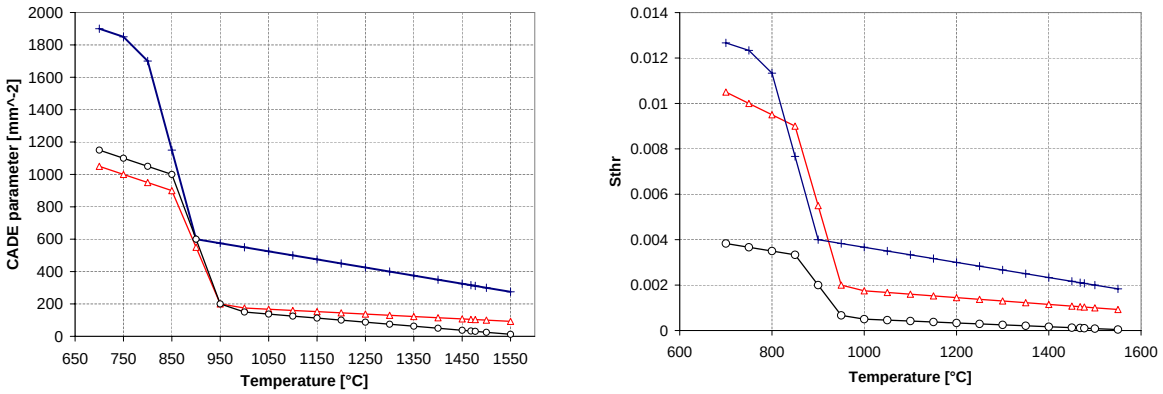

(a) N_I curves (b) Whole damage path

Figure 4.19: Damage curves as a function of the temperature for the different steel grade studied with ∘ for **A**, Δ for **B** and + for **C**

4.3.5.2 Effect of F_n

F_n is a parameter that has almost no influence on the damage moment as shown in Section 4.2. Nevertheless, it is possible to relate the parameter F_n to the rate of free C and N available in each steel grade in order to nucleate new precipitates. Indeed, more present free CN, the faster the nucleation is, as they consist in the precipitates basis with which other elements react.

With this point of view, grade **B** that has a low amount of C will have a low value of F_n, contrary to **A** and **C** that will present an early and fast nucleation due to their elevated amount of C.

Looking at N, all the steel grades contain more or less the same amount of this component, thus no difference can be observed.

On the other hand, between **A** and **C**, F_n level should be different despite the values obtained. This is to relate to the fact that the Ti and Al rates are different.

It is expected that the F_n is lower for the grade containing the highest Ti rate, because the whole C and N are consumed before Nb is able to react with those. Nevertheless, this is not verified because F_n of **A** is higher than the one of **C**. The Al rate is higher in **C** and has the same effect as Ti, this can explain the F_n level. By combining both element effects, it happens that Nb nucleates later for **C** than for **A** as shown in Section 3.1.2.2 in Figures 3.10 and 3.12. This could explain why F_n is lower for **C** than for **A**.

Thus, when the available amount of C is high, the nucleation of new precipitates is fast. On the contrary, the lower is the C content, the lower is the number of detrimental precipitates created. This phenomenon is influenced by other alloying elements that appears before Nb, as Ti or Al. They react at higher temperatures with C or N and they capture the available components that could form detrimental precipitates.

4.3.5.3 Effect of N_{max}/N_I and the end of the nucleation

The N_{max}/N_I level influences b_{min} value such as when N_{max}/N_I is high, b_{min} is small and thus the nucleation is lengthened because the interdistance between two cavities can decrease more. So the end of the nucleation is lead by the amount of precipitable components available that could form detrimental precipitates as Nb(C,N) and V(C,N).

The effect of N_{max}/N_I is clearly related to the Nb content. **B** contains a little more than four times the amount of Nb in **C** and **A**. So are the N_{max}/N_I values. **B** presents the highest value (70), widely over the two other steel grades studied that present more or less the same value of N_{max}/N_I (40 and 30).

V content of the different steels studied is clearly different, nevertheless it has no clear effect on the N_{max}/N_I value. This can be due to the inertia of the nucleation of this component. It has been determined that V needs more or less 16 hours to reach equilibrium. The tensile test lasts at the maximum 1 hour. Thus, the CN could not form. This is clearly the case in CC conditions because the casting lasts 30 minutes in general. This is not enough to precipitate V(C,N). The effect of V in the damage of the slab during the CC is to eliminate in the high temperature area of the unbending.

Finally, the most important part of the damage evolution, the end of the nucleation, is driven by the amount of Nb present in the steel composition. This confirms the literature review about the different precipitates present in the matrix during CC and their severity for the health of the slab. Nb has been detected as the most relevant additional element of the steel that could lead to damage in the CC slab during the unbending process.

Moreover, the micrographic analysis (Section 4.3.3) showed coarse Nb precipitates in the steel matrix. A small amount of V has been detected but no clear precipitate was found on the pictures. Particularly grade **B** showed clear precipitates after a tensile test at a temperature of 900°C and a strain rate of $10^{-3}s^{-1}$. **C** and **A** grades, in almost the same test conditions, showed two times smaller precipitates.

4.4 Validation of the Macro-Meso transfer

Finally, in order to validate the obtained damage parameters, the transfer of the macroscopic recording of the hot tensile test simulation to the mesoscopic representative cell has to be checked in order to be sure that the stresses and the strains obtained in the cell are representative of the macroscopic loading history undergone during hot tensile tests.

The idea of this section is to compare the stresses computed in the root element of the tensile test simulation and the results obtained in the transition area of the representative cell. In other words, the goal here is to check the consistency of the data transfered from the macroscopic to the mesoscopic simulation.

In this study, not only the equivalent stress, but all the components of the stress tensor will be analyzed. Indeed, as explained earlier, the equivalent stress is not representative of the real stress state in the sample. This is due to the fact that different stress states could lead to the same equivalent stress.

The observed stresses are, in the tensile test reference frame, the radial stress σ_{rr}, the axial stress σ_{zz}, the circumferential stress $\sigma_{\theta\theta}$ and the shear stress $\sigma_{r\theta}$. The stresses are compared to the one coming from the cell with an adapted reference system as explained in Section 4.1.1.

All the steel grades and HTT cases are checked in order to be sure that all the cases are valid. The transfer is studied for each steel grade separately in the following chapters.

4.4.1 Macro-Meso transfer for steel grade A

The stresses coming from the macroscopic HTT simulation, are compared to the mean stresses obtained in the transition area of the representative cell. The first case studied is 22085B (Figure 4.20).

The last graph that represents the equivalent stress is, as expected, the same for macroscopic and mesoscopic results. The axial stress presents the same level as the equivalent stress. This is due of the fact that the test is a tensile test and the main forces are applied in the axial direction of the tensile test sample. So the principal direction of the stress is the axial one. For the axial stress, the curves are also overlapping. Even if the axial stress is the main one, radial, circumferential and shear stresses are present in the tensile test sample.

The radial stress is very low ($\approx$ 5MPa). On this graph and by such a small scale it is possible to see that the macroscopic and the mesoscopic results are not perfectly following the same path. Though, this difference is very small, as it is more or less 0.2MPa where the curves diverge the maximum. Thus, 4% of error, and approximately 0.01% of he equivalent stress ($\approx$ 200MPa).

Analyzing this error, it can be due to the hypothesis made at the beginning, that the shear stresses are ignored because to small in comparison to the axial and radial stresses. Indeed, looking at the shear stresses comparison graph, the macroscopic

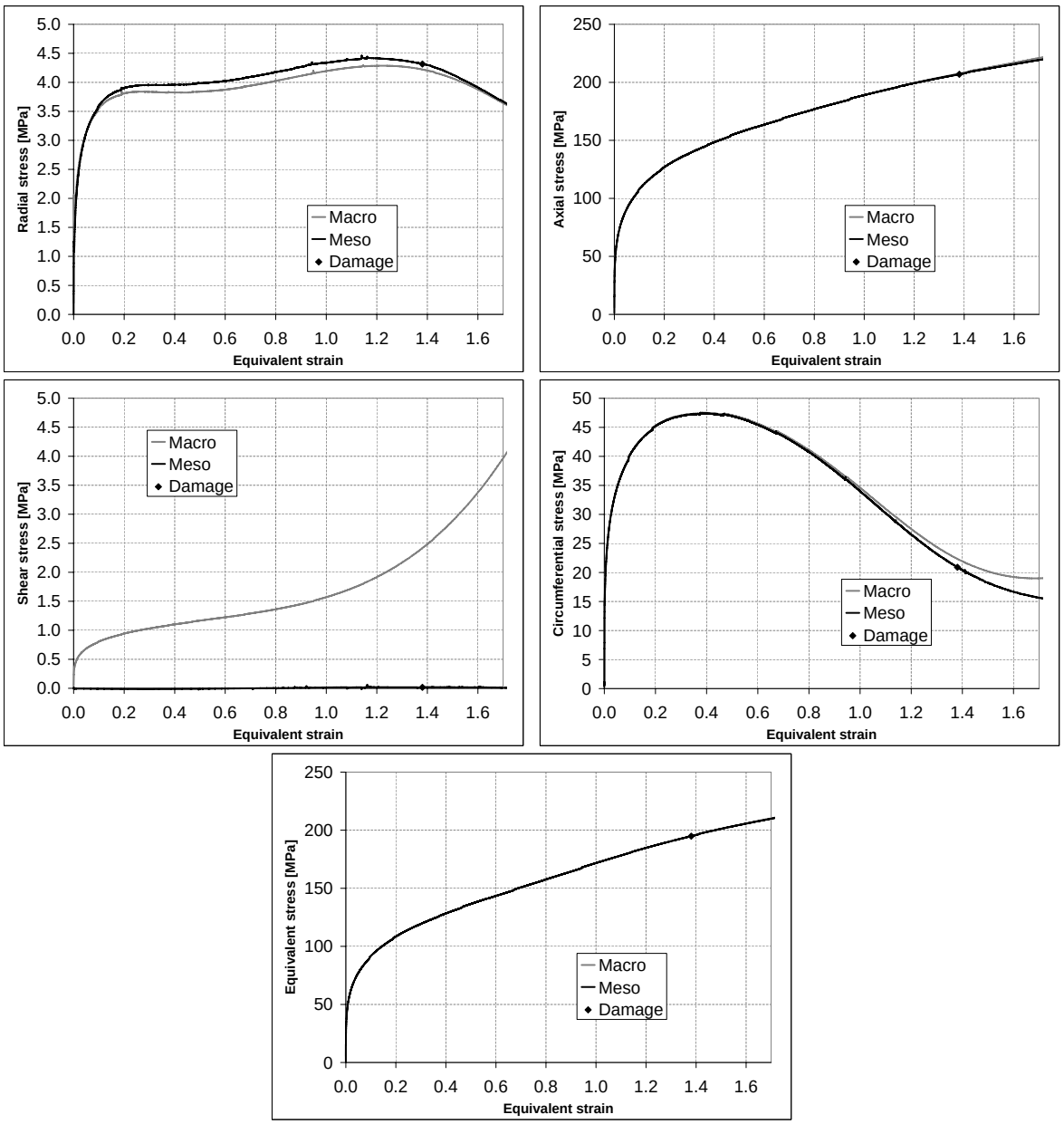

Figure 4.20: Comparison of the stresses obtained for the same case 22085B for macroscopic and mesoscopic simulations

simulation presents a shear stress at the notch root that is approximately at the level of 1.5MPa, when the mesoscopic simulation has 0MPa of shear. This is due to the fact that these stresses are not applied to the representative cell. This stress level is clearly very low compared to all the others. Nevertheless, at the damage moment the shear stress reaches almost 2.5MPa and it increases continuously with strain.

This evolution of the shear stress could be the reason of the divergence of the radial stress, but also the circumferential one. Around the strain of 1 (100% of deformation), the slope of the shear stress starts to evolve more rapidly. At this moment the mesoscopic circumferential stress diverges from the macroscopic one. At the moment of damage the difference is about 2MPa. This difference is increasing with equivalent strain and reaches approximately 5MPa at 1.7 of strain. The divergence is about 10% at the damage moment and 25% at 1.7. At the damage moment the divergence is still acceptable but begins to be important for bigger strains.

In conclusion, the shear stress of the macroscopic simulation should be taken into account when transferring the stresses and strains to the representative cell. In this particular case the macroscopic to mesoscopic transfer has been validated because the damage happens before the divergence between the circumferential stress of the two different simulations is too huge. Thus, this study could be restricted to the observation of the circumferential stress in each case and the difference between both curves at the mesoscopic damage moment.

The curves are grouped together according to the strain rate of the case in order to see the differences between varying temperatures and to be more readable.

All the figures obtained (Figures 4.21(a) to 4.21(c)) show a good correlation between macroscopic and mesoscopic circumferential stresses with a divergence at the end, around the damage moment.

The explanations of the case 22085B (Figure 4.21(a)) have been given before. The divergence between both analyzed curves is acceptable as it is only 4% at the damage moment. At 900°C, the divergence is almost null when damage appears the first time and the curves only diverge later.

The last case is the most critical. Indeed, at 950°C the damage appears later than at lower temperatures. This is due to the high temperature but this causes a more important divergence at failure. This value has therefore to be considered with care. In the results of the damage moment difference between experimental and numerical displacements (Table 4.13), it is also possible to see that the relative difference is among the highest. Nevertheless, this value is acceptable when supposing that the damage should have occurred earlier and thus when the curves have not diverged as much.

At a theoretical strain rate of $5 \cdot 10^{-3}\text{s}^{-1}$ (Figure 4.21(b)), the three cases available at 850, 900 and 950°C present a low divergence at the moment of the damage. At these strain rates again, the most critical case is the one of the highest temperature. This time, Table 4.13 shows a good agreement between experimental and numerical damage moments. The divergence stays in an acceptable range of 10%.

The two last available cases at 10^{-3}s^{-1} and 850 and 900°C show a really good convergence of the curves (Figure 4.21(c)). Even after the damage moment no divergence

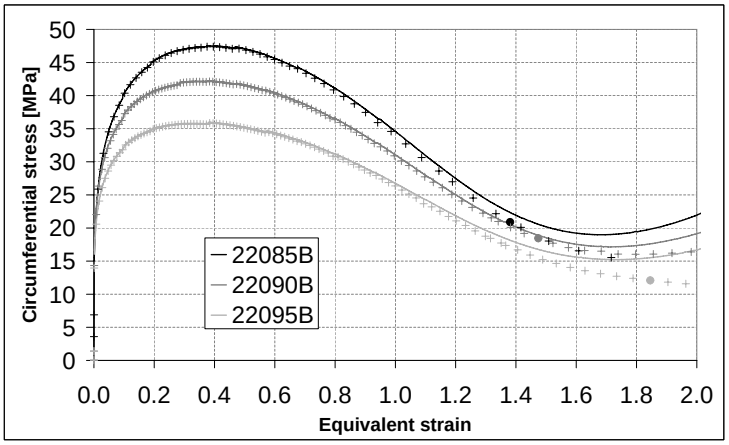

(a) $\dot{\varepsilon} = 10^{-2}\mathrm{s}^{-1}$

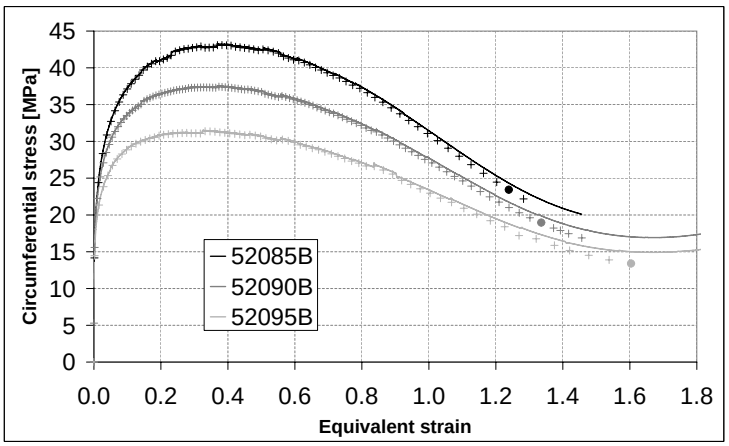

(b) $\dot{\varepsilon} = 5 \cdot 10^{-3}\mathrm{s}^{-1}$

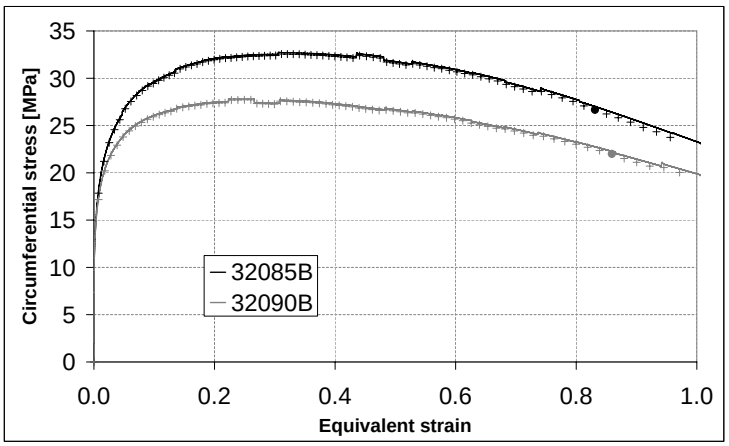

(c) $\dot{\varepsilon} = 10^{-3}\mathrm{s}^{-1}$

Figure 4.21: Comparison of the circumferential stress obtained for case R2, **A** for 3 different strain rates at various temperatures (- Macroscopic, + Mesoscopic, · Damage)

is observed between the macroscopic and mesoscopic circumferential stresses.

For steel grade **A**, over 8 available cases, only one is questionable in the point of view of the macroscopic to mesoscopic simulation data transfer. The set of parameters obtained in the previous chapter is thus numerically validated for grade **A**.

4.4.2 Macro-Meso transfer for steel grade B

The same validation work has been conducted on grade **B**. The circumferential stress has been observed and the cases consequently validated or not. The circumferential stress curves obtained for **B** are compiled in Table 4.22(a) to 4.22(c) and analyzed hereafter.

The two cases available at strain rate $10^{-2}s^{-1}$ present diverging circumferential stress curves around the damage moment (figure 4.22(a)). Nevertheless, at the damage moment, this difference in stress value is not significant enough to eliminate these tests from the damage law parameters adjustment of **B** grade.

At $5 \cdot 10^{-3}s^{-1}$, the case at 950°C presents an important gap between macroscopic tensile test simulation and the corresponding representative cell calculation (Figure 4.22(b)). The stress level is about 30MPa and the difference 10MPa. This error over 30% is too high for this calculation, as experimental and numerical displacements for the first damage are more or less equal (Table 4.15). The macroscopic to mesoscopic transfer has to be check in this case. Both other cases show adequate correlation between the curves until damage.

Figure 4.22(c) shows perfectly matching circumferential stress curves. At $10^{-3}s^{-1}$ the rheological law of the tensile test and representative cell simulations of grade **B** are in agreement until the first crack appearance. At these strain rates, the cracks appear earlier because of the low strain rate and the ability of the defects to migrate and to form faster failures in the material.

Grade **B** presents a very good correlation of the data transfer for all the cases available, excepted one (52095F). Indeed, most of the time the divergence shows a lower value for the mesoscopic calculation and in this case, the mesoscopic and macroscopic curves are inverted. The macroscopic circumferential stress is lower than the one extracted from the transition area of the representative cell.

4.4.3 Macro-Meso transfer for steel grade C

For **C**, the available cases contains R4 samples. These samples which presented for **A** and **B** a wrong experimental to numerical correlation should be studied with particular attention in order to be sure that no mistake enters the damage parameters adjustment with those.

Moreover, the results of the displacement reached at the first damage appearance are very disparate (Table 4.17) and this could be due to rheological incoherences.

Apart from the curve at 700°C, the cases for the strain rate $5 \cdot 10^{-3}s^{-1}$ are relevant (Figure 4.23(a)). At 800 and 900°C, the data transfer was successful even though at

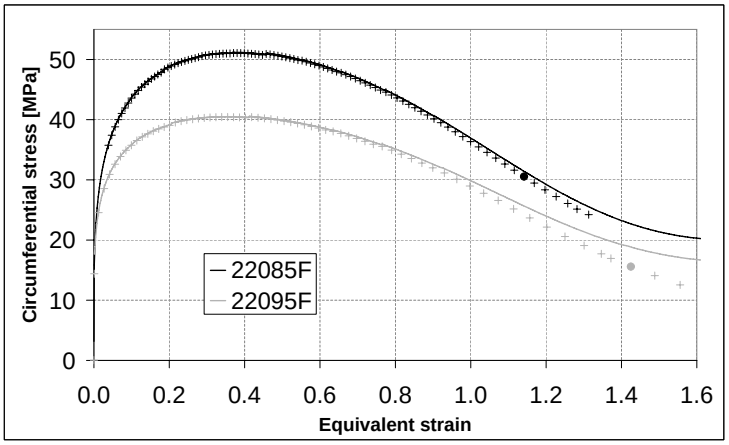

(a) $\dot{\varepsilon} = 10^{-2}\mathrm{s}^{-1}$

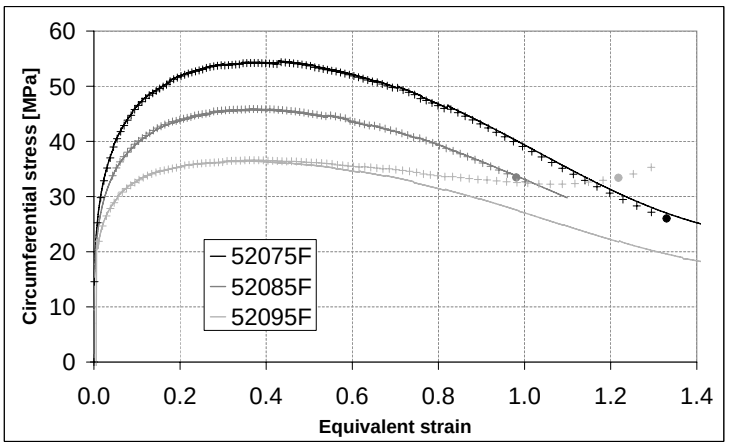

(b) $\dot{\varepsilon} = 5 \cdot 10^{-3}\mathrm{s}^{-1}$

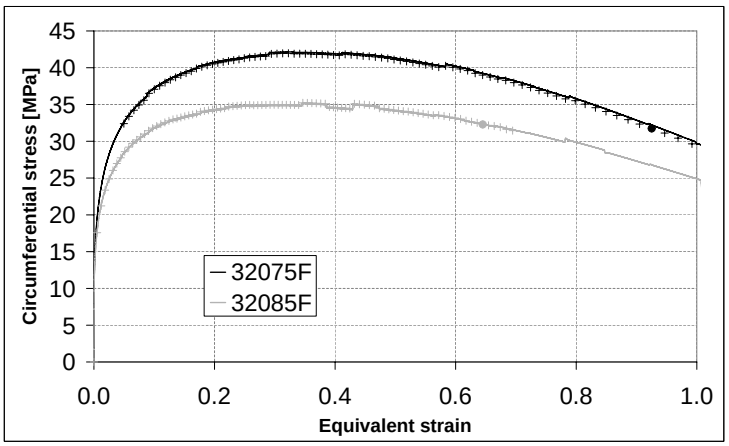

(c) $\dot{\varepsilon} = 10^{-3}\mathrm{s}^{-1}$

Figure 4.22: Comparison of the circumferential stress obtained for case R2, **B** for 3 different strain rates at various temperatures (- Macroscopic, + Mesoscopic, · Damage)

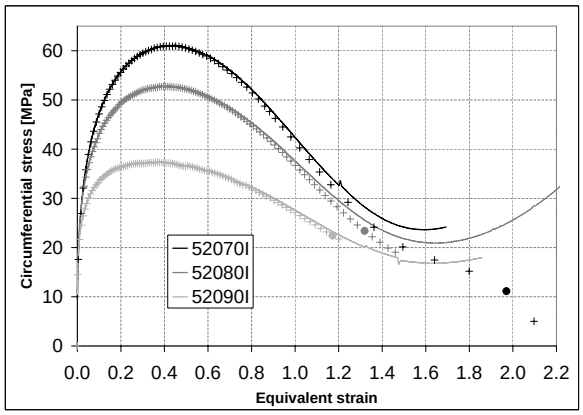

(a) R2, $\dot{\varepsilon} = 5 \cdot 10^{-3}\mathrm{s}^{-1}$

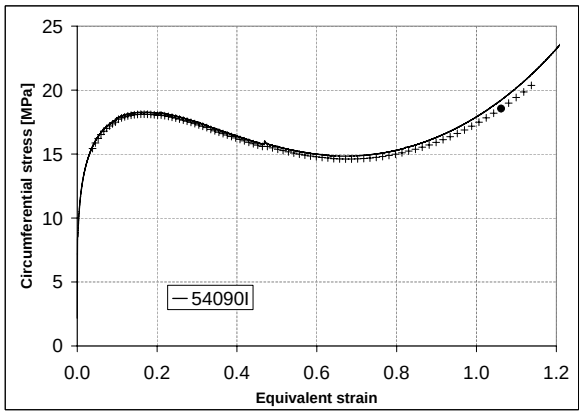

(b) R4, $\dot{\varepsilon} = 5 \cdot 10^{-3}\mathrm{s}^{-1}$

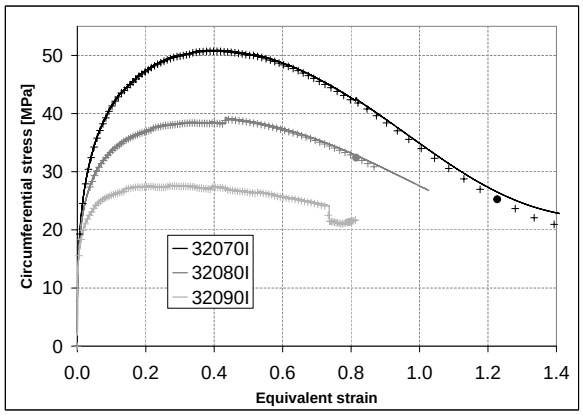

(c) R2, $\dot{\varepsilon} = 10^{-3}\mathrm{s}^{-1}$

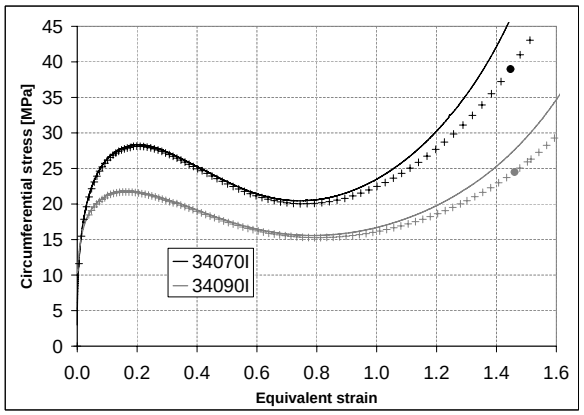

(d) R4, $\dot{\varepsilon} = 10^{-3}\mathrm{s}^{-1}$

Figure 4.23: Comparison of the circumferential stress obtained for case **C** for 2 different strain rates and sample shapes at various temperatures (- Macroscopic, + Mesoscopic, · Damage)

800°C, the curves are slowly diverging before the damage appearance.

At 700°C the damage occurs very late and thus, far after the start of the divergence. The table of comparison of the experimental and numerical case (Table 4.17) shows effectively that the numerical damage moment happens after the experimental one and the difference observed between both curves is about 30% which would require the analysis of the data transfer.

Figure 4.23(b) shows one unique case obtained for sample shape R4 and strain rate $5 \cdot 10^{-3}s^{-1}$. The circumferential stress behavior of this sample shape is slightly different of the one for R2 shapes. By comparing the same strain rate, the stress level is lower and the strain before change of slope also. This is due to the smaller useful surface and is wanted for this study in order to obtain different stress strain histories to adapt the damage law parameters.

As well as for R2 sample shapes, this case presents a slight divergence of the stresses recorded in the tensile test sample root element and in the representative cell. This divergence is low enough to validate the data transfer from macroscopic to mesoscopic simulation and the adjustment on this case.

At $10^{-3}s^{-1}$, the R2 samples show a good correlation of the studied curves (Figure 4.23(c)). Even sudden variations are followed by the representative cell through the forces and the strains that have been imposed on the edges of it. At the damage moment, the curves are matching or diverging a little bit.

The two last cases for **C** are R4 samples at $10^{-3}s^{-1}$ (Figure 4.23(d)). The divergence starts as soon as the curves start to increase. At the damage moment the difference for both cases is about 5MPa over the 30 or 40MPa reached by the macroscopic circumferential stress. This means that the highest error is about 16% which is acceptable in this study.

Among the 9 cases available for the damage law parameters adjustment for grade **C**, one case is disputable and has to be analyzed further. Whatever R2 or R4 sample shapes, the data transfer form macroscopic to mesoscopic simulations is achieved and could be extended to other sample shapes.

4.4.4 Conclusions about the Macro-Meso transfer

Some cases should be checked because of the unmatching circumferential stress values between the macroscopic and mesoscopic simulations.

Though, the transfer of the forces and the displacement is globally well controlled, even if the curves diverges around the damage moment. This transfer could be more accurate by taking the shear stress into account, as it seems to generate divergences in the other components of stresses.

All the sample shapes are supported by the data transfer, thus it could be applied on the final analysis of the CC damage behavior. Indeed, the stress and strain fields from the CC macroscopic simulations could be applied on the representative cell that reacts as expected to the imposed loading as demonstrated in the analysis above.

4.5 Conclusion of the mesoscopic study of the crack appearance in CC

Chapter 4 is the application of STEP D exposed in Section 2.2.4. The parameters of the damage law are determined here by inverse analysis in order to load a numerical cell, representative of the steel in the CC conditions with its grains and grain boundaries. Giving the possibility to the grain boundary to show damage and thus to follow the crack appearance in CC conditions.

Section 4.1.1 sets the relation between the hot tensile tests that are taken as basis for the inverse analysis, and the representative cell. The so called Macro-Meso transfer is set here by:

- the positioning of the representative cell in the hot tensile test sample by analogy with S. Castagne's study with compression test samples;
- the choice of the record location;
- the implementation of the automatic calculation of the load to apply to the representative cell.

In order to understand the way the parameters of the damage law impacts the evolution of the crack, the sensitivity of the law to 7 parameters (a_0, b_0, F_n, N_I, $\dot{\varepsilon}_e/\dot{\varepsilon}_B$, N_{max}/N_I and ψ) have been studied.

The predominant role of the cavity tip angle ψ, the both parameters playing a role on nucleation start N_I and end N_{max}/N_I and the viscosity parameter between grain and boundary ($\dot{\varepsilon}_e/\dot{\varepsilon}_B$) have been established.

In section 4.3, the damage law fitting for all the three peritectic steel grades studied is exposed. Different means have been exploited to determine the damage law parameters that represent a physical behavior.

- Literature survey based on previous researches on the defect appearance topic (Section 4.3.1).
- Calculations based on the rheological law parameters (Section 4.3.2).
- Micrographic analysis with SEM, TEM and STEM microscopes (Section 4.3.3).
- The remaining parameters (F_n, N_I, N_{max}/N_I and D_{dam}) are adjusted on the basis on HTT on notched samples (4.3.4).

The validation of the damage law parameter determination has been validated in Section 4.4. Some incoherency have been determined in this section. When reaching high strains, the mesoscopic stress results show a small divergence with the macroscopic ones. The Macro-Meso transfer method is not meant to be the cause of this discrepancy. The hypothesis of the negligible shear stress should be revised in order to improve this part.

Chapter 5

Industrial application

One of the critical problems encountered during CC is the formation of transversal cracks, especially in peritectic steels. The defects are enhanced by the precipitation of some particular compounds during CC of steel. These particular compounds are known in literature to be Nb and V which precipitate between 800 and 1100°C during the unbending process of CC. In order to follow this damage process, a mesoscopic damage model has been developed and validated on peritectic steel grades with hot tensile tests.

The next step of this study is to model the CC in order to extract the stress and the strain fields from the numerical simulation. For the validation of the damage law parameters, the stress and strain histories extracted from an element of the steel slab traveling in the continuous caster will be used to determine the damage level reached by the material within a mesoscopic representative cell.

The numerical model of the CC, called Thercast, developed by Transvalor has been used. This software can be used to model in several ways the continuous caster. The whole slab can be modeled through the so called transient simulation detailed hereafter or only the interesting part, the "ingot" simulation. The entire continuous caster characteristics are implemented and taken into account. This program is presented in the first Section 5.1.

Different cases have been studied in order to understand the way the CC process parameters and the chemical compounds of the steel influences the damage. These cases are presented in Section 5.2 and the results are analyzed from a macroscopic point of view.

The transfer of the parameters from Thercast to Lagamine, where the mesoscopic damage model is implemented is explained. It is the key point of the results of the damage calculation in Section 5.3.

The last part is a conclusion on the application of the mesoscopic damage law on an industrial case.

5.1 THERCAST program

THERCAST software is a forging code. It numerically simulates the three-dimensional thermomechanical phenomena associated to solidification and cooling in continuous casting of ferrous material by finite elements. The coupled thermomechanical calculations permits the software to take into account the interaction between the mold and the steel slab. The whole continuous casting process is then modeled, from the mold to the cold slab. Each part of the continuous caster and the slab is represented by an independent finite element mesh. On each domain, the mechanical and thermal problems are solved.

Tetrahedral linear elements are used to discretize the slab and the continuous caster. In order to learn more about the thermal and mechanical resolution, information can be found in Costes's thesis [Cos04].

The stresses and temperatures are calculated in the slab mesh according to the deformation of the steel (free surface movement, contraction, boundary conditions, etc.) occurring during solidification.

The different parameters of the calculation in the slab are:

- visco-plastic rheological law in the liquid and semi-liquid areas
- elasto-visco-plastic rheological law in the semi-solid and solid areas
- thermal (imposed temperature, imposed flow, convection/radiance with the ambient) and mechanical (imposed speed and/or pressure) boundary conditions applied to the faces of the slab
- calculation of the strains, residual stresses, final shape
- automatic remeshing and adaptative meshing
- good control of the mass balance

5.2 Continuous caster results on grade C application

At the exit of the continuous caster, some important quality points are checked. This is necessary for the correct behavior of the material on the downstream mills and the end quality of the product.

The presence of transversal cracks is verified. As explained in the introduction, the transversal cracks can be situated just under the shell and thus not visible. That is why the slabs are systematically milled after CC, which is a huge loss of material.

As explained in Chapter 1, different defects cause damages during CC of steel. The particular case of transversal cracking has been detected on **C** CC slabs. Their location and size are important to know, in order to understand and to discover the potential cause of the damage. THERCAST program has been used to model the continuous caster and to detect some anomalies or weak points as explained hereafter.

5.2.1 Defects detected on the continuous caster of C

In general, the transversal crack defect is detected on the intrados of the slab. The cracks are located near the corner (30-50mm from the corner) or in the center part of the broad face for the 300mm profile thickness. The length of these cracks is about 20mm.

Two causes are supposed to induce the transversal crack appearance;

- The thermal path of the slab with high mechanical constrains;
- The roll wear.

The first one is studied here.

5.2.2 THERCAST calculations performed on C caster

It has been shown by industrial trials that a change of the cooling strategy (slower cooling in the last sections) decreases the defect occurrence. This phenomenon has to be understood in order to master the process and to increase for the long term the quality of slabs.

So, with the help of THERCAST, the influence of the modification of the secondary cooling on the transverse cracks appearance is studied. Numerical simulations are performed with different cooling rates in the unbending area. Eight calculations are performed in order to compare the critical cases of a reference colling profile compared to a modified cooling profile that is expected to be less detrimental. Thus, two secondary cooling profiles have been studied on four different areas of the caster. The studied areas are compiled in Table 5.1.

Area studied	Classical temperature profile	Modified temperature profile
Center large face	Intrados	Intrados
	Extrados	Extrados
Corner large face	Intrados	Intrados
	Extrados	Extrados

Table 5.1: Numerical cases studied on the C continuous caster

The modification of the profile consists in the decrease of the cooling in segment 10 from 174W/m^2/°C in the reference case to 10W/m^2/°C + emissivity (0.85) in the modified case. Table 5.2, presents the whole cooling process from the mold to the exit for the classical and the modified profiles.

The first one, the classical profile, is the usual way of cooling for the peritectic steel grades on the continuous caster of C. The slab is constantly cooled with water spray flows, inducing different heat transfer coefficients.

The second cooling way is called Modified temperature profile. The difference between both is located in the last part of the caster from 13.915 to 19.678m of metallurgical length, which is segment 10 of the continuous caster. For this cooling solution

Area	Exchange type	Classical temperature profile	Modified temperature profile
Mold	Extracted flux	$891.54 kW/m^2$	
Area 1	Heat transfer coefficient	$516 W/m^2/°C$	
Area 3		$360 W/m^2/°C$	
Area 4		$217 W/m^2/°C$	
Area 6		$207 W/m^2/°C$	
Area 8		$200 W/m^2/°C$	
Area 10 13.915 to 19.678m		Water cooling $174 W/m^2/°C$	Calm air cooling $10 W/m^2/°C$ + emissivity (0.85)

Table 5.2: Heat transfer for both studied classical and modified temperature profiles determined for the study of the transversal crack in CC

no sprays are used. The slab cools down by calm air cooling. In this configuration, the heat transfer between the slab and the air is taken into account, as well as the emissivity which leads to slower cooling of the slab than with the water cooling.

Complementary technical data is used for the calculation of the continuous caster of **C** and should be mentioned.

- Slab thickness: 300mm
- Slab width: 2100mm
- Casting speed: $0.5 m.min^{-1}$
- Rheology: Parameters determined in Section 3.1.3 and compiled in Table 3.5

Two different types of calculation exist in THERCAST (see Figure 5.1).

- In a first approach called the **transient simulation**, the process is modeled as it happens in reality. The steel is filling the caster until there is no liquid steel in the mold anymore. Then, the slab migrates through the caster with its casting speed. The process stops when the whole slab quits the process.
- Another strategy is the **ingot simulation**. This solution models only a part of the slab that is running through the caster. An ingot of a few meters (1.60m) length is migrating through the caster. The length of this ingot is calculated in order to keep contact with at least 3 or 4 rolls. The slab can also be divided through the width depending on the studied part.

The transient simulation is too greedy from the CPU time point of view and computer capacity. That is why the ingot simulations are performed. Moreover, the piece of slab is cut in the length direction in order to study only the wanted part as explained hereafter. Therefore slices of the slab are modeled, either the center part or the corner (in gray in Figure 5.2) within this thesis.

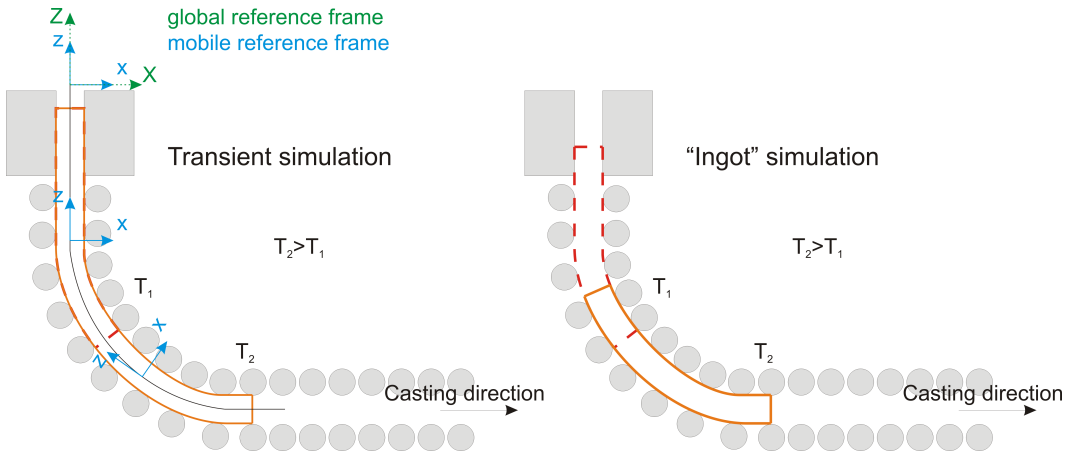

Figure 5.1: Slab path through the caster and reference frame for both calculation possibilities, the transient and the ingot simulation

Sensors recording the stresses and the strains are embedded in THERCAST simulation. For instance in the center part when a slice of the central part of the slab migrates through the caster. A few hypotheses are made at the lateral boundaries of the slices in order to keep the material integrity. In addition, in the upstream and downstream boundaries of the ingot, some hypotheses are made in order to take into account the current material placed over and under the ingot.

When the sensor is located at the corner, only the edge is modeled and calculated to get the wanted stress and strain fields.

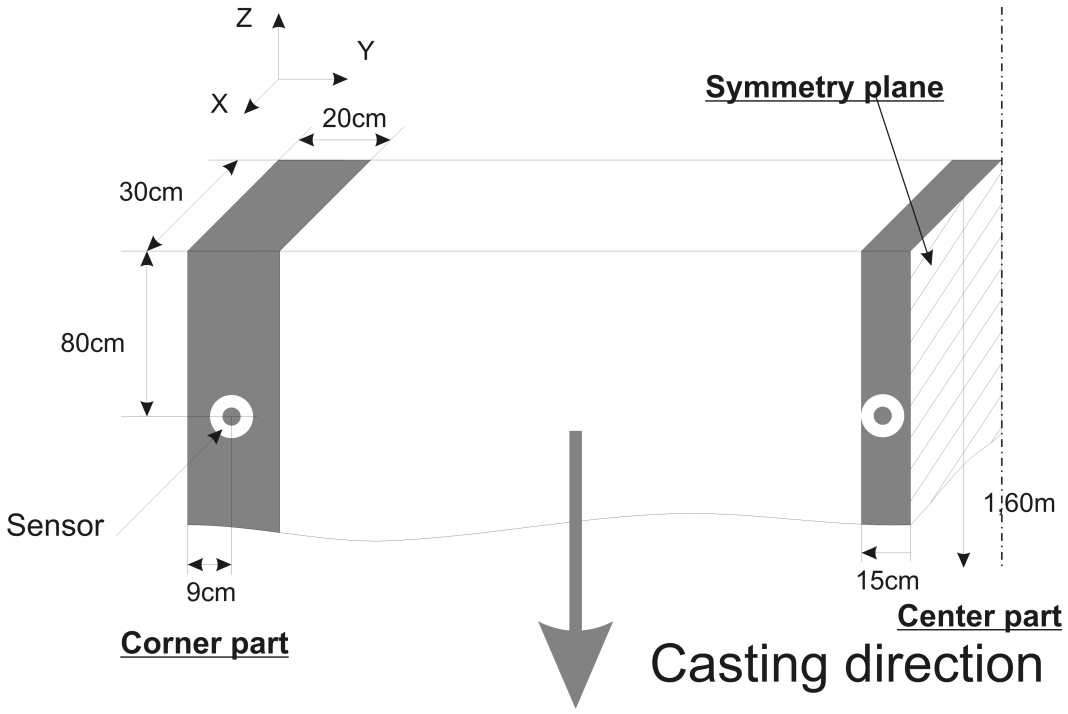

Figure 5.2: Sensor positions on the slab in the THERCAST simulation for the two options, edge or center part study

One transient simulation has been performed simulating the whole slab because

the results that were expected were situated in the first part of the continuous caster and thus, they do not need much calculation time. The advantage of this simulation is that no hypotheses are requested about the axial forces and the edge, upstream and downstream boundary conditions. All the simulations are driven by the casting velocity.

The results obtained by the ingot simulations have been validated by the transient one known to be more accurate in the first part of the caster.

5.2.3 THERCAST results on C caster

The model of **C** caster in THERCAST finite elements program is given in Figure 5.3. The mold, each roll and each cooling system (not on this picture) are modeled in order to have the most faithful representation of the caster and to be able to model all the factors leading to damage in CC slabs.

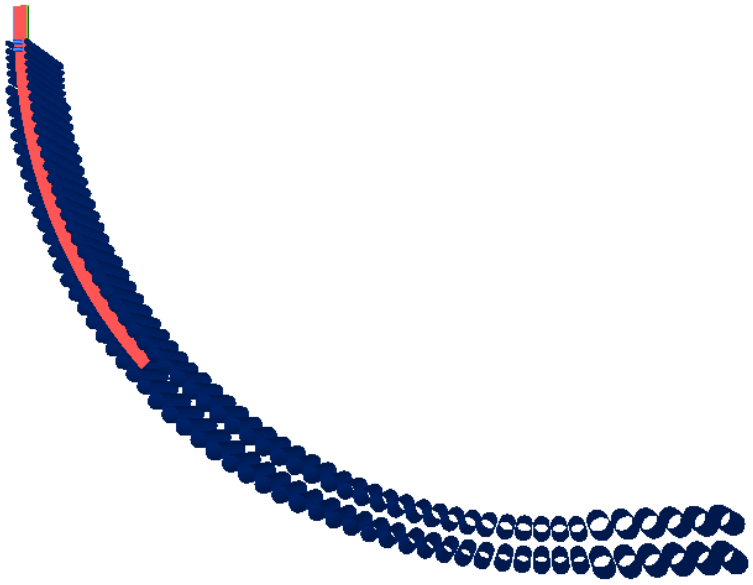

Figure 5.3: THERCAST graphical representation of the continuous caster of **C**

5.2.3.1 Study of the thermal behavior

The first analysis within the results is the impact of the new cooling strategy on the slab temperature in the several studied areas of the slab. Important differences in the recorded temperatures are detected in segment 10 due to the change in cooling strategy as seen in Figures 5.4 and 5.5.

As shown in Figure 5.6, the ductility trough is situated around temperatures between 800 and 1000°C. More accurately, one can choose the range 750°C to 900°C as the most dangerous one, yielding to necking lower than 30%. This temperature range corresponds in Figure 5.4 to the temperature of the slab broad face center in area 10 that is more precisely the unbending area located at a metallurgical length of approximately 18 to 20 meters. The modification of the secondary cooling profile elevates the slabs temperature for each sensor by about 40°C.

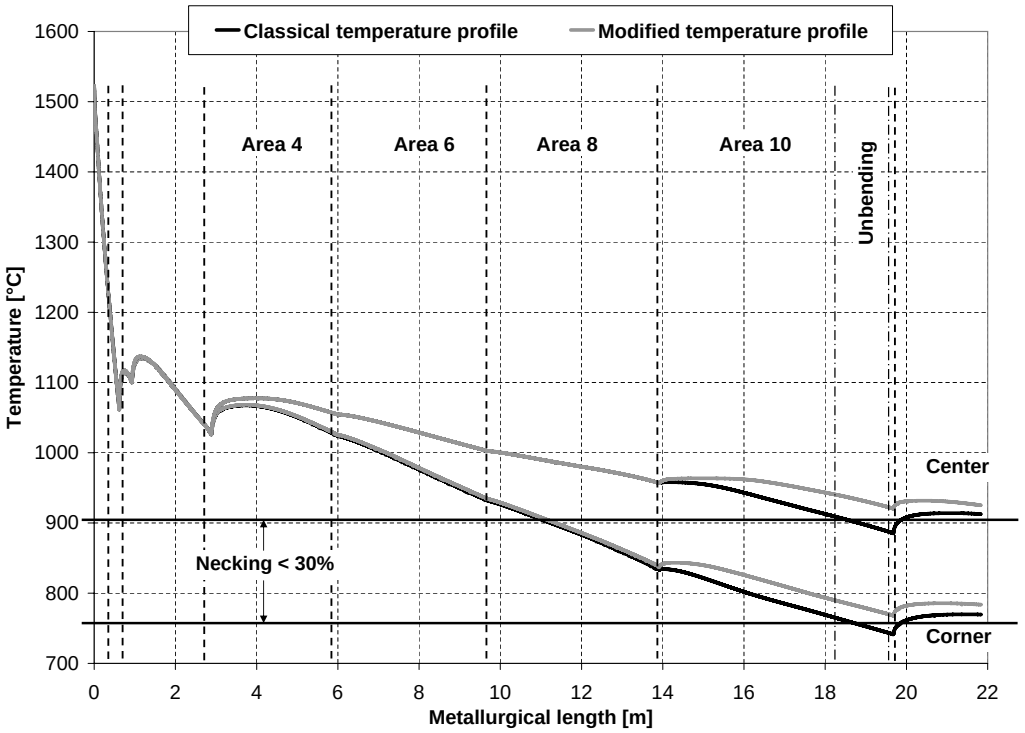

Figure 5.4: Temperature profile of the slab extrados of the **C** case with the marked temperature area of low necking as shown in Figure 5.6

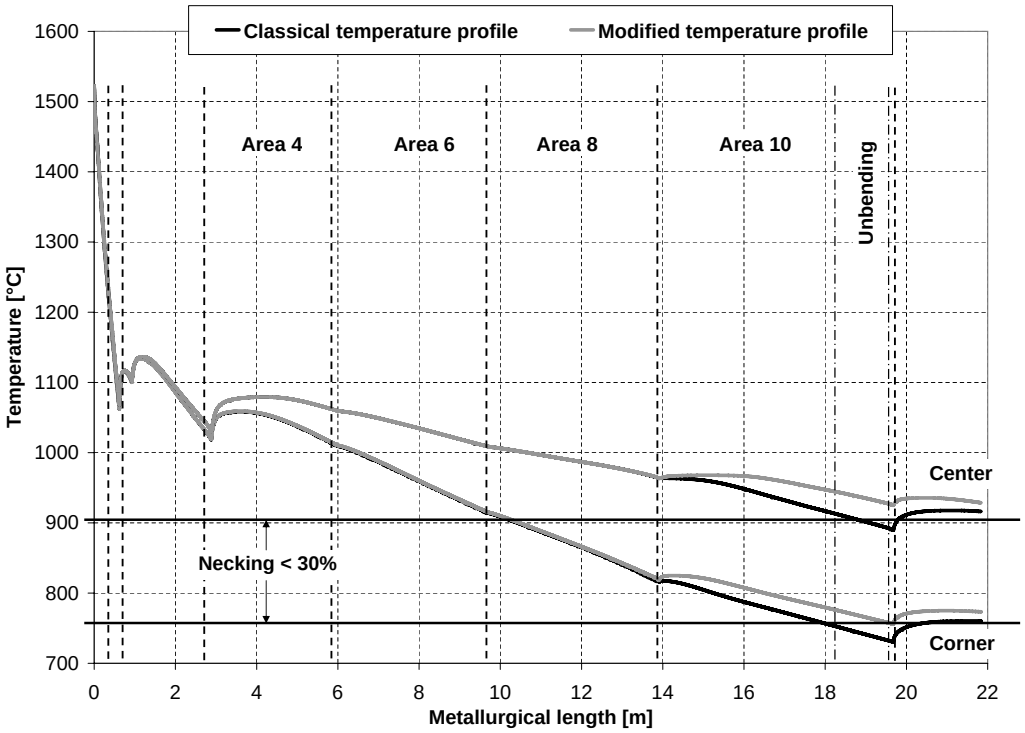

Figure 5.5: Temperature profile of the slab intrados of the **C** case with the marked temperature area of low necking as shown in Figure 5.6

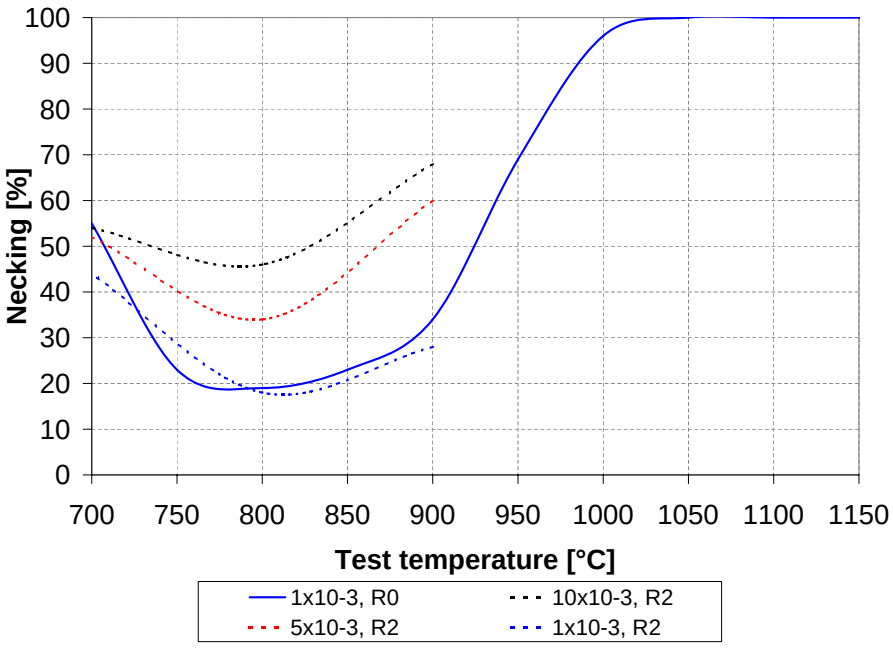

Figure 5.6: Ductility curves of grade **C** determined by HTT

This temperature increase does not exactly bring the slab out of the ductility gap but in the center part, the temperature at the unbending moment reaches approximatively 950°C which is the beginning of the ductility trough that presents necking values not as severe as at 900°C. Indeed, at 900°C the necking is about 35% which is very low compared to the 70% at 950°C. Considering that the necking is critical below 50%, the temperature reached with the modified profile is expected to be less deleterious. So, the casting configuration associated to the modified temperature profile strongly decreases the risk of transversal crack appearance in the center part of the slab.

In the corner, the temperature of the intrados and the extrados of the slab lays around 750°C which is a dangerous level for the ductility. With or without modification of cooling profile, the temperature stays in a dangerous zone during unbending as the necking values are around 20%. Indeed, even if the temperature is increased up to 850°C, the necking remains in low values.

For this special part, the stress level reached in the slab is still dangerous for the material integrity.

5.2.3.2 Study of the mechanical behavior

5.2.3.2.1 Mechanical constraints in the slab with the classical cooling profile

Observing the stress field differences (see Figure 5.2 to remember x, y and z directions), at the sensors location of the slab, between both cooling profiles, first conclusions can be drawn for the damage location and severity.

Looking at the stress fields comparison between intrados and extrados for the reference case at the center of the slab (Figure 5.7(a)), the stress levels of each component

of the stress tensor are more or less at the same level until 17m. At this moment, the intrados side begins to show high tensile stresses, especially in Z direction which is the casting direction. This is due to the unbending of the slab. Indeed, the intrados of the slab is elongated in order to straighten the piece of material.

On the extrados, the material undergoes the opposite phenomenon. The slab is compressed. This is observable in Figure 5.7(a) where σ_{yy} and σ_{zz} strongly decrease to become negative.

This explains why the transversal cracks are mainly discovered on the intrados of the slab. At the unbending moment when the temperatures are unfavorable for ductility, the intrados of the slab undergoes high tensile stresses in the casting direction and thus, the shell of the slab splits perpendicular to the casting direction.

When comparing intrados and extrados for the same cooling profile, the corner stress records (Figure 5.7(b)) present also more or less the same behavior until 17m. In the corner, the stress in the Y direction stays all the time in compression when it reaches tension in the center part at the intrados. The cooling of the material imposes a contraction in the width and thus a compression in this dimension.

The stress in the Z direction, as for the center part, presents an important increase in tension at the intrados side of the slab and compression at the extrados side. The high tensile stress in Z direction could lead to damage by transversal cracking in the corner as well as in center part of the slab.

5.2.3.2.2 Study of the cooling profile modification effect

Now the effect of the modification of the cooling strategy on the stress field should be studied (Figure 5.8).

Whatever considering the center or the corner, the effect of the cooling profile starts at 14m of metallurgical length, due to the modification of the cooling strategy in Area 10 of the continuous casting mill.

In the **center** part of the slab (Figures 5.8(a) and 5.8(c)), the stresses are affected by the elevation of temperature that produces an effect covering the mechanical one. The slab reaches a safe part of the ductility trough in terms of temperature and stays in compression. Between 14 and 16m, σ_{yy} and more especially σ_{zz} go to compression. Looking at the temperature profiles (Figures 5.4 and 5.5), when the cooling is stopped, the temperature increases slightly and permits the material to stay in compression due to the elevation of its volume by dilatation and the cold edges that traps the dilatation. The temperature increase of the slab shell due to the temperature homogenization with the core lasts until 16m and then, the slab cools down again.

After 17m, when the sensor enters the unbending area, the intrados stresses increase as it was the case for the classical cooling profile but they do not reach the stress levels of the last one due to the remaining temperature difference that induces a temperature homogeneity difference, beneficial for the material at this level of the process. On the extrados, the effect after 17m is the same. The material presents a lower cooling rate for the modified profile and thus, the compression is not as marked due to the tension created by the temperature difference between shell and core. The level reached by the stresses is less important in compression, however it stays in a good configuration for

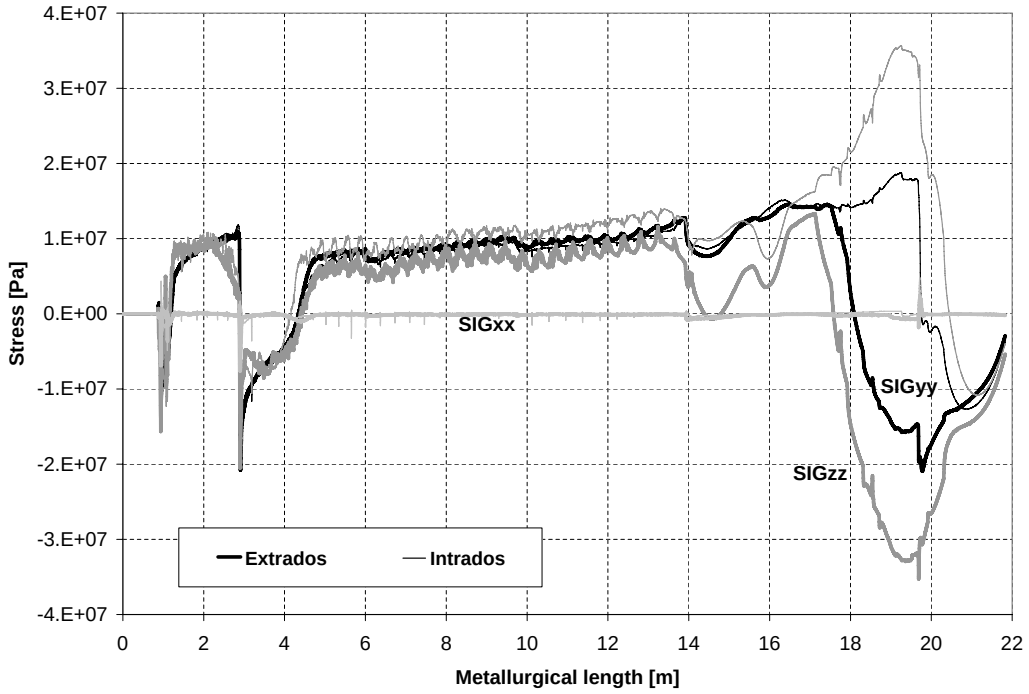

(a) Slab surface center

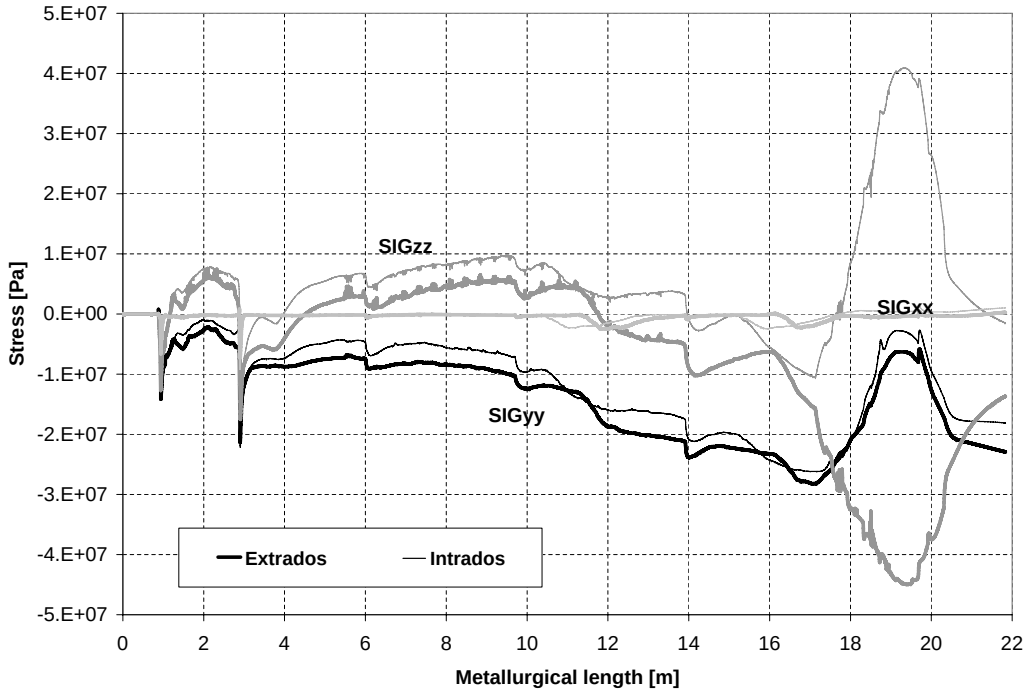

(b) Slab surface corner

Figure 5.7: Evolution of the stress components during the CC process applied to **C** the classical cooling profile

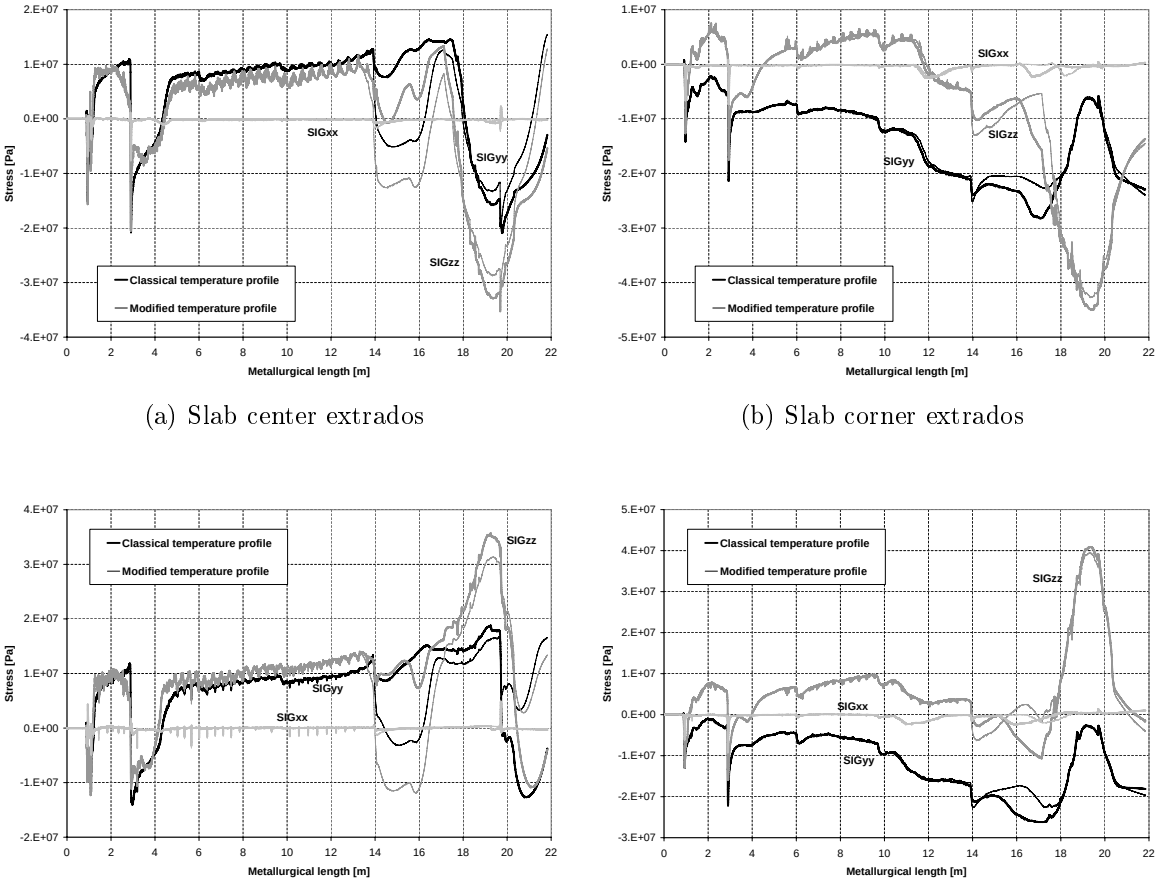

(a) Slab center extrados

(b) Slab corner extrados

(c) Slab center intrados

(d) Slab corner intrados

Figure 5.8: Evolution of the stress components during the CC process applied to **C** for the comparison between cooling profiles

the material integrity.

In the **corner** (Figures 5.8(b) and 5.8(d)), the modification effect of the cooling strategy is not as clear. Between 14 and 18m, the stress is less in compression. This elevation of stress level is due to local tensions in the material. Indeed, the corner is made of two faces that emit heat and thus, the corner is always cooler than the shell center part.

Reaching the unbending area, the stresses go back to their initial level of compression. Though, the peek of σ_{zz} in the intrados reached after 18m (Figure 5.8(d)) is as high as before and in a dangerous area of the ductility trough. This elevated stress is due to the low temperature and high tensile constraints in this part of the continuous caster and the slab. This configuration has to be carefully analyzed in the following part of this study where the damage levels are studied.

5.3 Continuous caster to representative cell

5.3.1 Data transfer from the macroscopic simulation to the mesoscopic representative cell

The data transfer consists in applying the stress and strain states computed by the macroscopic numerical simulation of the CC process with THERCAST to the mesoscopic numerical simulation of the representative cell with LAGAMINE.

As presented in Section 5.2.2, sensors provide data from the macroscopic simulation. Two positions have been chosen for the sensors. One on the broad face center and the other in the corner. In the finite element mesh, these sensors are linked to one tetrahedron (Figure 5.9) that migrates through the caster with the piece of material studied.

One sensor provides the stress and strain fields of the 4 nodes of the tetrahedron to which it is linked. Three nodes of this element are located on the surface layer of the slab while the other one is within the material core.

The different results at one node of the sensor are given hereafter:

- Complete stress tensor: σ_{xx}, σ_{yy}, σ_{zz}, σ_{xz}, σ_{yz}, σ_{xy}
- Temperature
- Position: P_x, P_y, P_z
- Strain: ε_{eq}, $\dot{\varepsilon}_{eq}$, $\dot{\varepsilon}_m$

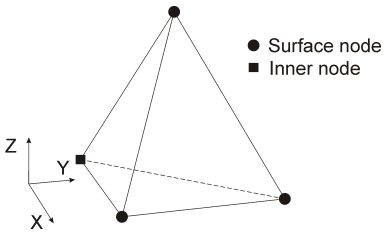

Figure 5.9: Nodal position of the sensor

The stresses and the strains are given in the local reference frame linked to the element moving, and rotating with it. The displacements of the nodes are given in the global reference frame as shown in Figure 5.1. As the slab rotates, the values of the position of the nodes have to be put in the mobile reference system. This mobile reference system is at each moment the same as the one of the representative cell. It migrates through the continuous caster just as the sensor does. The two reference

frames are shown side by side in order to understand their correlation (Figures 5.10(a) and 5.10(b)).

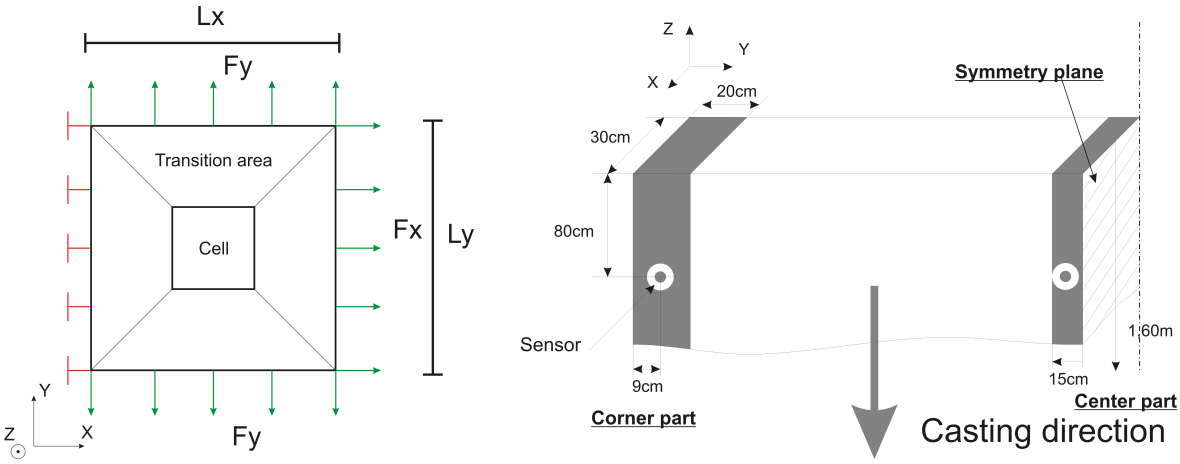

(a) LAGAMINE local frame (b) THERCAST global frame

Figure 5.10: Reference systems in the corresponding directions

The boundary conditions required within the representative cell in order to simulate the CC have been presented in Section 2.1.5. In X and Y directions (local axes), Figure 5.10(a), forces are applied to the cell. In Z direction a displacement is required as presented in the following table (Table 5.3). The correlation between both reference frames (LAGAMINE and mobile THERCAST) is defined and the boundary conditions applied to the representative cell are presented in order to highlight the parameters needed from the sensors. This loading is required to apply the right stress and strain fields to the mesoscopic simulation.

Direction	LAGAMINE	THERCAST	Loading applied on the mesoscopic cell
Large face direction	**X**	*Y*	**Fx**=Ly · *EPSzz* · Lz · *EPSxx* · *SIGyy*
Casting direction	**Y**	*Z*	**Fy**=Lx · *EPSyy* · Lz · *EPSxx* · *SIGzz*
Small face direction	**Z**	*X*	**Dz**=Lz · *EPSxx*

Table 5.3: Correspondence of the reference frames for THERCAST and LAGAMINE codes and calculation of the forces to apply to the representative cell, with representative cell size Lx, Ly and Lz as defined in Section 3.3

In order to calculate the forces and the displacements imposed on the representative cell, the complete stress and strain tensors are required. The stress components σ_{xx}, σ_{yy} and σ_{zz} are computed as the average stress values of the four nodes. The strain components ε_{xx}, ε_{yy} and ε_{zz} used in Table 5.3 are calculated from the nodal positions that are changing according to the time and to the position in the continuous caster.

5.3.2 Calculation of the strain field

The results of the strain tensor as a function of the nodal displacement for one case are compiled in Figure 5.11.

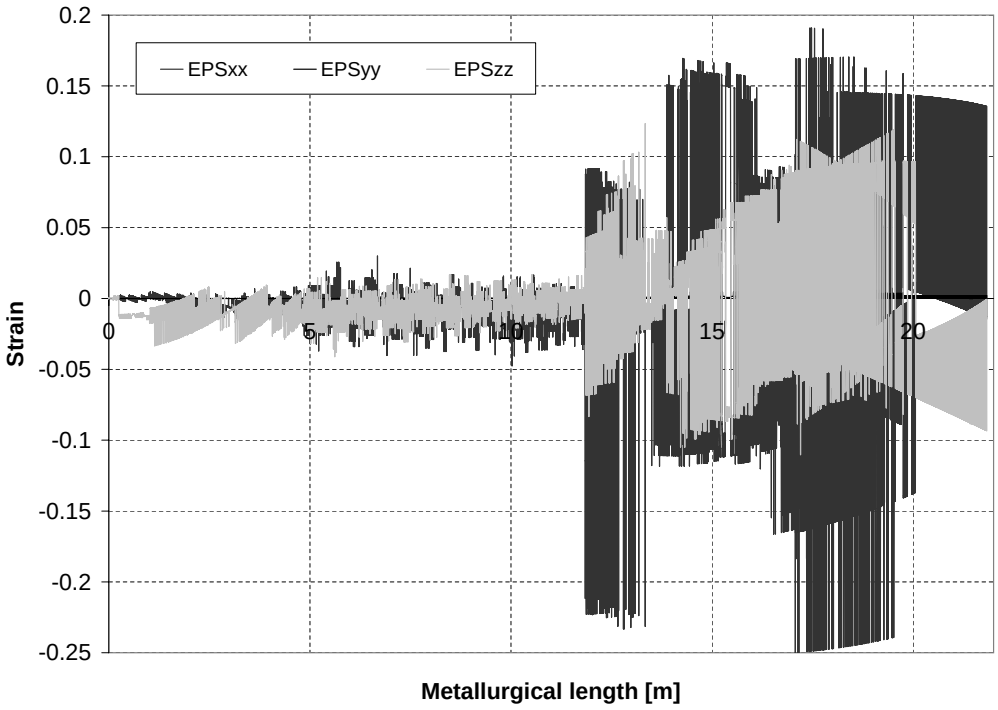

Figure 5.11: Strain field obtained through calculations of the tetrahedron nodes displacement

Huge noise can be seen on the curves. A mean tendency is difficult to find. Such results could not be exploited because of the sensitivity of the damage model to the strain rate,

The amplitude of the variation is not correlated to the roll position or to variation of the values of the heat transfer coefficient. Such cyclic correlation will be shown in Figures 5.15 and 5.16 on stress components values. Here, non physical perturbations are reported.

In order to improve the data transfer between THERCAST and LAGAMINE, the noise on the strain data has to be understood. The lack of precision in the THERCAST output parameters is the key point. The output values are given in scientific form and in meters with a precision of five significant digits as shown on the extract of the data table put in relation with the equivalent stress calculation (Figure 5.12).

When the position of one node is between 1 and 9.99m, the precision in mm is 10^{-1}. When the position is over 10m, the precision is 1mm. The tetrahedron initial nodes position is compiled in Table 5.4 that means approximately an edge size of 5mm. With such a precision of about 1mm, the results are not accurate enough to compute th correct strain tensor. To study the damage in the mesoscopic cell with total confidence,

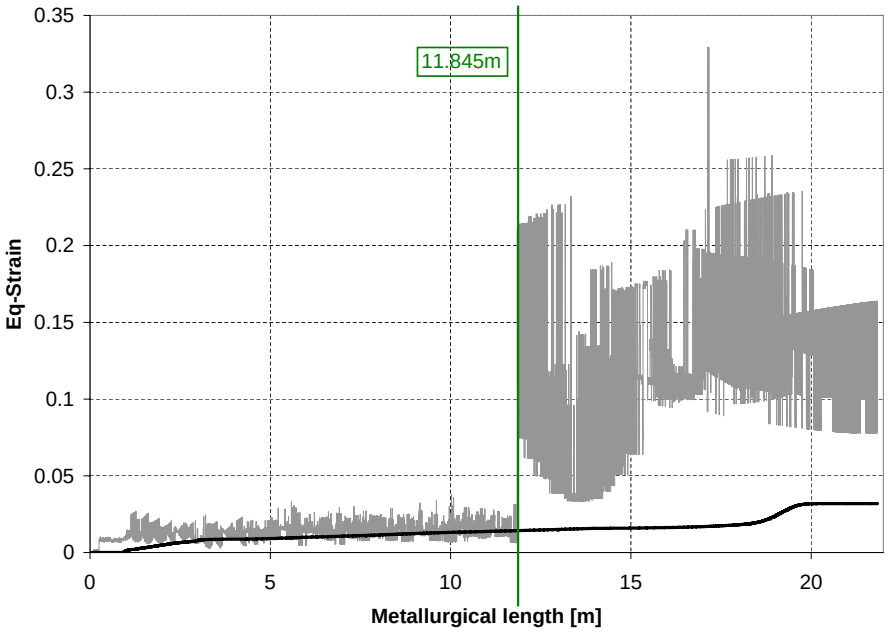

(a) Equivalent strain calculation

Time	POSITION_X	POSITION_Y	POSITION_Z	Met Length
1513.2	5.244100	1.037000	-9.985500	11.820000
1513.6	5.246800	1.037000	-9.987400	11.823000
1514.0	5.249500	1.037000	-9.989300	11.826000
1514.4	5.252200	1.037000	-9.991200	11.830000
1514.8	5.255000	1.037000	-9.993000	11.833000
1515.2	5.257700	1.037000	-9.994900	11.836000
1515.6	5.260400	1.037000	-9.996800	11.840000
1516.0	5.263100	1.037000	-9.998700	11.843000
1516.4	5.265800	1.037000	**-10.001000**	11.846000
1516.8	5.268500	1.037000	**-10.002000**	11.850000
1517.2	5.271200	1.037000	**-10.004000**	11.853000
1517.6	5.273900	1.037000	**-10.006000**	11.856000
1518.0	5.276600	1.037000	**-10.008000**	11.860000
1518.4	5.279300	1.037000	**-10.010000**	11.863000
1518.8	5.282000	1.037000	**-10.012000**	11.866000
1519.2	5.284700	1.037000	**-10.014000**	11.870000
1519.6	5.287500	1.037000	**-10.015000**	11.873000
1520.0	5.290200	1.037000	**-10.017000**	11.876000
1520.4	5.292900	1.037000	**-10.019000**	11.880000
1520.8	5.295600	1.037000	**-10.021000**	11.883000

(b) Data extract from THERCAST

Figure 5.12: Equivalent strain calculation results compared to the data provided by THERCAST

one should have access to more accurate results.

X	Y	Z	Position
-0.15	1.06008	0.790638	Surface node
-0.15	1.05286	0.790693	
-0.15	1.05616	0.785325	
-0.147141	1.05581	0.790976	Inner node

Table 5.4: Initial nodes position in m of the center extrados case sensor

It has been decided to simplify the strain results. The mean value of the strain is calculated over the whole process. The results have been divided into two parts. The first one is not influenced by the cooling profile change (See Figure 5.13) while the second part starts just before the cooling profile change. This way, the results obtained in the first part remain exactly the same between the reference and the modified cooling profiles and the strains in the second part are representative of the different cooling strategies.

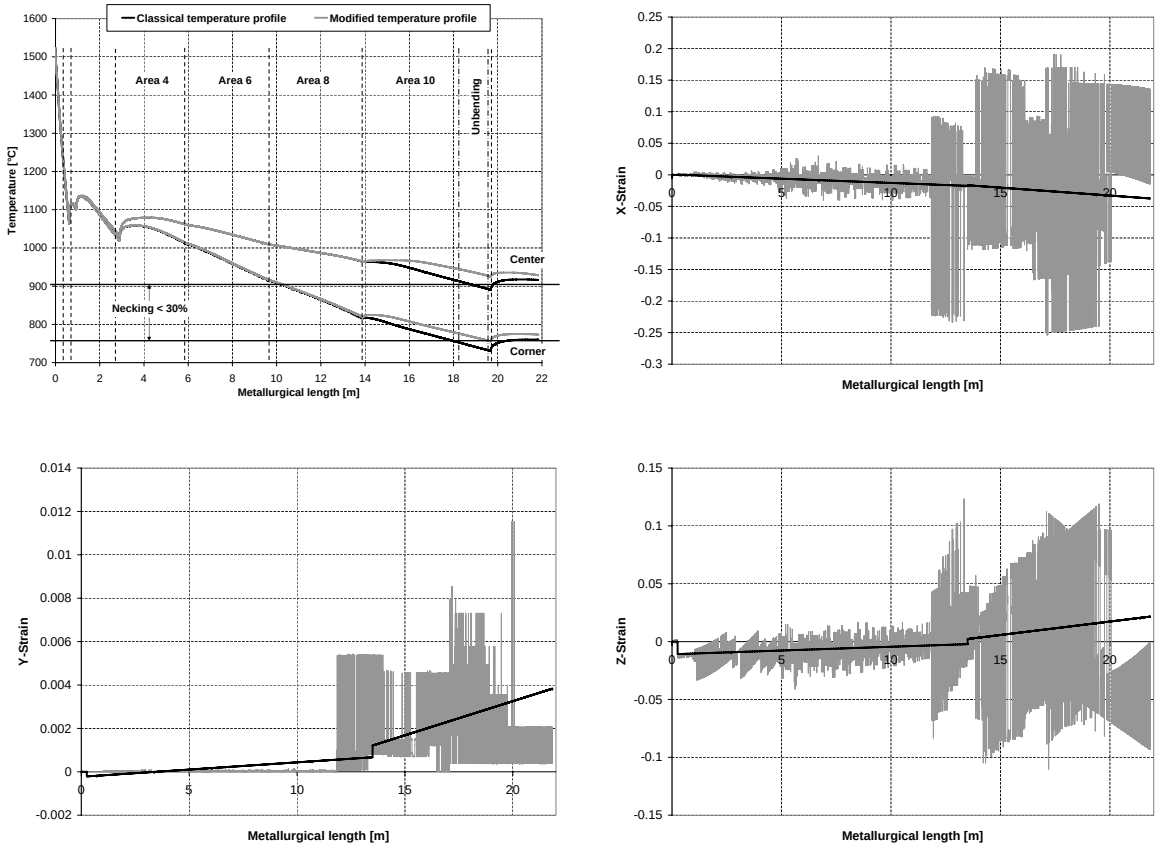

Figure 5.13: Results of the calculated strain components of the slab center intrados with the classical cooling profile (black line) that will be used for the representative cell loading

To conclude to this section, some improvements have definitively to be made in the field of the THERCAST output results. The best way to solve this problem is to have

directly the strain field as an output data. This is possible but not within this thesis as the available version of THERCAST gives no access to the result output format, this option not yet being implemented in the user interface.

5.4 Data transfer validation

5.4.1 Classical transfer to the representative cell

The classical way to transfer the macroscopic results to the representative cell has been defined for the rheological parameters definition. The forces are imposed on the edges of the cell in the X and Y directions and the displacement is prescribed on the thickness of the cell, the Z direction as presented hereafter:

- **Fx**=Ly · *EPSzz* · Lz · *EPSxx* · *SIGyy*
- **Fy**=Lx · *EPSyy* · Lz · *EPSxx* · *SIGzz*
- **Dz**=Lz · *EPSxx*

Important remark : Hereafter, all the results are expressed in the representative cell reference frame (Figure 5.14).

- X = transverse direction in CC
- Y = casting direction in CC
- Z = thickness in CC and in the cell (generalized plane strain)

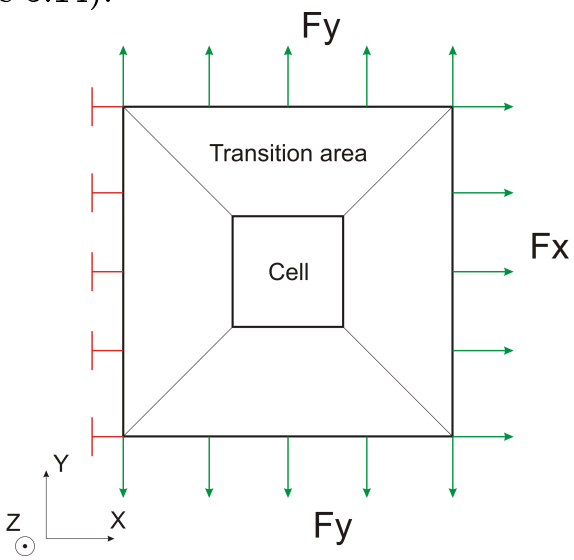

Figure 5.14: LAGAMINE reference frame

In order to validate the transfer, the THERCAST and LAGAMINE stress curves are compared in each direction of the representative cell (Figure 5.15).

Looking at the stresses comparison in the X and Y directions, the correlation is very good when passing from macroscopic to mesoscopic simulation. It is possible to remark that when the stress changes brutally or when the stress slopes are steep, the LAGAMINE simulation calculated stress level is shifted. This point can be avoided by decreasing LAGAMINE time steps. Nevertheless, this accuracy is sufficient to validate the data transfer from THERCAST to LAGAMINE in the X and Y directions. As seen in Figure 5.16, zoom of the X-stress comparison (Figure 5.15), even the smallest variations are reproduced by the calculation.

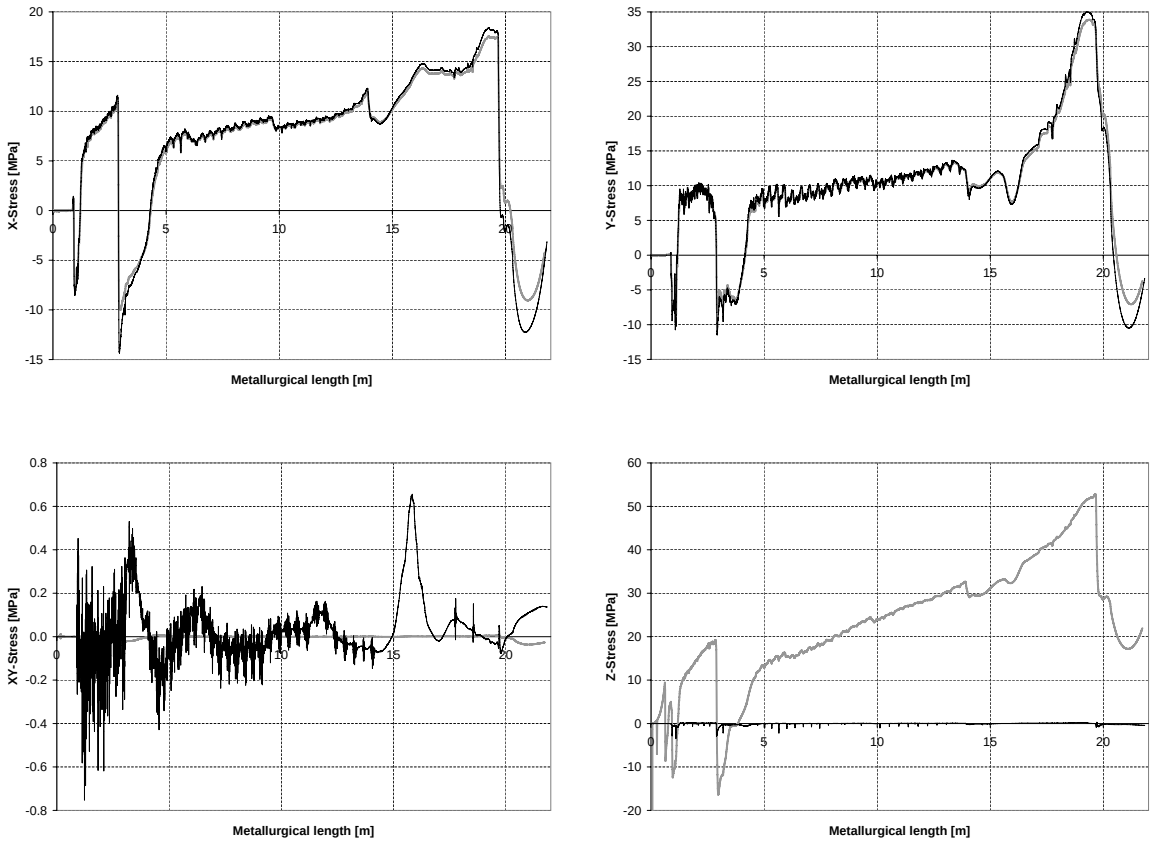

Figure 5.15: Stress fields comparison between THERCAST and LAGAMINE of the slab center intrados with the classical cooling profile (THERCAST, black - LAGAMINE, grey)

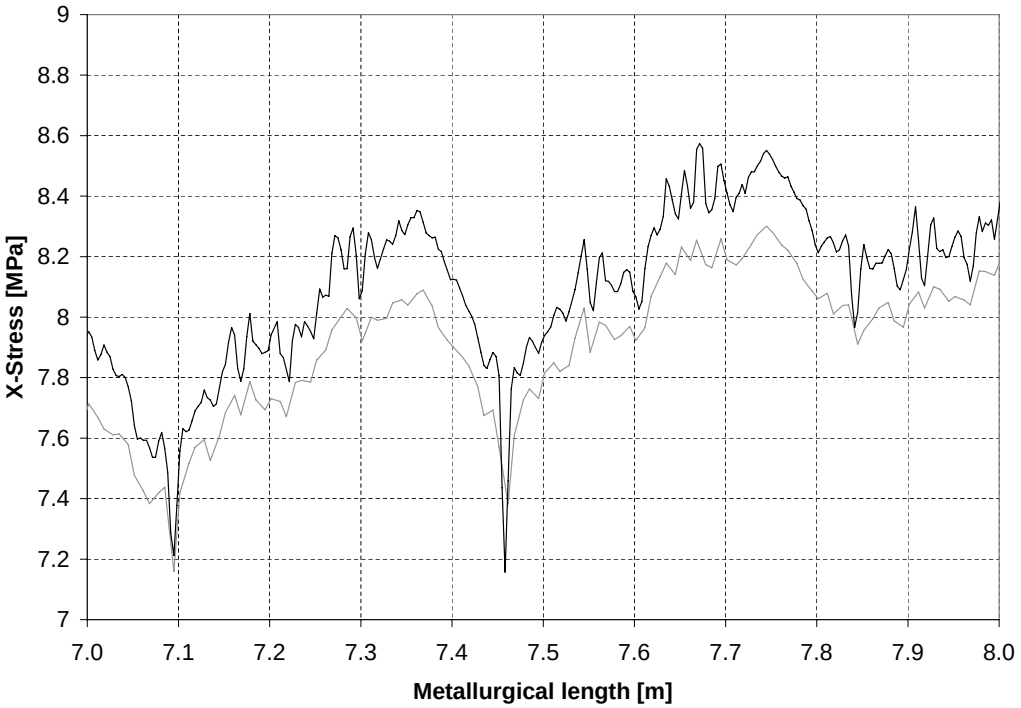

Figure 5.16: Zoom on the stress field comparison

Indeed, each time the slab passes from one roll to the other or from one cooling spray to the other, the stress and the strain tensors are affected. This fact is shown by the cyclic variation of the stress level. This variation is quite well transmitted to the representative cell. The stress cycles and the roll positions have not been deeply analyzed in this study but they could be the starting point of an improvement of the strain field calculation. More accurate strain mean values could be reached by calculating the mean strain for each roll and cooling changes in order to take physical variation of the strain components into account.

Now watching at the shear stress values (XY-stress), the initial hypothesis neglecting this stress is validated. Indeed, the shear does not reach the level of 1MPa of stress and thus it is not predominant compared to the stresses in X and Y directions.

Beside all these good values, the LAGAMINE stress in Z direction does not fit at all to the expected ones of THERCAST. The THERCAST macroscopic model expects more or less no stress in this direction, when LAGAMINE gives a stress almost equivalent to the one in the X and Y directions. The LAGAMINE Z-stress reaches 50MPa at the end of the simulation.

This difference could be explained by the way the boundary conditions are imposed in this direction. Indeed, the Z direction is driven by the displacement. In the displacement calculation only the strain in THERCAST X direction (slab thickness direction) is taken into account. As an important approximation on this value is expected, leading to high divergence with the wanted stress value. This error has to be fixed before to compute new LAGAMINE calculations.

5.4.2 Transfer tests done on one element

In order to check the data transfer from THERCAST to LAGAMINE, the forces and displacements are imposed to a unique solid element without damage interface element. These interface elements could interact with the final element stress level and thus, possible errors of the LAGAMINE program are reduced when one uses one single solid element.

For this data transfer study, four different boundary conditions on Z direction are studied. All the different configurations of Table 5.5 are used to reach the wanted stress field in the representative cell.

In the directions X and Y, no change of stress level could be observed. The predicted Z-stress curves are compiled in Figure 5.17.

SOLUTION A

The Figure 5.17(a) shows the result when the classical boundary condition is imposed. The displacement is calculated through THERCAST data and imposed to the node defining the generalized plane strain degree of freedom (thickness of the slice). In this case the Z-stress obtained by the LAGAMINE calculation does not correspond to the THERCAST output as seen before on the representative cell.

Direction	LAGAMINE	THERCAST	Loading applied on the mesoscopic cell
Wide face direction	**X**	*Y*	**Fx**=Ly · *EPSzz* · Lz · *EPSxx* · *SIGyy*
Casting direction	**Y**	*Z*	**Fy**=Lx · *EPSyy* · Lz · *EPSxx* · *SIGzz*
Narrow face direction	**Z**	*X*	A. **Dz**=Lz · *EPSxx* B. **Fz**=Lx · *EPSyy* · Ly · *EPSzz* · *SIGxx* C. **Dz**=0 D. **Dz**=free of any displacement

Table 5.5: Correspondence of the reference frames for THERCAST and LAGAMINE codes and calculation of the forces to apply to the representative cell, with cell size Lx, Ly and Lz

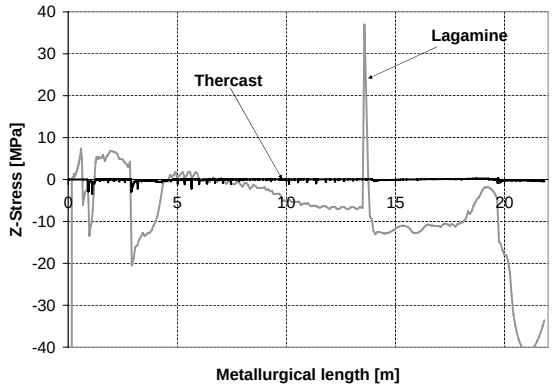

(a) **Dz**=Lz · *EPSxx*

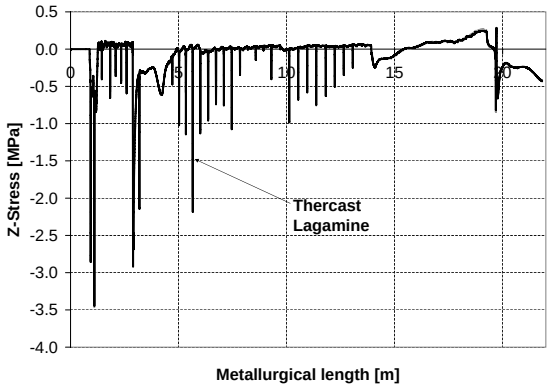

(b) **Fz**=Lx · *EPSyy* · Ly · *EPSzz* · *SIGxx*

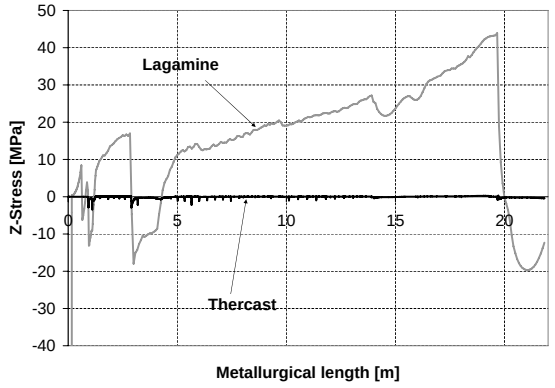

(c) **Dz**=0

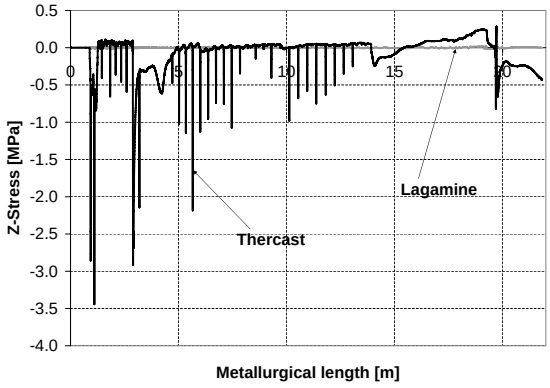

(d) **Dz**=free of any displacement

Figure 5.17: Z-stress configuration comparison of the slab center intrados with the classical cooling profile (THERCAST, black - LAGAMINE, grey)

Solution b

The first tested alternative is to apply the third force. So, forces are imposed in each direction to the element. As expected, the results obtained (Figure 5.17(b)) is that the two curves (Thercast and Lagamine) overlap perfectly (one curve to be seen in Figure 5.17(b)).

This can be explained by the fact that **Fz** calculated value is stress dependent. The stresses present higher accuracy than the strains. Thus, the forces precision is increased by the use of this boundary condition.

Unfortunately, the data transfer from Thercast to Lagamine with the boundary condition b is not possible when increasing the number of elements of the cell. The implicit iterative calculation does not converge due to the fact that when the thickness node moves, the Z-stress changes in each element. The out-of-balance force in Z direction is calculated and never reaches zero as it should be at equilibrium. The forces reached in each element should be the one imposed whereas for the moment it is the mean value of the whole cell that is taken into account.

One test has been performed on a cell containing 100 elements and no damage element. The results at the beginning of the simulation corresponds to the ones of the macroscopic simulation. Nevertheless this simulation had to be stopped because the calculation did not converge due to the important amount of elements to compute in the Z direction.

Solution c

Because of the impossibility to use solution b to transfer the data, other possibilities have been checked. Figure 5.17(c) shows the results of the Z-stress when the displacement in Z direction is prevented (plane strain condition). In this case , the mesoscopic stresses diverge from the macroscopic stresses and thus, this solution is not usable.

Solution d

The last solution, d, is to impose nothing in Z direction. The slice thickness degree of freedom is free. In this case, one observes that the Z-stress computed stays approximately at a value of 0MPa (Figure 5.17(d)). This solution has also been tested on the representative cell but with the same issues than the solution with the force imposed. No convergence could be reached.

Conclusion

In order to improve the final results, the data transfer from the macroscopic simulation to the mesoscopic one should be improved (correct ε_{zz}, see accuracy problems in Thercast results Section 5.3.2). Nevertheless, qualitative results are given hereafter with the no-displacements solution c (assumption of plane strain) for all the cooling cases studied at each position in the slab for **C** continuous caster.

5.5 Damage results for the CC application on C grade

The following calculations are made with the following boundary conditions in order to obtain qualitative results on the damage behavior for different cooling cases in several areas of the slab produced on the **C** continuous caster.

- **Fx**=Ly · *EPSzz* · Lz · *EPSxx* · *SIGyy*
- **Fy**=Lx · *EPSyy* · Lz · *EPSxx* · *SIGzz*
- **Dz**=0

The results of the representative cell simulation for all the cases studied in this thesis are given in Figure 5.18. The damage plotted along the metallurgical length is the maximum damage value (a/b) happening within all the interface elements representing the grain boundaries.

Comparing first the curves for each separated case, one can observe that the center of the slab is more sensitive to the cooling profile modification than the corner. To explain this, it is interesting to go back to the stress curves (Figures 5.8(a) to 5.8(d)) that show a stress level modification in the center of the slab, while in the corner, a only slight difference is observed.

The cooling profile difference mainly helps to decrease the stresses in the center from tensile stresses to compression ones. This is the main reason why the damage decreases at this place. Indeed, tensile stresses lead to an opening of the cavities around the precipitates while compression delays the damage increase.

In Figures 5.18(a) and 5.18(c), the damage between 14 and 17m decreases with the modified temperature profile. The cavities are not able to grow as this part remains in compression state (Figures 5.8(a) and 5.8(c)).

On the contrary, in Figures 5.18(b) and 5.18(d) that represents the corner of the slab, no difference on the damage curves is seen for the two different profiles. This observation can be correlated to the stress field obtained by THERCAST, where the difference is not as marked in the corner as in the center of the slab.

Looking at the curves in general, the conclusion that the intrados damage is higher can be drawn. Indeed, high stresses are reached when unbending the slab and this in a temperature range that is particularly detrimental to the material.

Finally, the damage is also higher in the corner of the slab. Due to higher triaxiality differences (Figures 5.8(b) and 5.8(d)), the damage increases faster in the corner.

It should also be mentioned that the damage level reached at the end of the process is more or less 0.02 except for the slab corner intrados where it reaches almost 0.05. These values are far from the 0.5 threshold value chosen for crack prediction. This observation confirms that the results obtained here are only qualitative ones and should be validated since cracks are detected in these conditions in the actual process.

The fact that a tensile stress is applied in the Z direction instead of the one calculated by THERCAST (almost zero) should increase the damage developement.

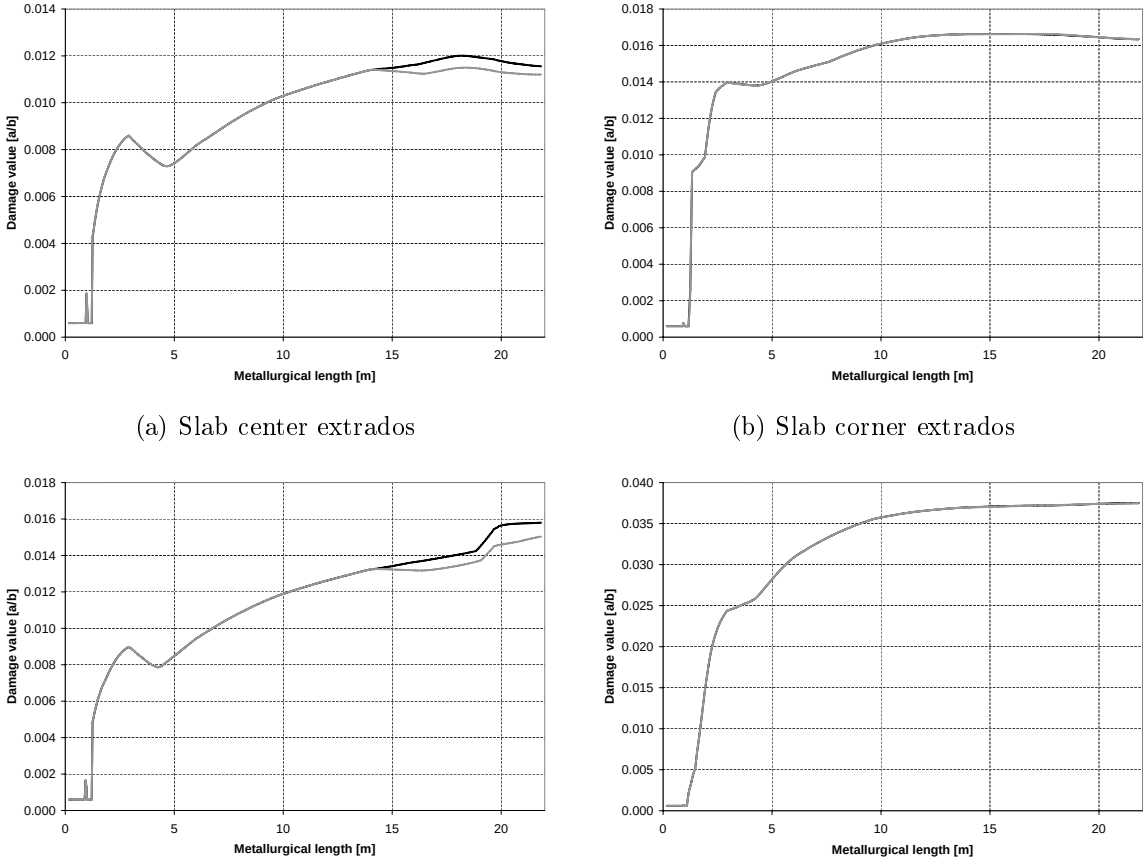

(a) Slab center extrados

(b) Slab corner extrados

(c) Slab center intrados

(d) Slab corner intrados

Figure 5.18: Damage comparison between cooling strategies (Classical temperature profile, black - Modified temperature profile, grey)

So the too low damage result seems quite unexpected and not logical. The components σ_{xx} and σ_{yy} in Figure 5.15 and 5.16 are well reproduced. Where could be the error?

→ In the macroscopic THERCAST model :

A. boundary conditions

B. rheological law

→ In the LAGAMINE damage model :

C. model theory of the damage mechanisms modeling

D. parameters identification

ERROR A OR B

Additional experimental results such as the force measurements during the CC process could validate both, the rheology B and the boundary conditions A. However, we did not have access to these results.

ERROR A

The fact that tensile and compression tests performed in two different laboratories give consistent results in agreement for the model simulation until 20% of strain is in favor of a validated rheological model A.

As well as the fact that Koslowsky phenomenological model already used by the industrial partner predicts stress-strain curves close to the model used.

An opposite conclusion could be derived from the fact that for **C**, only 9 over 18 test simulations give force-displacement curves similar to the experimental one. It is representative of a bad rheological law or a too low amount of tests to be representative of the actual material behavior. Let us remind that due to the cost, each test has been performed only once.

ERROR C

What about the damage model itself? It neglects phase transformation and appearance of ferrite film around the grain. One should perhaps couple the model to phase transformation prediction which could be expressed by a strong variation of some damage model parameters like $\dot{\varepsilon}_e/\dot{\varepsilon}_B$ parameter for instance assumed constant here.

The fraction of strain rate present within the grain core and the grain boundary should be affected by the deep change of the boundary where thin ferrite films develop.

ERROR D

The difficult task of finding a consistent set of parameters as well as the lack of statistics within our experimental data explain that the damage parameter set is far from being totally reliable and needs additional investigation.

5.6 Conclusions on the practical case

The caster of **C** has been faithfully model in a macroscopic scale. The mold, the rolls and the several spray systems have been implemented into the THERCAST program. Modeling sensors, the stress components and temperatures are recorded at each moment of the CC process. Various cases have been studied in order to determine how to avoid the transversal crack event. One process improvement should be reached by the modification of the cooling profile in the continuous caster. By decreasing the cooling during unbending, the material is less susceptible to be damaged.

Observing the stress curves at the output of THERCAST, it could be seen that high tensions are observed in the unbending area (17-20m). These stresses are especially detrimental since the material presents a temperature between 800-1000°C. This temperature range is specific in the peritectic steel family to provoke low ductility.

In this area the cooling strategy is then modified and the stress level is decreased in the dangerous area of the continuous caster. The central part of the slab is more sensitive to this new cooling profile than the corner part.

THERCAST data have been transferred to the representative mesoscopic cell computed by the LAGAMINE program. At this scale the grains and grain boundaries are modeled and a damage law calculates the damage behavior in the representative cell. The data transfer presented some issues that have not been entirely solved yet.

- The results of the strain field within THERCAST has to be more accurate in order to get the stress variations due to the continuous caster rolls and sprays.
- The precision of the output records of THERCAST has to be improved.
- The prescription of forces in the three space directions should be made possible by a more robust implicit approach or an explicit approach could be developed.

Due to these calculation problems, the last part of the work which is the comparison between classical and modified profile has been made with partially wrong stress values (only in Z direction). These first results give qualitative values for the comparison.

Even if the damage results are qualitative ones, the results obtained seem to be quite logical. Nevertheless, it is necessary to validate these conclusions with a good data transfer between both THERCAST and LAGAMINE software.

The final application on the **C** continuous caster has been done for 8 cases detailed in Table 3.8. It has been observed that with a softer cooling at the end, the rate of defect decreases in the center part of the slab when in the corner the effect is negligible.

In the corner it has been observed that the damage is higher than in the center. So, process improvements should be made in order to reduce the damage in the corner by giving another way to modify the cooling profile at this particular place of the slab. If, as assumed, the different behaviors in central and corner parts are due to a higher temperature gradient in the center, one should think about how to locally increase the temperature gradient.

Conclusion and perspectives

Sylvie Castagne developed during her thesis [Cas07a] a damage model based on the opening of the cracks at the grain boundary by modeling interface elements coupled with a specific damage law. This damage model has been developed and validated on microalloyed steels. The aims of this study were:

- to extend the model for crack prediction at the grain scale, referred to as the mesoscopic scale, to peritectic and stainless steel grades;
- to validate it in order to obtain a model able to predict the crack appearance as a function of different parameters such as the composition and the thermo-mechanical paths;
- to analyze the case of the **C** continuous caster with different cooling strategies.

Achievements

The first step of this study was to choose in a clever way the different steel grades in order to study the aimed effects on the crack appearance in CC slabs as the precipitation state or the ferrite level crack dependence.

From the 5 first selected steel graded (3 peritectic and 2 stainless steels), the work focused on the peritectic steels. This limitation has been governed by time and cost considerations. From the cost point of view, only the 3 peritectic steel grades could have been investigated deeply. Despited all the efforts, the investigations were still not sufficient.

- only one experiment was performed on each tensile test configuration for the damage parameters identification
- no statistical micrographic investigation on precipitates could have been achieved because of lack of time and budget.

Nevertheless, three peritectic steel grades were particularly chosen for their sensitivity to crack appearance and for their different microstructures due to the steel composition that affects the precipitation quantity, size, position, shape, the moment of appearance of precipitates and ferrite in the matrix, as well as the ductility trough position and deepness.

An important survey of literature has been achieved at the University of Liège, but also in the different Research centers of ArcelorMittal Metz and Isbergues and at the Research Institute in Aachen. All these different parts brought their own contribution to a better knowledge of the problem. The numerical simulation and the microscopic analyses parts essentially came from Liège, the practical knowledge was brought by the industrial partners whereas the IEHK in Aachen offered more specialized skills in metallurgy and experimentation technics.

The performed literature review helped to confirm the fact that the transversal cracks appearing in the CC slab after the process are intergranular and their formation mechanism is known. The cracks propagate by cavitation at the grain boundaries and by grain sliding. The cavitation has been explained by void nucleation, growth and coalescence. The cavities mainly evolve by diffusion and creep deformation at elevated temperatures.

Moreover, an effect of the thin ferrite film formed along the grain boundaries has been detected and enhances the cracking process.

These fracture mechanisms are taken into account through the model developed by S. Castagne that enables the evolution of a crack between grains of the steel matrix. The ferrite film formation could be better modeled by a correct set of parameters and the definition of their temperature dependence could allow modeling this phenomenon.

Before starting the experimental mechanical tests, a study of the thermal path that should be applied to the sample has been done. The first idea was to melt the sample before testing in order to obtain the desired microstructure. Unfortunately this thermal path had to be rejected since it generates an arbitrary defect named shrinkage hole in the tensile test sample. At the end, the study proved that it is possible to obtain the microstructure of a peritectic grade in CC conditions thanks to a simple thermal path performed in the hot tensile testing machine prior to the loading.

The rheology of each studied steel grade has been determined (for the five steel grades, peritectic + stainless). Hot tensile tests on smooth samples allowed characterizing the ductility trough position and deepness. The rheological Norton-Hoff law parameters, that represents physically the material behavior, have been determined for the three peritectic steel grades studied with the help of hot tensile tests and confirmed by compression tests. The study of the parameters showed the consistency of the defined parameters.

The numerical study of the sensitivity to the damage law parameters has shown that some parameters like the cavity tip angle Ψ, the initial cavity density for appearance of nucleation N_I and the threshold of the end of the nucleation N_{max} play an important role in the evolution of the damage. These parameters are thus easy to identify with a few mechanical tensile tests but they also have to be set with high accuracy because of their strong influence on the damage level.

Nevertheless, these results should have been determined by microscopic analysis in order to leave less uncertainties in the damage parameters determination. A better microscopic investigation could have been designed in order to improve this point.

The damage parameters for each peritectic steel have been determined through literature, microscopic analysis and hot tensile test experimentation. The parameters of the damage law are physical parameters. Some of them can be determined through

experimental testing.

A test campaign at three different testing temperatures, with three different testing sample shapes, and three different strain rates has been performed. A total amount of about 30 tests for each steel grade have been driven in order to determine as accurately as possible the damage parameters for each steel grade.

The relation between the damage parameters and the chemical composition of the several steels have been investigated and the physical aspect of the damage law has been validated. This part is made difficult by the fact that the steel grades are coming from the industry. Not only the studied components (Nb and V) do show an effect on crack appearance, but also others as Ti or Al do hide or enhance the effect on damage. From this point of view, the use of laboratory melts would have been easier to exploit.

Nevertheless, the composition comparison has been actually performed on industrial steel grades and thus, even if the damage parameters determination has been affected, the set of damage parameters could have been validated on a practical case. The two other steel grades (**A** and **B**) have to be continued in order to compare the components importance.

The ultimate goal of the study was to apply the determined rheological and damage parameters to one practical case of transversal crack in continuous casting and to validate the parameters.

Due to data transfer issues from the macroscopic model to the mesoscopic one, the conclusions driven from this study are qualitative as we still have a some troubles with the damage level prediction. Nevertheless, the damage evolution obtained through the practical case are consistent with the one expected and it gives an overview of the damage in the steel slab produced by CC.

At the end, the LAGAMINE mesoscopic representative cell has been delivered to the industrial partner with all the important tools necessary to the transfer between THERCAST and LAGAMINE.

In order to summarize, the following capital points have been achieved:

- The rheological parameters have been determined for five steel grades;
- A new methodology for the determination of the damage law parameters by hot tensile tests have been exposed and applied;
- The correlation between chemical composition and mechanical properties (ductility trough study) has been established;
- The mesoscopic tool has been provided to the industrial partner;
- A qualitative study of the crack appearance has been performed on one steel grade (**C**) according to the CC conditions.

Future work

The determination of the rheological and the damage parameters by hot tensile tests is the originality of this study. Nevertheless, operating this way, some troubles were encountered. Indeed, the determination of all the steps of the damage path was not possible. This could be avoided by the use of acoustic recording of the crack on the hot tensile test apparatus in order to detect the crack appearance and not only the damage moment.

The results presented in this study show that a multi-scale model of crack formation is ready to be used for the prediction of the fracture during continuous casting. Nevertheless, some numerical issues still have to be solved in order to obtain quantitative results on damage.

- At first, at a macroscopic scale, the reliability of the output results have to be improved by higher number of experimental tests in order to provide more accurate data to the mesoscopic scale simulation.
- The second key point is the development of a more robust implicit scheme on the global non linear FE code to model the representative cell with applied forces in the three space directions. This could help to obtain more accurate stress and strain results in each direction and thus quantitative damage results.
- An other solution could be to model the representative cell in three dimensions an thus to apply the forces in the three directions of space on every transition area edge node.

In order to extend the capabilities of the damage law used in this study, the stainless steel family could be studied. At the beginning of this thesis, the characterization of the damage in stainless steels was one of the aims as transversal cracks also affect them. Due to the time constraint and experimental issues, the study has been stopped after the determination of the rheological parameters which were defined.

In a further step, the damage law identification should ideally be performed by taking into account the two different phases (ferrite and austenite) present in the material in CC conditions. Some parameters (viscosity between grain and grain boundary $\dot{\varepsilon}_e/\dot{\varepsilon}_B$ for instance) could be modified when ferrite appears.

The phase transformation could be in a simplified way just dependent on a temperature threshold (identified through an experimental cooling similar to the actual one) or relying on a phase transformation model.

The model could be applied with parameter such as N_I or the nucleation length N_{max}/N_I defined with a gradient in order to simulate an heterogeneous density of carbides that differs in shape, size and especially frequency from the surface of the slab to the center.

Of course, additional information gathered on **C** case such as the following would be welcomed:

- force measurements during continuous casting process for validation of the macroscopic model;

- statistical microscopic analysis to get more reliable values of the cavity size a_0, the cavity interdistance b_0, N_I, N_{max} with average and standard deviation values;
- phase transformation investigation on **C** grade;
- additional tensile tests on identical sample geometry and on sharper notches, to improve the damage parameters identification step and to validate the set of parameters

This deeper investigation should help to provide a model predicting damage consistent with the industrial investigation.

Bibliography

[Ash72] M.F. Ashby. Boundary defects and atomistic aspects of boundary sliding and diffusional creep. *Surface Science*, 31:498–542, 1972.

[Ber04] M. Béres, T.E. Weirich, K. Hulka, and J. Mayer. TEM investigations of fine Niobium precipitates in HSLA steel. *Steel Research International*, 75(11):753–758, 2004.

[Ble04] W. Bleck. *Werkstoffkunde Stahl - für Studium und Praxis*. IEHK - RWTH, 2004.

[Bri77] J. K. Brimacombe and K. Sorimachi. Crack formation in the continuous casting of steel. *Metallurgical Transactions, Process Metallurgy*, 8B:489–505, 1977.

[Cas07a] S. Castagne. *Finite element mesoscopic analysis of damage in microalloyed continuous casting steels at high temperature*. PhD thesis, Université de Liège, 2007.

[Cas07b] S. Castagne, D. Talamona, and A.M. Habraken. A damage constitutive law for steel at elevated temperature: Identification of the parameters. *International Journal of Forming Processes*, 10(1):23–43, 2007.

[Col85] T.H. Coleman and J.R. Wilcox. Transverse cracking in continuously cast HSLA slabs - Influence of composition. *Materials science and technology*, 1:80–83, 1985.

[Con01] L. Condamin. Criquabilité superficielle en coulée continue: Mécanismes et actionneurs. Technical report, ARSA, 2001.

[Cos04] F. Costes. *Modélisation thermomécanique tridimensionnelle par éléments finis de la coulée continue d'aciers*. PhD thesis, École des Mines de Paris, 2004.

[Cro87] D.N. Crowther, Z. Mohamed, and B. Mintz. The relative influence of dynamic and static precipitation on the hot ductility of microalloyed steels. *Metallurgical transactions*, 18A:1929–1939, 1987.

[Cru59] C. Crussard, J. Plateau, R. Tamhankar, G. Henry, and D. Lajeunesse. *Fracture*, chapter A comparison of ductile and fatigue fractures, pages 524–561. John Wiley, New York, 1959.

[Cum05] G. Cumino, A. Mannucci, M. Vedani, and J. C. Gonzalez. Solidification structure and properties of Nb-V microalloyed steels. *Super-High Strength Steels*, 2005.

[Dav04] V. R. Davé, M. J. Cola, M. Kumar, A. J. Schwartz, and G. N. Hussen. Grain boundary character in alloy 690 and ductility-dip cracking susceptibility. *Welding Journal*, Supplement to the Welding Journal:1–5, January 2004.

[Fra01] D. Francois and A. Pineau. Fracture of metals: Ductile fracture. *Physical aspects of fracture*, 1:125–146, 2001.

[Gie94] E. van der Giessen and V. Tvergaard. Development of final creep failure in polycrystalline aggregates. *Acta Metallurgica*, 42:959–973, 1994.

[Gra59] N. J. Grant. *Fracture*, chapter Intercrystalline failure at high temperature, pages 562–578. John Wiley, New York, 1959.

[Hab98] A.M. Habraken and S. Cescotto. Contact between deformable solids: The fully coupled approach. *Mathematical and Computer Modelling*, 28(4-8):153–169, 1998.

[Hei03] A. Heinrich. *Modélisation thermomécamique de la coulée continue d'acier en deux dimensions*. PhD thesis, École Nationale Supérieure des Mines de Paris, October 2003.

[Lee05] Y.K. Lee, J.M. Hong, C.S. Choi, and J.K. Lee. Continuous cooling transformation temperatures and microstructures of Niobium bearing microalloyed steels. *Materials Science Forum*, 475-479:65–68, 2005.

[Liu98] Y. Liu, Y. Kageyama, and S. Murakami. Creep fracture modeling by use of continuum damage variable based on voronoï simulation of grain boundary cavity. *International Journal of mechanical sciences*, 40(2-3):147–158, 1998.

[Lud07] K.G. Ludlow, V.and Bain, S. Riaz, K. Muller, J. Wans, G. Alvarez de Toledo, S. Zajac, and D. Senk. Precipitation of nitrides and carbides during solidification and cooling. Technical report, ARSA, 2007.

[Mae87] Y. Maehara, H. Tomono, and K. Yasumoto. Effect of notch geometry on hot ductility of austenite. *Transaction ISIJ*, 27:103–109, 1987.

[Man96] P.A. Manohar, T. Chandra, and C.R. Killmore. Continuous cooling transformation behaviour of microalloyed steels containing Ti, Nb, Mn and Mo. *ISIJ International*, 36(12):1486–1493, 1996.

[MATH] E.W. Weisstein. Voronoi diagram. From MathWorld. A Wolfram Web Resource. http://mathworld.wolfram.com/VoronoiDiagram.html.

[MATTER] http://www.matter.org.uk.

[Min79] B. Mintz and J.M. Arrowsmith. Influence of microalloying additions on hot ductility of steels. In *International Conference on hot working and forming process*, Sheffield, 1979.

[Min91] B. Mintz, S. Yue, and J. J. Jonas. Hot ductility of steels and its relationship to the problem of transverse cracking during continuous casting. *International Materials Reviews*, 36(5):187–217, 1991.

[Min93] B. Mintz and R. Abushosha. Influence of Vanadium on hot ductility of steel. *Ironmaking and Steelmaking*, 20(6):445–452, 1993.

[Min96] B. Mintz. Importance of Ar3 temperature in controlling ductility and width of hot ductility trough in steels, and its relationship to transverse cracking. *Materials science and technology*, 12:132–138, 1996.

[Min99a] B. Mintz. The influence of composition on the hot ductility of steels and to the problem of transverse cracking. *ISIJ International*, 39(9):833–855, 1999.

[Min99b] B. Mintz, A. Cowley, R. Abushosha, and D.N. Crowther. Hot ductility curve of an austenitic stainless steel and importance of dynamic recrystallisation in determining ductility recovery at high temperatures. *Materials Science and Technology*, 15:1179–1185, October 1999.

[Moh02] Z. Mohamed. Hot ductility behavior of Vanadium containing steels. *Materials Science and Engineering*, 326A:255–260, 2002.

[Mor01] H. Morand, M. Kandel, J.Y. Lamant, B. Weisgerber, M. Hecht, and K. Harste. Improvement of surface quality on peritectic and microalloyed slabs. In *ICS 2001*, 2001.

[Nee80] A. Needleman and J.R. Rice. Plastic creep flow effects in the diffusive cavitation of grain boundaries. *Acta Metallurgica*, 28:1315–1332, 1980.

[NIST] http://www.metallurgy.nist.gov.

[Onc99] P. Onck and E. van der Giessen. Growth of initially sharp crack by grain boundary cavitation. *Journal of the Mechanics and Physics of Solids*, 47(1):99–139, 1999.

[Ouc82] C. Ouchi and K. Matsumoto. Hot ductility in Nb-bearing high-strength low-alloy steels. *Transaction ISIJ*, 22:181–189, 1982.

[Pan05a] A. Pandit, A. Murugaiyan, A. Saha Poder, A. Haldar, D. Bhattacharjee, S. Chandra, and R.K. Ray. Strain induced precipitation of complex carbonitrides in Nb-V and Ti-V microalloyed steels. *Scripta Materialia*, 53:1309–1314, 2005.

[Pan05b] M. Pant. Der Einfluss von Kupfer und Nickel auf die Strangvergiessbarkeit von Warmarbeitsstahl 1.2343. In *20. Aachener Stahlkolloquium*, 2005.

[Pap03] Y. Le Papillon, W. Jäeger, M. Konig, B. Weisberger, and M. Jauhola. Determination of high temperature surface crack formation criteria in continuous casting and thin slab casting. Technical report, European Commission, 2003.

[Pas03] F. Pascon. *2D1/2 thermal-mechanical model of continuous casting of steel using finite element method*. PhD thesis, University of Liège, 2003.

[Pas06] F. Pascon, S. Cescotto, and A.M. Habraken. A 2.5D finite element model for bending and straightening in continuous casting of steel slabs. *International Journal for Numerical Methods in Engineering*, 68:125–149, 2006.

[Pas07] F. Pascon and A.M. Habraken. Finite element study of the effect of some local defects on the risk of transverse cracking in continuous casting of steel slabs. *Computer Methods in Applied Mechanics and Engineering*, 196(21-24):2285–2299, April 2007.

[Pro00] A. Prodhan, S. R. S. Reddy, and S. N. Prasad. Studies on solidification, aging and forgeability of modified stainless steels. *Journal of Materials Processing Technology*, 103:324–331, 2000.

[Rev94] T. Revaux, P. Deprez, J. P. Bricout, and J. Oudin. In situ solidified hot tensile test and hot ductility of some plain carbon steels and microalloyed steels. *ISIJ International*, 34(6):528–535, 1994.

[Sch92] K. Schwerdtfeger. Rißanfälligkeit von Stählen beim Stranggießen und Warmumformen. Technical report, European Commission, 1992.

[Sch07] R. Schwartz, S. Castagne, and A.M. Habraken. Numerical study to identify the material parameters of a damage law. *Computer Methods in Materials Science*, 7(2):237–242, 2007.

[Str07] S. Stratemeier, D. Senk, B. Böttger, E. Subasic, and K. Göhler. Simulation and modeling of hot ductility for different steel grades. In *Second STEELSIM conference, Graz*, 2007.

[Suz82] H.G. Suzuki, S. Nishimura, and S. Yamaguchi. Characteristics of hot ductility in steels subjected to the melting and solidification. *Transaction ISIJ*, 22:48–56, 1982.

[Suz84] H.G. Suzuki, S. Nishimura, and Y. Imamura, J.and Nakamura. Embrittlement of steels occurring in the temperature range from 1000 to 600°C. *Transactions ISIJ*, 24:169–177, 1984.

[Tho86] B.G Thomas, J.K. Brimacombe, and I.V. Samarasekera. The formation of panel cracks in steel ingots: A state-of-the-art review. *ISS transactions*, 7:7–20, 1986.

[Tho02] B.G. Thomas. Modeling of the continuous casting of steel - past, present and future. *Metallurgical Transactions, Process Metallurgy*, 66(6):795–812, 2002.

[Tve84] V. Tvergaard. On the creep constrained diffusive cavitation of grain boundary facets. *Journal of the Mechanics and Physics of Solids*, 32(5):373–393, 1984.

[Wol97] M.M. Wolf. Initial solidification and strand surface quality of peritectic steels. *Continuous casting*, 9:1–46, 1997.

[Yua06] X.Q. Yuan, Z.Y. Liu, S.H. Jiao, L.Q. Ma, and G.D. Wang. The onset temperatures of gamma to alpha-phase transformation in hot deformed and non-deformed Nb micro-alloyed steels. *ISIJ International*, 46(4):579–585, 2006.

[Yue95] S. Yue, J.J. Jonas, and B. Mintz. Relationship between hot ductility and cracking during the continuous casting of steel. *13th PTD conference proceedings*, 13:45–52, 1995.

[Zhu95] Y.Y. Zhu and S. Cescotto. Unified and mixed formulation of the 4-node quadrilateral elements by assumed strain method: Application to thermomechanical problems. *International Journal for Numerical Methods in Engineering*, 38:685–716, 1995.

Appendix A

Micrographs from B grade used for Thermal path determination

Description of the chemical etching

The samples have been quenched after applying the thermal path, thus the current microstructure is the one of the steel at high temperature and the austenitic microstructure is immediately visible. The samples have been etched with different solutions. However the austenitic grain boundaries are difficult to observe since the microstructure is bainitic and the grain boundaries are easier to recognize in a martensitic structure.

Micrographs

The micrographs are made in the center part of the sample where the microstructure should correspond to the target one. Indeed, it is in the center part of the sample that the fracture will occur and where the experimental values are taken.

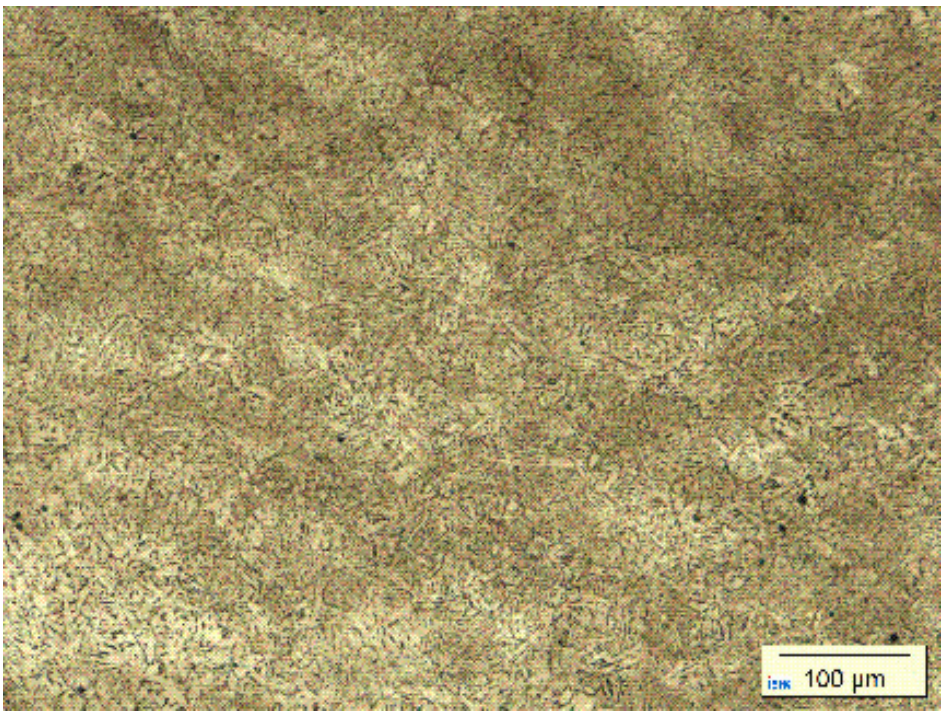

Figure A.1: **S1** - 1min, 1250°C - magnification: **200x**

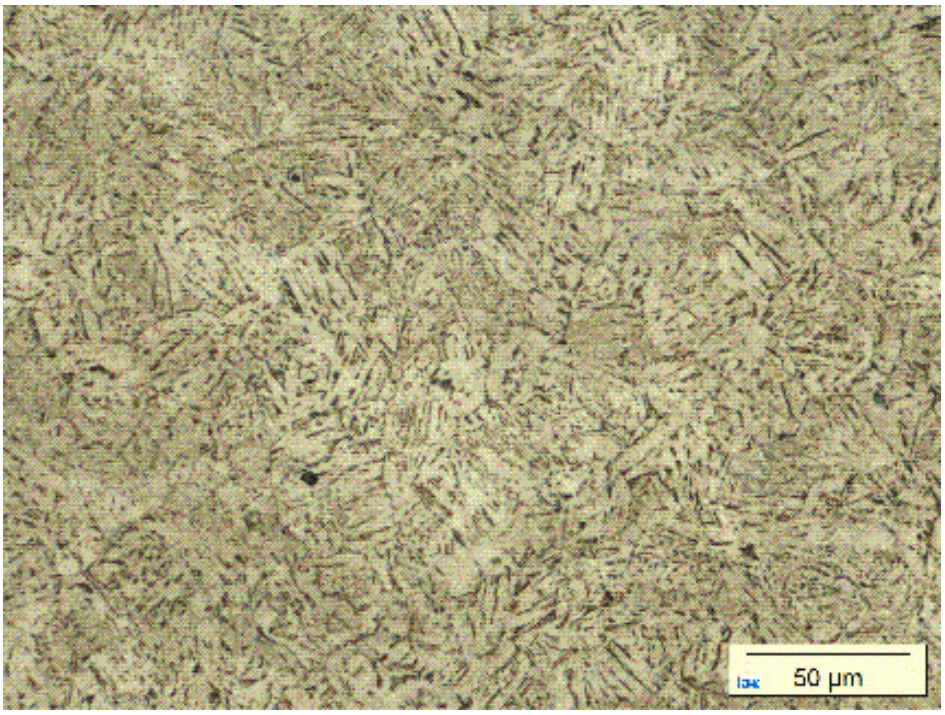

Figure A.2: **S1** - 1min, 1250°C - magnification: **500x**

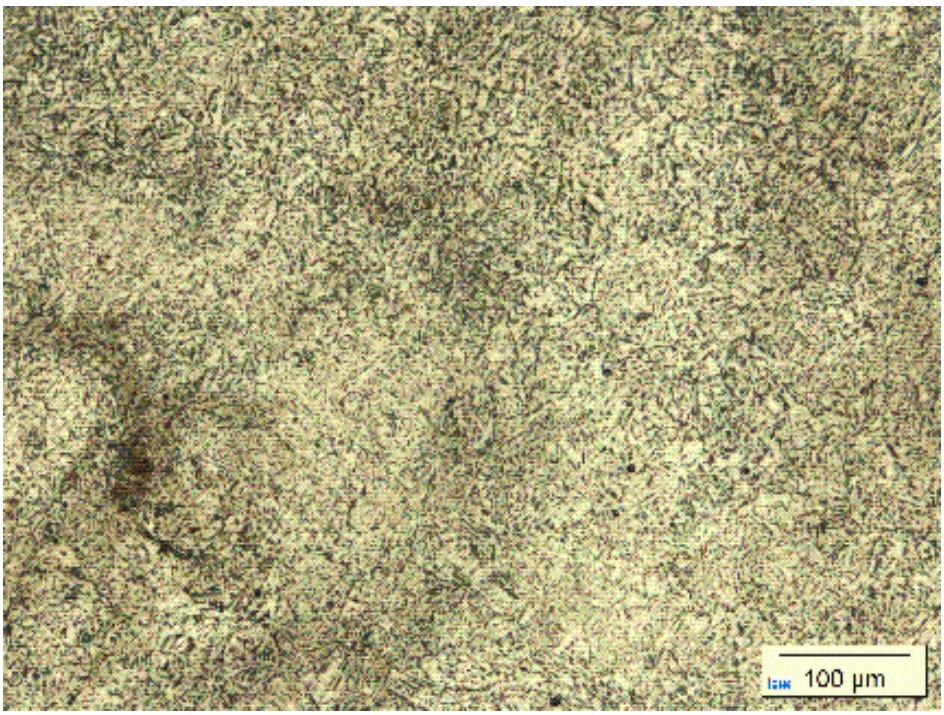

Figure A.3: **S2** - 2min, 1250°C - magnification: **200x**

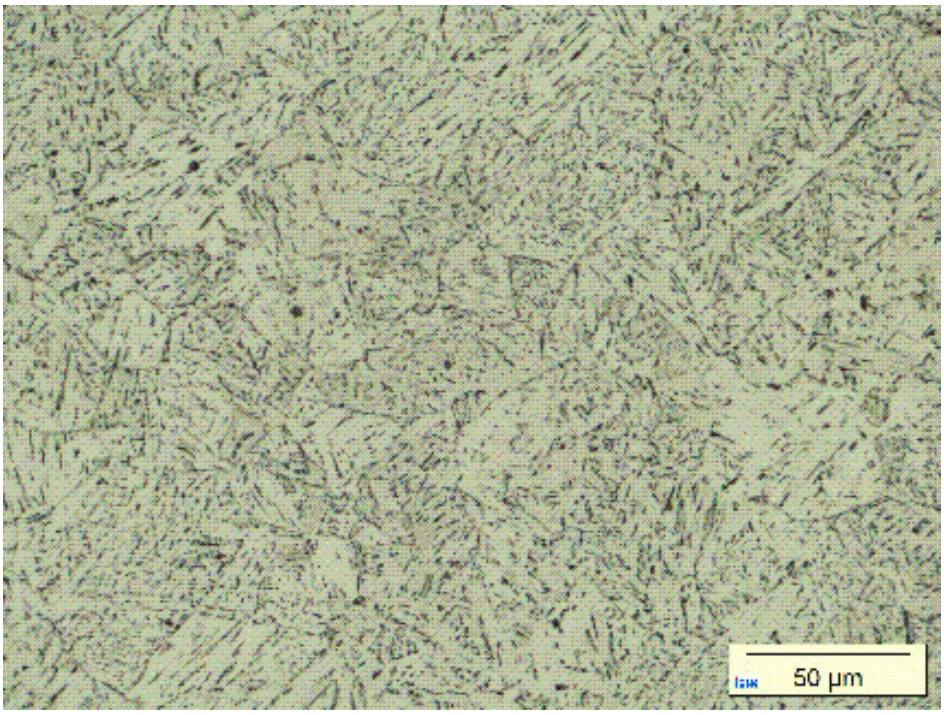

Figure A.4: **S2** - 2min, 1250°C - magnification: **500x**

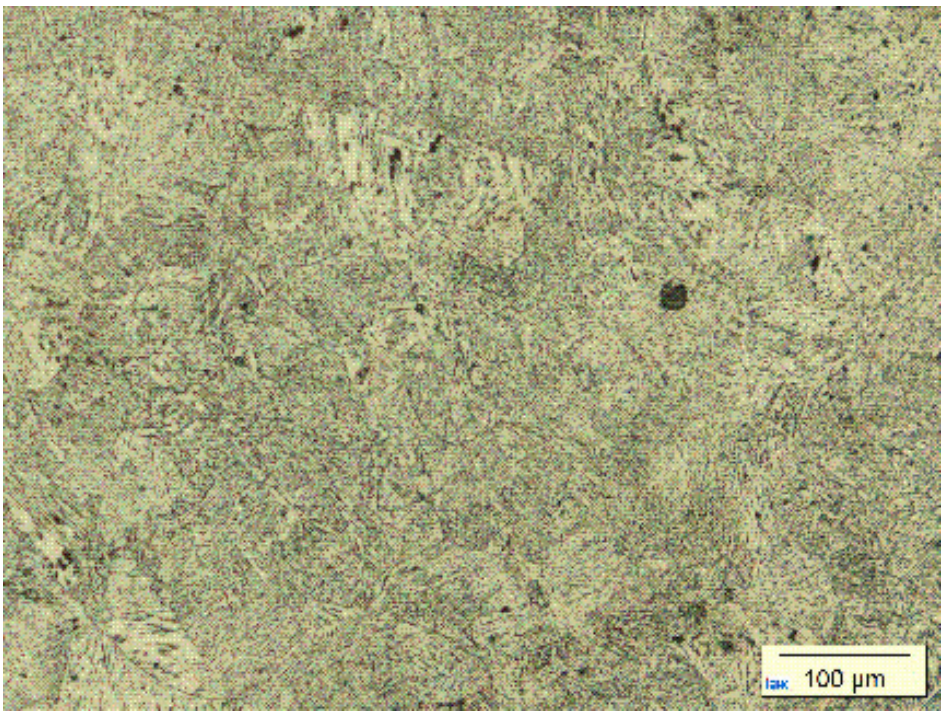

Figure A.5: **S3** - 5min, 1250°C - magnification: **200x**

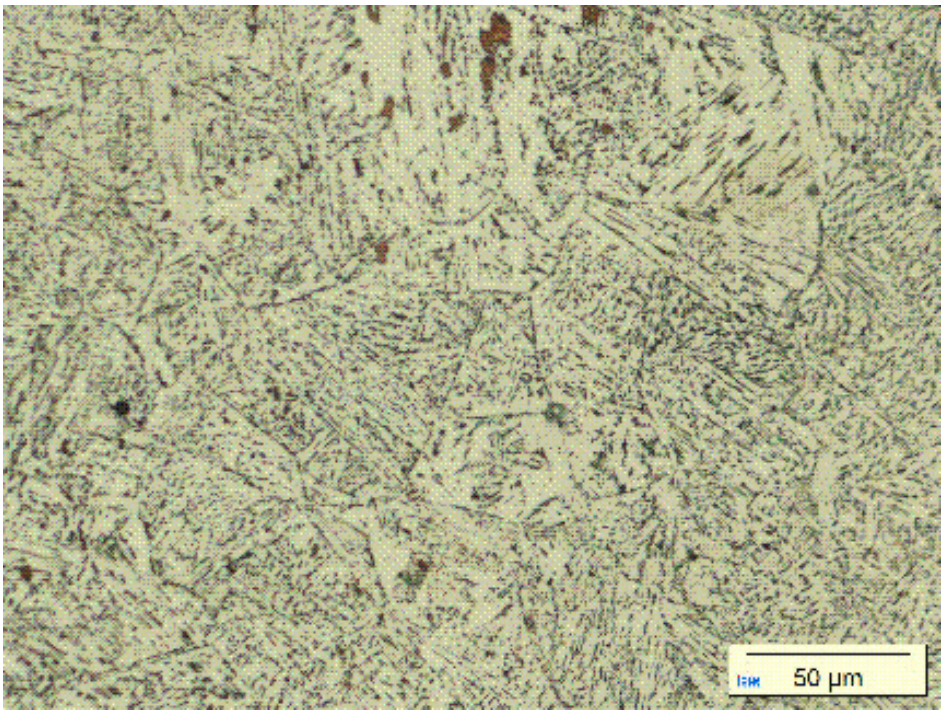

Figure A.6: **S3** - 5min, 1250°C - magnification: **500x**

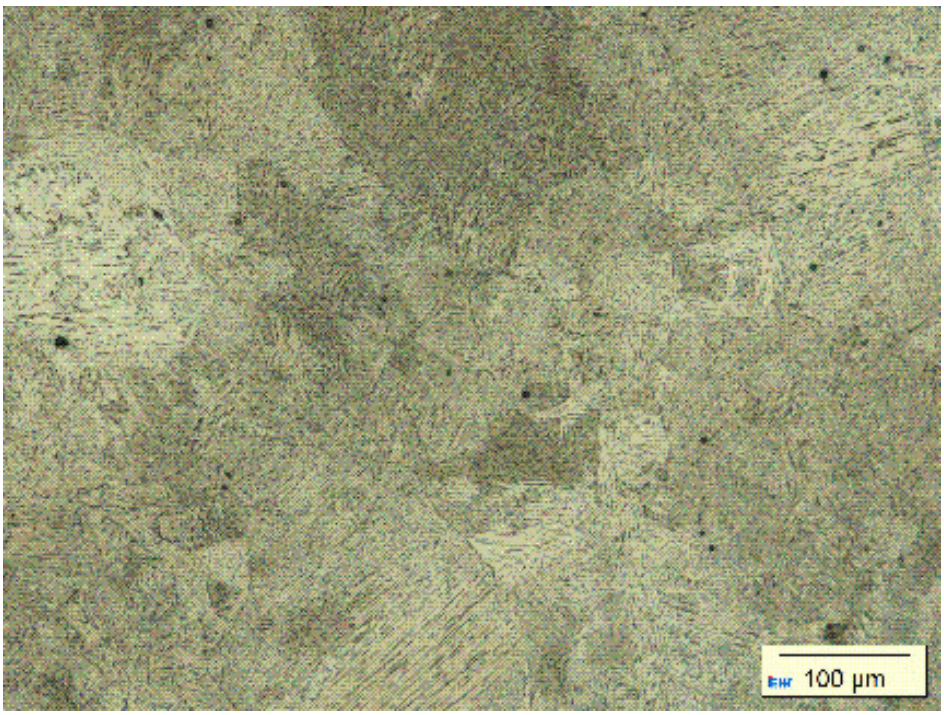

Figure A.7: **S4** - 10min, 1250°C - magnification: **200x**

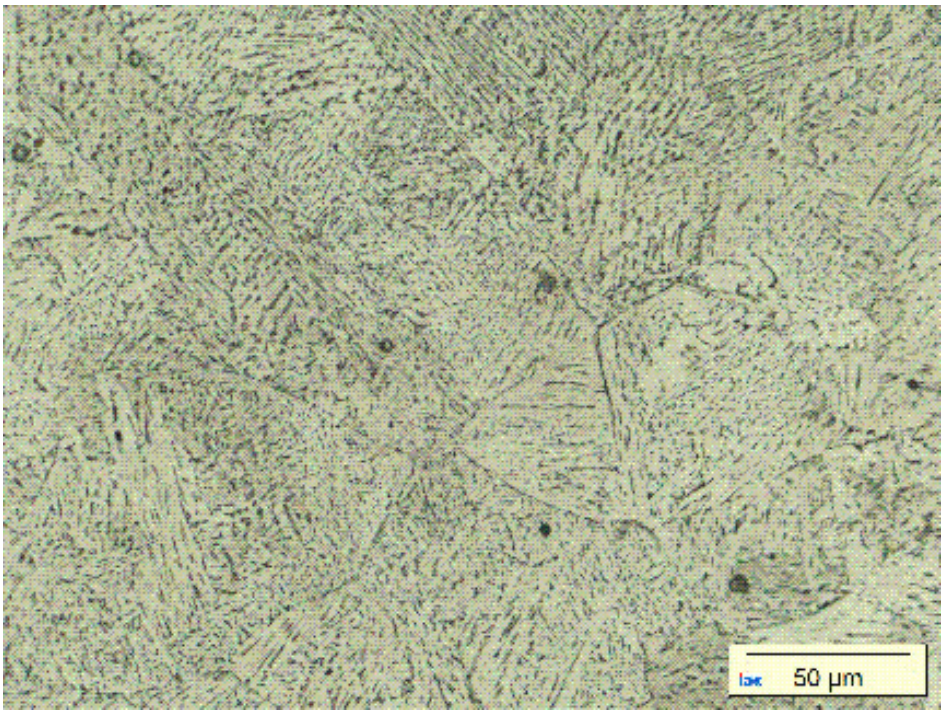

Figure A.8: **S4** - 10min, 1250°C - magnification: **500x**

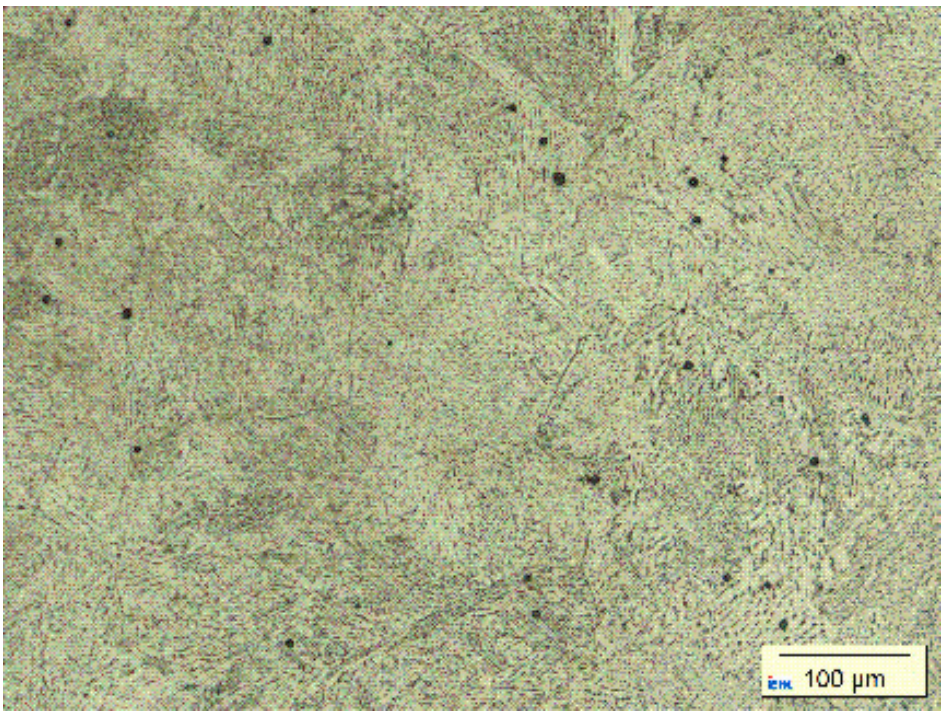

Figure A.9: **S5** - 1min, 1350°C - magnification: **200x**

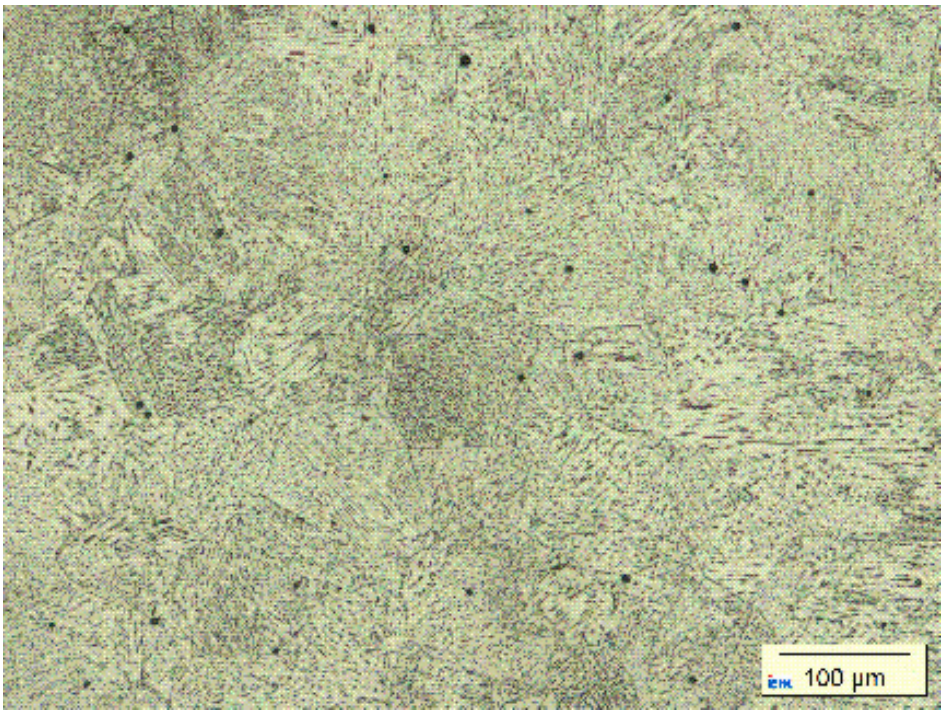

Figure A.10: **S6** - 2min, 1350°C - magnification: **200x**

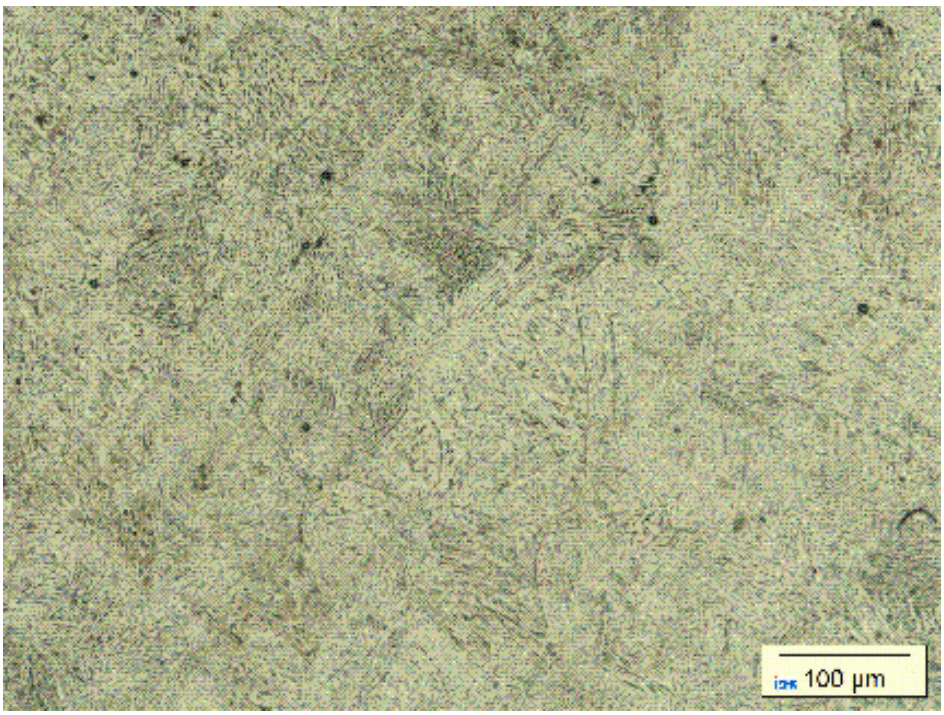

Figure A.11: **S7** - 5min, 1350°C - magnification: **200x**

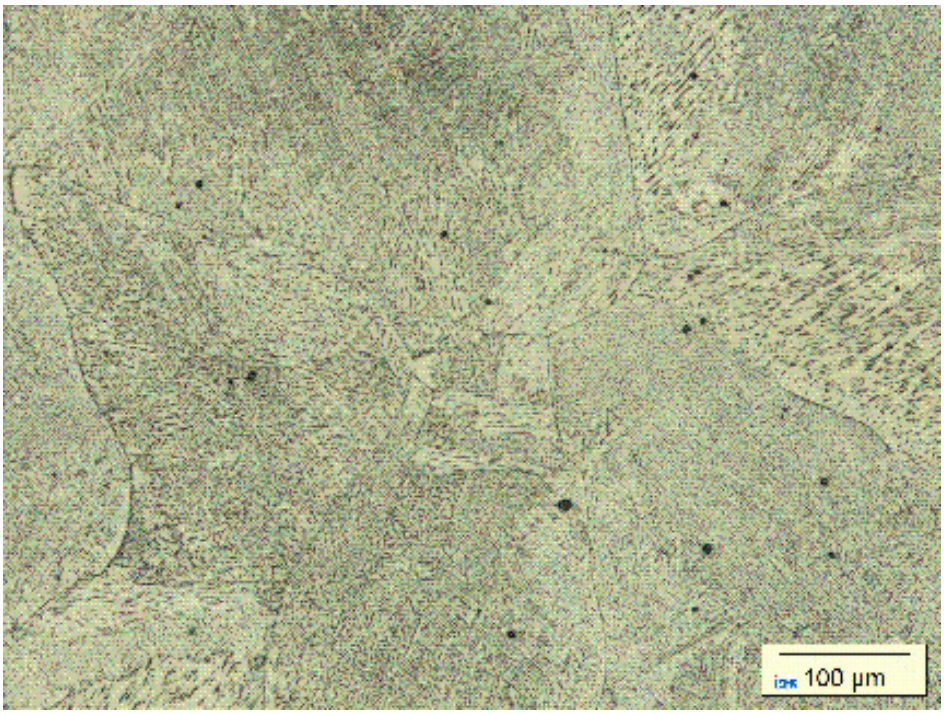

Figure A.12: **S8** - 10min, 1350°C - magnification: **100x**

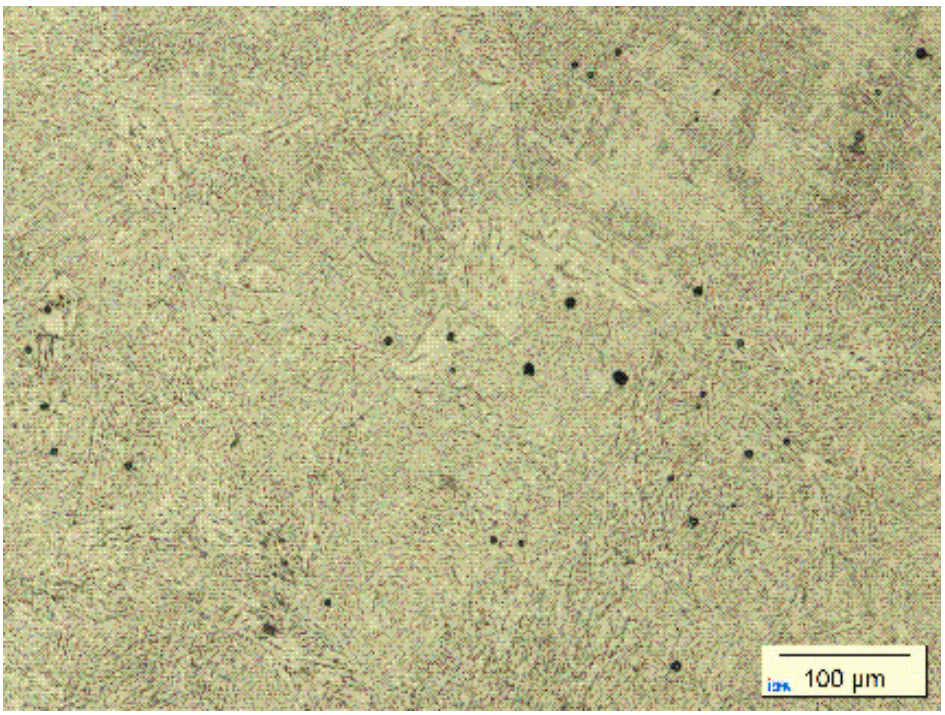

Figure A.13: **S9** - 1 cycle - magnification: **200x**

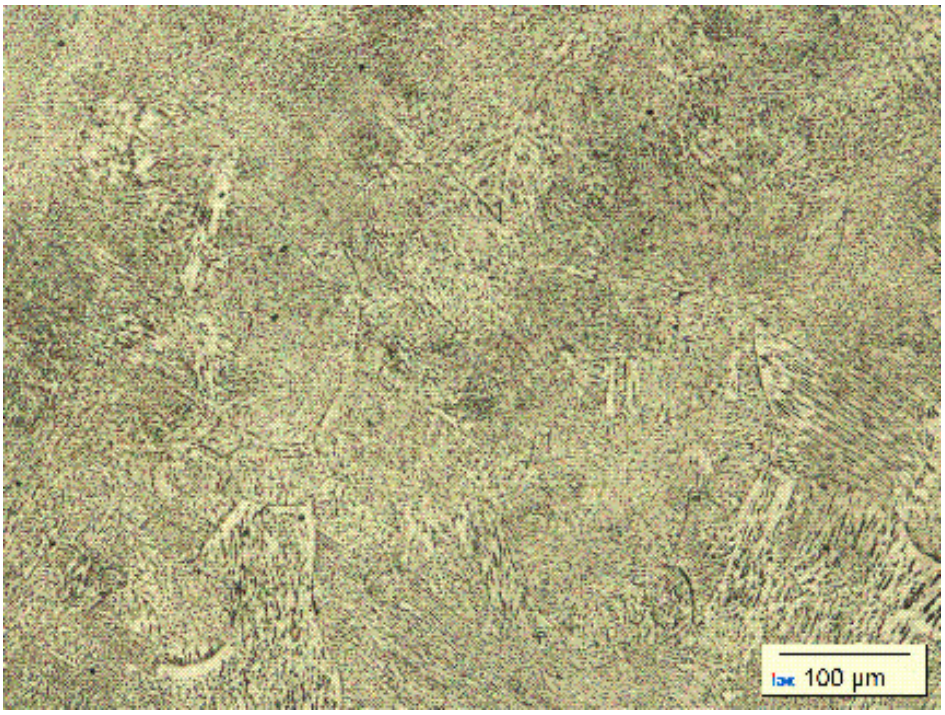

Figure A.14: **S10** - 2 cycles - magnification: **200x**

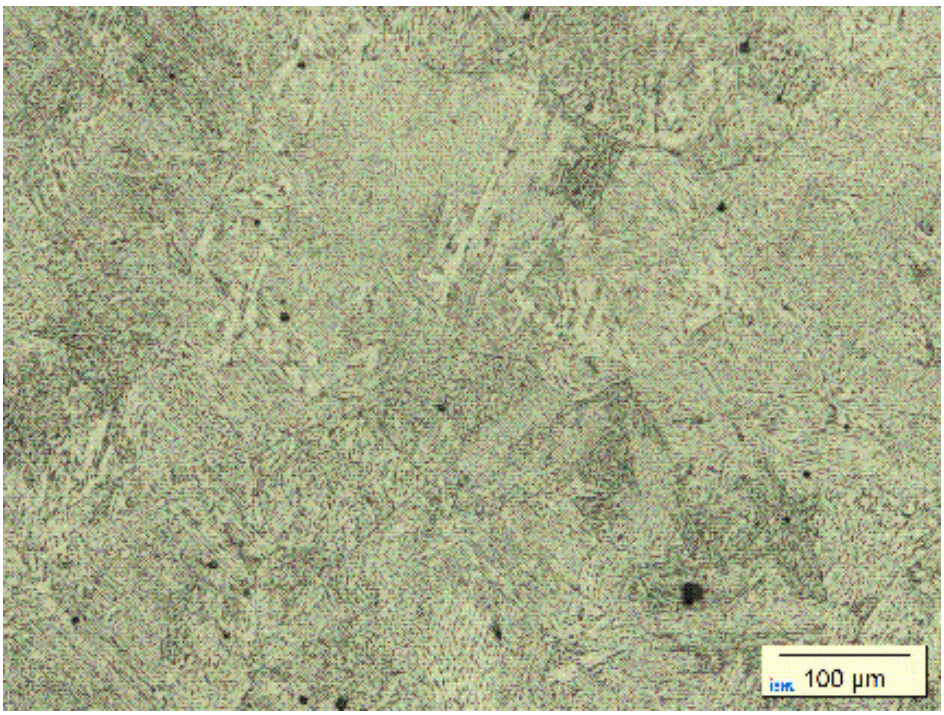

Figure A.15: **S11** - 3 cycles - magnification: **300x**

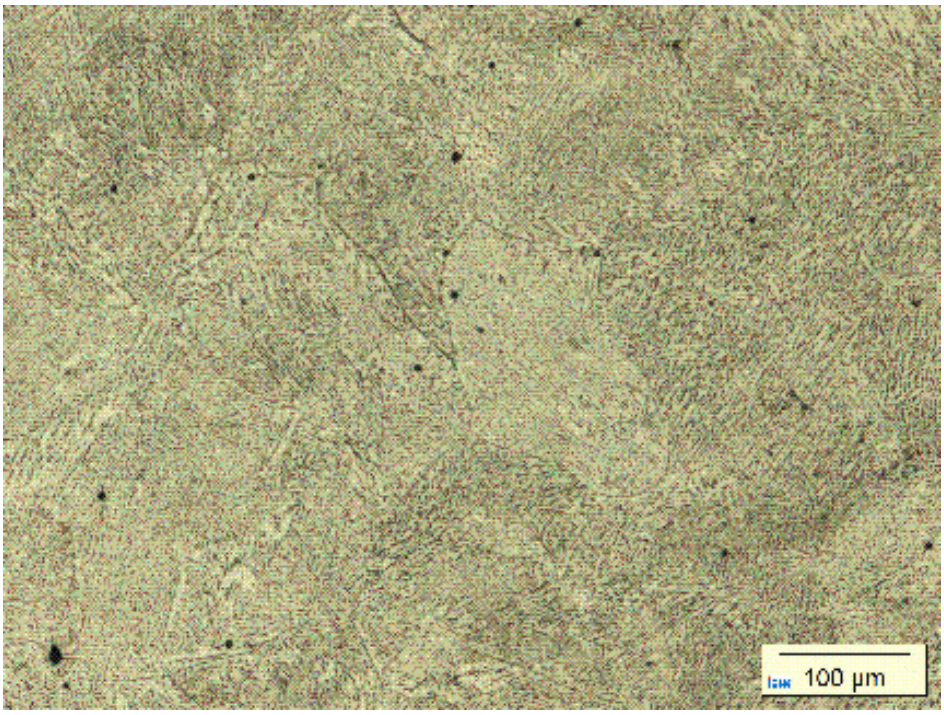

Figure A.16: **S12** - 4 cycles - magnification: **200x**

Appendix B

Sensitivity analysis figures

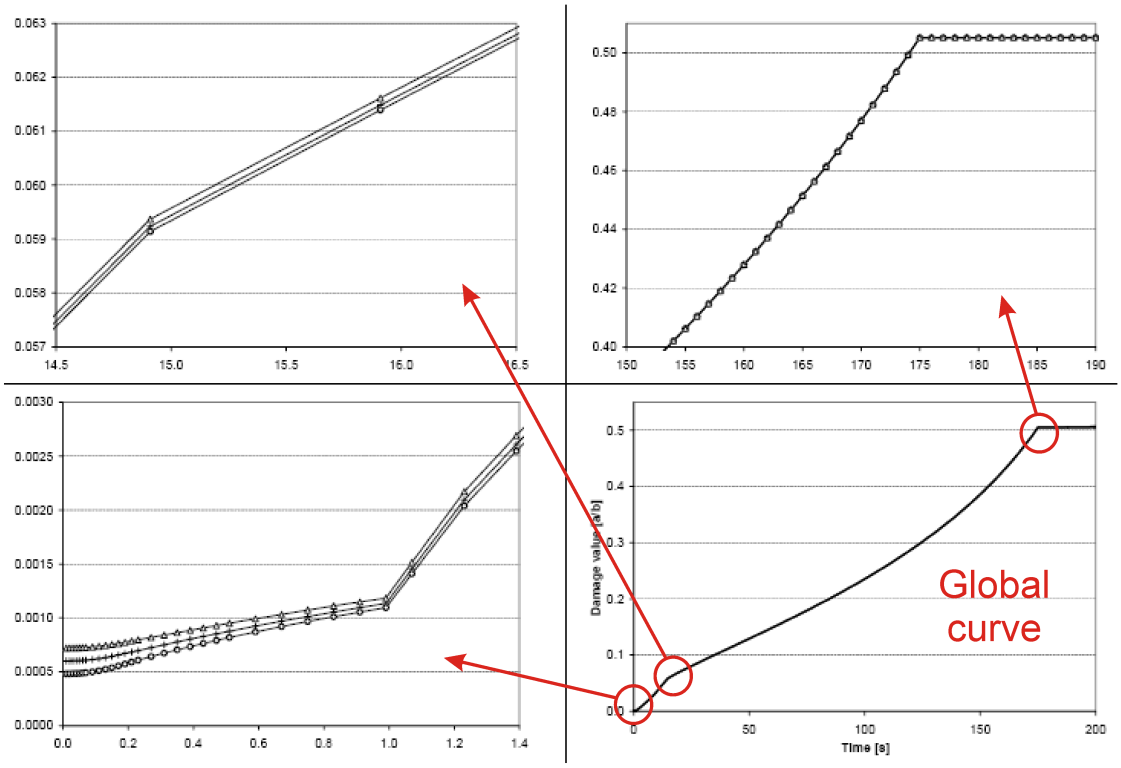

Figure B.1: Layout of the sensitivity analysis graphs with in the lower right corner the reference global graph and the enlargements in the other parts of the picture with in the lower left corner, the enlargement of the nucleation start, in the upper left corner, the enlargement of the nucleation end and in the upper right corner, the enlargement of the damage moment

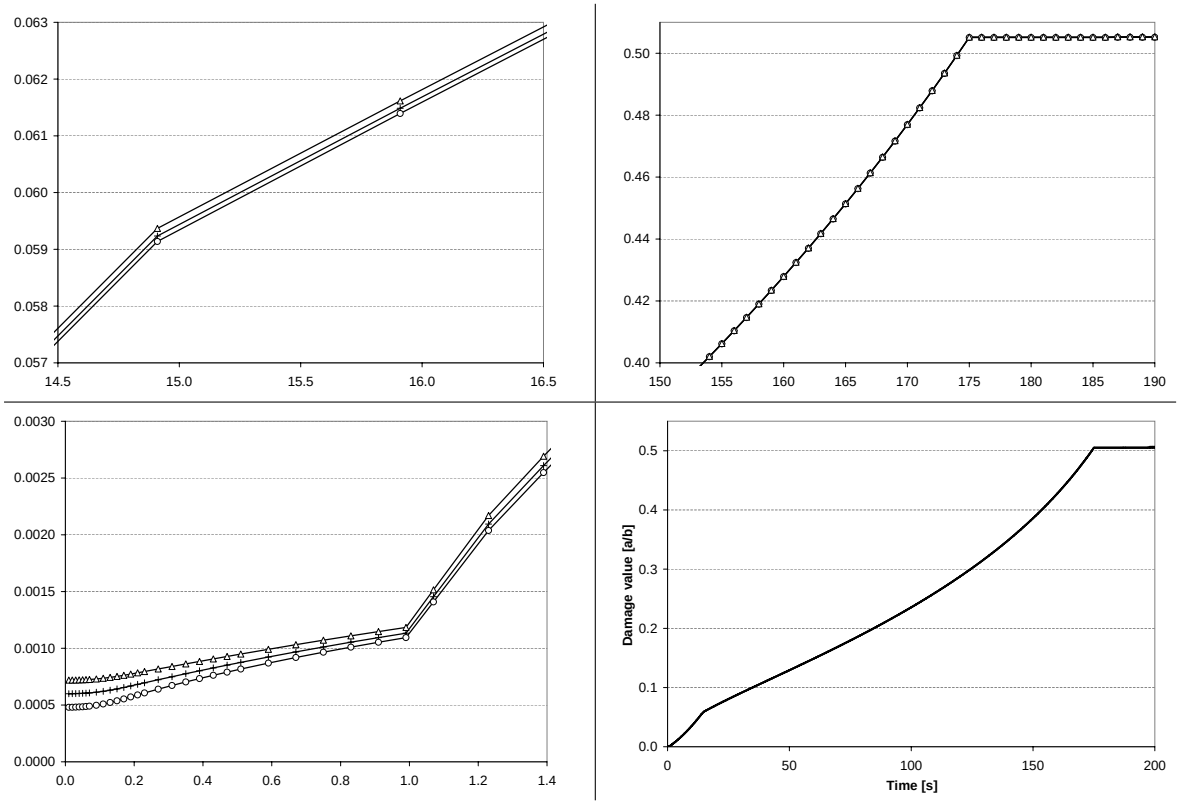

Figure B.2: Influence of the variation of the parameters a_0 on the damage evolution (+ Reference, ∘ Reference - 20% ,Δ Reference + 20%)

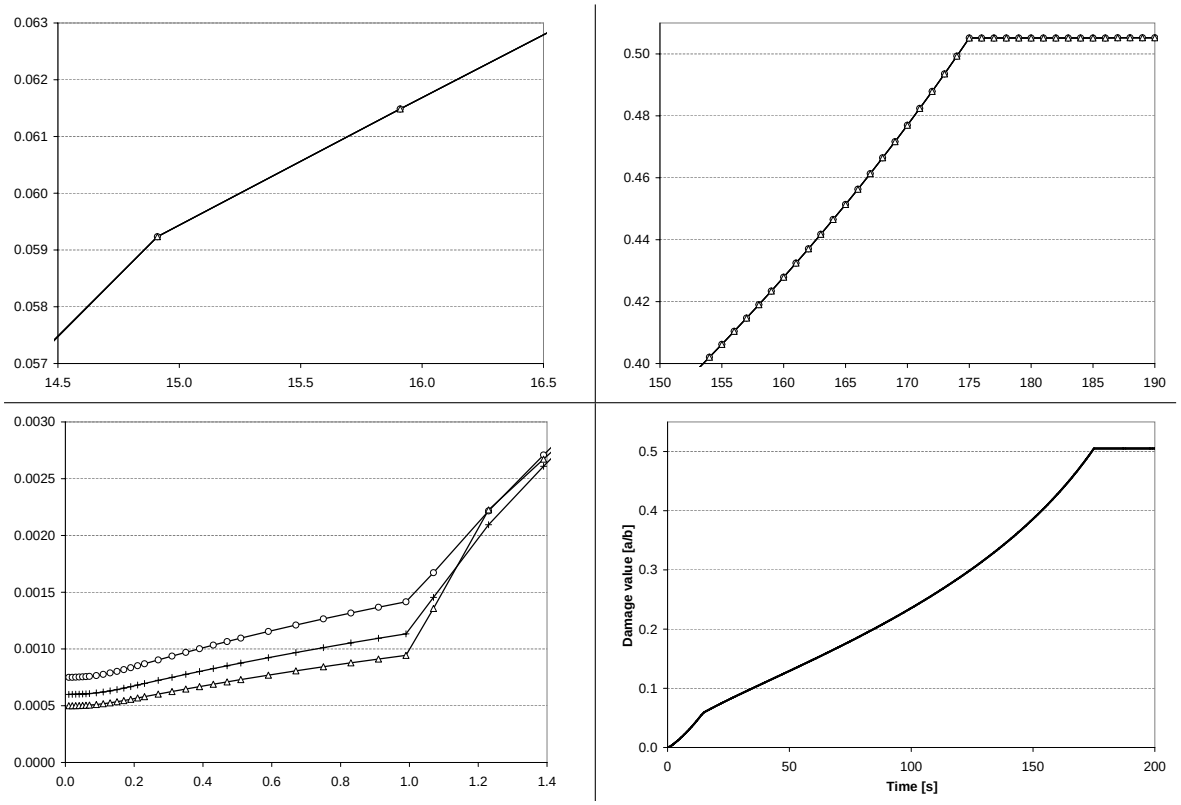

Figure B.3: Influence of the variation of the parameters b_0 on the damage evolution (+ Reference, ∘ Reference - 20% ,Δ Reference + 20%)

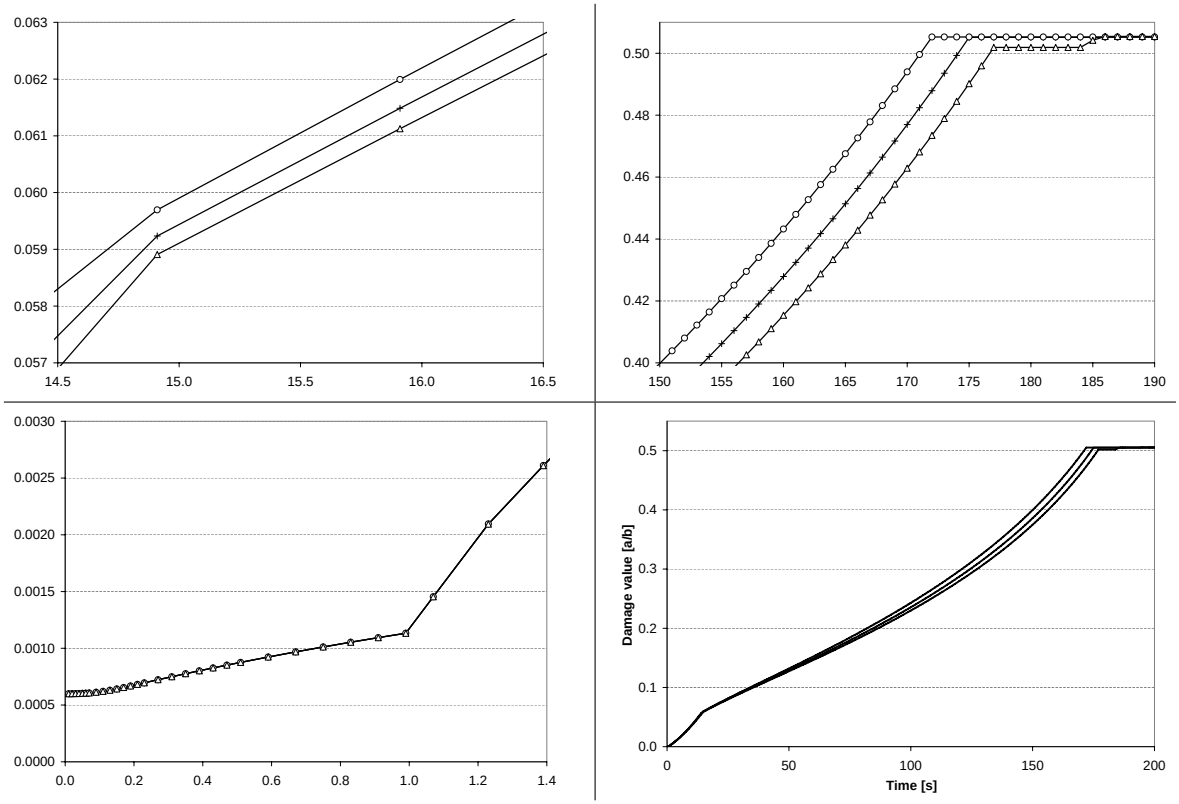

Figure B.4: Influence of the variation of the parameters $\dot{\varepsilon}_c^e/\dot{\varepsilon}_B$ on the damage evolution (+ Reference, ∘ Reference - 20% ,Δ Reference + 20%)

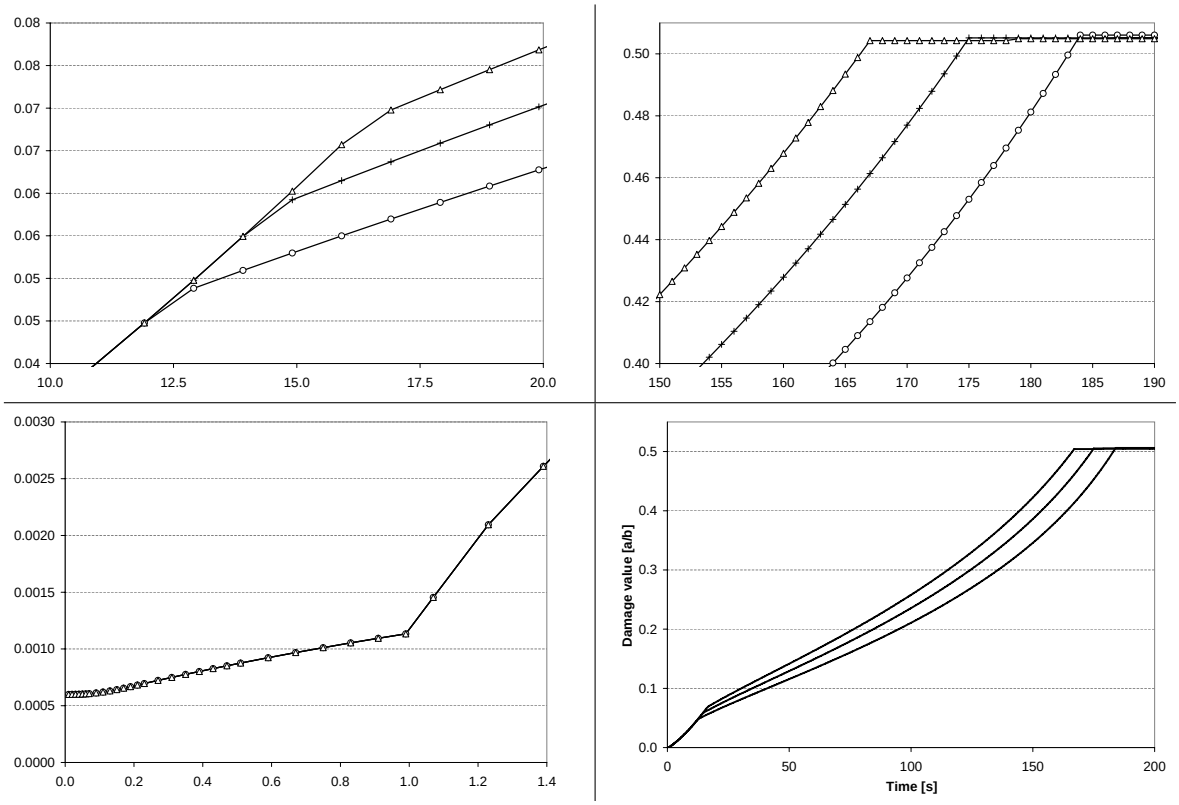

Figure B.5: Influence of the variation of the parameters N_{max}/N_I on the damage evolution (+ Reference, ∘ Reference - 20% ,Δ Reference + 20%)

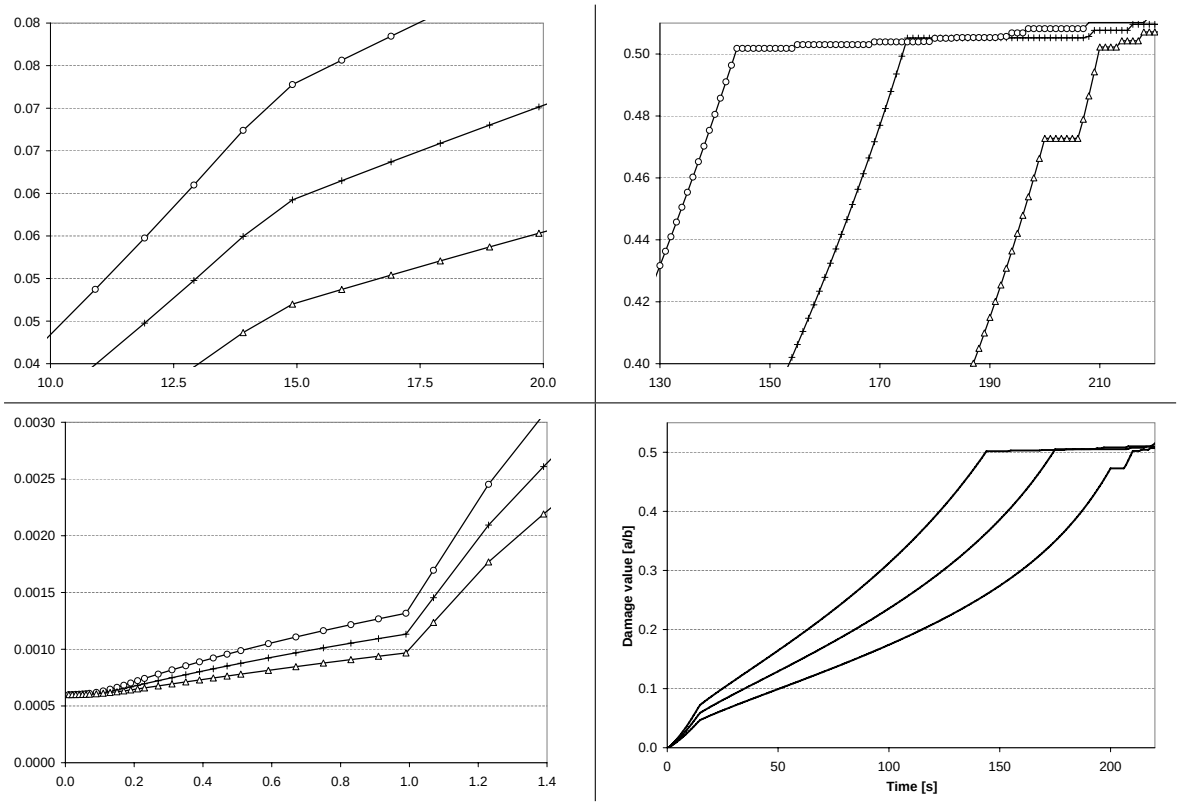

Figure B.6: Influence of the variation of the parameters ψ on the damage evolution (+ Reference, ∘ Reference - 20% ,Δ Reference + 20%)

Appendix C

SEM-EDS study

Surface preparation

The analysis have been performed in as-polished conditions with a 1μm roughness in the final polishing. There is a silver bypass made on the Bakelite to allow conduction of the sample while performing SEM-EDS analysis.

SEM device and specifications

SEM device: ESEM FEG XL-30 Philips
Accelerating voltage: 10kV
Spot size: 4
Working Distance: 10mm
Detectors: SE (secondary electron), BSE (Backscattered Electron), EDS (Energy Dispersive X Rays)

Operating method

Sample surface is scanned following a 1mm width band at a magnification of 100 x beginning from the lower edge up to the upper one (following Figure) and leading to an overall scanned area of 10mm^2.

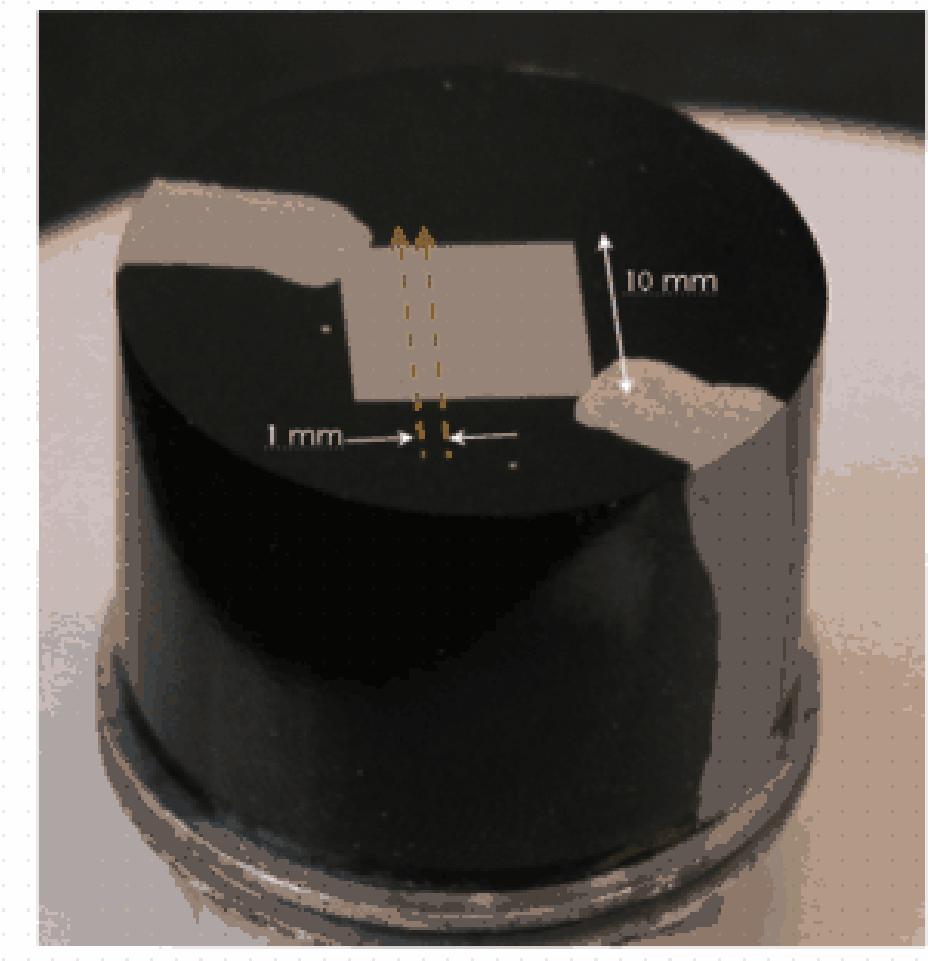

Figure C.1: Dimensions of the mounted and polished sample - Location of the scanned area of $10mm^2$ (tan arrows) and silver bypass on the Bakelite

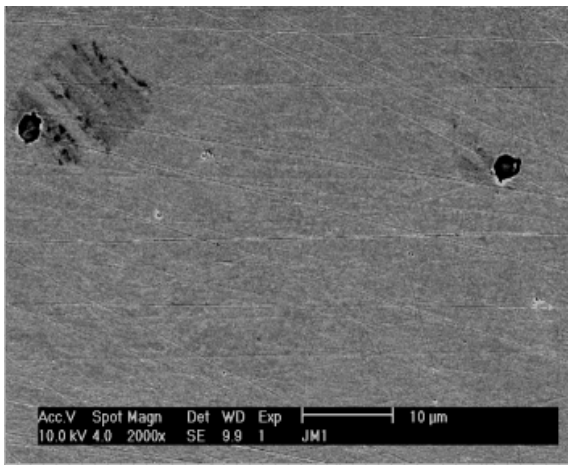

Figure C.2: Overview of zone 1 - SE image

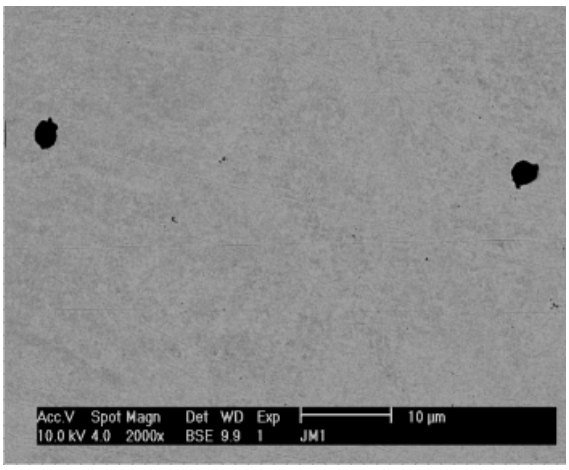

Figure C.3: Related BSE image of zone 1

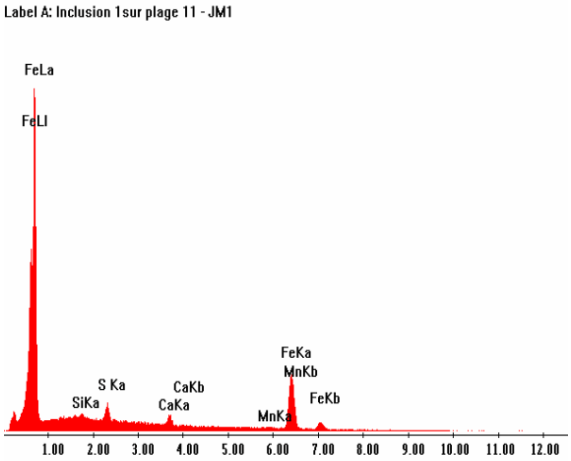

Figure C.4: General EDX spectrum on zone 1

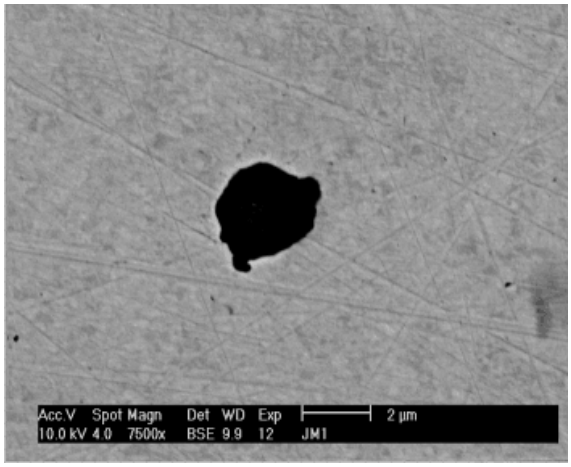

Figure C.5: Inclusion from the right side of zone 1

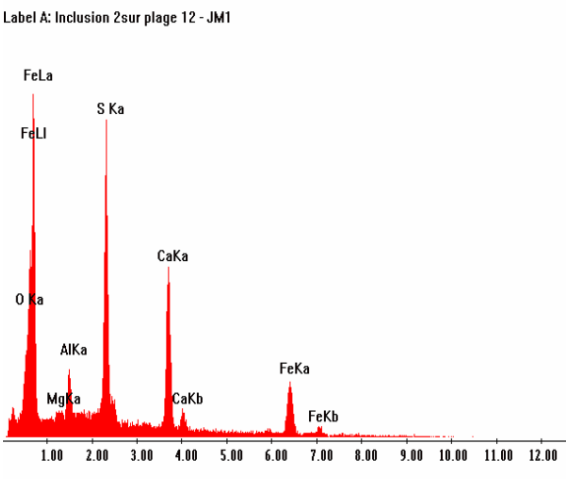

Figure C.6: Related EDS spectrum focused on inclusion of Figure C.5 (CaS associated with a small (Al, Mg)O)

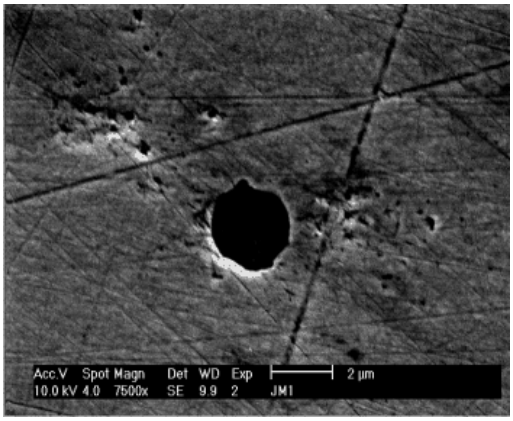

Figure C.7: Inclusion on zone 2 (SE Image)

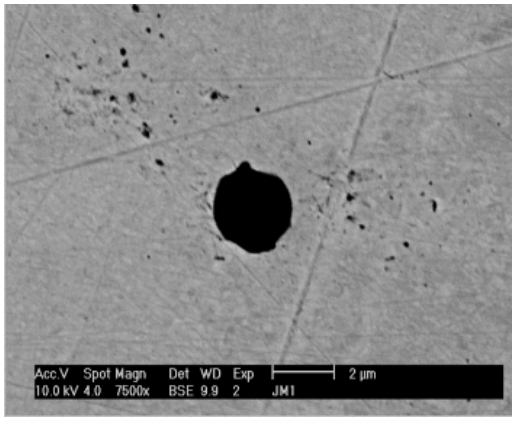

Figure C.8: BSE image related to Figure C.7

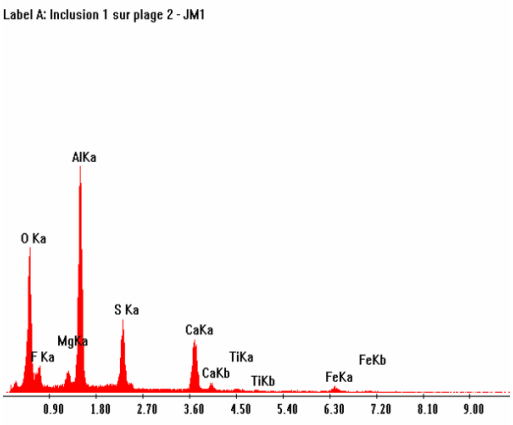

Figure C.9: Related EDS spectrum focused on inclusion of Figure C.7 and C.8 (Complex (Al,Mg)O/CaS type)

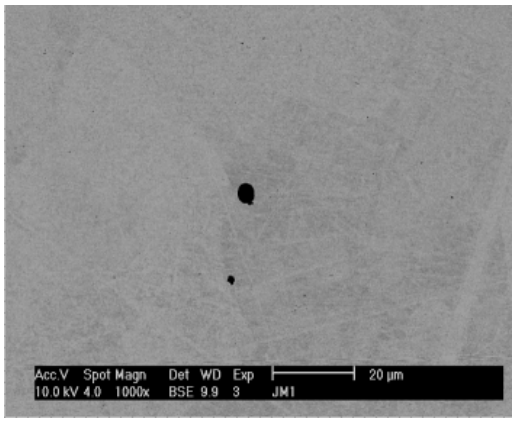

Figure C.10: Inclusion on zone 3 (BSE Image)

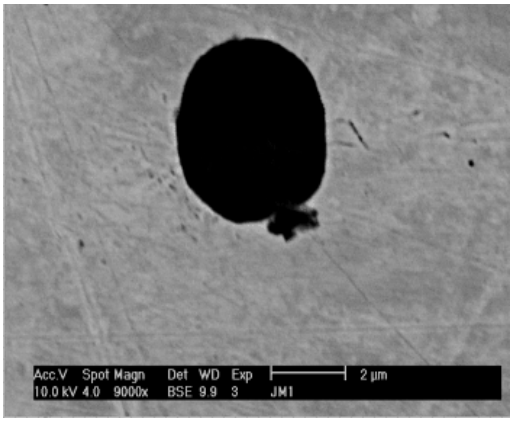

Figure C.11: Same as Figure C.10, with higher amplification(BSE Image)

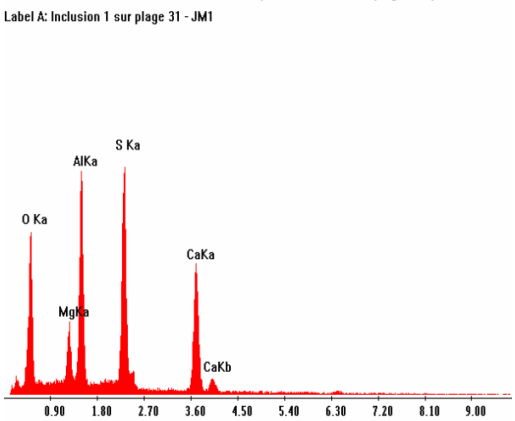

Figure C.12: Focused EDS spectrum on inclusion of zone 3 (Complex (Al,Mg)O/CaS type)

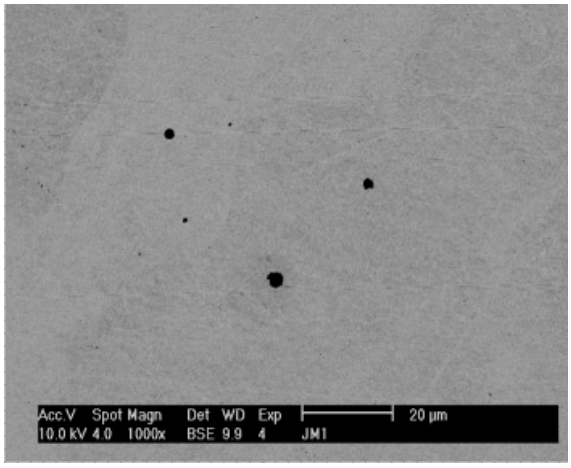

Figure C.13: Inclusions on zone 4 (BSE Image)

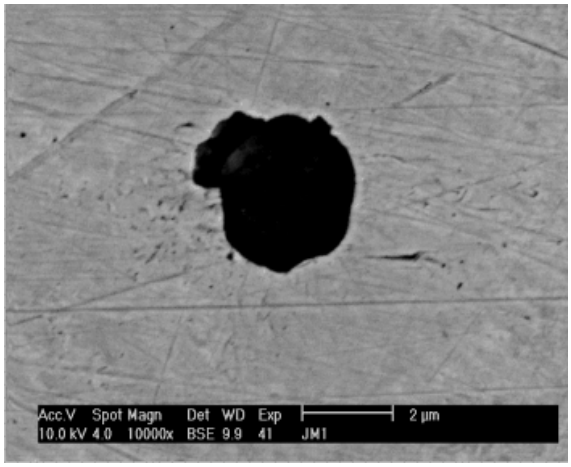

Figure C.14: Inclusion on the lower area of zone 4 (BSE Image)

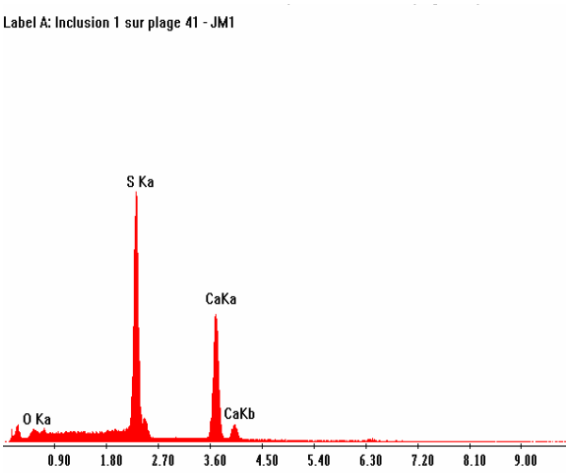

Figure C.15: Focused EDS spectrum on inclusion of Figure C.14 (CaS type)

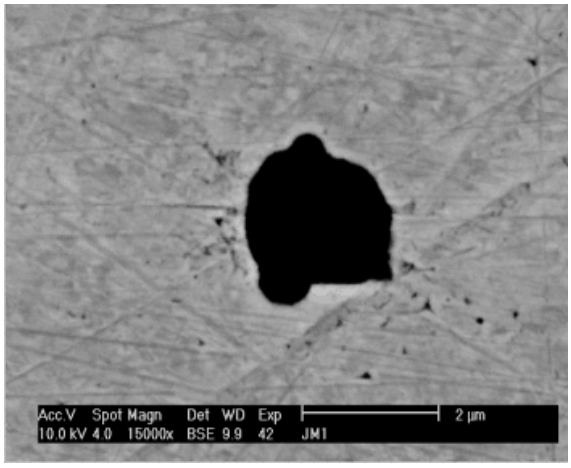

Figure C.16: Inclusion on the upper right area of zone 4 (BSE Image)

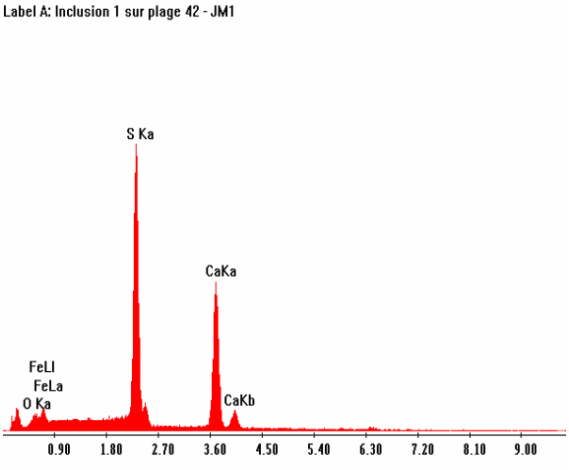

Figure C.17: Focused EDS spectrum on inclusion of Figure C.16 (CaS type)

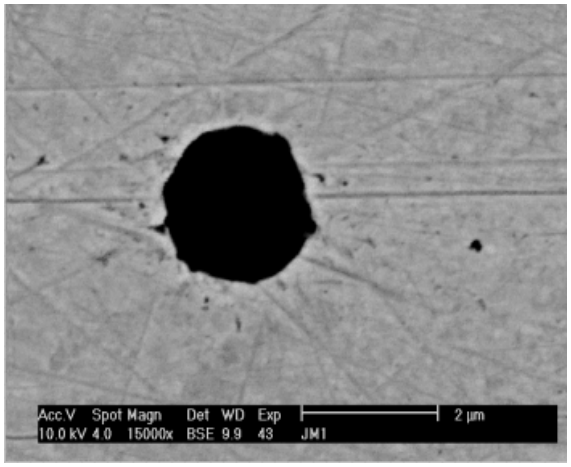

Figure C.18: Inclusion on the upper left area of zone 4 (BSE Image)

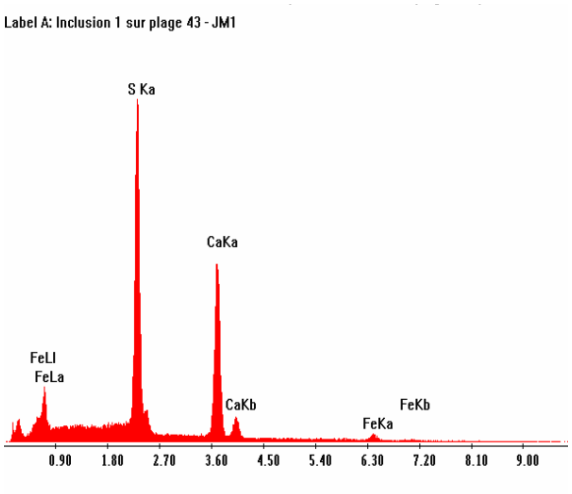

Figure C.19: Focused EDS spectrum on inclusion of Figure C.18 (CaS type)

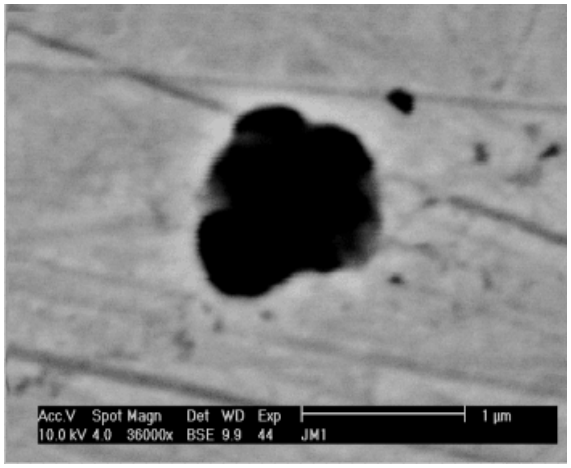

Figure C.20: Small inclusion at the left side of bigger inclusion of Figure C.18 (BSE Image)

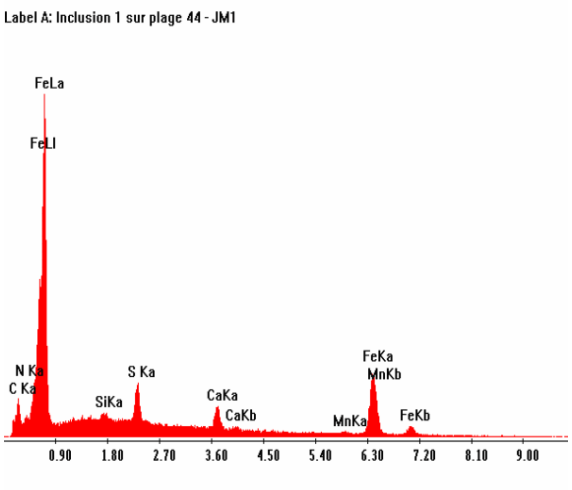

Figure C.21: Focused EDS spectrum on inclusion of Figure C.20 (CaS type)

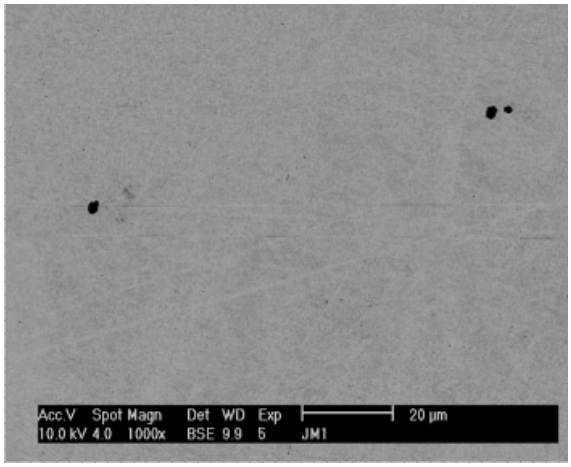

Figure C.22: Overview of zone 5 - BSE image

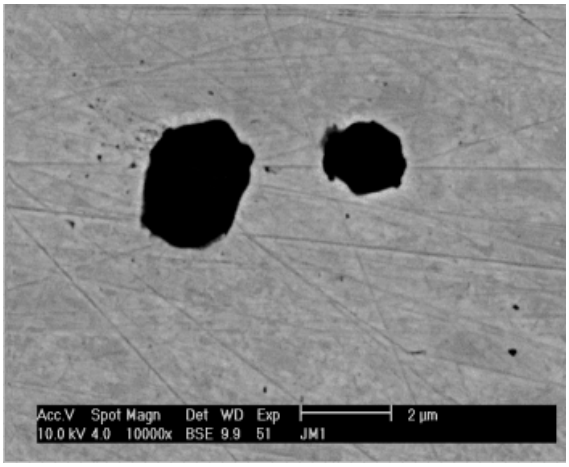

Figure C.23: Cluster of inclusions on the right side of Figure C.22

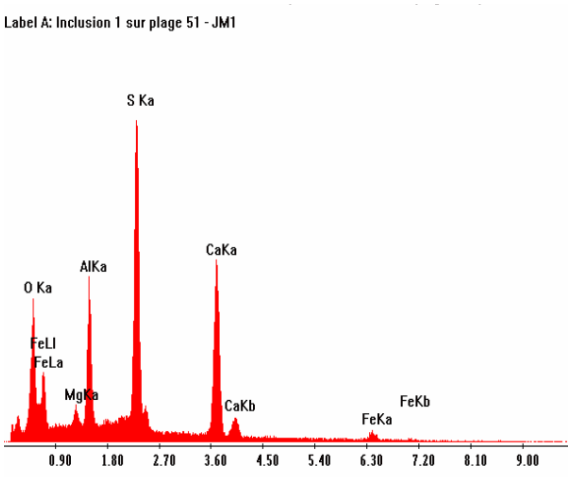

Figure C.24: Focused EDS spectrum on inclusion on the left side of Figure C.23 (Complex CaS/(Al,Mg)O type)

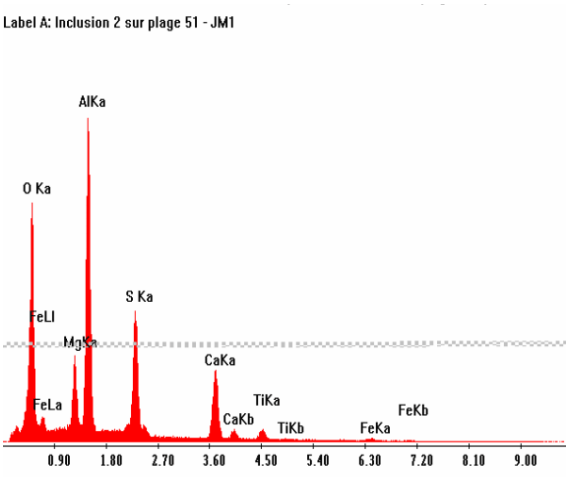

Figure C.25: Focused EDS spectrum on inclusion on the right side of Figure C.23 (Complex (Al,Mg)O/CaS type, with small and undefined amount of Ti)

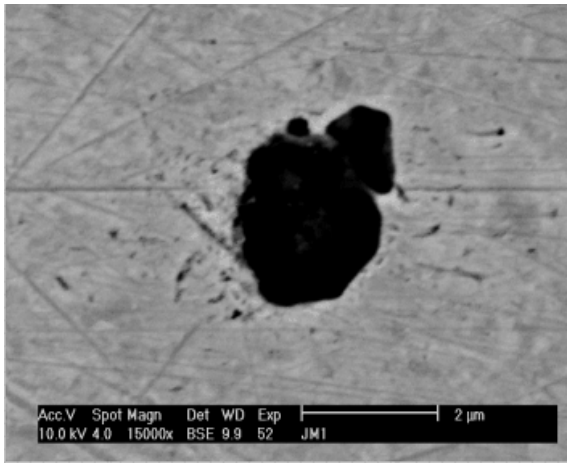

Figure C.26: Complex inclusion on zone 5 (center) - BSE Image

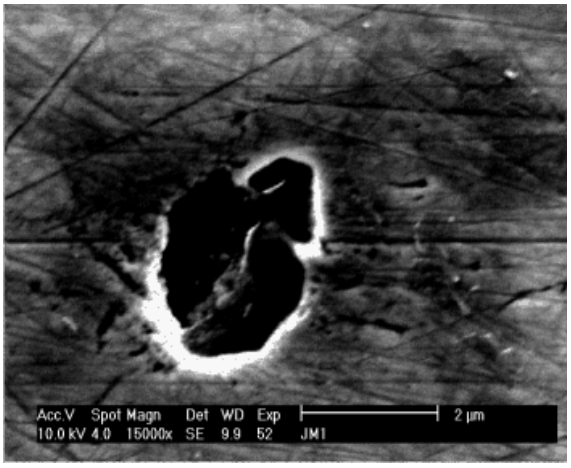

Figure C.27: SE image related to Figure C.26

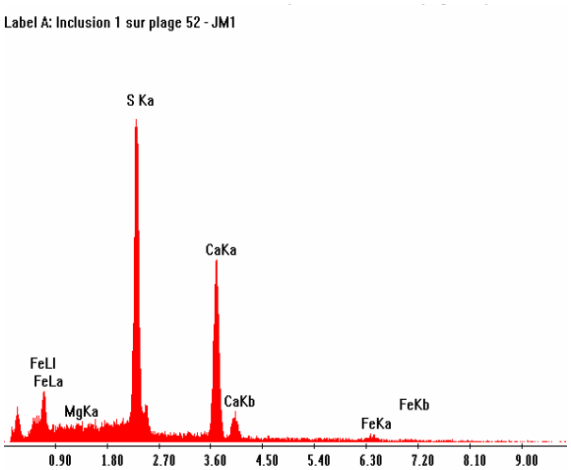

Figure C.28: Focused EDS spectrum on the centre of inclusion of Figure C.26-C.27 (CaS type)

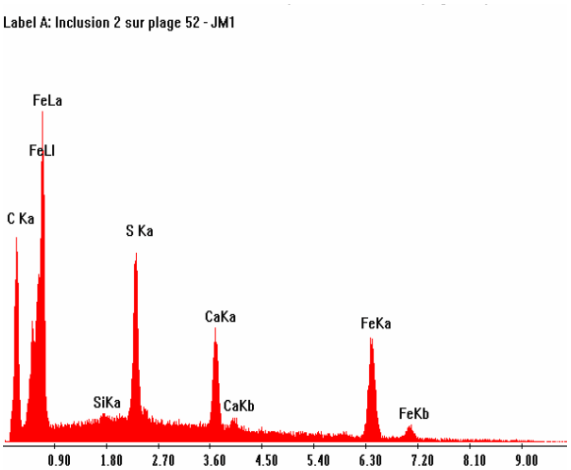

Figure C.29: Focused EDS spectrum on the upper zone of the inclusion of Figure C.26-C.27 (CaS type)

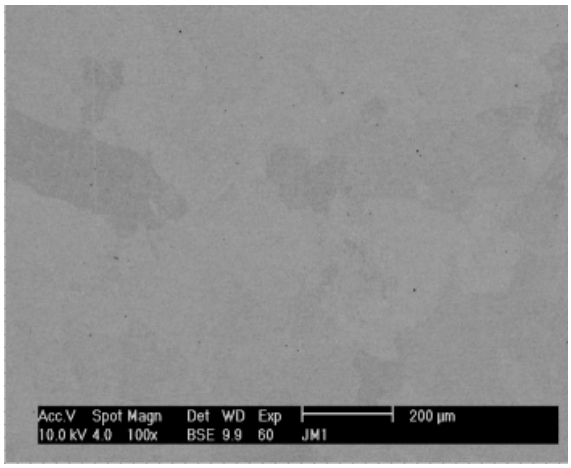

Figure C.30: Overview of zone 6, matrix - BSE image

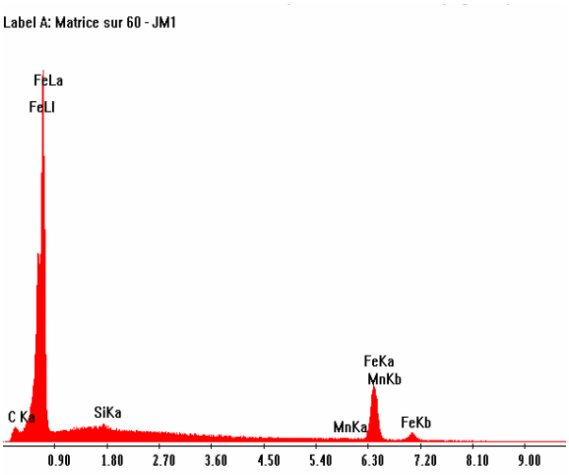

Figure C.31: General EDS spectrum in Figure C.30

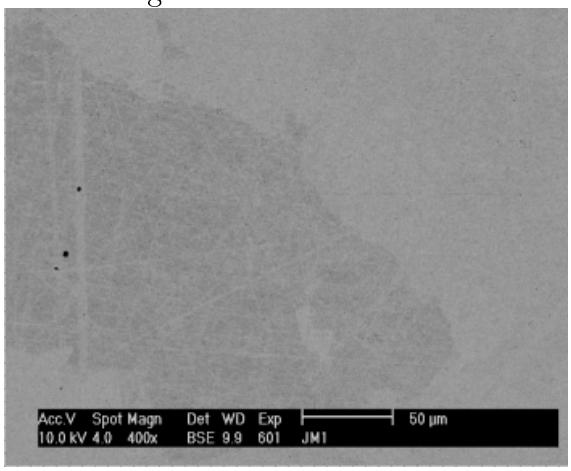

Figure C.32: Dark area on the upper left side of Figure C.30 (BSE Image)

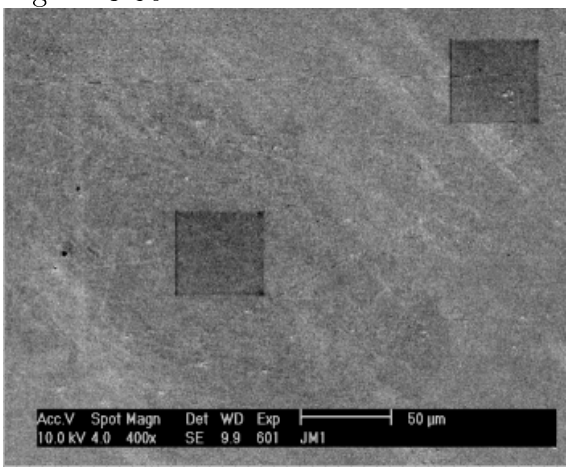

Figure C.33: Related SE image of Figure C.32, with corresponding EDS marks

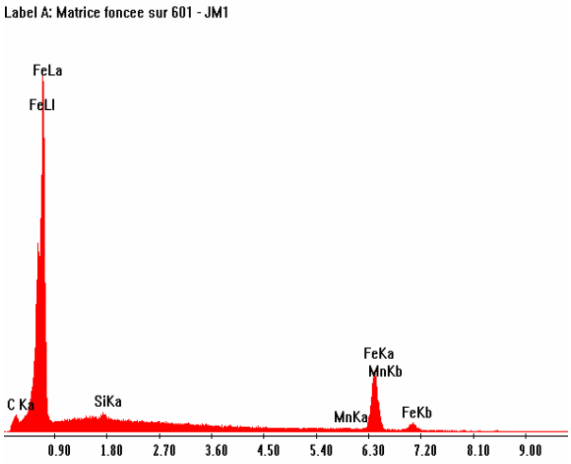

Figure C.34: Focused EDS spectrum on the left side of Figure C.33 (dark gray area in Figure C.32)

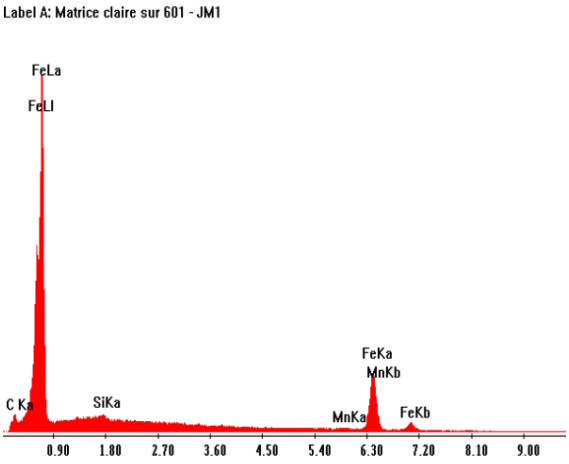

Figure C.35: Focused EDS spectrum on the left side of Figure C.33 (light gray area in Figure C.32)

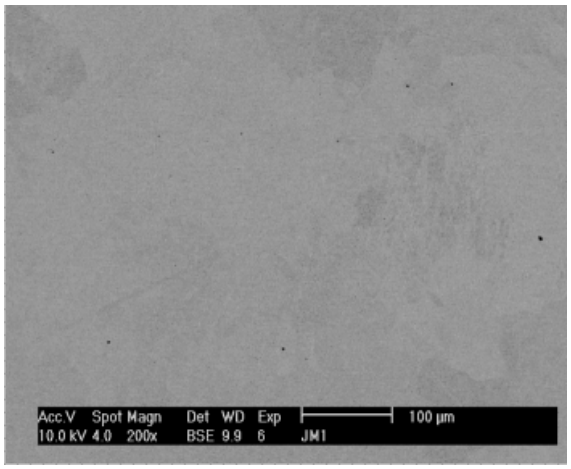

Figure C.36: Light area on the right side of Figure C.30 (BSE Image)

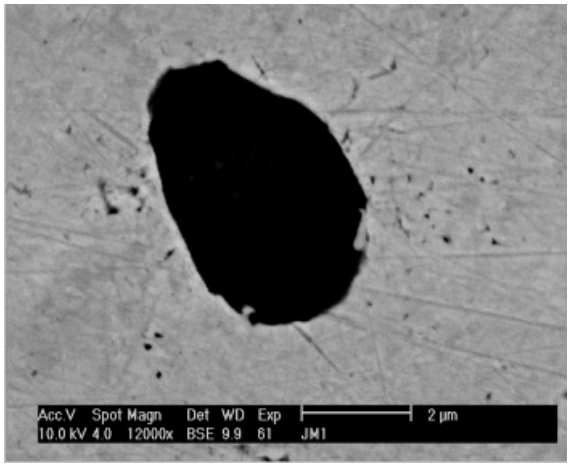

Figure C.37: Inclusion on the right side of Figure C.36 (BSE Image)

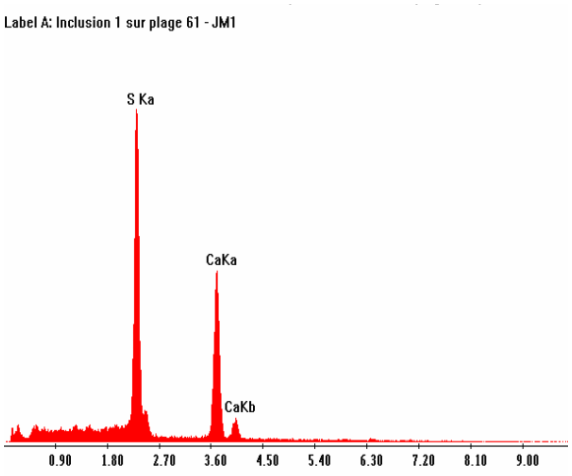

Figure C.38: Focused EDS spectrum on the inclusion of Figure C.37 (CaS type)

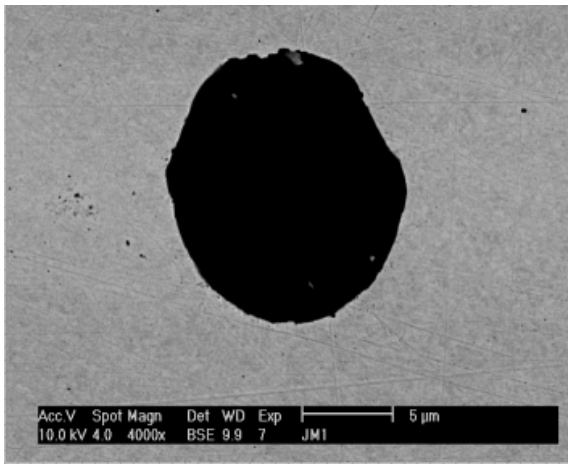

Figure C.39: Globular Inclusion on zone 7 (BSE Image)

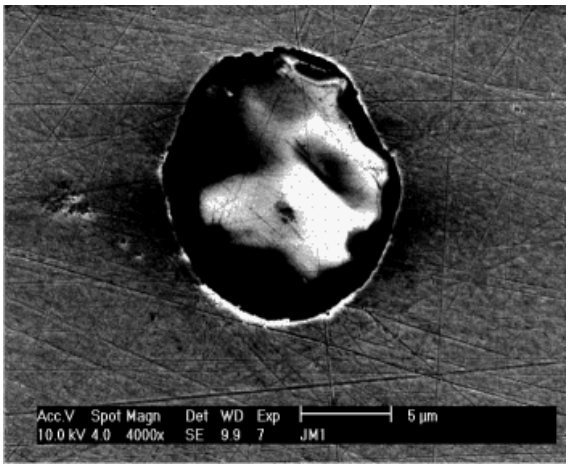

Figure C.40: SE image related to Figure C.39

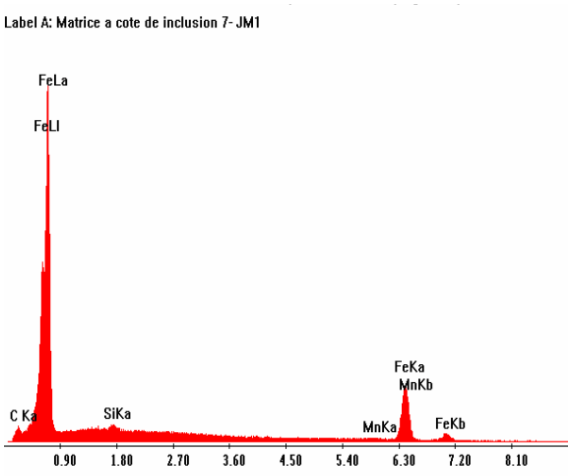

Figure C.41: Focused EDS spectrum on the matrix in the vicinity of inclusion of Figure C.39-C.40

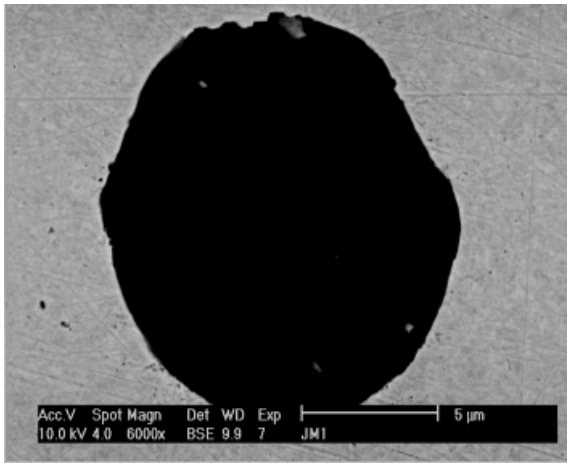

Figure C.42: Globular Inclusion on zone 7 (BSE Image)

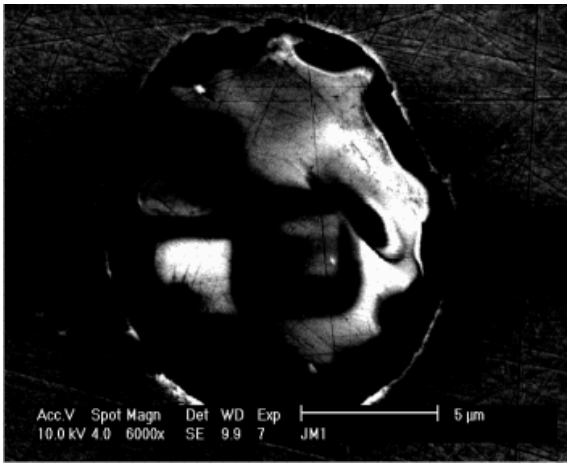

Figure C.43: SE image related to Figure C.42

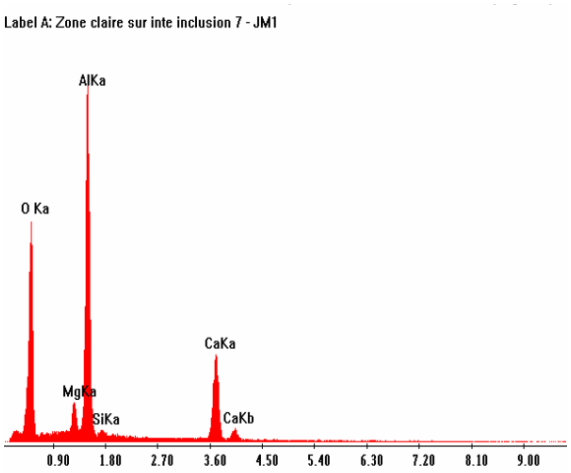

Figure C.44: Focused EDS spectrum on the light zone of inclusion ((Al; Mg)O associated with CaS)

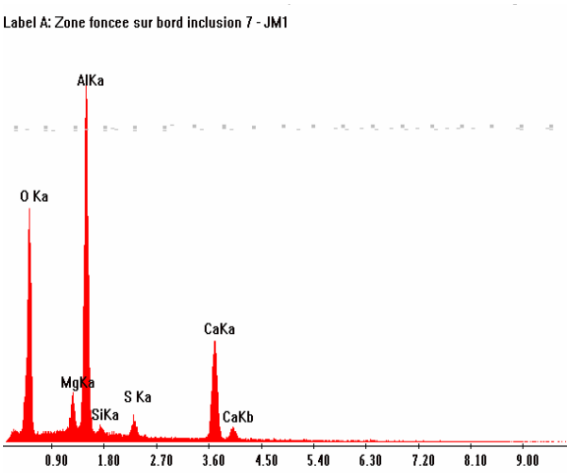

Figure C.45: Focused EDS spectrum on the center of inclusion of Figure C.45((Al; Mg)O associated with CaS)

Appendix D

ISO643

DIN EN ISO 643 Ber 1:2004-07

Tabelle C.1 — Auswertung der Anzahl Körner als Funktion verschiedener Parameter

Korngrößen-Kennzahlen G	Anzahl m der Körner je Quadratmillimeter			Mittlerer Korndurchmesser $\overline{d}$	Mittlere Kornfläche $\overline{a}$	Mittlere Länge des Linienschnittsegments $\overline{l}$	Mittlere Anzahl Schnittpunkte der Körner je Millimeter Messlinie
	Nennwert	Grenzwerte		mm	mm^2	mm	
		von (ausschließlich)	bis (einschließlich)				
−7	0,062 5	0,046	0,092	4	16	3,577	0,279
−6	0,125	0,092	0,185	2,828	8	2,529	0,395
−5	0,25	0,185	0,37	2	4	1,788	0,559
−4	0,5	0,37	0,75	1,414	2	1,265	0,790
−3	1	0,75	1,5	1	1	0,894	1,118
−2	2	1,5	3	0,707	0,5	0,632	1,582
−1(00)	4	3	6	0,500	0,25	0,447	2,237
0	8	6	12	0,354	0,125	0,320	3,125
1	16	12	24	0,250	0,062 5	0,226	4,42
2	32	24	48	0,177	0,031 2	0,160	6,25
3	64	48	96	0,125	0,015 6	0,113	8,84
4	128	96	192	0,088 4	0,007 81	0,080	12,5
5	256	192	384	0,062 5	0,003 90	0,056 6	17,7
6	512	384	768	0,044 2	0,001 95	0,040 0	25,0
7	1 024	768	1 536	0,031 2	0,000 98	0,028 3	35,4
8	2 048	1 536	3 072	0,022 1	0,000 49	0,020 0	50,0
9	4 096	3 072	6 144	0,015 6	0,000 244	0,014 1	70,7
10	8 192	6 144	12 288	0,011 0	0,000 122	0,010 0	100
11	16 384	12 288	24 576	0,007 8	0,000 061	0,007 07	141
12	32 768	24 576	49 152	0,005 5	0,000 030	0,005 00	200
13	65 536	49 152	98 304	0,003 9	0,000 015	0,003 54	283
14	131 072	98 304	196 608	0,002 8	0,000 007 5	0,002 50	400
15	262 144	196 608	393 216	0,002 0	0,000 003 7	0,001 70	588
16	524 288	393 216	786 432	0,001 4	0,000 001 9	0,001 20	833
17	1 048 576	786 432	1 572 864	0,001 0	0,000 000 95	0,00 87	1 149

ANMERKUNG In dieser Tabelle werden die Werte unterschiedlicher Parameter für gleichachsige Körner angegeben.

Figure D.1: ISO643 table for the visual determination of the grain size by micrographic analysis

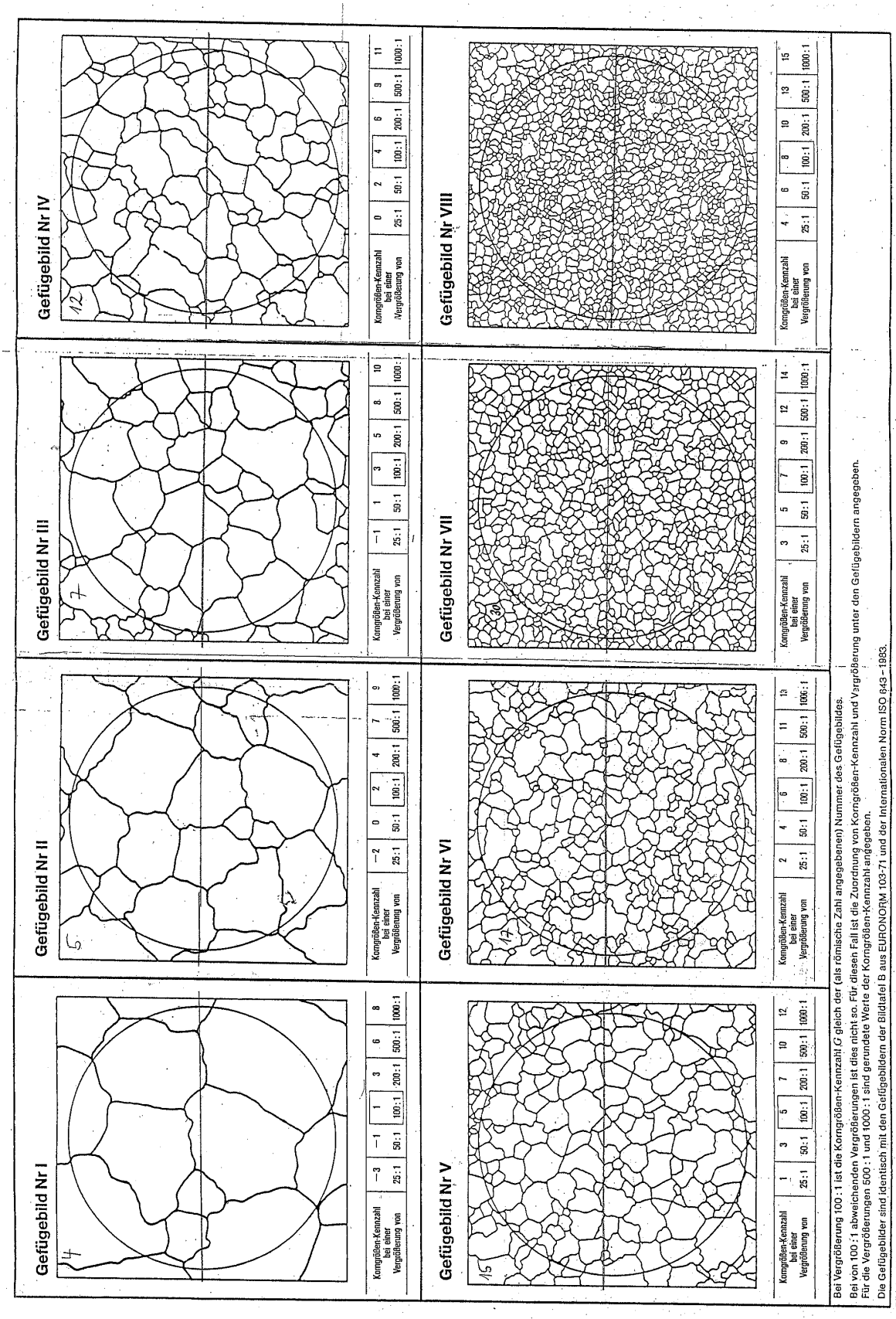

Figure D.2: ISO643 comparison micrographs for the determination of the grain size by micrographic analysis

Appendix E

Rheological law correlation with experimental HTT

R2	$1 \cdot 10^{-2} s^{-1}$	$5 \cdot 10^{-3} s^{-1}$	$1 \cdot 10^{-3} s^{-1}$
850 °C	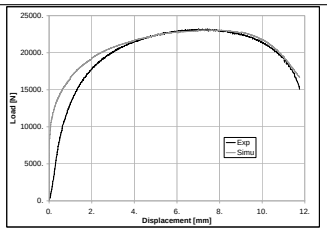	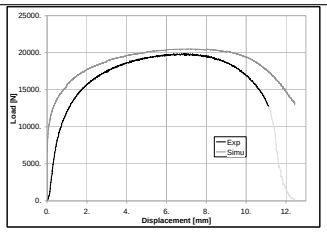	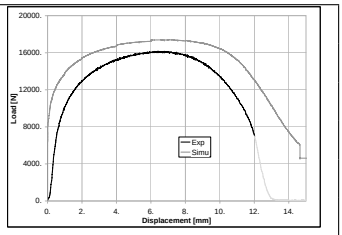
900 °C	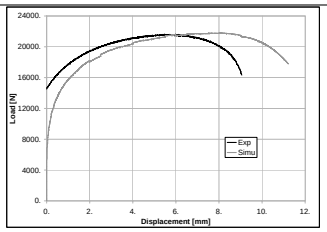	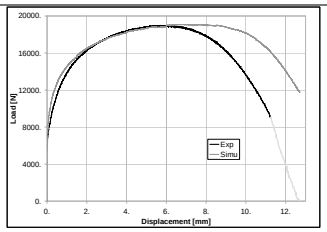	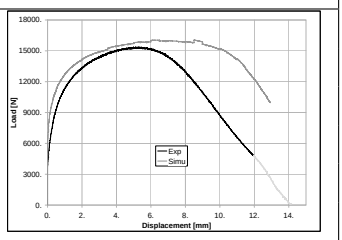
950 °C	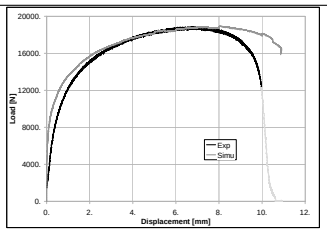	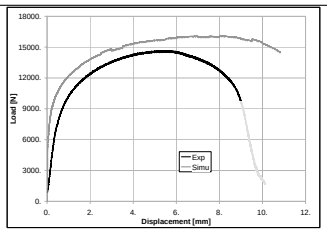	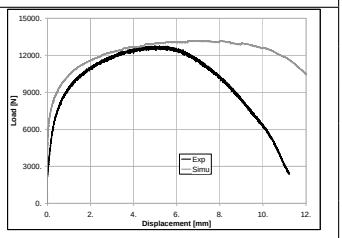

Table E.1: Macro-Meso flow curves of **A** steel grade for R2 sample shape

R4	$1 \cdot 10^{-2} s^{-1}$	$5 \cdot 10^{-3} s^{-1}$	$1 \cdot 10^{-3} s^{-1}$
850 °C	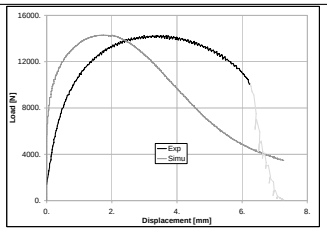	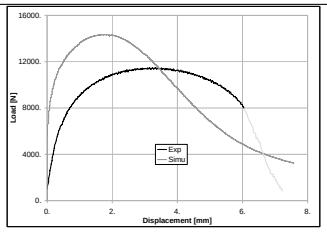	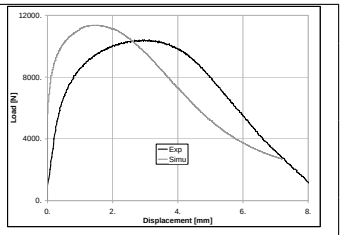
900 °C	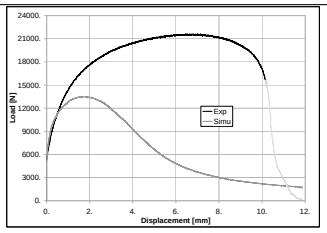	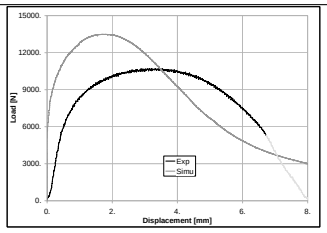	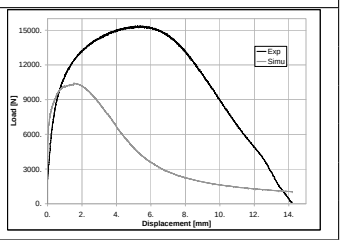
950 °C	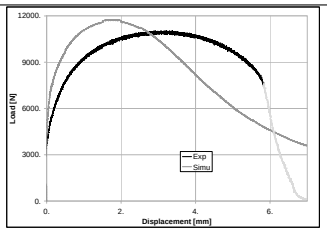	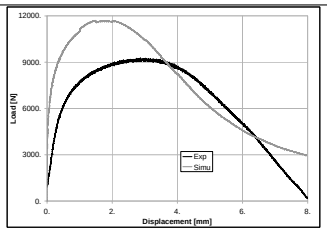	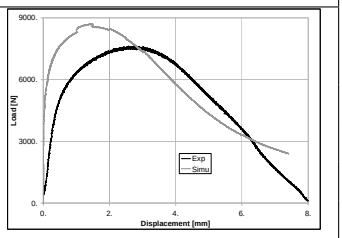

Table E.2: Macro-Meso flow curves of **A** steel grade for R4 sample shape

R2	$1 \cdot 10^{-2} s^{-1}$	$5 \cdot 10^{-3} s^{-1}$	$1 \cdot 10^{-3} s^{-1}$
750 °C		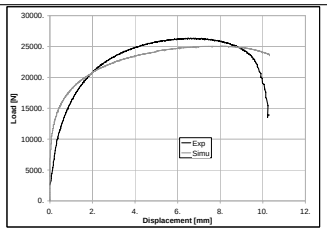	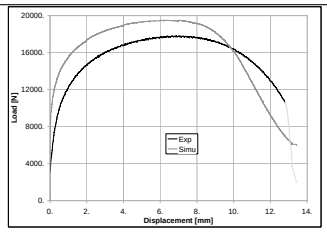
850 °C	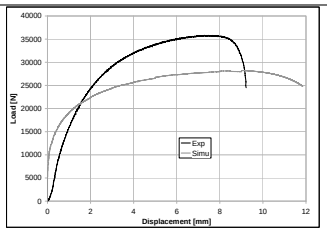	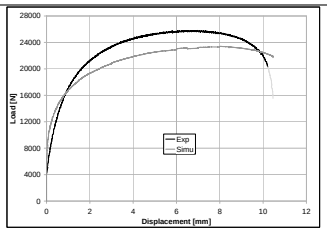	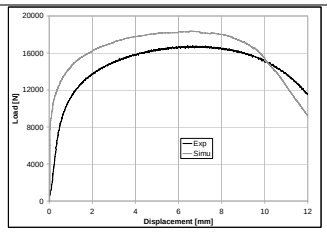
950 °C	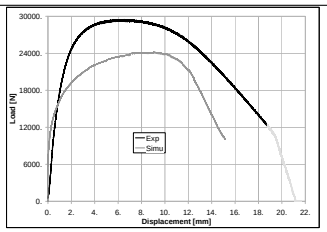	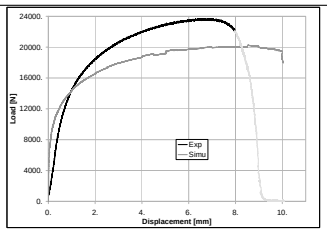	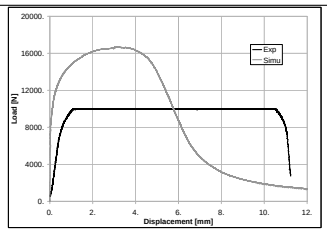

Table E.3: Macro-Meso flow curves of **B** steel grade for R2 sample shape

R4	$1 \cdot 10^{-2} s^{-1}$	$5 \cdot 10^{-3} s^{-1}$	$1 \cdot 10^{-3} s^{-1}$
750 °C	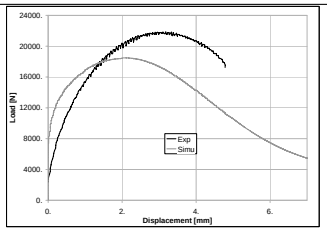	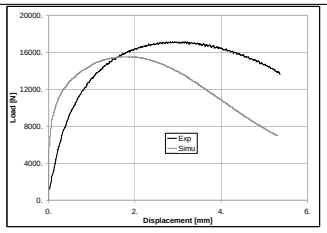	
850 °C	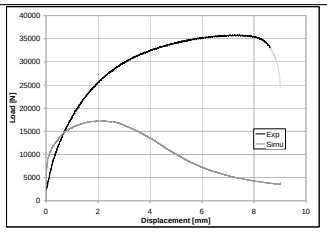	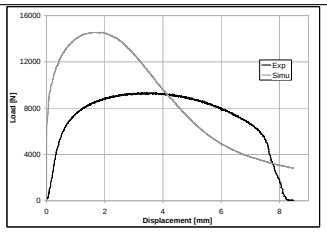	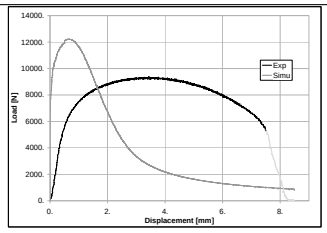
950 °C	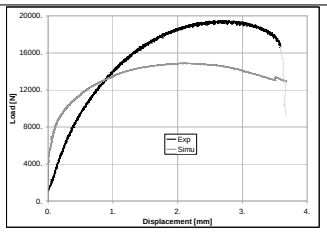	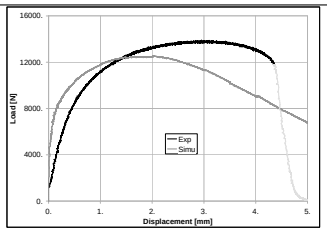	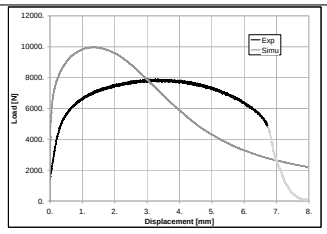

Table E.4: Macro-Meso flow curves of **B** steel grade for R4 sample shape

R2	$1 \cdot 10^{-2} s^{-1}$	$5 \cdot 10^{-3} s^{-1}$	$1 \cdot 10^{-3} s^{-1}$
700 °C	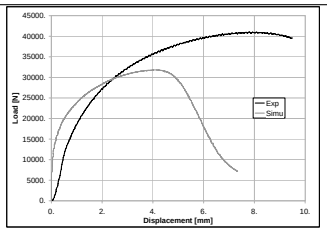	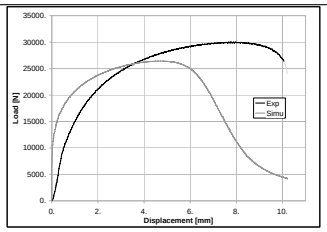	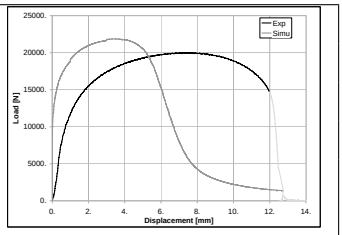
800 °C	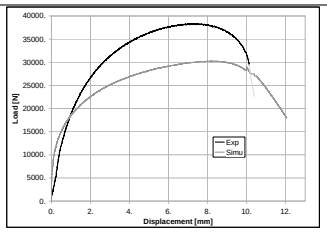	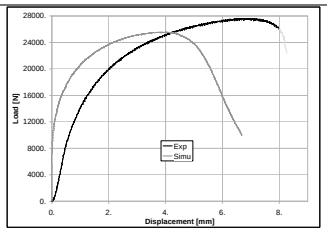	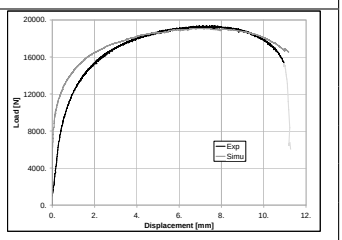
900 °C	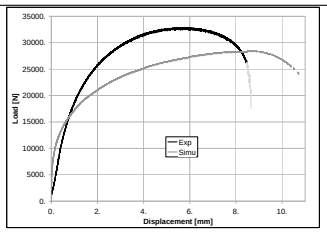	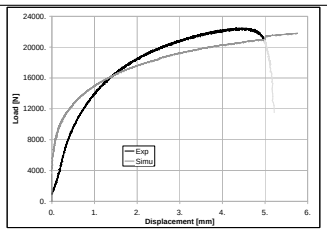	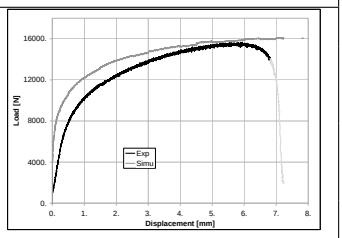

Table E.5: Macro-Meso flow curves of **C** steel grade for R2 sample shape

R4	$1 \cdot 10^{-2} s^{-1}$	$5 \cdot 10^{-3} s^{-1}$	$1 \cdot 10^{-3} s^{-1}$
700 °C	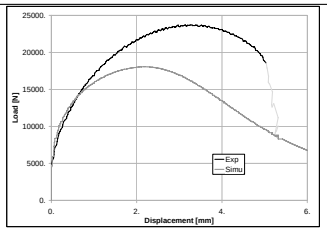	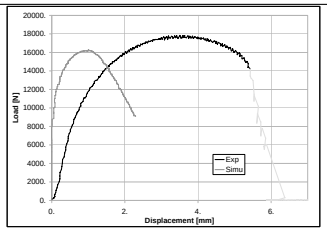	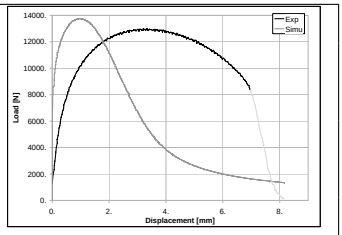
800 °C	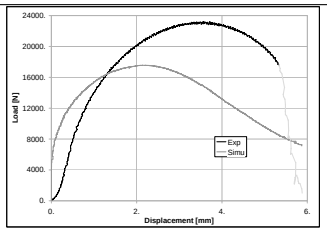	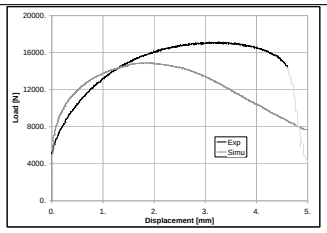	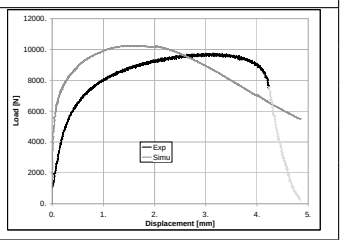
900 °C	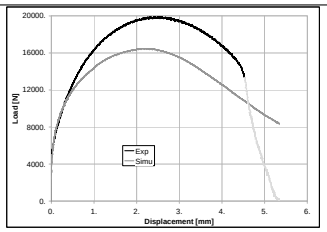	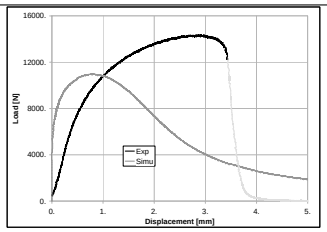	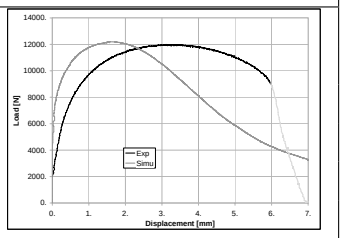

Table E.6: Macro-Meso flow curves of **C** steel grade for R4 sample shape

Appendix F

Damage moments comparison of HTT flow curves

22085B	52085B
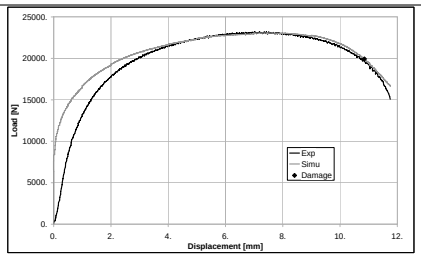	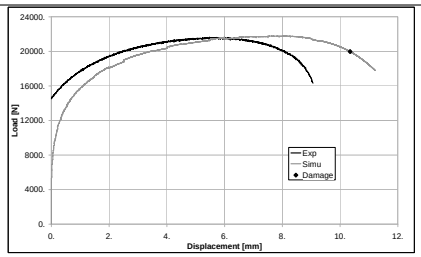
32085B	
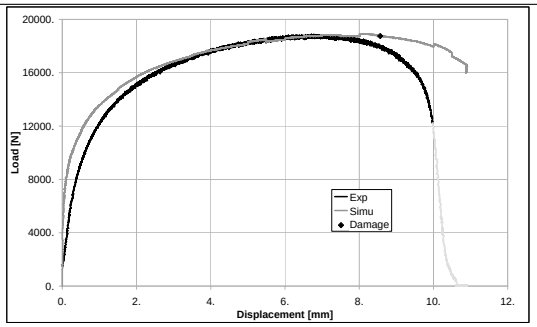	
22090B	**52090B**
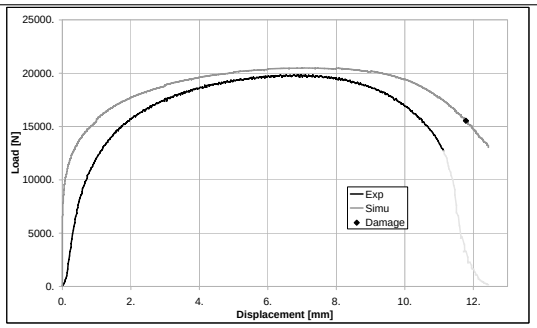	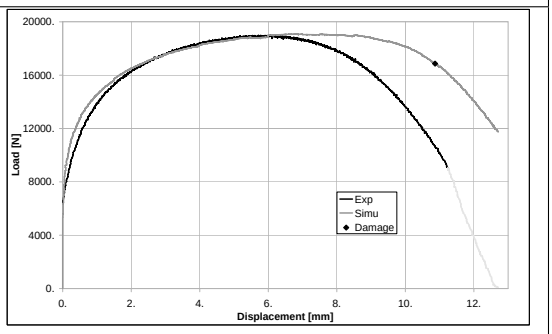
32090B	
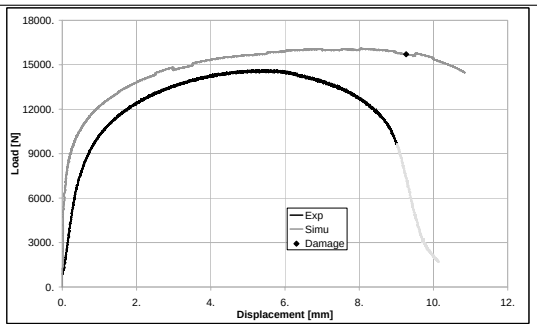	
22095B	**52095B**
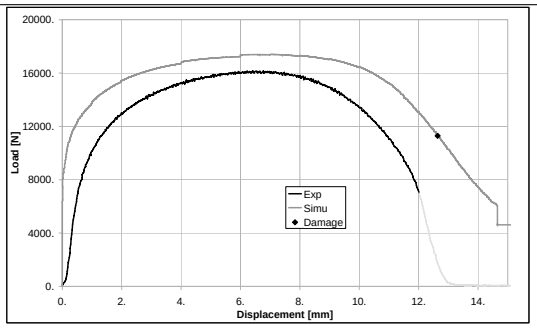	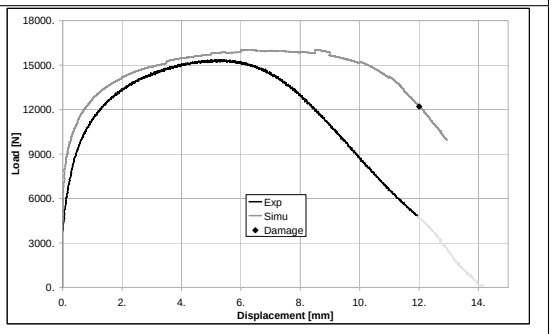

Table F.1: Macro-Meso flow curves of **A** steel grade

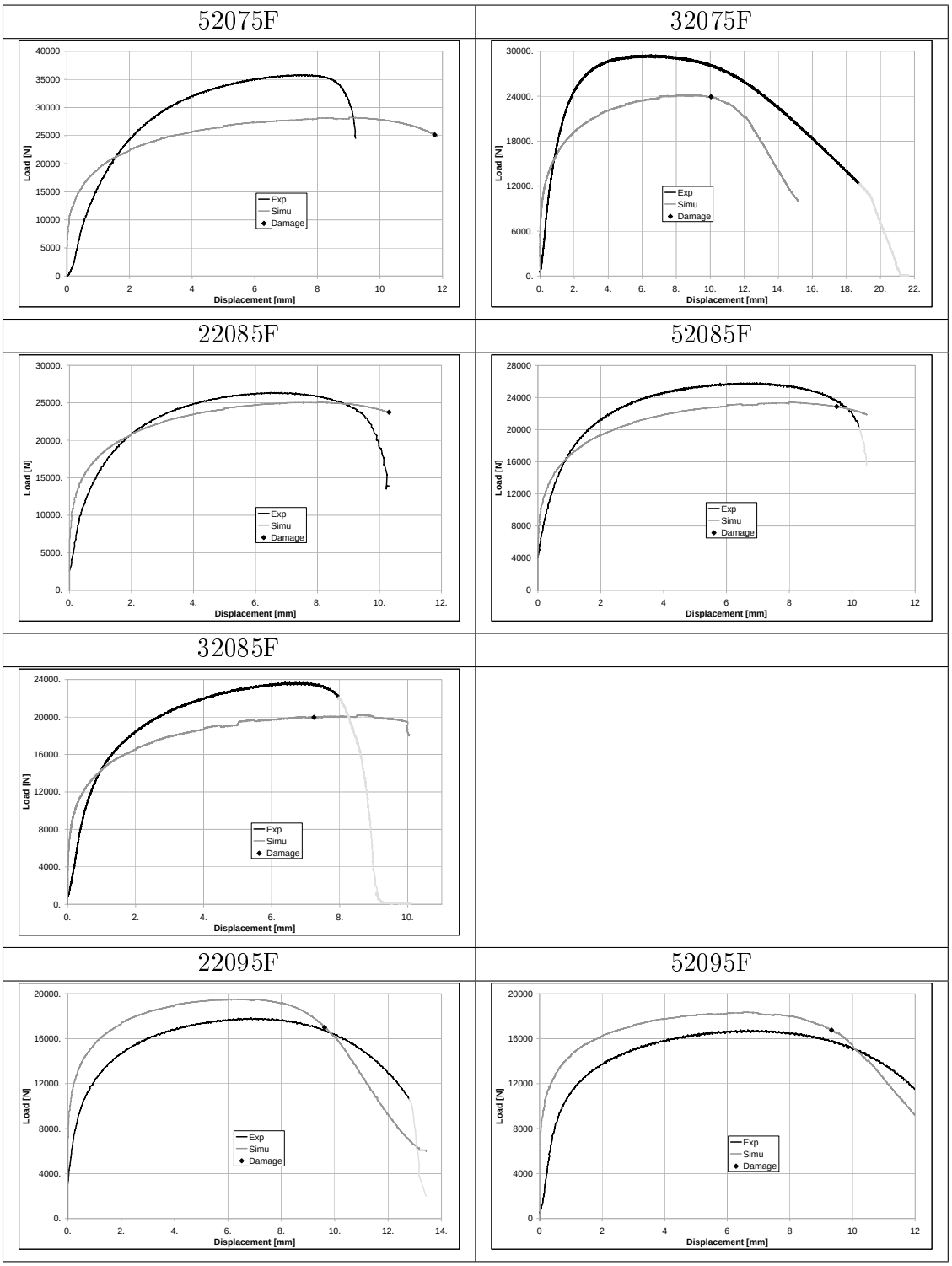

Table F.2: Macro-Meso flow curves of **B** steel grade

52070I	32070I
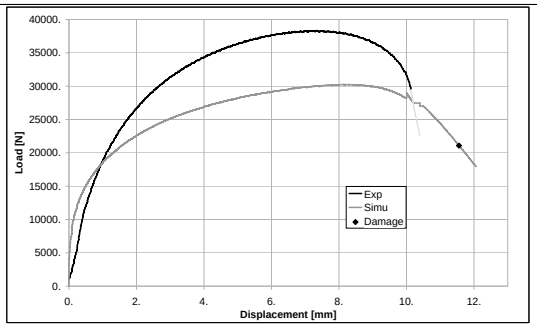	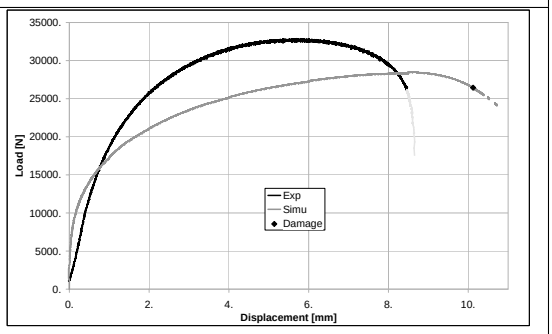
34070I	
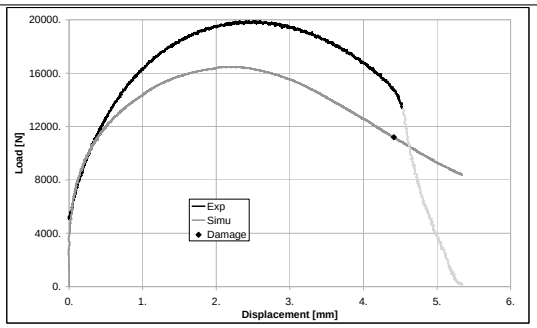	
52080I	32080I
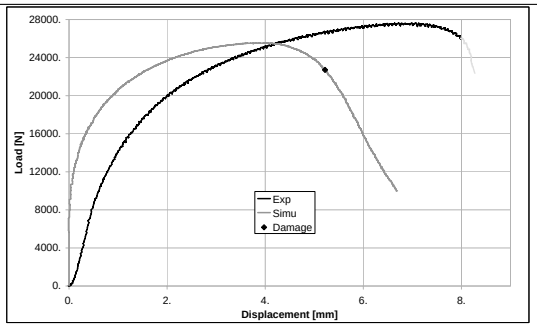	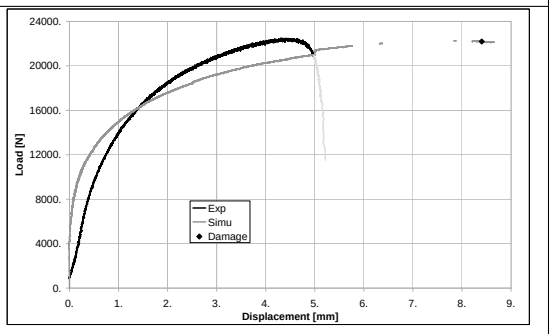
52090I	54090I
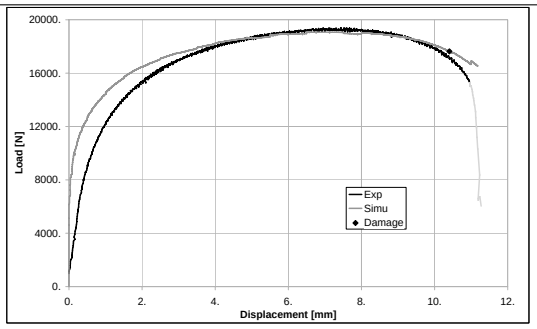	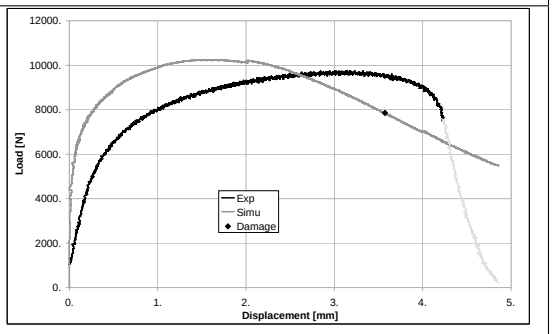
32090I	34090I
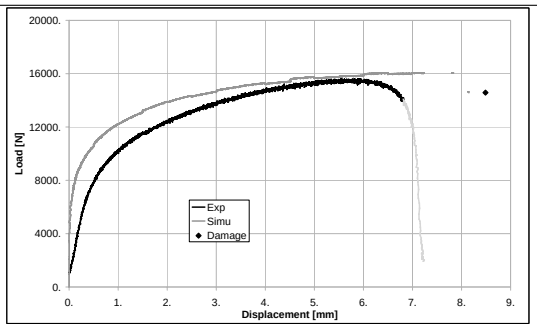	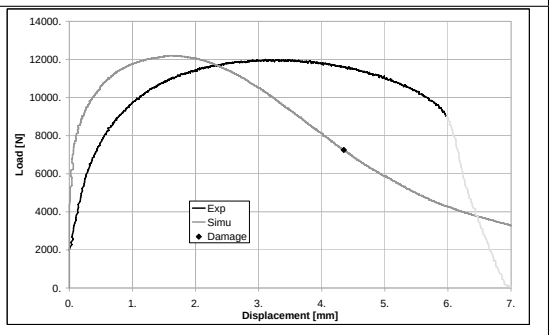

Table F.3: Macro-Meso flow curves of **C** steel grade